Modélisation multi-dimensionnelle de la propagation des ondes sismiques dans des milieux linéaires et non-linéaires

Multi-dimensional modeling of seismic wave propagation in linear and nonlinear media

Elif ORAL

Ecole Doctorale: Sciences, Ingénierie, Environnement
Spécialité: Géotecnique

Thèse présentée pour obtenir le grade de
Docteur de l'Université Paris-Est

Soutenue le 1 décembre 2016 devant le jury composé de:

Jean François Semblat	Président du jury
Luis Fabián Bonilla	Directeur de thèse
Céline Gélis	Encadrant de thèse
Donat Fäh	Rapporteur
Philippe Guéguen	Rapporteur
Fernando Lopez-Caballero	Examinateur
Harsha S. Bhat	Examinateur

Résumé

L'aléa sismique est l'un des plus importants désastres naturels qui affectent une grande population partout dans le monde. Pour cette raison, la prédiction du mouvement sismique rêvet une grande importance dans l'évaluation de l'aléa sismique dans les zones à forte densité de population, qui pourraient se localiser oú les conditions de site suscitent la susceptibilité à l'amplification sismique. Ce dernier fait partie des facteurs les plus importants en ce qui concerne le mouvement sismique conséquent. Lorsque le champ d'onde incident est suffisamment fort et la résistance du sol est relativement faible, le comportement non-linéaire introduit des changements considérables tels que l'endommagement du sol et pour les sols saturés granulaires la mobilité cyclique et la liquéfaction. Dans ce travail, j'étudie la modélisation numérique de la propagation des ondes sismiques dans des milieux complexes en 1D/2D en prenant en compte le comportement non-linéaire du sol et en basant sur la méthode des éléments spéctraux (SEM). De plus, sous les sollications sismiques très fortes, le paramètre de pression interstitielle, qui pourrait emmener le sol aux phénomènes de liquéfaction, devient très important pour les sols saturés. Dans cette étude, dans un premier temps, la propagation des ondes sismiques a été modelisée sur une composante (1C) dans les milieux linéaires et nonlinéaires en utilisant la méthode numérique des éléments spéctraux. Les rhéologies viscoélastique et nonlinéaire sont implementées par le méthode de technique des variables de mémoire et le modèle élastoplastique d'Iwan, respectivement. Ensuite, le modèle 1D - trois composantes (3C) est développé et une comparaison préalable sur l'effet de la considération des approches 1C et 3C est faite. L'effet de pression interstitielle est implementé dans le code 1D-3C et le site américain Wildlife Refuge Liquefaction Array (WRLA), qui a été frappé par le séisme de Superstition Hills en 1987 a été étudié. Le changement de la réponse du sol sous les différents hypothèses de rhéologie du sol et de mouvement d'entrée est étudié. Le mouvement calculé est noté d'être amplifié pour les basses fréquences et atténué pour les hautes fréquences en raison de l'excès de pression interstitielle dans les sols liquéfiables. Par ailleurs, il a été conclu que le sol est plus nonlinéaire sous le chargement triaxial dans l'approche 3C et plus dilatant dû à la nonlinéarite élevée. En dépit de la similitude entre les accélérations et les vitesses en surface des approches 1C et 3C, une importante différence dans le déplacement en surface entre les deux approches est notée. Les

analyses sont répétées pour deux sites japonais Kushiro Port et Onahama Port, qui ont été influencés par le séisme de Kushiro-Oki en 1993 et le séisme de la côte Pacifique de Tohoku en 2011, respectivement. Il a été montré que les changements apportés par la nonlinéarite ne sont pas identiques dans toute la gamme de fréquence concernée et l'influence du comportement des sols non-cohésives sur la propagation des ondes sismiques dépend fortement des propriétés du modèle et des conditions de chargement. Dernièrement, le code SEM est avancé en 2D en considérant les mêmes modèles implementés en 1D-3C pour la nonlinéarité du sol et les effets de pression interstitielle. Le code SEM 2D est mis en application dans un modèle de bassin sédimentaire dont la géometrie est assymmétrique et le profile du sol est composé des couches possédant différentes propriétés nonlinéaires. La propagation des ondes de P-SV et SH a été analysée sur le modèle en considérant des conditions de sol sec (analyse de contrainte totale) et saturé (analyse de contrainte effective). La differentiation du mouvement calculé en surface est très dépendante de conditions de chargement. L'analyse de contrainte effective résulte en plus de déformations dans les couches superficielles par rapport à l'analyse totale. De plus, la nonlinéarité des matériaux est traduite par la diminution de la vitésse sismique qui prolongerait la durée de propagation des ondes à l'intérieur du bassin et les reflections aux frontières de bassin-rocher entraînent plus de nonlinéarite dans les coins du bassin. Cette thèse révèle la possibilité de la modélisation du comportement nonlinéaire du sol en prenant en compte l'effet de pression interstitielle dans les études de la propagation des ondes sismiques en couplant les modèles différents avec la méthode des éléments spéctreaux. Ces analyses contribuent à l'identification et la compréhension des phénomènes majeures qui se déroulent dans les couches superficielles en respectant les conditions locales et les mouvements d'entrées, ce qui rend ce travail très important pour les études spécifiques de sites.

Mots-clés: Propagation des ondes sismiques, nonlinéarité du sol, mobilité cyclique, viscoélasticité, méthode des éléments spéctraux.

Abstract

Earthquakes are one of the most significant destructing natural hazards affecting a large population worldwide. For this reason, ground motion predictions are critical to evaluate the seismic hazard in highly populated areas, which in some cases, are located on site conditions prone to seismic amplification. Soil amplification is one of the most important factors affecting the earthquake ground motion. When the incident wave field is strong enough and the soil strength is relatively weak, nonlinear material behavior appears, introducing important changes such as soil degradation, and if the material is granular and water saturated, cyclic mobility and liquefaction. In this work, I study the numerical modeling of wave propagation in 1D/2D complex media that include nonlinear soil behavior under the framework of the spectral element method (SEM). The consideration of soil nonlinearity holds an important place in order to achieve simulations consistent with real observations for strong seismic shaking. Additionally, in the presence of strong ground motion in saturated soils, pore pressure becomes an important parameter to take into account for related phenomena such as flow liquefaction and cyclic mobility. In this study, first, one component (1C) - seismic wave propagation is modeled in linear and nonlinear media in 1D based on the spectral element numerical method. Viscoelastic and nonlinear soil rheologies are implemented by use of the memory variables technique and Iwan's elastoplastic model, respectively. Then, the same study is extended to a 1D - three component (3C) model and a preliminary comparison on the effect of using 1C and 3C approaches is made. Then, the influence of excess pore pressure development is included in the 1D-3C model and the developed numerical model is applied to realistic case on the site of Wildlife Refuge Liquefaction Array (USA) which is affected by the 1987 Superstition Hills event. The ground motion modification for different assumptions of the soil rheology in the media and different input motions is studied. The calculated motion is found to be amplified on low frequency and damped in high frequency range due to excess pore pressure development. Furthermore, the soil is found to be more nonlinear under triaxial loading in 3C approach and more dilatant due to higher nonlinearity. Despite the similitude in surface acceleration and velocity results, significant differences in surface displacement results of 1C and 3C approaches are remarked. Similar analyses are performed on two Japanese sites Kushiro Port and Onahama Port, which are influenced by the 1993 Kushiro-Oki and the

2011 off the Pacific coast of Tohoku earthquakes, respectively. It has been shown that the nonlinearity-related changes are not homogeneous all over the concerned frequency band and the influence of cohesionless soil behavior on wave propagation is highly dependent on model properties and loading conditions. Lastly, the 2D SEM code is developed by taking into account soil nonlinearity and pore pressure effects similarly to 1D-3C SEM code. The developed 2D SEM code is applied to a 2D sedimentary basin site where the basin geometry is asymmetrical and soil profile consists of layers with different nonlinearity properties. P-SV and SH 2D wave propagation considering dry (total stress) and saturated (effective stress) soil conditions are performed. The calculated surface motion differs significantly as a function of the input motion loading conditions and the resultant deformation in superficial layers can be very high in effective stress analysis compared to total stress analysis. Furthermore, material nonlinearity is traduced by a reduction of the seismic wave speed making wave propagation takes longer time inside basin media and the reflections on bedrock-basin boundaries lead the soil in basin edges to higher nonlinearity. This study shows the possibility of modeling nonlinear soil behavior including pore pressure effects in seismic wave propagation studies by coupling different models with spectral element method. These analyses help identifying and understanding dominant phenomena occurring in superficial layers, depending on local conditions and input motions. This is of great importance for site-specific studies.

Acknowledgements

I feel the necessity of reminding the reader that this manuscript, which will be considered quite limited in a very close future given the fast-growing technology and human demands, represents the "permanent" effort of a 3 years work.

I owe the highest gratitude to Fabian, Céline and Élise for everything that they contributed to my life in such a short time not only scientifically but also in sense of humanity. We have a saying that the Earth keeps turning for the sake of kindhearted people. No doubt that you are the protagonists of them!

I would like to thank also to dear jury members for devoting time to the review and examination of my study.

Il ne faut pas oublier remercier Louise Attaque pour avoir composé la chanson "Léa" (See http://www.youtube.com/watch?v=aGJC0KAPeYA), qui m'a inspirée d'apprendre passionnément français et éventuellement de venir jusqu'à Paris en tant que quelqu'un qui n'imaginait jamais de faire une thèse. Grace à eux, j'ai connu des gens adorables à travers cette aventure. Merci beaucoup vivement à tout le personnel de Berssin (y compris tous les membres de la secte de banane) et 7ème/8ème étage de Fahrenheit! Je garderai toujours votre soutien et les souvenirs de 3 ans avec moi. Je remercie aussi les chercheurs de l'IFSTTAR, les participants de Groupe Iwan pour leur aide à mon travail.

Elbette her daim gönlümden geçeni yapmam için desteğini esirgememiş olan, hayatımı daha eğlenceli ve anlamlı kılan kocaman kalpli çekirdek aileme ve de Trabzon, İzmir, Ankara, İstanbul, Paris, Avrupa ve dünyanın farklı köşelerine dağılmış ama yanımda olmayı başaran biricik arkadaşlarıma ayrıca çok teşekkür ediyorum (here the author thanks a lot to all of her beloved friends from all around the world!).

Table of contents

List of figures

List of tables

General Introduction

Numerous studies have shown that the ground response at a specific site is strongly controlled by local soil properties like the impedance contrast between the bedrock and overlying layers (e.g. Kramer, 1996 [91]), constitutive material model and incident motion complexity (e.g. Gélis and Bonilla, 2012 [52]; 2014 [53]) and site geometry (e.g. Graves, 1993 [55]; Moczo et al., 1996 [117]; Olsen and Archuleta, 1996 [120]). Site effects may produce locally severe damages, even for a moderate earthquake at long distances. In addition, heavy damages can take place when structures resonate with amplified frequencies by the soil response, as clearly seen in the 1985 Michoacan earthquake (Seed et al., 1988 [141]; Singh et al., 1988 [145]). Thus, any evaluation of seismic hazard should include the study of site effects.

Many observations from past earthquakes, for example, the 1994 Northridge, 1995 Hyogo-Ken Nanbu (Kobe), 1999 Chi Chi, 2000 Tottori (Japan), 2011 Tohoku earthquakes (Aguirre and Irikura, 1997 [1]; Field et al., 1998 [45]; Roumelioti and Beresnev, 2003 [134]; Kokusho, 2004 [86]; Pavlenko and Irikura, 2006 [123]; Bonilla et al., 2011 [18]) as well as laboratory data (e.g. Seed and Idriss, 1969 [140]; Vucetic and Dobry, 1991 [158]; Darendeli, 2001 [25]) show that nonlinear soil response is pervasive during strong motion. High energy dissipation and shear modulus decrease due to nonlinearity may lead the soil to lose its strength significantly and this could result in longer duration of wave propagation by increasing the contrast between soil layers and in higher amplification in some frequency bands (e.g. Gélis and Bonilla, 2012 [52]). The nonlinear soil behavior could be modeled using several methods. Traditionally, it is approximated by the equivalent linear method (Schnabel et al., 1972 [139]). This method has widely been used because few parameters and low computational time effort are required (Bardet et al., 2000 [11]; Kausel and Assimaki, 2002 [82]). However, under high level of input motion, the equivalent linear method is found to overestimate the material strength (Joyner and Chen, 1975 [79]; Yoshida and Iai, 1998 [160]; Hartzell et al., 2004 [61]; Stewart et al., 2008 [149]; Kaklamanos et al., 2015 [80]). Conversely, nonlinear soil consitutive models based on stress-strain relationship of soil under cyclic behavior have been used in nonlinear site analyses. Some of the past studies

evaluate successfully one-component (1C) shear wave propagation (Lee and Finn, 1978 [96]; Pyke, 2000 [128]; Hashash and Park, 2001 [64]; Bonilla et al., 2005 [16]). On the other hand, many researchers contributed to the development of nonlinearity models with multiaxial interaction making it possible to model soil nonlinearity on three-component (3C) (Mroz, 1967 [118]; Dafalias and Popov, 1977 [24]; Prevost, 1977 [126]; Wang, 1990 [159]). Nevertheless, many of these models require a lot of parameters to define soil nonlinearity. In our study, we choose the Masing-Prandtl-Ishlinskii-Iwan (MPII) model based on the formulation of Iwan (1967) [76] for nonlinearity as adopted in Joyner and Chen (1975) [79], Joyner (1975) [78], Gandomzadeh (2011) [48], Santisi d'Avila et al. (2012) [137], Pham (2013) [125]. MPII models the nonlinearity by a set of nested yield surfaces consisting of simple elastic springs and Coulomb friction elements. It requires only the modulus reduction ratio as a function of strain for the modeled soil which is readily obtained from laboratory data or the literature for a wide soil class (Vucetic and Dobry, 1991 [158]; EPRI, 1993 [39]; Ishibashi and Zhang, 1993 [73]; Darendeli, 2001 [25]). In such approach, the damping is related to the stress-strain hysteretic behavior at soil that follows Masing criteria (Masing, 1926 [106]). Thus, at low strain, this model does not take into account any damping coming from nonlinearity. To that respect, this elastoplastic model is not realistic at low strain, since, when travelling in the Earth, seismic waves are attenuated due to intrinsic attenuation of materials during their propagation. In some nonlinear models, this viscous attenuation is implemented by means of Rayleigh damping model and its variations where the attenuation is frequency-dependent (e.g. Park and Hashash, 2004 [122]; Gandomzadeh, 2011 [48]). As an alternative, viscoplastic rheological models can be used, which in turn requires determination of many parameters for soil (e.g. di Prisco et al., 2007 [34]). Here, we model the total energy dissipation in visco-elastoplastic soil models as the sum of viscoelastic attenuation and hysteretic attenuation similarly to Assimaki et al. (2011) [9]; Gélis and Bonilla (2012 [52], 2014 [53]).

Moreover, the stiffness of cohesionless saturated soils may change further due to excess pore pressure development under undrained cyclic loading (Ishihara, 1985) [74]. Soil behavior changes between contractive and dilatant manners in cyclic mobility. It has been shown that this may lead the soil to have sudden change in strength. Particular characteristics such as high frequency spiky waveforms in accelerograms after certain earthquakes can be related to these sudden changes in soil strength (Iai et al., 1995 [71]; Bonilla et al., 2005 [16]; Bonilla et al., 2011 [18]; Laurendeau et al., 2016 [95]). In order to take into account cyclic mobility in seismic wave propagation, effective stress analysis is used for cohesionless liquefiable soils. For the purpose of modeling pore pressure effects, we follow the time evolution of

shear work. Indeed, laboratory experiments have shown that pore pressure is proportional to time evolution of shear work during cyclic loading (Towhata and Ishihara, 1985 [154]). Iai et al. (1990) [69] extended the model to also simulate the cyclic mobility using few parameters that can easily be obtained by laboratory data (Iai et al., 1990 [69]; 1995 [71]; Bonilla et al., 2005 [16]). More recently inversion of recorded ground motion on vertical arrays has permitted to compute the same parameters (Roten et al., 2013 [131]; 2014 [132]).

Such constitutive models can be coupled with the wave propagation equations to simulate strong motion propagation in subsurface layers. Many numerical methods can be used to solve the seismic wave equations. One of the most commonly used method is the finite difference method (FDM), which has been extensively studied by many researchers (Madariaga, 1976 [101]; Virieux, 1986 [157]; Levander, 1988 [97]; Graves, 1996 [56]; Saenger et al., 2000 [135]; Moczo et al., 2002 [116]). Although its implementation is relatively straightforward, FDM can present some limitations in modeling non planar topographies or complex interfaces inside the medium. Another approach which facilitates the adaptation of mesh to complex geometries in 3D is the finite element method (FEM) (Lysmer and Drake, 1972 [100]; Marfurt, 1984 [104]; Bielak et al., 2005 [13]). However, the global mass matrix needs to be inverted at each time step, which results in heavy time computations. Combining different methods such as FDM and FEM has been proposed by several researchers as a solution (e.g. Moczo et al., 1997 [114]; De Martin et al., 2007 [31]; Ducellier and Aochi, 2012 [35]). As a promising alternative approach, the discontinuous Galerkin finite element method (DGM) is based on exchange of numerical fluxes between adjacent elements and provide high order direct solution (Käser and Dumbser, 2006 [81]; Delcourte et al., 2009 [33]; Etienne et al., 2010 [41]; Peyrusse et al., 2014 [124]). The spectral element method (SEM), which is another high-order finite element method, has been used in geophysics since years for seismic wave propagation modeling (Faccioli et al., 1997 [42]; Komatitsch and Vilotte, 1998 [89]; Seriani, 1998 [143]; Ampuero and Vilotte, 2002 [3]; Festa and Vilotte, 2005 [44]; Mercerat et al., 2006 [112]; Delavaud, 2007 [32]; Smerzini et al., 2011 [146]). It provides easiness of mesh adaptability to complex geometries with higher precision than finite difference and low-order finite element methods. Some recent studies using SEM for seismic wave propagation take into account nonlinear soil behavior (Stupazzini and Zambelli, 2005 [151]; di Prisco et al., 2007 [34]; Stupazzini et al., 2009 [150], He et al., 2016 [66]). In our work, we take advantage of the numerical method choice of SEM in sense of precision, mesh adaptability easiness for medium variability and computation time.

Main objective of this study is to understand the seismic wave propagation in complex media such as sedimentary basins and soil profiles with subsurface heterogeneity by taking into account soil nonlinearity and excess pore pressure development. For this purpose, we develop a numerical tool for numerical modeling of seismic wave propagation in linear and nonlinear media, by means of coupling relative simple soil constitutive models. In addition to elastic parameters (density, shear and pressure wave velocities, thickness, attenuation), we need cohesion and friction angle for total stress analysis (nonlinearity with no pore pressure effects). Finally, if pore pressures are seek (effective stress analysis), we need 4 additional parameters (Iai et al. 1990 [69] model parameters). Thanks to relative easiness of model requirements in terms of parameter number, our code provides easiness of adaptation to model different types of soils such as dense or loose soils consolidated under different conditions. In 1D wave propagation modeling, we extend the 1D-1C spectral element code developed during the PhD thesis of Delavaud (2007) [32] for an elastic linear medium to 1D-3C and couple it first with viscoelastic model of Liu and Archuleta (2006) [98], then with the MPII model for nonlinearity and at last with the Iai et al. (1990) [69] model for pore pressure development effects. For the coupling of nonlinearity with pore pressure effects, we benefit from the study of Pham (2013) [125] who models 1D-3C seismic wave propagation based on finite element method. The work of Pham (2013) [125] is the extension of previous studies on finite-element wave propagation modeling in nonlinear media without pore pressure effects (Gandomzadeh, 2011 [48]; Santisi d'Avila et al. 2012 [137]). We carry this chain of work forward with this thesis by taking advantage of spectral element method modeling.

Furthermore, strong motion recordings in Mexico city during the 1985 Michoacan earthquake reveals that the observed large amplifications were related to the trapping of waves inside the Mexico sedimentary basin, leading to a strong amplification of wave propagation at a period related to the basin properties (shape and mechanical properties) (Sanchez-Sesma et al. 1998 [136], Kawase and Aki, 1989 [83]). Heavy damages on structures related to the amplification of ground motion due to topographic effects in past earthquakes such as the 1909 Lambesc earthquake (Angot, 1910 [4]), the 1984 Loma Prieta earthquake (Hartzell et al., 1984), the 1985 Chile earthquake (Celebi and Hanks, 1986 [20]), the 1999 Athens earthquake (Gazetas et al., 2002 [49]; Assimaki et al., 2005 [8]) can be shown as evidence of the influence of superficial geological layers. Apart from such recordings, multi-dimensional modeling allows to study these effects. Many studies model the wave propagation in 2D and 3D basin models with complex geometries. As example to small sedimentary basin models, past studies on Nice model (Gelis et al., 2008 [51]; Gandomzadeh, 2011 [48]), Grenoble

model (Bonilla et al., 2006 [17]; Stupazzini et al., 2009 [150]) in France, central Italian basin model (Smerzini et al., 2011 [146]) and Rome model (Bonilla et al., 2010 [15]) in Italy can be cited. Among large-scale models, California basin (Olsen and Archuleta, 1996 [121]; Komatitsch et al., 2004 [87]; Roten et al., 2012 [133]), Caracas basin (Venezuela) (Delavaud, 2007 [32]) have been studied. Among these studies that consider elasticity in the modeled media (e.g. Olsen and Archuleta, 1996 [121]; Delavaud, 2007 [32]; Smerzini et al., 2011 [146]) compare multi-dimensional modeling with 1D and show that interference of refracted waves with the basin geometry results in surface wave formation at basin edges in multi-dimension and as a result inside the basin wave propagation is amplified and longer. Roten et al. (2012) [133] models wave propagation in Wasatch Fault (Utah, USA) in 3D and include soil nonlinearity in 1D, such that interaction of nonlinear response with multi-dimensional effects is not studied in a fully multi-dimensional nonlinear approach. Other studies that take into account soil nonlinearity (Bonilla et al., 2006 [17]; Stupazzini et al., 2009 [150]; Bonilla et al., 2010 [15]; Gandomzadeh, 2011 [48]) compare linear and nonlinear approaches and reveal that under high nonlinearity (where shear strength of the soil is decreased considerably), basin response is exposed to a notable attenuation. In some of the models of aforementioned studies, energy shift to lower frequencies is noted such that wave propagation duration becomes longer due to lowered medium velocity under nonlinearity. In Stupazzini et al. (2009) [150], nonlinearity is shown to lead to higher PGV values in basin edges. Some of the other studies which model the wave propagation in multi-dimensional nonlinear media are Takemiya and Adam, (1998) [152], Hartzell et al., (2002) [62], Roten et al., (2009) [130], Dupros et al. (2010) [37], Gelagoti et al. (2010) [50], Gélis and Bonilla (2012 [52], 2014 [53]); He et al., 2016 [66]. Given the influence of multi-dimensional effects in wave propagation, in our study, we also model the 2D P-SV and SH seismic wave propagation in nonlinear media. In addition to nonlinear analysis, we take into account pore pressure effects in liquefiable soils, differently than the aforementioned studies. For this purpose, we make use of the version 2.3.8 of the 2D spectral element code of SEM2DPACK (Ampuero, 2002 [2]). It is an open source code to use of scientific community and all the versions of the code are available in http://sourceforge.net/projects/sem2d/files/sem2dpack/ address. SEM2DPACK provides P-SV and SH modeling of wave propagation by accounting for different source mechanisms in a 2D medium. Some of the applications of SEM2DPACK cover the modeling of dynamic rupture on non-planar faults and seismic wave radiation (Madariaga et al., 2006 [102]), fault reflections from fluid-infiltrated faults (Haney et al., 2007 [59]), non-linear wave propagation in damaged rocks (Lyakhovsky et al., 2009 [99]), wave propagation around a prototype nuclear waste storage tunnel (Smith and Snieder, 2010 [147]), benchmark for wave propagation in heterogeneus media (O'Brien and Bean, 2011

[119]) and dynamic rupture model of the 2012 off-Sumatra earthquake (Meng and Ampuero, 2012 [108]). Within the scope of this thesis, we have contributed to SEM2DPACK new features regarding the nonlinear behavior of surficial soil layers.

Moreover, the verification and validation of numerical codes holds a great importance for further uses of the codes in future studies in terms of ground motion prediction. Verification is made through the comparisons of the solutions of different numerical codes. For validation, the calculated solutions are compared to the observations by means of recorded data. In this sense, borehole and surface records in the studied site models are needed. Thus far, certain benchmarks are organized for verification and validation of numerical codes. One of the benchmarks of verification of 1D/2D/3D numerical wave propagation codes is organized for the 3rd international symposium on the effects of surface geology (ESG 2006) (Chaljub et al., 2007 [21]; Dumbser et al., 2007 [36]; Tsuno et al., 2009 [155]). Alpine valley of Grenoble (France) is used as the test model in this benchmark. The comparisons made between 18 different numerical codes (1D, 2D and 3D) have shown a satisfactory agreement between the codes up to 2 Hz. Amplification of ground motion due to multi-dimensional effects is found to be overestimated in elasticity and underestimated in 1D numerical modeling. EUROSEISTEST verification and validation project (E2VP) is arranged as a follow-up benchmark to ESG2006 by 2D and 3D modeling of target site of Mygdonian basin in Greece (Mauffroy et al., 2015 [107]; Gélis et al., 2016) for verification and validation of numerical codes. The ground motion predictions of the solution of six participants are shown to be in satisfactory agreement up to 4 Hz. In addition, another benchmark is organized by the Pacific Earthquake Engineering Research Center (PEER) (USA) for verification of codes of wave propagation modeling in 1D nonlinear media by comparison to 1D vertical array data (Kwok et al., 2006 [93]; PEER, 2008). In this benchmark, equivalent linear method is compared to fully nonlinear analyses and it has been shown that better estimation of ground motion is obtained in nonlinear analysis under the loading of strong input motion that exerts higher strains (such as 1%). Another international benchmark on 1D nonlinear site response is PRENOLIN project , in which 23 nonlinear numerical codes are involved (Régnier et al., 2016 [129]). The benchmark consists of an initial verification phase on 1D canonical models (theoretical models which are not based on real data) and a validation phase where the tests are performed for japanese sites monitored by K-Net and KiK-NET network. It is the first benchmark in which borehole data is used for validation. Main differences between the codes due to nonlinearity are found to arise from constitutive models that may differ by viscous damping implementation and nonlinear shear strength representation. During this thesis, we participated with 1D-1C nonlinear SEM code in the Iwan group benchmark

which is organized in the framework of PRENOLIN project for the verification of numerical codes using MPII model of Iwan (1967) [76] (Mercerat et al., 2016). Also, the 1D-1C SEM code is verified for viscoelasticity on realistic models and 1D-3C SEM code is validated in American liquefaction site model of Wildlife Refuge Liquefaction Array for three-component nonlinearity with pore pressure effects. Lastly, the 2D SEM code that we use in our study (SEM2DPACK) is verified in several benchmarks for 2D wave propagation (De la Puente et al., 2007 [30]; 2009 [29]; O'Brien and Bean, 2011 [119]).

In this work, first, the spectral element method and the soil constitutive models that we use in our study (Liu et al, 2006 [98] model for viscoelasticity; MPII model of Iwan (1967) [76] for nonlinearity and Iai et al. (1990) [69] for pore pressure effects) are explained with main formulations of the models in Chapter 1. Second, the 1D-1C wave propagation modeling for viscoelastic and nonlinear media is studied and verification tests are shown in Chapter 2. A sensitivity analysis is performed in the 1D-1C SEM code for the effect of spectral element polynomial degree, Iwan spring number (plasticity surface number) for nonlinearity and choice of soil constitutive model on precision of the solution and computational cost is explored at the end of the chapter. Afterwards, the 1D-3C wave propagation modeling on a canonical model and validation of the 1D-3C nonlinear SEM code with pore pressure effects on Wildlife Refuge Liquefaction Array model are detailed in Chapter 3. In the same chapter, two more applications of the 1D-3C SEM code on real liquefaction site models are analyzed. Then, in Chapter 4, the verification tests on the developed 2D nonlinear SEM code with pore pressure effects are shown by comparisons with 1D SEM code results. In Chapter 5, the 2D P-SV and SH wave propagation modeling in a sedimentary basin model are discussed for total and effective stress analyses using broadband simple impulse signals with different PGA intensities. Finally, in Chapter 6, general conclusions of the study are developed after the obtained results and perspectives for further studies concerning 1D and 2D SEM wave propagation modeling are listed.

Chapter 1

Principles of wave propagation modeling in linear and nonlinear media

Principles of wave propagation modeling in linear and nonlinear media

1.1 Introduction

In this chapter, the methods that are employed in this thesis are explained. First, the numerical method of spectral element is presented with keynotes. Second, soil constitutive models for elastic and inelastic soil rheologies are shown. Thus, viscoelasticity model of Liu and Archuleta (2006) [98], nonlinearity model of MPII (Iwan, 1967) [76] and liquefaction front model of Iai et al. (1990) [69] used throughout this work are explained in depth. Principal theory behind the methods and the scheme of their implementation into spectral element code are detailed.

1.2   Spectral element method

1.2.1   Theoretical formulation

Many numerical methods can be used to solve the seismic wave equations. One of the most commonly used method is the finite difference method (FDM), which has been extensively studied by many researchers (Madariaga, 1976 [101]; Virieux, 1986 [157]; Levander, 1988 [97]; Graves, 1996 [56]; Saenger et al., 2000 [135]; Moczo et al., 2002 [116]). Although its implementation is relatively straightforward, FDM can present some limitations in modeling non planar topographies or complex interfaces inside the medium. Another approach which facilitates the adaptation of mesh to complex geometries in 3D is the finite element method (FEM) (Lysmer and Drake, 1972 [100]; Marfurt, 1984 [104]; Bielak et al., 2005 [13]). However, the global mass matrix needs to be inverted at each time step, which results in heavy time computations. Combining different methods such as FDM and FEM has been proposed by several researchers as a solution (e.g. Moczo et al., 1997 [114]; De Martin et al., 2007 [31]; Ducellier and Aochi, 2012 [35]). As a promising alternative approach, the discontinuous Galerkin finite element method (DGM) is based on exchange of numerical fluxes between adjacent elements and provide high order direct solution (Käser and Dumbser, 2006 [81]; Delcourte et al., 2009 [33]; Etienne et al., 2010 [41]; Peyrusse et al., 2014 [124]). The spectral element method (SEM), which is another high-order finite element method, has been used in geophysics since years for seismic wave propagation modeling (Faccioli et al., 1997 [42]; Komatitsch and Vilotte, 1998 [89]; Seriani, 1998 [143]; Ampuero and Vilotte, 2002 [3]; Festa and Vilotte, 2005 [44]; Mercerat et al., 2006 [112]; Delavaud, 2007 [32]; Smerzini et al., 2011 [146]). It provides easiness of mesh adaptability to complex geometries with higher precision than finite difference and low-order finite element methods. Some recent studies using SEM for seismic wave propagation take into account nonlinear soil behavior (Stupazzini and Zambelli, 2005 [151]; di Prisco et al., 2007 [34]; Stupazzini et al., 2009 [150], He et al., 2016 [66]). In our work, we take advantage of the numerical method choice of SEM in sense of precision, mesh adaptability easiness for medium variability and computation time. In this section, a detailed explanation of the formulation of the spectral element method for solving seismic wave equation is made.

In a medium which makes part of an open domain $\Omega \subset \mathbb{R}^d$ in real number set of dimension d, the displacement field u for a given time t in $t \in \mathbb{I}$ can be defined as $u : \Omega \times \mathbb{I} \to \mathbb{R}^d$, where time domain of interest is $\mathbb{I} = [0, T] \in \mathbb{R}_+$. In such a medium, the equation of wave motion can be expressed by the Euler-Lagrange equation of elastodynamics as Equation 1.1.

$$\rho \dot{v} = div(\sigma) + f \tag{1.1}$$

where $\rho(x)$ is mass density, $f(x,t)$ is external body force and σ is symmetrical Cauchy stress tensor as $\sigma : \Omega \times \mathbb{I} \to S \in \mathbb{R}^{d \times d}$. S is subspace of symmetrical second order tensors of dimension $d(d+1)/2$.

The Equation 1.1 is also called the strong formulation of wave motion and requires heavy computational time in order to be solved. By integrating the Equation 1.1 and multiplying with a test function w, the weak (variational) formulation is obtained as shown in Equation 1.2.

$$\int_{\Omega} \rho \dot{v} w d\Omega = \int_{\Omega} f w d\Omega - \int_{\Omega} \sigma : \nabla w d\Omega \tag{1.2}$$

The variational formulation of the elastodynamics equation considers the associated space of admissible displacement variations at a given time t so that $S^t := u(x,t) : \Omega \times \mathbb{I} \to \mathbb{R}^d | u \in H^1(\Omega)^d \forall t \in \mathbb{I}$. In this consideration, $H^1(\Omega)$ denotes the space of vector fields defined on Ω that are square integrable and have square integrable first-order partial derivatives in space, over the domain Ω. Then, the associated space of admissible displacement variations at a given time t is $\delta S := w(x) : \Omega in \mathbb{R}^d | w \in H^1(\Omega)$. In the variational formulation, velocity-displacement couple of (u,v) is searched in $S^t \times S^t$ for $\forall w \in \delta S$ and $\forall t \in \mathbb{I}$.

In order to insure the spatial discretization, the solution is considered to belong to a subspace $S^{t,h}$ of S^t where h holds for a dimension-related parameter. With this consideration, the solution $u^h \in S^{t,h}$ is searched for each test function $w^h \in S^{t,h}$ and for each time $t \in \mathbb{I}$. This approach is called Galerkin approximation and the weak formulation can be rewritten as follows:

$$\int_{\Omega} \rho \dot{v}^h w^h d\Omega = \int_{\Omega} f w^h d\Omega - \int_{\Omega} \sigma : \nabla w^h d\Omega \tag{1.3}$$

In finite element methods, the Equation 1.3 is solved by means of discretization of the domain Ω. Numerical integration is applied on integration points based on basis functions. For determination of integration points, several rules can be referred to. One of the main characteristics of the spectral element method is the choice of integration rule. Instead of using integration rules such as Simpson rule or trapezoidal rule where the integration is based on solutions by interval, SEM uses a quadrature rule. In 1D, a quadrature rule provides the

following approximation for an integral:

$$\int_b^a f(x)dx \simeq \sum_{i=0}^n \omega_i f(x_i) \tag{1.4}$$

where x_i is one of the n integration points in interval $[a, b]$ and ω_i is the corresponding weight for each integration point.

In SEM, the integration points are calculated based on 'Gauss-Lobatto-Legendre' (GLL) type of quadrature rule. The points are the roots of the polynomial expression given in Equation 1.5, where L_n' substitutes for the first derivative of Legendre polynomial of n degree (as formulated in Equation 1.6). These integration points are called hereafter GLL nodes/points.

$$P_n(\xi) = (1 - \xi^2)L_n'(\xi) \tag{1.5}$$

$$L_n(\xi) = \frac{1}{n!2^n}\frac{\partial^n}{\partial \xi^n}(\xi^2 - 1)^n \tag{1.6}$$

The quadrature rule of Gauss-Lebatto-Legendre provides $N + 1$ nodes so that inclusion of extreme points in boundaries becomes more efficient for solving polynomial integrals and the integration is exact for polynomials of degree $2N - 1$ (Maday and Patera, 1989 [103]).

In SEM, the medium is dicretised by subdomains Ω_e such that $\Omega : U_{e=1,n_e}\Omega_e$ for n subdomains. For each subdomain Ω_e, a reference element with coordinates in cartesian coordinate system of ξ is created as the image of subdomain. The GLL points are defined on these reference elements and the numerical integration is applied on reference elements. GLL points are defined in the $\square = [-1, 1]^d$ domain (d is the dimension), such that a reference element corresponds to a linear segment in 1D, a square in 2D and a cube in 3D. The transformation from a subdomain to its reference element is made by an invertible mapping function $\mathbb{F}_e$ so that $x = \mathbb{F}_e(\xi) \in \Omega_e$ and $\xi = \mathbb{F}_e^{-1}(x) \in \square$. An example of such transformation is shown in Figure 1.1 for 2D, where the reference square element is related to a physical element with real coordinates by means of $\mathbb{F}_e$ function.
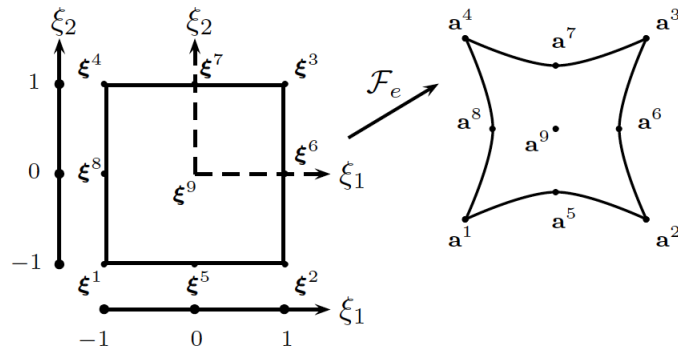
Fig. 1.1 Example of transformation of a 2D reference element with 9 GLL points (left) to a physical element (extracted from Komatitsch, 1997 and modified after Delavaud, 2007).

For a reference element, the integration points are determined by the roots of Equation 1.5 as mentioned above. For example, in 1D, the GLL points are solved in $[-1, 1]$ interval. For the use of second degree of Legendre polynomials ($N = 2$), Equation 1.5 provides (N+1) roots so that three GLL points are assigned on the 1D reference element. The distribution of three points is equidistant, so that the element is similar to discretization of finite element method that uses 3 points on element (See Figure 1.2). On the other hand, when the polynomial degree is increased, GLL points are no longer equidistant and the inner points get closer to extremities. When the polynomial order is 3, four GLL points are assigned on the reference element and the minimum grid distance is 0.2765 times the element size (Since in the figure, element length corresponds to 2 units, the minimum grid distance is equal to $(1 - 0.447)/2$). As another example, for the fourth order polynomial degree, the minimum grid distance on the reference element with 5 points is decreased to 0.175 of the element size.
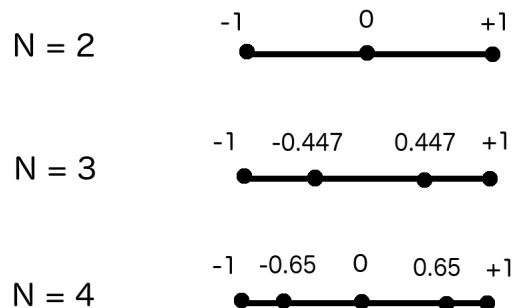
Fig. 1.2 Example of Gauss-Lobatto-Legendre integration point distribution on a 1D reference element for 2nd, 3rd and 4th polynomial degree.

Once the GLL points are defined for a given polynomial degree, the weights of the GLL points in Equation 1.4 are determined by means of the orthogonal Lagrange polynomials associated with the GLL nodes (See Equation 1.7).

$$\omega_i = \int_{-1}^{1} L_i(\xi) d\xi \tag{1.7}$$

The choice of lagrangian interpolation provides spectral convergence of interpolation error to SEM, which justifies its name and gives high precision of solution to the method (Delavaud, 2007). With the orthogonality of Lagrange polynomials, the formulation of mass matrix in SEM results in a diagonal matrix, which reduces computational time cost in time-stepping schemes for the solution of the equation of elastodynamics for which the inversion of mass matrix is frequently required. Given the Gauss-Lobatto-Legendre quadrature rule and lagrangian interpolation associated with the integration points, SEM differs from other finite element numerical methods.

By using Gauss-Lobatto-Legendre quadrature rule with lagrangian polynomials, the discrete expression of $\int_\Omega \rho \dot{v}^h w^h d\Omega$ in Equation 1.3 can be rewritten in 3D as follows:

$$\int_\Omega \rho \dot{v}^h w^h d\Omega = \sum [w^h u^h](\xi_\alpha^N, \xi_\beta^N, \xi_\gamma^N) J^e(\xi_\alpha^N, \xi_\beta^N, \xi_\gamma^N) \omega_\alpha \omega_\beta \omega_\gamma \tag{1.8}$$

where α, β, γ are the three-dimensional cartesian coordinates, ω is the weight for GLL nodes and J^e is the determinant of Jacobian matrix F^e of the mapping function $\mathbb{F}^e$ such that $F^e = [\frac{\partial \mathbb{F}}{\partial \xi_i}]$. Since the equation belongs to the elementary expression, e denotes elementary version for the parameters.

1.2.2   Time integration

Following the discretization of the space, the weak formulation is discretisized in time and solved for each time step Δt. In this aspect, the time integration schemes used for solving time-dependent differential equations can be classified as explicit and implicit methods. In implicit methods, a stable solution is searched for the system by taking into account the system state for current time step t and next time step $t + \Delta t$. For this reason, iterative analyses are performed for the solution converge to a stable solution. Although the solution is unconditionally stable (stable for any time step), they require very heavy computational time costs. Explicit methods, on the other hand, solve the equation for the next time step

$t + \Delta t$. They are advantageous in sense of computational time since no iterative analysis is required. To ensure the stability of explicit time-marching solver, the time step has to verify the Courant-Friedrichs-Lewy (CFL) condition (See Equation 1.9).

$$n_c = \Delta t \frac{v_{max}}{\Delta x_{min}} \tag{1.9}$$

In this equation, n_c holds for Courant number, V_{max} is the maximum velocity of the modeled media and Δx_{min} is the minimum distance between GLL points of the media. We use explicit time integration method and consider 0.3 as the controlling value of CFL for all the applications in this study. To avoid artificial wave dispersion, the element size d is chosen by respecting the relation $d \leqslant \lambda_{min} N / ppw$ where λ_{min} is the shortest wavelength propagating in the medium, N is the polynomial degree and ppw is the number of grid points per wavelength (Seriani and Priolo, 1991 [144]; 1993 [127]). In the aforementioned study, authors show that for a correct wave propagation the use of $ppw = 5$ is needed while finite difference and low-order finite element methods require the values between 15 and 30. This aspect of SEM is discussed in detail in Chapter 2.5.1.

The system of equations to be solved is formulated based on a time integration scheme. For the 2nd order Newmark scheme where total energy is conserved, following equations are written for displacement u and velocity v parameters as follows:

$$u^{n+1/2} = 1/2(u^n + u^{n+1}) \tag{1.10}$$

$$v^{n+1} = v^n + \Delta t \mathbb{M}^{-1}[F_{ext}^{n+1/2} - F^{int}(u^{n+1/2}) + F_{trac}^{n+1/2}] \tag{1.11}$$

In the equation 1.11, $\mathbb{M}$ is elementary mass matrix, $\mathbb{F}^{ext}$ holds for external forces, $\mathbb{F}^{int}$ for internal forces and $\mathbb{F}^{trac}$ for traction forces. Parameters denoted with n hold for the values expanded on time interval $[t_n, t_{n+1}]$.

In our study, we choose velocity-stress formulation so that the main parameter in the system is velocity v (Festa and Vilotte, 2005 [44]). The system of equation that we refer to is rewritten as in Equation 1.12.

$$v^{n+1} = v^n + \Delta t \mathbb{M}^{-1}[F_{ext}^{n+1/2} - F^{int}(\sigma^{n+1/2}) + F_{trac}^{n+1/2}] \tag{1.12}$$

In this formulation, internal forces are calculated as a function of stress σ by Equation 1.13, in which D is the discrete derivative matrix operator (detailed in Festa and Vilotte, 2005 [44]; Delavaud, 2007 [32]). The equation is first solved element by element. Then, the solution is assembled in a global matrix, for which the continuity between the elements is insured.

$$F_i^{int,e} = \sum_{j=1}^{d} D_j^T \sigma_{ij}^e J^e \omega. \tag{1.13}$$

External forces $\mathbb{F}^{ext}$ are non-zero for the cases there is an excitation on a GLL node with a point source or a double couple. For other cases, it is equal to zero. Traction force $\mathbb{F}^{trac}$ is only for the traction applied on the boundary of the model.

The procedure followed in order to solve the system of equation (Equation 1.12) is illustrated in Figure 1.3. At each time step, a prediction phase is applied such that the velocity calculated from the previous time step t_n is used. Then, the strain rate ∇v is computed. For the cases, incident wave motion is inserted in the system, the velocity of the incident wave for the given time step is also used for strain rate computation. In this way, the strain rate contribution by incident wave is added to the ∇v. Next step is the determination of the strain increment $\Delta \varepsilon$. The calculated strain increment $\Delta \varepsilon$ is used for the computation of stress parameter σ. Internal force F^{int} in the system corresponding to the computed stress $\sigma^{n+1/2}$ is calculated. If an external force or traction on boundary exist, they are taken into account in order to calculate total forces F, such that the total force corresponds to total body force of the system f in Equation 1.1. Afterwards, the current velocity v^{n+1} of the system is updated with total force matrix.

$$v^n$$

If incident wave field is inserted

$$\nabla v \quad + \quad \nabla v_{\text{incident}}$$

$$\Delta \epsilon = \nabla v \Delta t$$

$$\sigma^{n+1/2}$$

If traction is applied on boundary

If external force is applied

$$F_{trac}^{n+1/2} \quad - \quad F^{int}(\sigma^{n+1/2}) \quad + \quad F_{ext}^{n+1/2}$$

$$F$$

$$v^{n+1} = v^n + \Delta t \mathbb{M}^{-1} F$$
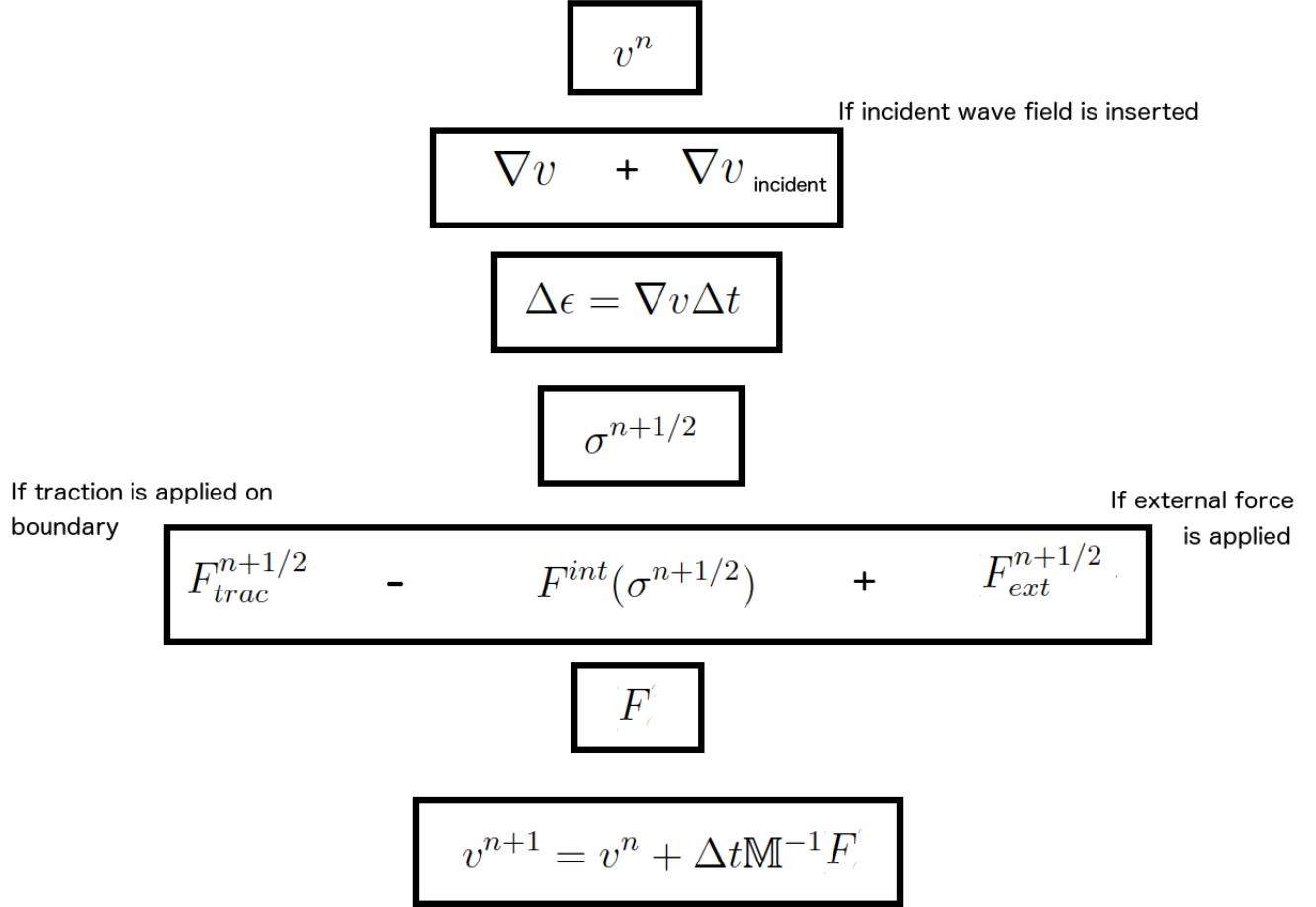
Fig. 1.3 Representation of the procedure followed in time integration for the spectral element method.

1.2.3 1D and 2D spectral element application

In this PhD study, in order to study the wave propagation in linear and nonlinear media, we make use of 1D and 2D SEM codes that provide the solution of wave propagation in linear media. We implement different soil constitutive models to these codes for taking into account nonlinear media as well as additional boundary conditions that are necessary for further applications. In 1D, we use the 1D SEM code of Delavaud (2007) [32], while in 2D we refer to the 2D SEM code SEM2DPACK of Ampuero (2002) [2]. 2D SEM code models P-SV and SH wave propagation. For P-SV waves, the elastodynamics equation of wave motion

in Equation 1.1 is written in terms of horizontal and vertical partial terms of external force (f_x and f_z for horizontal and vertical directions respectively) and stress σ, time derivative of velocity (v_x and v_z for horizontal and vertical directions respectively) as follows:

$$\rho \frac{\partial v_x}{\partial t} = (\frac{\partial \sigma_{xx}}{\partial x} + \frac{\partial \sigma_{xz}}{\partial z}) + f_x \tag{1.14}$$

$$\rho \frac{\partial v_z}{\partial t} = (\frac{\partial \sigma_{zz}}{\partial z} + \frac{\partial \sigma_{xz}}{\partial z}) + f_z \tag{1.15}$$

For SH waves, Equation 1.16, in which v_y is velocity field out of plane (x,z) and f_y is the force on the same direction, is employed.

$$\rho \frac{\partial v_y}{\partial t} = (\frac{\partial \sigma_{xy}}{\partial x} + \frac{\partial \sigma_{yz}}{\partial z}) + f_y \tag{1.16}$$

In both 1D and 2D SEM codes, the studied model is discretisized by a mesh structure. This mesh is composed of linear segments in 1D, while in 2D quadrangles are employed in element compositions. In 2D, it is possible to create structured or unstructured meshes. In structured meshes, the domain is discretisized by adjacent elements that share a common element face. On other other hand, in unstructured meshes, elements that are connected by a node are not necessarily defined with same elementary face. More details in mesh preparation for 2D SEM code can be found in the manual of SEM2DPACK (Ampuero, 2012).

In order to evaluate the results at certain locations of the mesh, receivers are specified by coordinates. The 1D and 2D SEM codes offer the possibility of defining receivers at any point inside the mesh. For a receiver which corresponds to a GLL node of the mesh, exact calculated values for the parameters at the corresponding GLL node are assigned to the receiver. For other points, a lagrangian interpolation is applied to the GLL nodes of the element that contains the receiver, in both 1D and 2D SEM codes.

In addition to mesh structure, the boundary conditions are needed to be specified in the created model of 1D and 2D SEM codes. The first boundary condition is free surface. It is modeled with Neumann condition and the traction is set to zero. Thus, the $\mathbb{F}^{trac}$ in Equation 1.12 is equal to zero for free surface boundary condition. In the applications of 1D and 2D SEM codes, it is used for the upper boundary (ground surface level).

The second boundary condition is rigid boundary. It is defined by Dirichlet condition where null velocity is imposed on the boundary. Accordingly, in the formulation, the velocity is forced to be zero for rigid boundary condition. Therefore, total strain rate ∇v is zero in Figure 1.3. Waves propagating towards the rigid boundary are completely reflected back, so that all the incoming energy to rigid boundary remains inside the model. It is used with absorbing layers (explained below) in our study.

Another boundary type is borehole condition. It has been implemented in both 1D and 2D SEM codes during this PhD work. Similarly to rigid boundary condition, incoming waves towards the boundary are completely reflected back. On the other hand, the velocity of the boundary is imposed as a function of time for a given duration. In other words, an incident wave field is defined on the boundary as a function of time. The defined velocity field is used in strain computation as shown in Figure 1.3. In applications, borehole boundary condition is used as bottom boundary for the real models where borehole data record (wave field recorded at a given depth) is available. Also, for the canonical models where incident wave field is inserted through the boundary and the energy is set to remain inside the model.

Periodic boundary condition is another boundary type employed in our study. It is only available in the 2D SEM code, where it has been already implemented originally. Periodic boundary condition is used in the 2D applications of our study for lateral boundary limits. It forces left and right boundaries to have identical velocity fields, such that an infinite domain is created horizontally.

The last boundary condition that has been used is Classical Perfectly Matched Layers (C-PML). C-PML type of boundaries (Bérenger, 1994) are considered as numerical boundary condition where the incoming energy into C-PML is artificially attenuated in infinite domain. The C-PML are implemented with a velocity-stress based system of equations. They are created by stretching real coordinates space to complex space in frequency domain (See Equation 1.17).

$$\tilde{x} = x + \frac{\Sigma(x)}{i\omega} \tag{1.17}$$

where ω is angular frequency, $\Sigma(x)$ is an arbitrary function and x is the distance from the interface between medium and C-PML. Attenuation is done exponentially by means of $\Sigma(x)$ function as expressed by Equation 1.18. In the equation, Δx is the distance from the C-PML interface (unit distance in reference element coordinates system), h is C-PML thickness, A

and *n* are constants. From our numerical tests, $A = 10$ is found to give satisfactory results for $n = 2$. More details can be found in (Festa and Nielsen, 2003 [43]; Festa and Vilotte, 2005 [44]; Delavaud, 2007 [32])

$$\Sigma(x) = A\frac{c_p}{h}(\Delta x)^n \tag{1.18}$$

Depending on the direction of attenuation, the ultimate point is forced to have null displacement. For this reason, C-PML is implemented as an additional domain and the last node of the C-PML domain is defined with Dirichlet boundary where no displacement takes place. C-PML boundary condition was originally implemented in 1D SEM code. In 2D SEM code, different absorbing layer conditions are available such as Clayton and Engquist (1977) [23] and Stacey (1988) [148]. Since C-PML is proved to be effective (no reflection) for both P and S waves (Festa and Nielsen, 2003 [43]; Komatitsch and Tromp, 2003 [88]; Festa and Vilotte, 2005 [44]; Meza-Fajardo and Papageorgiou, 2008 [113]), it has also been implemented in 2D SEM code during this thesis. Attenuation is possibly made for vertical propagation on upward and downward direction. C-PML are used in bottom boundaries for elastic rock conditions where the incoming energy underneath rock layer is attenuated. Also, in the applications, an incident wave field is defined between studied model domain and C-PML. The incident wave is inserted by means of velocity field as a function time and the inserted velocity is employed as shown in Figure 1.3.

Moreover, the 1D SEM code follows only the time scheme which is mentioned above with the procedure illustrated in Figure 1.3. In 2D SEM code, there exist several options for time integration schemes such as explicit Newmark, explicit HHT-alpha, quasi-static and leap-frog time schemes. In 2D SEM, all the developments in 2D SEM code during this study are done for leap-frog time integration scheme accordingly to the velocity-stress system of equations which follows the procedure in 1.3. In future studies, these features could be added to other time integration schemes.

Lastly, the material properties of the domains in the discretisized model are required for 1D and 2D SEM solution of wave propagation. The original 1D and 2D SEM codes provide solutions for elastic medium. During this PhD study, different soil constitutive models have been implemented in 1D and 2D SEM codes so that it is possible to define elastic, viscoelastic and/or nonlinear models. In the next section, these soil constitutive models are explained in detail.

1.3 Constitutive models for soil rheology

In this section, constitutive soil models for elasticity and nonlinearity which are used in order to relate strain and stress parameters in the followed time procedure for solving wave equation (Figure 1.3) are explained. First, the formulations used in elasticity are explained briefly. Second, the viscoelastic model of Liu and Archuleta (2006) [98] is presented. Afterwards, the elastoplasticity model from family of Masing-Prandtl-Ishlinskii-Iwan (MPII) model of Iwan (1967) [76] is detailed. Lastly, the Iai et al. (1990) [69] model for including pore pressure effects in nonlinearity is shown.

1.3.1 Elasticity model

In an elastic and isotropic medium, the relation between material strain and stress can be written by Equation 1.19 based on Hooke's law:

$$\sigma_{ij} = \lambda \delta_{ij} \varepsilon_{kk} + 2\mu \varepsilon_{ij} \tag{1.19}$$

In this equation, Lamé coefficients are denoted by λ and μ, δ is Kronecker symbol and ε is the infinitesimal strain tensor. Lamé coefficients can be expressed by medium velocity such as $\mu = \rho V_s^2$ and $\lambda + 2\mu = \rho V_p^2$ where V_s, V_p are shear and pressure velocities of the medium, respectively. The strain tensor is written in function of displacement field as in Equation 1.20.

$$\varepsilon(u) = \frac{1}{2} [\nabla u + (\nabla u)^T] \tag{1.20}$$

The material elasticity has been originally implemented in the 1D and 2D SEM codes. In next sections, the inelastic soil constitutive models that are implemented during this study for defining viscoelastic and nonlinear media are presented.

1.3.2 Viscoelasticity model

In a purely elastic material, all the energy stored in the material during loading is returned with unloading, so that there is no energy loss in the material. For elastic materials, stress is proportional to strain by the elastic modulus (Hooke's law - Equation 1.19). In engineering, most of the materials are defined by this linear elasticity law for small strains ($< 10^{-6}$)

(Ishihara, 1996 [75]). The opposite state of the pure elasticity is viscosity where the material does not return any of the energy stored during loading. In reality, every material deviates from Hooke's law depending on its viscosity level and behaves in viscoelastic way which is the state between the two extreme states, elasticity and viscosity (Lakes, 1999 [94]; Moczo and Kristek, 2005 [115]; Vincent, 2012 [156]). Since when traveling in the Earth, seismic waves are attenuated due to intrinsic attenuation of materials during their propagation, they can be modeled by viscoelastic models (Moczo and Kristek, 2005 [115]).

Two major experiments are done on viscoelastic materials: transient and dynamic experiments. The first transient experiment, creep test, is the sudden application of constant stress where the deformation change with time is noted. The second transient experiment is stress-relaxation test where the specimen is deformed and the stress value under constant deformation is noted. The simplest representation of viscoelastic rheology is given by the Boltzmann superposition principle (Moczo and Kristek, 2005 [115]; Vincent, 2012 [156]):

$$\sigma(t) = \int_{-\infty}^{t} \psi(t - \tau)\dot{\varepsilon}(\tau)d\tau \tag{1.21}$$

where $\sigma(t)$ and $\dot{\varepsilon}(t)$ stand for stress and time derivative of strain, respectively, while $\psi(t)$ is stress relaxation function. Based on this representation, it can be stated that the stress at a given time t is calculated by the entire strain history until time t. Regarding that the integral in Equation 1.21 mathematically signifies a time convolution, the equation can be rewritten as follows:

$$\sigma(t) = \psi(t) * \dot{\varepsilon}(t) \tag{1.22}$$

Given that $\psi(t)$ is the stress response to a Heaviside unit step function in strain, Equation 1.22 becomes:

$$\dot{\sigma}(t) = M(t) * \dot{\varepsilon}(t) \tag{1.23}$$

where time-dependent viscoelastic modulus is $M(t)$ and equals to $\dot{\psi}(t)$.

The Fourier transform of the Equation 1.23 results in following equation:

$$\sigma(\omega) = M(\omega).\varepsilon(\omega) \tag{1.24}$$

where $M(\omega)$ is the complex, frequency-dependent viscoelastic modulus.

For a generalized Maxwell body with n mechanism (See Figure 1.4), the frequency-dependent viscoelastic modulus $M(\omega)$ can be formulated as in Equation 1.25, where M_r is relaxed modulus, δM is the difference between unrelaxed modulus M_u and relaxed modulus M_r. Each term with $a_j \frac{\delta M}{\omega_j}$ refers to viscosity, whereas $a_j \delta M$ corresponds to elastic modulus and M_r holds for additional elastic elements.

$$M(\omega) = M_r + \sum_{j=1}^{n} a_j \delta M \frac{i\omega}{i\omega + \omega_j} \tag{1.25}$$
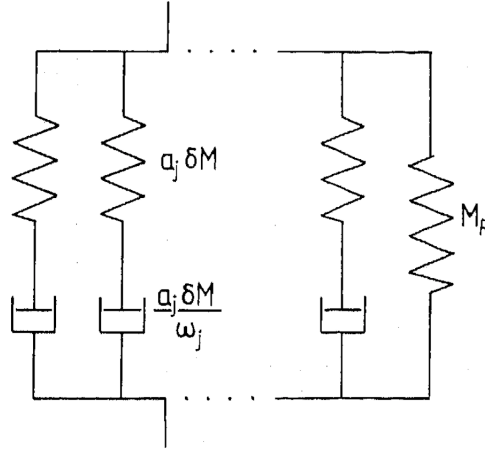
Fig. 1.4 Rheological model for generalized Maxwell body with viscosities $a_j \frac{\delta M}{\omega_j}$ and elastic moduli $a_j \delta M$ (after Emmerich and Korn, 1987 [40]).

The intrinsic attenuation in a viscoelastic media could be quantified by introducing the quality factor Q parameter and it is a function of frequency-dependent viscoelastic modulus $M(\omega)$ as shown in Equation 1.26.

$$Q(\omega) = \frac{ReM(\omega)}{ImM(\omega)} \tag{1.26}$$

Including Q effect in time domain is of interest while modeling wave propagation in complex media according to Liu and Archuleta (2006) [98]. There are a number of studies about the implementation of viscoelastic attenuation in time domain by using the so-called

memory variables. Including Q effects, by modeling as a function of frequency with the aid of memory variables, may dramatically increase storage and computation time problems for the numerical methods (Day and Minster, 1984 [28]; Emmerich and Korn, 1987 [40]; Day and Bradley, 2001 [26]). In this study, for the purpose of viscoelasticity implementation, the model of Liu and Archuleta (2006) [98] is used. It has been implemented in spectral element numerical method in De Martin (2011) and verified in a benchmark model of Southern California Earthquake Center. In the study of Liu and Archuleta (2006) [98], the relaxation time set and two sets of weight coefficients are optimized in order to model a constant Q for a sufficiently large range ($5 < Q < 5000$) on frequency band $0.01 - 50Hz$, so that it can be easily adapted to numerical algorithms for a maximum storage and time computation efficiency. Figure 1.5 displays this agreement between the modeled Q values as a function of frequency for different target Q values $(5, 20, 100, 1000, 5000)$.
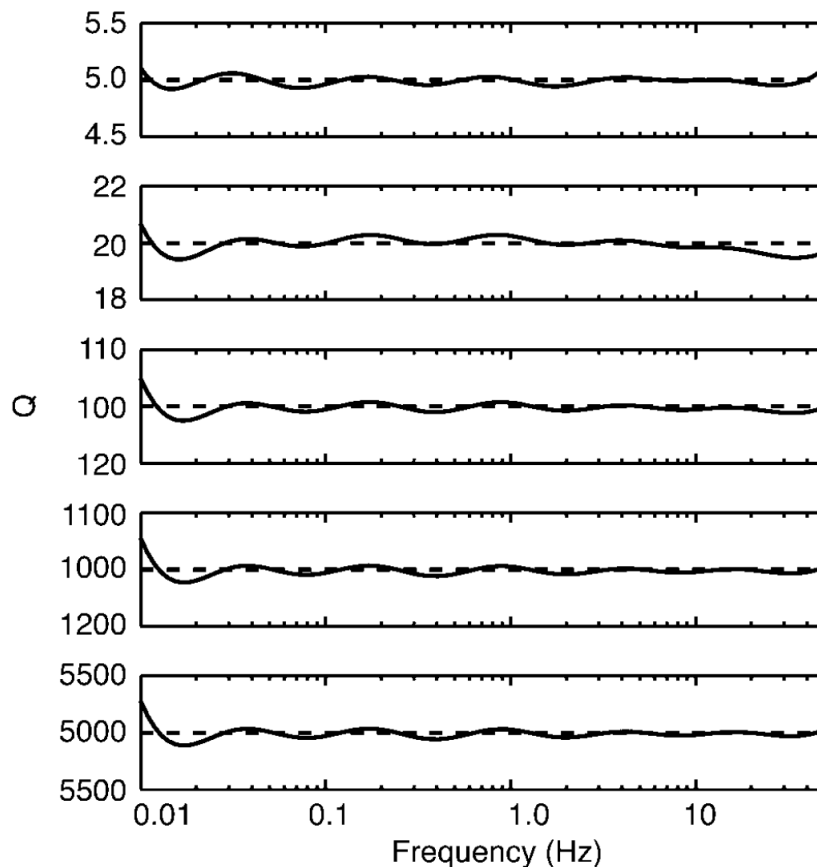
Fig. 1.5 The fit between model Q and target Q value of 5 (top panel), 20 (second panel), 100 (third panel), 1000 (fourth column) and 5000 (bottom panel) in frequency band of $0.01 - 50Hz$ (after Liu and Archuleta, 2006 [98]).

The relation between stress and deformation for elastic media is replaced by the following viscoelastic formula:

$$\sigma(t) = M_u[\varepsilon(t) - \sum_{k=1}^{N} \zeta_k] \tag{1.27}$$

where M_u is the unrelaxed modulus, N is the number of relaxation functions and memory variable is denoted as ζ_k.

Memory variables ζ_k are formulated based on first-order differential equation as follows:

$$\tau_k \frac{d\zeta_k(t)}{dt} + \zeta_k(t) = w_k \varepsilon(t) \tag{1.28}$$

For a material with the phase velocity c and density ρ, the unrelaxed modulus M_u, which is the instantaneous elastic response of the viscoelastic material, can be written as:

$$M_u = \frac{c^2 \rho}{|1 - \sum_{k=1}^{N} \frac{w_k}{1 + i\omega_r \tau_k}|} \tag{1.29}$$

In this equation, ω_r accounts for the reference frequency at which c phase velocity is observed and w_k, τ_k are weight coefficients and relaxation time functions respectively. The values of w_k, τ_k and the other coefficients necessary to calculate w_k in Equations 1.30-1.31 are given in Table 1.1.

$$w_k^Q = \chi(\chi \alpha_k + \beta_k) \tag{1.30}$$

$$\chi = \frac{3.071 + 1.433 Q^{-1.158} \ln(Q/5)}{1 + 0.415 Q} \tag{1.31}$$

for $5 \leq Q \leq 5000$.

Table 1.1 Coefficients for modeling Q (after Liu and Archuleta, 2006 [98]).

k	τ_k	α_k	β_k
1	1.72333E-3	1.66958E-2	8.98758E-2
2	1.80701E-3	3.81644E-2	6.84635E-2
3	5.38887E-3	9.84666E-3	9.67052E-2
4	1.99322E-2	-1.36803E-2	1.20172E-1
5	8.49833E-2	-2.85125E-2	1.30728E-1
6	4.09335E-1	-5.37309E-2	1.38746E-1
7	2.05951	-6.65035E-2	1.40705E-1
8	13.2629	-1.33696E-1	2.14647E-1

1.3.3   Material nonlinearity

In this thesis, the nonlinear soil behavior is approximated by a three-dimensional constitutive model which is based on multi-surface plasticity of Iwan (1967) [76]. The model belongs to a family of Masing-Prandtl-Ishlinskii-Iwan (MPII) model (Segalman and Starr, 2008 [142]) according to Santisi d'Avila et al. (2012) [137]. This multi-dimensional nonlinear model has been implemented in finite difference (Joyner and Chen, 1975 [79]; Joyner, 1975 [78]) and finite element formulations (Gandomzadeh, 2011 [48]; Santisi d'Avila et al., 2012 [137]; Pham, 2013 [125]). Hereafter, MPII model is used as a reference to this explanation of the model. We follow the formulation of Joyner and Chen (1975) [79]. For a given strain increment matrix, the corresponding total stress increment matrix is calculated based on deviatoric stress and strain parameters.

In 1D, soil nonlinearity is approximated by the characteristic backbone curve of the soil and 1D rheological model is shown in Figure 1.6. It consists of N linear springs and Coulomb friction units. Friction units are activated only when yielding takes place. In other words, friction units remain locked until the applied stress exceeds the yield stress for the unit Y_i. When the yield stress Y_i is exceeded, material is no longer considered elastic and plasticity is assumed to take place for the ith spring. Spring constants represent the slopes of stress-strain curve for N intervals in the characteristic backbone curve of the soil (See Figure 1.7).
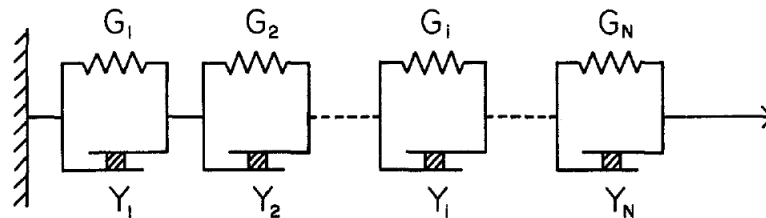
Fig. 1.6 1D rheological model of Iwan (1967) (after Joyner, 1975 [78]).
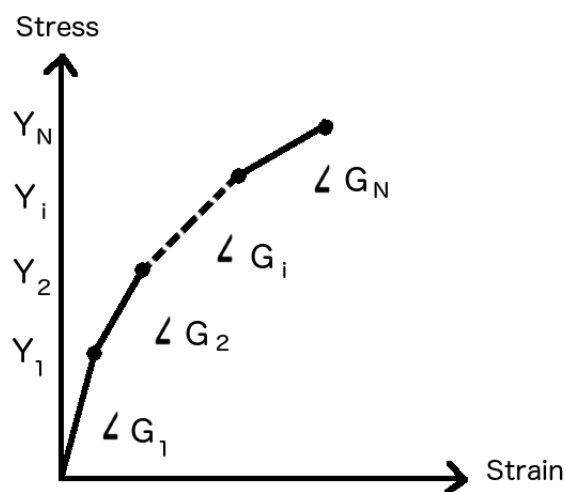
Fig. 1.7 Shear stress-strain curve for 1D rheological Iwan model with N springs. Yielding stress values are denoted by *Y* and shear modulus by *G*.

The backbone curve could be constructed by means of hyperbolic model developed by Hardin and Drnevich (1972) [60] (the reader can find the details in that paper). Equation 1.32 shows the relation between shear modulus G and shear strain γ for hyperbolic model, where G_0 is the initial shear modulus and γ_{ref} is the reference shear strain that is the shear strain corresponding to the half of ultimate shear strength.

$$\frac{G}{G_0} = \frac{1}{1 + \gamma/\gamma_{ref}} \qquad (1.32)$$

For pressure-independent models, reference strain is taken as input parameter and the hyperbolic backbone curve is accordingly constructed for given reference strain. For pressure-dependent models, on the other hand, reference strain is computed as shown in Equation 1.33.

$$\gamma_{ref} = \frac{\tau_{max}}{G_{corrected}} \qquad (1.33)$$

In this equation, τ_{max} is maximum shear strength and $G_{corrected}$ is the corrected shear modulus used in the simulations. $G_{corrected}$ is calculated by normalizing the initial shear modulus by the effective mean stress σ_{mid} applied at the middle of soil layer (See Equation 1.34), so that shear modulus is pressure-dependent. Soil is more linear at depth and more nonlinear close to surface.

$$G_{corrected} = G_0 \sqrt{\left|\frac{P_0}{\sigma_{mid}}\right|} \qquad (1.34)$$

where P_0 is effective mean stress and equal to the arithmetic mean of the stress components of axial directions and the effective mean stress applied at the middle of soil layer $\sigma_{mid} = \rho g h(\frac{1+2K_0}{3})$ for corresponding depth h (K_0 is the coefficient of Earth at rest).

Maximum shear strength τ_{max} can be formulated as a function of cohesion C, failure line angle of the soil ϕ_f and the initial mean effective stress applied on soil σ as follows (Jaeger et al., 2007 [77]):

$$\tau_{max} = C cos\phi + \sigma sin\phi \qquad (1.35)$$

It should be noted that all the parameters used in the formulations of this section are effective parameters. Therefore, for saturated soils, instead of total stress matrix, effective stress matrix with dry soil parameters are taken into account.

For the cases where enough experimental data is available for the studied soil model, it is possible to construct the hyperbolic backbone curve for the soil without referring to Equation 1.32 but by means of numerical interpolation of the provided data. In such a case, given data

is interpolated in order to fit the backbone curve to specified Iwan spring number.

In the formulation of Iwan (1967) [76], three-dimensional model of nonlinearity is presented based on standard incremental plasticity theory of Fung (1965) [47] by introducing a family of yield surfaces (Joyner, 1975 [78]). In his formulation, yield surfaces are expressed by the following formula:

$$F_n(s_{ij} - \alpha_{nij}) = k_n^2 \tag{1.36}$$

where F_n is the yield function for the nth yield surface, α_{nij} is the origin of the same surface and k_n is constant for yield stress associated with the nth surface. For kinematic hardening of Prager type, the translation for each surface can be written in terms of plastic strain as in Equation 1.37 where C_n is a constant for the nth surface. Then, Equation 1.38 applies for the normality condition of plastic strain to yield surface.

$$d\alpha_{nij} = C_n de_{pnij} \tag{1.37}$$

$$de_{pnij} = L_n h_n \frac{\partial F_n}{\partial s_{ij}} \tag{1.38}$$

In this equation, h_n is determined by the assumption of Fung (1965). Under the loading ds_{rs}, the plastic state must lead to another plastic state so that the center of the plasticity surface translates. With normality condition for center translation and stress increment, Equation 1.39 can be written.

$$h_n = \frac{1}{C_n} \frac{(\partial F_n / \partial s_{rs}) ds_{rs}}{(\partial F_n / \partial s_{kl})(\partial F_n / \partial s_{kl})} \tag{1.39}$$

For the case the yield function does not exceed k_n value or unloading, L_n parameter is set to zero, while for other cases it is equal to 1 as follows:

$$L_n = 0 \text{ if } F_n < k_n^2 \text{ or } \frac{\partial F_n}{\partial s_{ij}} ds_{ij} < 0$$

$$L_n = 1 \text{ if } F_n = k_n^2 \text{ or } \frac{\partial F_n}{\partial s_{ij}} ds_{ij} \geq 0$$

In case of yielding ($L_n = 1$), the nth surface is considered to be activated, similarly to the 1D representation of the model.

Following the formulation in the study of Joyner (1975), for a given strain increment matrix $d\varepsilon_{ij}$, the corresponding total stress increment matrix $d\sigma_{ij}$ is calculated based on deviatoric strain de_{ij} and stress ds_{ij} parameters. The total deviatoric strain increment de_{ij} can be calculated by the total strain increment matrix $d\varepsilon_{ij}$ as in Equation 1.40.

$$de_{ij} = d\varepsilon_{ij} + d\varepsilon_m \delta_{ij} \tag{1.40}$$

where $d\varepsilon_m$ is the mean strain increment written as $d\varepsilon_m = \frac{1}{3}(tr(d\varepsilon))$.

In the constitutive model, the total deviatoric strain increment de_{ij} is related to the deviatoric stress increment ds_{ij} by Equation 1.41. In this equation, the term with deviatoric stress increment matrix ds_{ij} and the initial shear modulus G_0 corresponds to the elastic part of the deviatoric strain increment according to the linear elasticity theory (See Chapter 1.3.1), while the plastic part of the deviatoric strain increment is written in terms of Q_{ijrs} parameter.

$$de_{ij} = Q_{ijrs}ds_{rs} + 1/2G_0 ds_{ij} \tag{1.41}$$

Q_{ijrs} tensor is calculated accumulatively for each plasticity surface by means of the corresponding yield function and partial derivatives as in Equation 1.42.

$$Q_{ijrs} = \sum_n \frac{L_n(\partial F_n/\partial s_{ij})(\partial F_n/\partial s_{rs})}{C_n(\partial F_n/\partial s_{kl})(\partial F_n/\partial s_{kl})} \tag{1.42}$$

By using Von Mises yielding condition, the yield function F_n and its partial derivative $\partial F_n/\partial s_{ij}$ can be written as follows:

$$F_n = 1/2(s_{nij} - \alpha_{nij})(s_{nij} - \alpha_{nij}) \tag{1.43}$$

$$\frac{\partial F_n}{\partial s_{ij}} = s_{nij} - \alpha_{nij} \tag{1.44}$$

C_n and k_n values are determined by means of characteristic backbone curve of the soil. k_n values are set to yield stress for each spring and C_n values are calculated by Equation 1.45.

$$\frac{1}{C_j} = \frac{\varepsilon_{j+1} - \varepsilon_j}{k_{j+1} - k_j} - \frac{1}{2G_0} - \sum_{n=1}^{j-1} 1/C_n \tag{1.45}$$

In numerical modeling, we follow the scheme shown in Figure 1.8. At each time step t, total stress increment $d\sigma_{ij}$ is calculated for total strain increment $d\varepsilon_{ij}$. For the first time step, we assume that no yield surface is activated and the current stress point remains inside the first plasticity surface. Thus, it is possible to apply linear elasticity in order to calculate the stress increment of the material for the given strain increment. For next time steps, first, the deviatoric strain parameter de_{ij} is computed by means of Equation 1.40. Second, the yield function F_n and its partial derivative $\partial F_n / \partial \sigma_{ij}$ are calculated by Equations 1.43-1.44. With these parameters, L_n parameter is calculated in order to check whether the nth surface yields. Then, E matrix is created by assembling elastic and plastic multipliers $1/2G_0$ and Q_{ijrs} with respect to Equation 1.41. This matrix relates the deviatoric stress increment matrix to deviatoric strain increment matrix. However, our code is based on velocity parameter (See Chapter 1.2.2) so that the main variable is strain increment for nonlinearity computations. In order to solve Equation 1.41, the E matrix is inverted and multiplied by deviatoric strain increment matrix. At this point, we assume that time steps are sufficiently small that inverse solution provides an acceptable approximation. Once, the deviatoric stress increment ds_{ij} is calculated, total deviatoric stress matrix s_{ij} is updated. Then, the translation of surface center for each activated yield surface α_{ij} is computed (See Equation 1.46). Lastly, the stress increment matrix $d\sigma_{ij}$ can be computed according to Equation 1.47.

$$\boxed{d\epsilon_{ij}}$$

$$\boxed{de_{ij}^{total} = d\epsilon_{ij} + d\epsilon_m \delta_{ij}}$$

$$F_n = 1/2(s_{nij} - \alpha_{nij})(s_{nij} - \alpha_{nij})$$

$$\frac{\partial F_n}{\partial s_{ij}} = s_{nij} - \alpha_{nij}$$

$$L_n = 0 \text{ if } F_n < k_n^2 \text{ or } \frac{\partial F_n}{\partial s_{ij}} ds_{ij} < 0$$

$$L_n = 1 \text{ if } F_n = k_n^2 \text{ or } \frac{\partial F_n}{\partial s_{ij}} ds_{ij} \geq 0$$

$$E = Q_{ijrs} + 1/2G_0$$

$$ds = E^{-1} de$$

$$d\sigma_{ij} = ds_{ij} + d\sigma_m \delta_{ij}$$

$$s_{ij}^{t+\frac{1}{2}} = s_{ij}^{t-\frac{1}{2}} + ds$$

$$\alpha_{nij}^{t+\frac{1}{2}} = s_{ij}^{t+\frac{1}{2}} - \frac{k_n(s_{ij}^{t+\frac{1}{2}} - \alpha_{nij}^{t-\frac{1}{2}})}{\sqrt{F_n}}$$
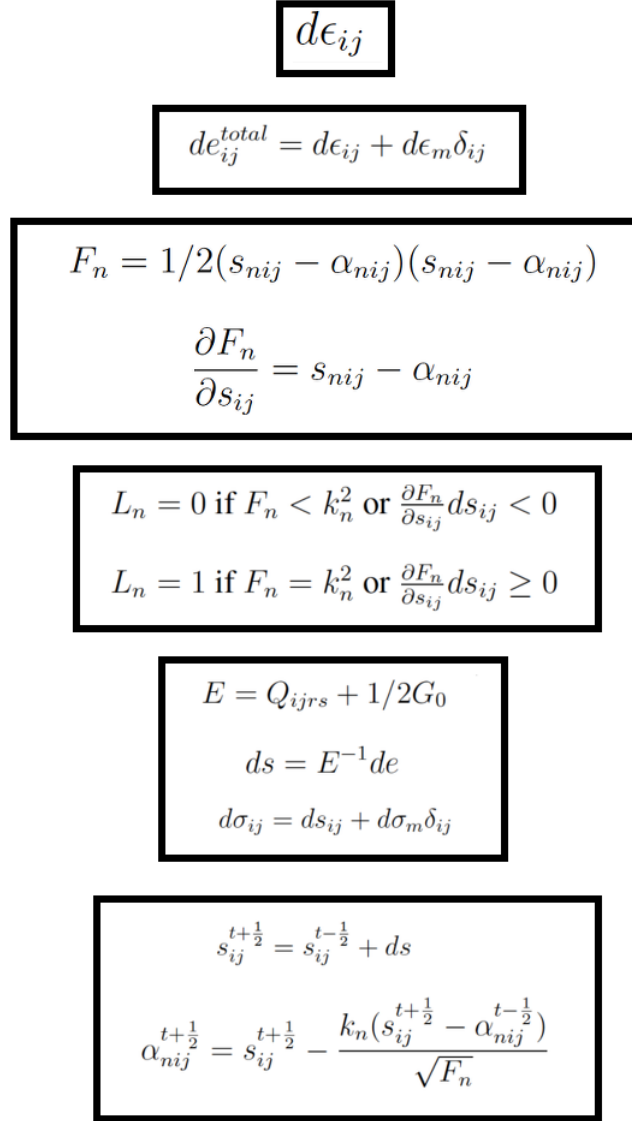
Fig. 1.8 Numerical flow followed for computation of total stress increment matrix for given total strain increment matrix.

$$\alpha_{nij}^{t+\frac{1}{2}} = s_{ij}^{t+\frac{1}{2}} - \frac{k_n(s_{ij}^{t+\frac{1}{2}} - \alpha_{nij}^{t-\frac{1}{2}})}{\sqrt{F_n}} \tag{1.46}$$

where the parameters with $t + \frac{1}{2}$ hold for updated values and those with $t - \frac{1}{2}$ for precedent time step values.

$$d\sigma_{ij} = ds_{ij} + d\sigma_m \delta_{ij} \qquad (1.47)$$

where $d\sigma_m$ is the mean stress increment and calculated by means of mean strain increment $d\varepsilon_m$ and bulk modulus K as $d\sigma_m = 3K d\varepsilon_m$.

1.3.4   Liquefaction front model

For the purpose of modeling the excess pore pressure generation under cyclic loading, we refer to the study of Iai et al. (1990) [69]. In their study, they follow a relation between the accumulated shear work and the mean effective stress that was observed in experimental data (Towhata and Ishihara, 1985 [154]). In this model, the soil follows two characteristic lines: Failure line and phase transformation line (See Figure 1.9). Failure line is described as ultimate limit for the soil such that when the line is exceeded, soil failure is assumed to occur. Phase transformation line is the limit to define whether the soil behavior is contractive or dilatant. The area remaining under phase transformation line is called contractive zone and the area between failure and phase transformation lines is dilatant zone. In the same figure, liquefaction front represents the envelope of stress points at equal shear work in normalized stress space relating the applied normalized deviatoric stress r and current normalized mean effective stress S on soil (normalization is done by division to initial mean effective stress). Depending on shear work accumulated under applied loading, the stress path is determined. Stress path is the trajectory of the points that the soil follows in the deviatoric plan. When this path remains under phase transformation line, soil is said to be contractive and under continuous loading, soil effective strength decreases and excess pore pressure develops in soil. On the other hand, for the case the stress path exceeds the phase transformation line, soil becomes dilatant and stress path changes direction so that effective strength increases and pore pressure decreases. The changes in contractive/dilatant soil behavior is tracked in this deviatoric plan. In our study, we couple the nonlinear MPII model with the model of Iai et al. (1990) [69] in presence of liquefiable soil layers, in the same way as Pham, 2013 [125] who coupled MPII model with Iai et al. (1990) [69] in a 1D-3C finite element code. At each time step, for the calculated total stress matrix, the accumulated plastic shear work increment and the current effective stress are computed. The backbone curve of the soil is reconstructed according to the current effective stress.
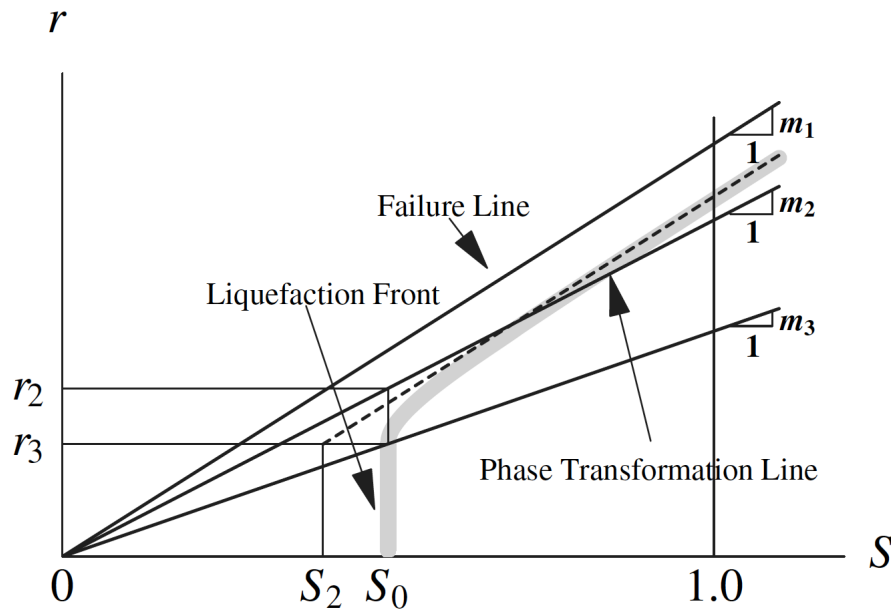
Fig. 1.9 Schematic plot of liquefaction front of Iai et al. (1990) [69] model in normalized stress space (after Iai et al., 1990 [69]). S holds for normalized mean effective stress and r is the normalized deviatoric stress.

The mechanism is numerically controlled by 5 parameters ϕ_p, p_1, p_2, w_1 and S_1. ϕ_p is the phase transformation line angle beyond which the material becomes dilatant and effective strength increases. In the model, the liquefaction front parameter S changes as a function of plastic shear work by exponential functions in two intervals (earlier and later period). The earlier and later intervals are determined by w_1 parameter. The function of decrease in S depends on p_1 parameter for initial interval and p_2 for the second interval of plastic shear work. Also, p_1 and p_2 are the parameters that control the curvature of stress path (normalized effective stress in soil). S_1 is the lowest numerical limit for S_0 parameter in order to avoid numerical instabilities. For more detailed explanation of the model, the reader is suggested to read Iai et al. (1990) [69]. In the following, the related formulation of the model is explained. In the formulations, the stress and strain parameters are based on the notation shown in Equation 1.48.

$$
\sigma = \begin{bmatrix} \sigma_{xx} \\ \sigma_{yy} \\ \tau_{xy} \\ \tau_{xz} \\ \tau_{yz} \\ \sigma_{zz} \end{bmatrix}, \varepsilon = \begin{bmatrix} \varepsilon_{xx} \\ \varepsilon_{yy} \\ \gamma_{xy} \\ \gamma_{xz} \\ \gamma_{yz} \\ \varepsilon_{zz} \end{bmatrix} \tag{1.48}
$$

Initial condition applied at each point of the model is calculated by means of Equation 1.49, in which ρ is dry soil density, g is gravity, h is the depth and K_0 is the coefficient of Earth at rest. K_0 is equal to 1 for isotropically consolidated soils. In this equation, two horizontal stress components σ_{xx} and σ_{yy} are considered initially identical and all the computations account for effective parameters. Thus, for saturated soils, dry density is taken into account by $\rho = \rho_{bulk} - \rho_{water}$.

$$
\begin{aligned}
\sigma(1) &= \rho g h K_0 \\
\sigma(2) &= \rho g h K_0 \\
\sigma(6) &= \rho g h
\end{aligned} \tag{1.49}
$$

For pressure-dependent models, the shear modulus is normalized by the mean effective stress applied at the middle of soil layer, as in Equation 1.34.

In Iai et al. (1990) [69] model, depending on the shear work exerted on the soil the liquefaction front parameter S_0 is determined. This parameter indicates how close to liquefaction state the soil is. For $S_0 = 0$, liquefaction is assumed to occur in soil. Since we do not model the ultimate state at which liquefaction takes place in the soil, S_1 parameter is used as controlling numerical value for minimum S_0. Initially, S_0 is set to 1 for the cases where initial deviatoric stress ratio is considerably low ($\tau_0/P_0 < 0.67 sin\phi_p$). For higher values of initial deviatoric stress ratio ($\tau_0/P_0 > 0.67 sin\phi_p$), S_0 is solved as the solution of second order polynomial in Equation 1.50. In this equation, S is the normalized mean effective stress and equal to 1 initially.

$$
S = \begin{cases} S_0, & \text{if } r \leq r_3 \\ S_2 + \sqrt{(S_0 - S_2)^2 + (\frac{r-r_3}{sin\phi_f})^2}, & \text{else} \end{cases} \tag{1.50}
$$

where $r_3 = 0.67sin\phi_p S_0$ and $S_2 = S_0 - \frac{sin\phi_p S_0 - r_3}{sin\phi_f}$.

As mentioned in Chapter 1.3.3, we calculate the total stress matrix corresponding to total strain increment at each time step. For liquefiable soil layers, after having calculated the total stress matrix, pore pressure effects are taken into account by following the liquefaction front model. For liquefaction front model, the scheme shown in Figure 1.10 is referred to. First, principal stress matrix σ_p for 3D total stress matrix is computed. Then, the current deviatoric stress applied in the soil is computed by Equation 1.51. Plastic shear work increment in the soil is calculated by Equation 1.52 by means of deviatoric stress s. It must be noted that differently than the work of Iai et al. (1990) [69], accumulated plastic shear work in soil is directly calculated by plastic strain increment in 3D formulation. In the original work, which is based on 2D formulation, first, total shear work in the soil is calculated and then elastic part is subtracted from total shear work so that plastic shear work is calculated. Also, in the subtraction, the 2D formulation employs another dilatancy parameter (c_1). Since the 3D formulation does not require such a subtraction and plastic shear work is calculated directly from Equation 1.52, we do not use c_1 parameter so that our model requires only 5 parameters instead of 6 parameters differently than the original paper.

$$\boxed{\sigma}$$

$$\boxed{\sigma_p}$$

$$\tau = \frac{\sigma_p(max) - \sigma_p(min)}{2}$$

$$dW_s{}^p = \sum_{i=1}^{3}\sum_{j=1}^{3}(s_{ij}d\varepsilon_{ij}{}^p)$$

$$W_s = W_s^{t-\frac{1}{2}} + dW_s.$$

$$w = W_s/W_n$$

$$S_0 = \begin{cases} 1 - 0.6(\frac{w}{w_1})^{p_1}, & \text{if } w \le w_1 \\ (0.4 - S_1)(\frac{w_1}{w})^{p_2} + S_1, & \text{if } w > w_1 \end{cases}$$

$$S = \begin{cases} S_0, & \text{if } r \le r_3 \\ S_2 + \sqrt{(S_0 - S_2)^2 + (\frac{r-r_3}{sin\phi_f'})^2}, & \text{else} \end{cases}$$

$$u = P_0'(1 - S)$$

$$\gamma_{ref}^{current} = \begin{cases} \gamma_{ref}, & \text{if } S_0 > S_b \\ \gamma_{ref}/(S_0/S_b), & \text{else} \end{cases}$$

$$G^{current} = P_0'sin\phi_f'S + \Delta$$
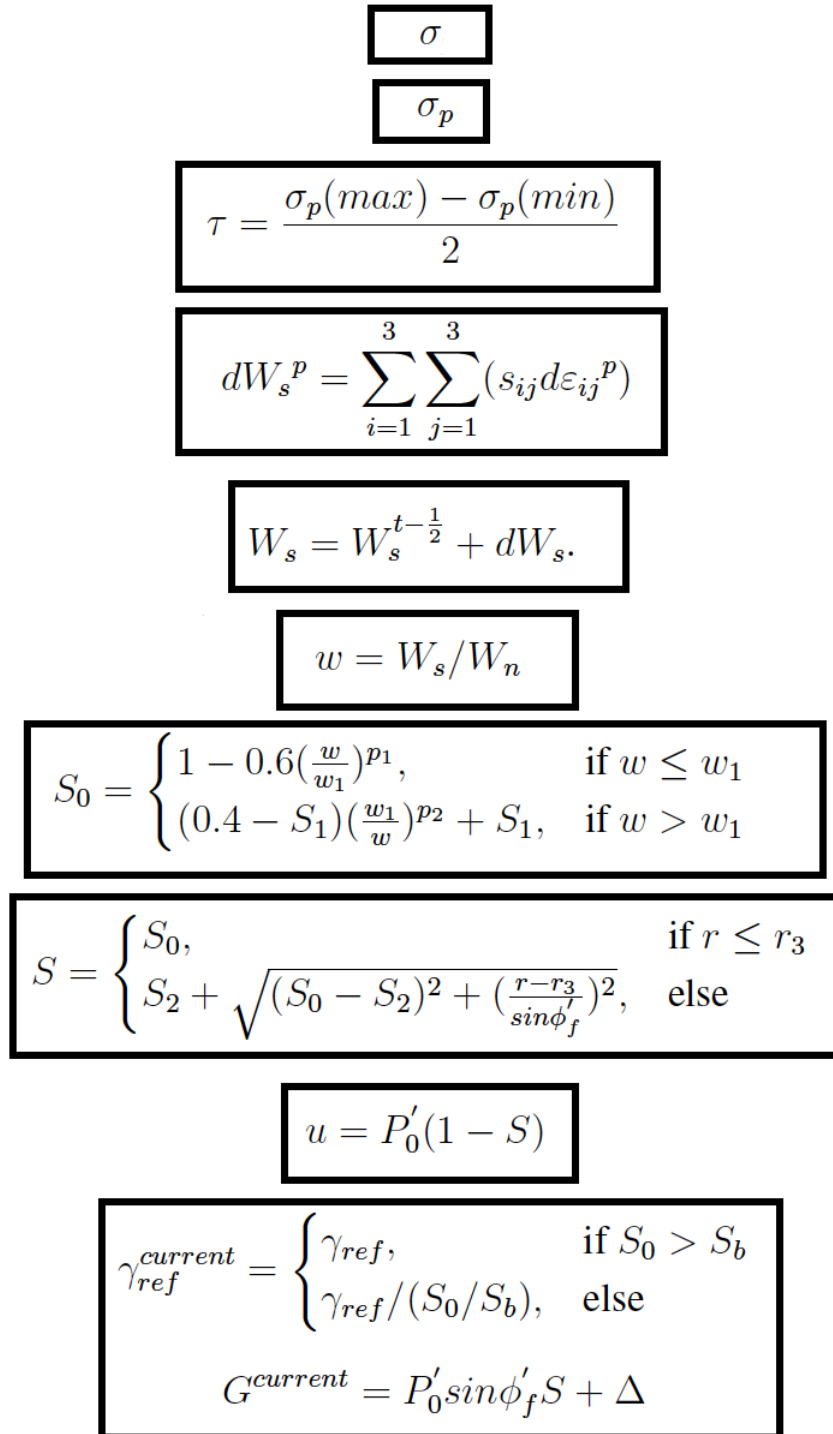
Fig. 1.10 Numerical flow followed for coupling of pore pressure effects and MPII model.

$$\tau = \frac{\sigma_p(max) - \sigma_p(min)}{2} \tag{1.51}$$

$$dW_s{}^p = \sum_{i=1}^{3} \sum_{j=1}^{3} (s_{ij} d\varepsilon_{ij}{}^p) \tag{1.52}$$

After the computation of the plastic shear work increment, a correction is applied by $dW_s = dW_s Cor$ for the case the plastic shear work increment is positive, otherwise the increment is considered to be zero. For the correction, the Equations 1.53-1.55 are referred to.

$$Cor = \begin{cases} 1, & \text{if } \frac{r}{cst} \leq 0.67 sin\phi_p \\ \frac{(sin\phi_f) - \frac{r}{cst}}{sin\phi_f - 0.67 sin\phi_p}, & \text{else} \end{cases} \tag{1.53}$$

$$cst = \begin{cases} 1, & \text{if } S \geq 0.4 + (S_b - 0.4)S_0/S_b \\ 0.4 + (S_b - 0.4)S_0/S_b, & \text{else} \end{cases} \tag{1.54}$$

$$S_b = \begin{cases} S_0, & \text{if } S_0 < 0.4 \\ 0.4, & \text{else} \end{cases} \tag{1.55}$$

The increment of plastic shear work dW_s is used for computation of the cumulative plastic shear work W_s. The increment is simply added to the precedent value of cumulative shear work $W_s^{t-\frac{1}{2}}$ such that $W_s = W_s^{t-\frac{1}{2}} + dW_s$. Then, the current shear work ratio w is computed as follows:

$$w = W_s/W_n \tag{1.56}$$

$$W_n = \frac{\tau_{max} \gamma_0}{2} \tag{1.57}$$

where W_n is the factor for shear work normalization and depends on the initial conditions of soil. Given that $\gamma_0 = \frac{\tau_{max}}{G_{corrected}}$, Equation 1.57 can be rewritten as:

$$W_n = \frac{(\tau_{max})^2}{2G_{corrected}} \qquad (1.58)$$

With the current shear work ratio in the soil w, the liquefaction front parameter S_0 is updated by Equation 1.59.

$$S_0 = \begin{cases} 1 - 0.6(\frac{w}{w_1})^{p_1}, & \text{if } w \le w_1 \\ (0.4 - S_1)(\frac{w_1}{w})^{p_2} + S_1, & \text{if } w > w_1 \end{cases} \qquad (1.59)$$

Lastly, the current normalized mean effective stress of the soil S can be calculated by the current liquefaction front parameter S_0 following Equation 1.50. Accordingly, the current pore pressure excess can be written as:

$$u = P_0(1 - S) \qquad (1.60)$$

Thus far, the procedure in order to calculate the change of mean effective stress as a function of shear work in the soil has been shown. For the purpose of coupling pore pressure effects with MPII model, we reconstruct the nonlinear backbone curve by using following equations. The new values of reference strain $\gamma_{ref}^{current}$ and shear modulus $G^{current}$ are computed by equations 1.61-1.63, respectively.

$$\gamma_{ref}^{current} = \begin{cases} \gamma_{ref}, & \text{if } S_0 > S_b \\ \gamma_{ref}/(S_0/S_b), & \text{else} \end{cases} \qquad (1.61)$$

$$G^{current} = P_0 sin\phi_f S + \Delta \qquad (1.62)$$

where Δ is formulated as:

$$\Delta = \begin{cases} 0, & \text{if } S_0 > S_b \\ (sin\phi_f - sin\phi_p)(S_b - S_0)(0.4/S_b)P_0, & \text{else} \end{cases} \qquad (1.63)$$

The MPII model parameters related to hyperbolic backbone curve such as C_n, which are detailed in Chapter 1.3.3, are recalculated with the current values of reference strain and shear modulus. A new hyperbolic backbone curve is constructed for the soil accounting for the corresponding changes in soil strength with current pore pressure rise. Then, for the next time steps, the new backbone curve is employed for nonlinearity computations and the calculated total stress matrix is used in order to execute the liquefaction front model flow as in Figure 1.10.

In Iai et al. (1990) [69], the model is tested for different kinds of soil, loose and dense soils following the laboratory work of Ishihara (1985) [74]. The experimental results are displayed on deviatoric plan with stress path and stress strain diagram in Figure 1.11 for dense soil and in Figure 1.12 for loose soils. After the coupling of 1D-3C SEM code with Iai et al. (1990) [69] model, dense and loose soil behaviors are modeled for one point in stress-controlled test without wave propagation. Soil properties that are used for these two tests are given in Table 1.2. $K_{modulus}$ accounts for the bulk modulus, while $G_{modulus}$ is the shear modulus, ϕ_f is the failure line angle.
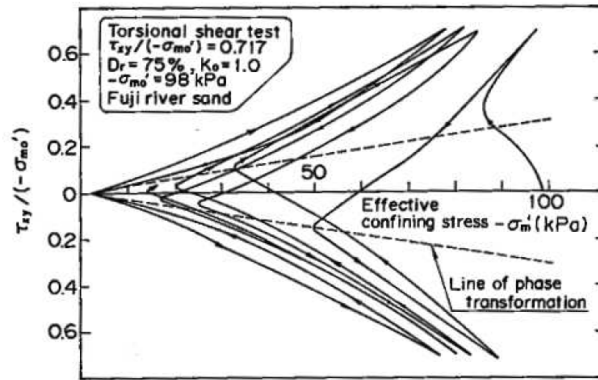
(a)
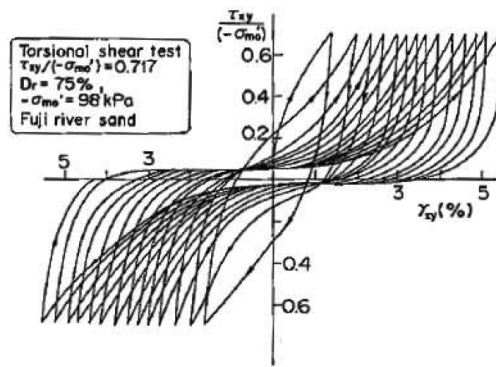
Fig. 1.11 Stress path (top) and stress-strain diagram (bottom) for dense sand after experimental results (after Ishihara, 1985 [74]).
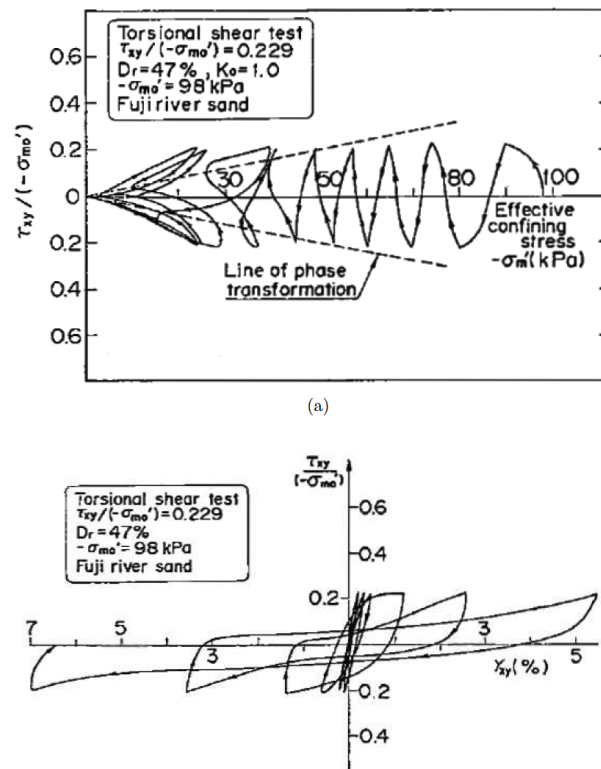
Fig. 1.12 Stress path (top) and stress-strain diagram (bottom) for loose sand after experimental results (after Ishihara, 1985 [74]).

Parameters	Loose Fuji River sand ($D_r = 47\%$)	Dense Fuji River sand ($D_r = 75\%$)
$K_{modulus}$	270,500 kPa	366,800 kPa
$G_{modulus}$	103,700 kPa	140,700 kPa
$sin\phi_{f'}$	0.87	0.91
$sin\phi_{p'}$	0.42	0.42
p_1	0.45	0.40
p_2	1.75 (1.40)	0.72
w_1	2.00	6.0 (2.85)
S_1	0.0035	0.0050

Table 1.2 Parameters for loose and dense soils to use in front saturation model tests (after Iai et al. 1990 [69]). Original values are shown between parenthesis if different.

In Figure 1.13, the numerical results are plotted in two panels. On top panel, stress-strain diagram (left) and stress path (right) for dense soil are displayed. The same representation is made for loose soil at bottom panel. Stress paths are plotted in deviatoric plan where normalized deviatoric stress is related to normalized mean effective stress (normalization is made by initial mean effective stress). For dense soil, initially, the normalized effective stress decreases due to the raise in pore water pressure until the stress path reaches to the phase transformation line. Beyond this line, the soil enters into dilatant zone and regains some strength, then the effective stress keeps decreasing with unloading. As the path gets closer to the origin of the diagram, the soil experiences successive increase and decrease in stiffness. On the other hand, for loose soil, stress path follows a contractive soil behavior trend such that effective strength decreases continuously until it is reduced to 0.4. Regarding the stress-strain diagrams, a significant difference is noted between dense and loose soil results. In both soil types, an expansion in hysteresis curves is seen. However, in dense soil, the stress-strain loops are closer to each other, while in loose soil, an increasing off-set between the curves can be remarked. This can be related to the fact that in loose soil, soil rigidity decreases continuously due to the continuous decrease in effective strength in successive loading cycles. Conversely, partial increase in dense soil rigidity results in narrow stress-strain loops until the soil reaches to strain over 6%.
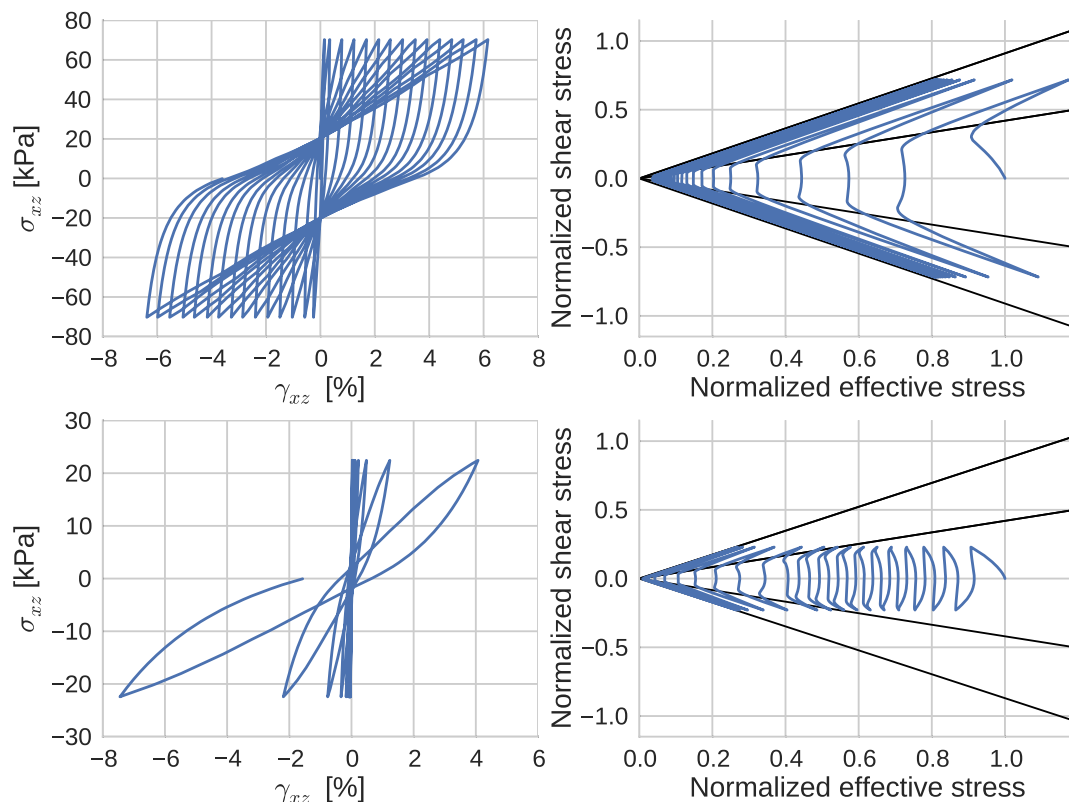
Fig. 1.13 Stress-strain curves for x-component (at left) and stress path (at right) for dense sand (top panel); for loose sand (bottom panel).

In Figure 1.14, the changes of stress, strain and pore pressure excess in 5 seconds are displayed for dense and loose soils. On top panel, stress values imposed on dense (left) and loose (right) soil models are seen. Since the tests are stress-controlled, maintained stress is 70 kPa for dense soil while it is reduced to 23 kPa approximately for loose soil (Deviatoric ratio is 0.717 for dense soil and 0.229 for loose soil as indicated in Figures 1.11-1.12 where initial effective mean effective stress equals to 98 kPa). In strain changes (middle panel), it is noted that for dense soil, the change is more gradual whereas the strong expansion of stress-strain curves between successive loading cycles results in sharp changes in strain values of loose soil. As a result of highly dilatant behavior, the oscillations of pore pressure excess are more apparent in dense soil (left of bottom panel). In loose soil, sudden rise of pore pressure excess and amplifications of oscillations after approximately 12 cycles is exhibited due to contractive behavior of loose soil.
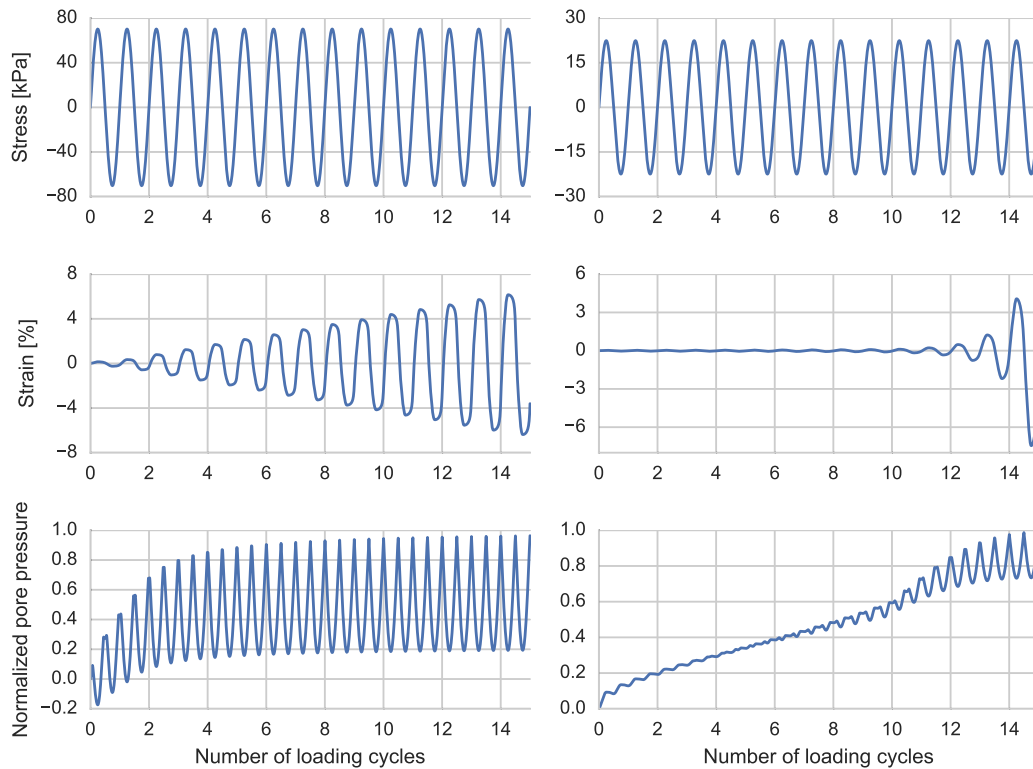
Fig. 1.14 Temporal change of stress (top), strain (middle) and pore pressure excess (bottom) for dense soil (left column) and loose soil (right column).

In addition, the typical soil behavior under cyclic loading is obtained for dense and loose soils after necessary modifications of certain dilatancy parameters. As shown in Table 1.2, only parameter change is applied to p_2 parameter for loose soil and to w_1 parameter for dense soil, so that the later dilatancy is slightly increased in loose soil and delayed for dense soil. The numerical simulation results are quite coherent with the experimental results obtained for dense and loose soil types in terms of soil tendency to cyclic mobility phenomenon. It demonstrates the efficiency of coupling of MPII model with Iai et al. (1990) [69] model.

Chapter 2

1D-1C wave propagation modeling: Code verification

1D-1C wave propagation modeling: Code verification

2.1 Introduction

In this PhD thesis, a multi-dimensional SEM code, which is capable of modeling viscoelastic and nonlinear media with pore pressure effects is developed. As a first step, we start by verification of coupling inelastic models in 1D SEM code for single shear component wave propagation (one component - 1C). In this chapter, first, implementation of viscoelastic damping in 1D SEM code is explained and verification tests through several benchmarks on canonical and realistic models are performed. Second, verification of nonlinearity is shown by benchmark results of 1D nonlinear SEM code with other numerical nonlinear methods on canonical and realistic elastoplastic models are shown. Afterwards, verified 1D SEM code is used for further explorations on

the effects of viscoelasticity and nonlinearity in 1D-1C shear wave propagation. A series of simulation results for consideration of different soil constitutive models are discussed. Lastly, a sensitivity analysis is performed for showing the influence of using different polynomial order degree in spectral element method, the number of Iwan springs in nonlinearity and the choice of soil constitutive models on precision and computational cost.

2.2   Implementation of viscoelastic damping

2.2.1   Numerical algorithm

For the implementation of new constitutive soil models in 1D SEM code, the 1D SEM code of Delavaud (2007) [32] has been used. The original 1D SEM code offers wave propagation modeling in linear media. For such media, elasticity is defined as material rheology (See Chapter 1.3.1). As new features, we implemented viscoelastic and nonlinear soil constitutive models, which are detailed in Chapter 1.3.2- 1.3.3. We model the total energy dissipation in soil as the sum of viscoelastic attenuation and hysteretic attenuation similarly to Assimaki et al. (2011) [9]; Gélis and Bonilla (2012 [52]; 2014 [53]).

For viscoelasticity, we refer to Liu and Archuleta (2006) [98] model, which is detailed in Chapter 1.3.2. According to the model, the degradation in strain due to viscous damping in the material $[\varepsilon(t) - \sum_{k=1}^{N} \zeta_k]$ is needed to be computed by Equation 1.28, for each time step. This viscous strain is multiplied by unrelaxed modulus M_u in order to express corresponding stress in material. For computation of M_u, model proposes 8 memory variables. In addition, elastic parameters of the medium such as density, shear and pressure wave velocities are required with viscoelasticity parameters of quality factors Q_s, Q_p (for shear and pressure waves) and reference frequency w_r.

In 1D SEM code, all the necessary equations are defined in a subroutine in order to calculate M_u for each material type in studied model, in the beginning of the simulation. Then, for each time step of simulation, strain rate $\dot{\varepsilon}$ is computed by means of velocity v. Afterwards, for viscoelasticity, degradation in strain rate $\dot{\varepsilon}_{viscoelastic}$ is computed and resultant viscoelastic stress is returned for each point in the mesh. This flow is illustrated in Figure 2.1. At the end of each time step, computed stress is used in calculation of current velocity for integration point.
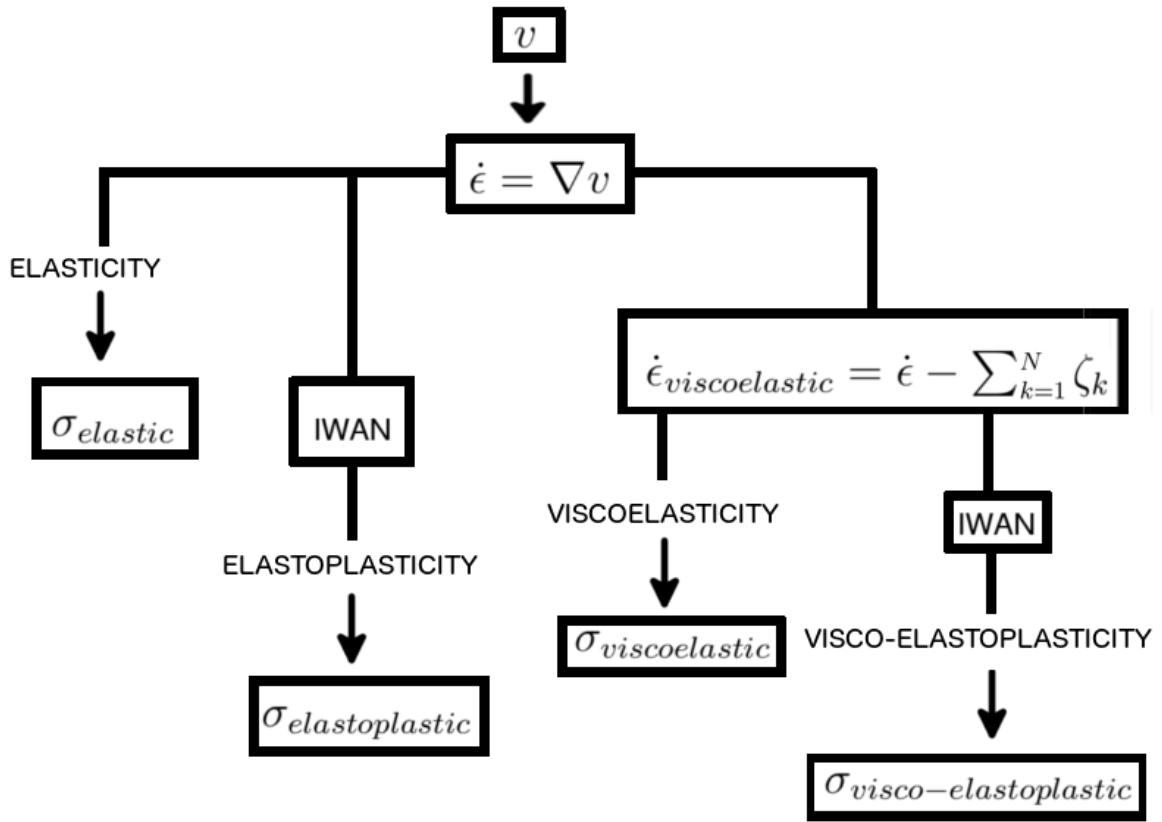
Fig. 2.1 Numerical work flow of 1D SEM code for different material constitutive models.

2.2.2   Quality factor verification

For the purpose of verification of quality factor in viscoelasticity, an homogeneous model with a length of 5000 meters is created by elements of 50 m size. Properties of the model and the simulation are shown in Table 2.1, where ρ is soil density, V_s is shear velocity, N is the polynomial degree of spectral elements, Q_s is quality factor for shear waves and w_r is reference frequency. At each element, 8th polynomial order degree is used so that 9 GLL points are defined on each element. At two extremities of the model, C-PML absorbing boundaries (each one defined as one element of 50 m size) are used. Quality factor is set as a tenth of shear wave velocity with reference frequency w_r equal to 1 Hz. Simulation time step is determined as 3.10^{-4} s.

Table 2.1 Properties of the model used in quality factor verification test.

$\rho\,[kg/m^3]$	$V_s\,[m/s]$	N	Q_s	w_r [Hz]	$\Delta t\,[s]$
2000	400	8	40	1	3.10^{-4}

The model described above is used with a Ricker source, of which the energy remains on the frequency range $0-10Hz$ and presents a peak at its central frequency of $4Hz$. Velocity time history and spectrum amplitude of the source are presented in Figure 2.2.
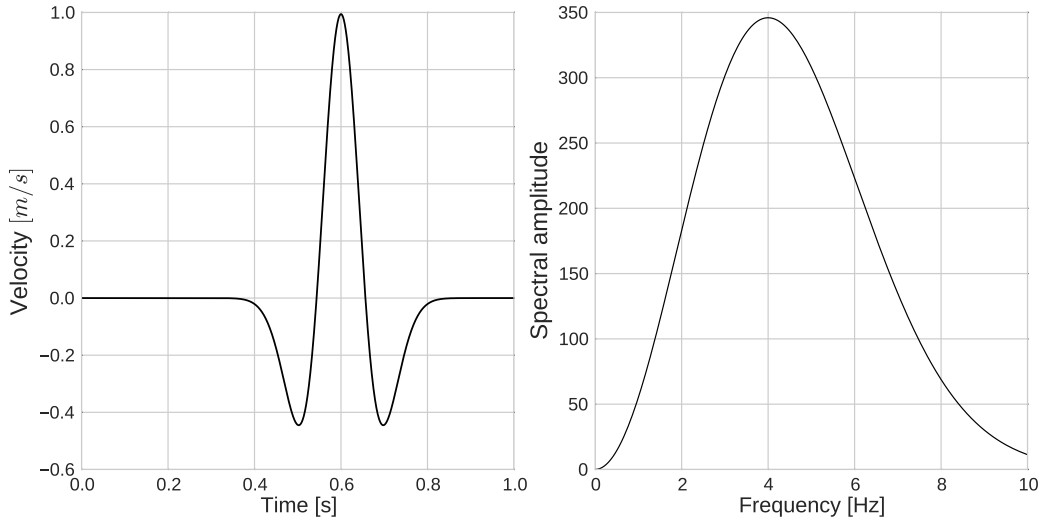
Fig. 2.2 Velocity time history of the Ricker source (left); Spectral amplitude of the Ricker source (right).

Quality factor Q during the wave propagation, which is held constant in each soil layer and assumed to be independent of frequency for all the simulations, can be calculated by the following formula where u is Fourier transformed displacement; v is wave speed; L is propagation distance and ω is corresponding frequency (Day and Bradley, 2001 [27]):

$$Q^{-1}(\omega) = \frac{-2v\ln|u(x+L,\omega)/u(x,\omega)|}{\omega L} \tag{2.1}$$

For such a calculation, we refer to the calculated velocities of the simulation so that the corresponding quality factors of wave propagation for the simulated velocity according to Equation 2.1 is compared to the constant Q value used in the simulation ($Q = 40$). For this calculation, velocity values of two receivers spaced with a distance of 1800 m ($L = 1800m$) are employed. It should be noted that such an analysis stands for a numerical verification of

quality factor implementation for 1D plane wave propagation in a medium with constant Q. It is different than quality factor verification tests in frequency domain as detailed in Liu and Archuleta, 2006 [98].

Figure 2.3 shows the calculated quality factors after simulation. On the frequency band $0.1 - 10$ Hz where enough energy is available for the source, a good match between the calculated Q values and the referred Q value ($Q = 40$) is noted. In this viscoelastic model with 8 memory variables, Q is shown to be nearly constant for the frequency interval $0.01 - 50Hz$ with small oscillations (See Chapter 1.3.2). The variations at lower frequencies in the figure are similar to those shown in Figure 1.5. The fit of calculated Q to the modeled value is provided for 8 memory variables of time τ_k, which are shown in Table 1.1. The corresponding frequencies for these variables account for the values around which oscillations are noted (e.g. $0.075Hz$, $0.486Hz$, $2.443Hz$ below 10 Hz). Oscillations can be decreased by a use of higher number of memory variables. Yet, this may result in computational time problems for the numerical model.
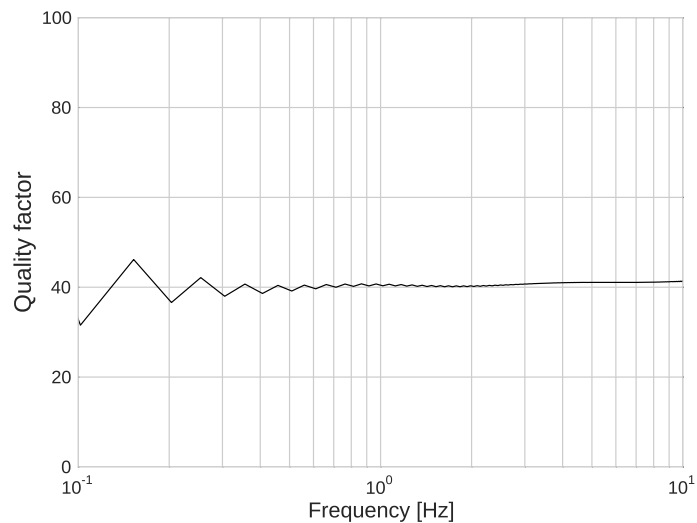
Fig. 2.3 Calculated quality factors for simulation with the Ricker source on the frequency band $0.1 - 10Hz$.

2.2.3   Viscoelasticity verification

Rome model

For the verification of the viscoelasticity implementation, we compare the 1D-1C SEM code with other numerical methods applied on the Rome (Italy) model that has been studied by Martino et al. (2015) [105]. The 1D Rome model extracted from one of the 2D models is composed of 14 soft layers overlying bedrock with velocity inversions (e.g. layer 4 has a higher velocity than layer 5). Table 2.2 displays a detailed description of the soil column, where ρ is soil density, V_s and V_p are shear and pressure wave velocities, Q_s and Q_p are quality factors for shear and pressure waves, respectively. The reference frequency w_r is set as $1Hz$ for all the layers. Such a complex model allows to track small differences between numerical methods up to high frequencies ($> 10Hz$). The input motion used is the same as in Peyrusse et al. (2014) [124], a Gaussian synthetic signal where the energy is on $[0 - 14]Hz$. Accordingly, the input motion is filtered by Butterworth low-pass filter below $14Hz$. Velocity time history with corresponding Fourier amplitude of the input motion (after filtering) are shown in Figure 2.4. A mesh corresponding to a resolution of $14Hz$ and 4th polynomial order (5 GLL points per element) is used. The element size changes in the $2.5 - 16m$ range all over the model depending on the local velocity of the medium and on each layer a maximum number of two elements are used. Minimum grid distance between GLL points of elements changes from 0.4375 to $2.8m$ (See Chapter 1.2.1), while in finite difference method (FDM) the element size is $0.5m$ for a resolution of $14Hz$ using 30 points per wavelength to avoid numerical dispersion (Bohlen and Saenger, 2006 [14]). The time step is set as $2.10^{-5}s$. The simulation is done by imposing the source at 100 m depth of the model. Elastic rock condition is used at the bottom of soil column, such that an element of C-PML (of same size as adjacent element) is defined under 100 m (See Chapter 1.2.3 for more detail of C-PML). An initial comparison between SEM, Haskell-Thomson (HT) and finite difference methods is made for elastic soil rheology consideration in the media. Figure 2.5 shows surface velocity time histories for SEM and HT with transfer functions of these two methods and FDM. Ground motion weakens with time due to energy loss with elastic rock condition at bottom boundary of the model. In frequency plan, high energy content is seen by resonance peaks on the whole frequency band and soil model complexity is present by various peaks. In Figure 2.6 another comparison is performed for viscoelastic soil constitutive model verification. SEM and HT methods give identical results and the motion is weaker than elasticity condition due to viscoelastic attenuation. At bottom of the same figure, transfer functions obtained by SEM, HT and FDM are compared. Since the input energy could be almost neglected above 14 Hz and the mesh resolution is valid in $[0 - 14]Hz$, the results are shown up to this frequency limit. The viscoelastic attenuation in the media can be remarked by the decrease in the values of resonance peaks compared to elasticity. Given the complexity of the media, the very good agreement between the results

of all the methods demonstrates the correct implementation of viscoelasticity.

Table 2.2 Soil properties at the Rome model.

Layer	Thickness $[m]$	$V_s[m/s]$	$V_p[m/s]$	$\rho[kg/m^3]$	Q_s	Q_p
1	10	220	490	1835	100	200
2	6	239	523	1876	15	30
3	16	260	1480	1967	100	200
4	13.5	417	1760	1957	50	100
5	10	212.5	1235	1865	35	70
6	2.5	417	1760	1957	50	100
7	7	713	2560	2141	50	100
8	3	545	2125	2078	35	70
9	2.5	610	2379	2078	35	70
10	3	675	2632.5	2078	35	70
11	2.5	740	2886	2078	35	70
12	3	805	3139.5	2078	5000	10000
13	2.5	870	3393	2078	5000	10000
14	2.5	935	3646.5	2078	5000	10000
Bedrock	16	1000	3900	2078	5000	10000
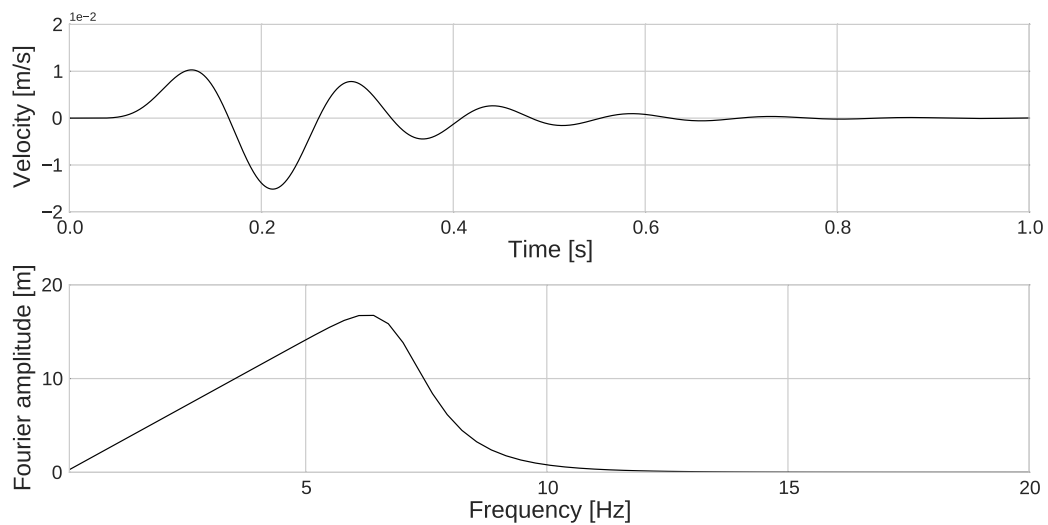
Fig. 2.4 Velocity time histories (left); Fourier amplitude (right) of the input motion used in Rome model.
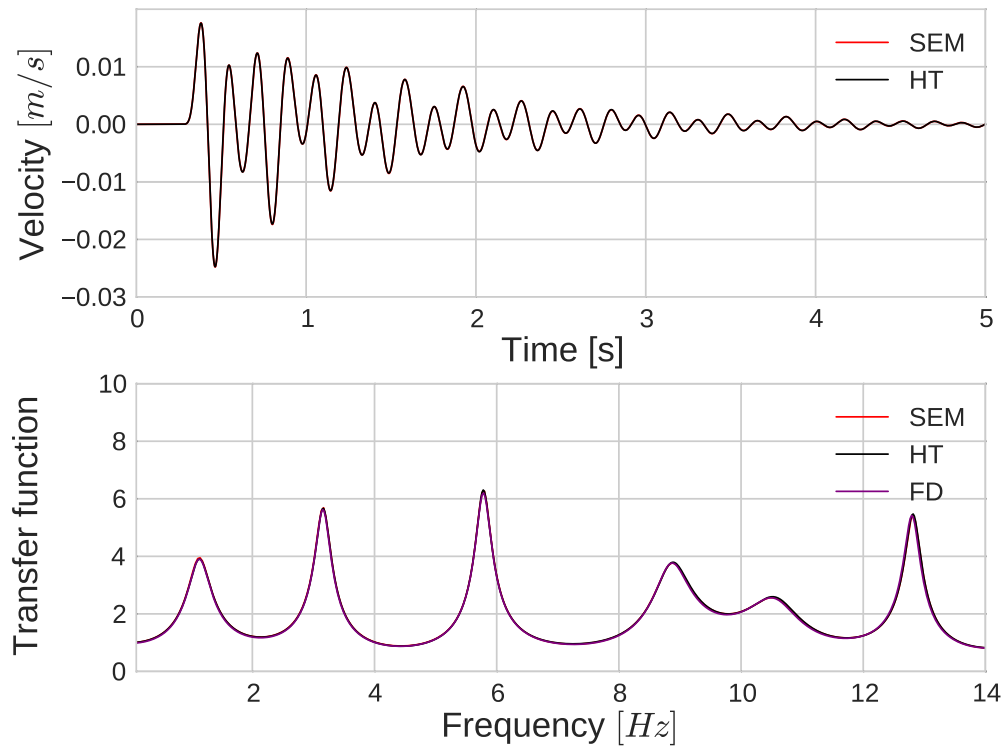
Fig. 2.5 Comparison between velocity time histories at surface from SEM (in red) and HT (in black) (top); Transfer functions obtained with SEM (in red), HT (in black) and FD (in purple) (bottom) for elasticity.
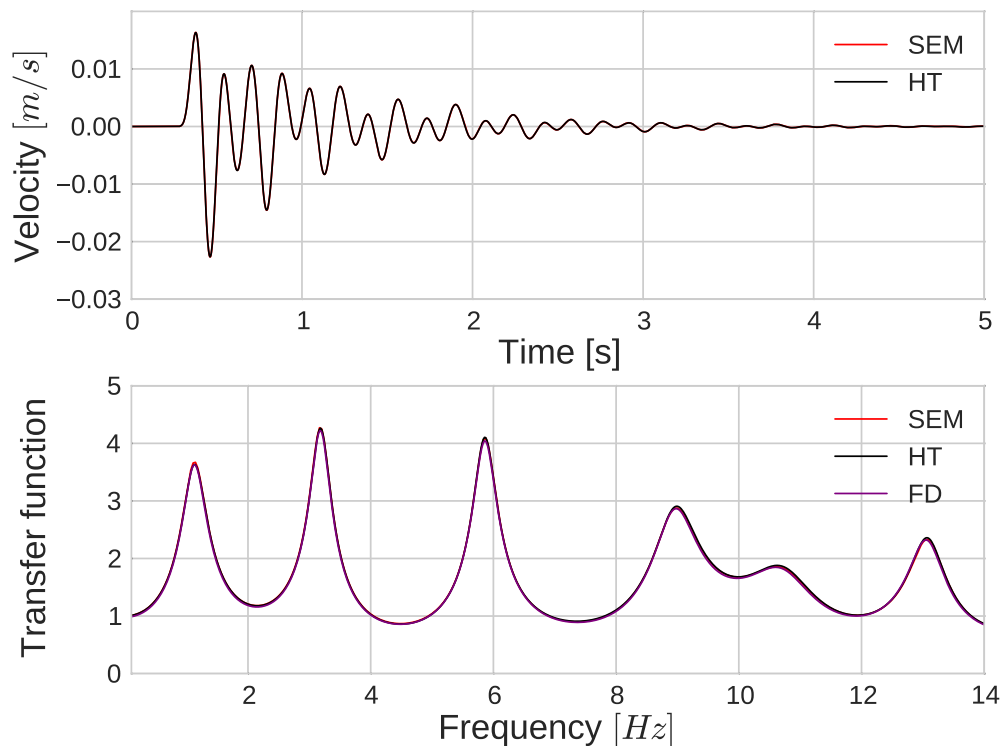
Fig. 2.6 Comparison between velocity time histories at surface from SEM (in red) and HT (in black) (top); Transfer functions obtained with SEM (in red), HT (in black) and FD (in purple) (bottom) for viscoelasticity.

In addition, Figure 2.7 displays maximum stress and strain profiles in Rome model for elasticity and viscoelasticity. The influence of viscoelastic attenuation is noted by strength loss (decrease in maximum stress) and strain damping all over the model. Change in soil rigidity (strength) is more visible in superficial soil layers, while the layers below $40m$ depth are concerned more by strain attenuation. This result reveals the impact of energy attenuation with viscoelasticity on soil conditions and wave propagation even under simple loading conditions.
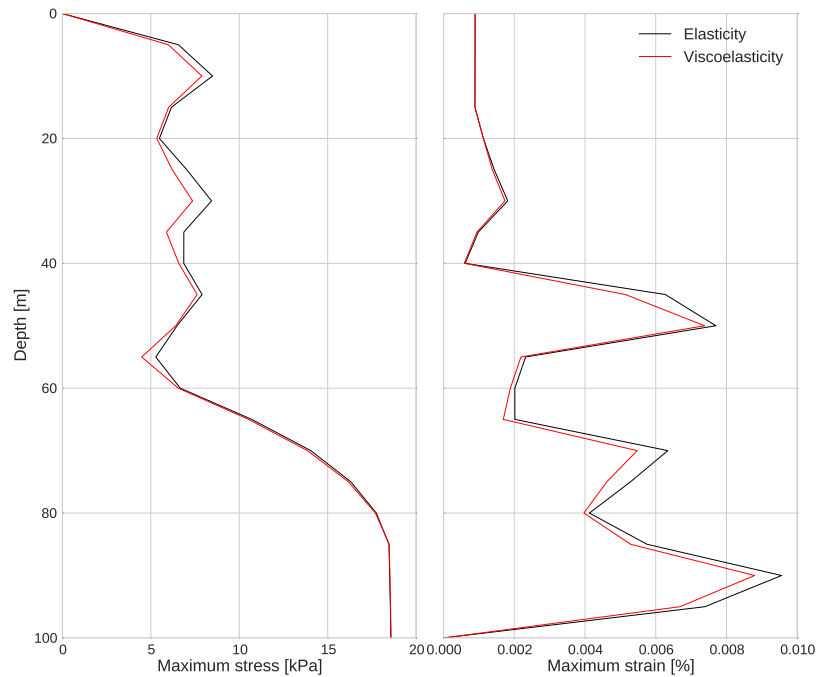
Fig. 2.7 Maximum stress profiles throughout the soil profile of Rome model for elasticity (in black) and viscoelasticity (in red) (left); Maximum strain profiles throughout the soil profile of Rome model for elasticity (in black) and viscoelasticity (in red) (right).

The results are also compared for different use of reference frequencies (1, 6 and 8 Hz) so that we investigate the influence of the reference frequency on wave propagation in viscoelastic media, similarly to Peyrusse et al. (2014) [124]. Figure 2.8 shows the transfer functions of SEM code results for the use of 3 different reference frequencies. We see an offset between the spectral curves, i.e., transfer function is shifted for different reference frequencies. Particularly, difference between 1 Hz and 6 Hz is more evident. This is related to the fact that reference frequency is inversely proportional to unrelaxed modulus (See Equation 1.29). For a higher reference frequency, unrelaxed modulus is weakened and in consequence medium velocity becomes smaller, so that the fundamental frequency and harmonics of the model are shifted to lower values. We see that calculated ground motion is highly dependent on reference frequency of the media. Therefore, it is possible to conclude that selection of reference frequency is important in numerical modeling of viscoelasticity.
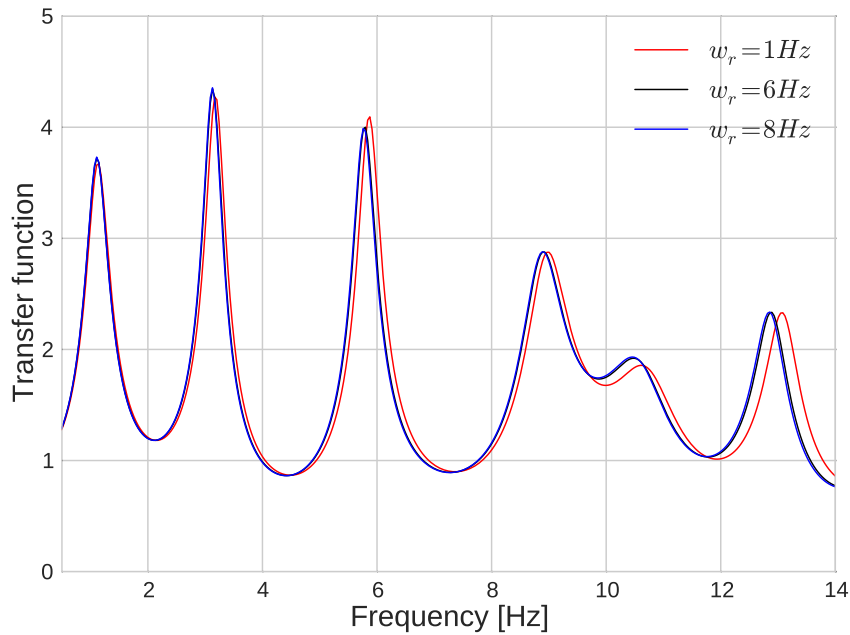
Fig. 2.8 Comparison between transfer functions obtained with SEM for models with reference frequency of 1 Hz (in red), 6 Hz (in black) and 8 Hz (in blue).

Volvi model

In previous section, the implementation of viscoelasticity has been verified successfully by benchmarking with different numerical methods on the realistic model of Rome (Italy). In this section, we use the model of Volvi (Greece) site, which has been studied by Peyrusse et al. (2014) [124], for further verification tests of viscoelasticity. The Volvi model differs from the Rome model by its higher depth and velocity profile where medium velocity increases with depth. Even though we already obtain satisfactory results on the Rome model where the model becomes complicated with velocity inversion, considering the relatively high abundance of provided data in Volvi (Greece) site, in this section we perform similar analyses on this real site as well. Also, it should be noted that we make use of Volvi model in the following chapters. The model properties is given in Table 2.3, where ρ is soil density, V_s and V_p are shear and pressure wave velocities, Q_s and Q_p are quality factors for shear and pressure waves, respectively. Reference frequency is taken as $1Hz$ all over the model. Input signal is defined as the same signal used in Rome model (See Figure 2.4). At bottom boundary of soil column, elastic rock condition is applied. The mesh is created for $14Hz$, where the energy content of the source is limited. Element sizes changes in $3-20m$ for soft layers and for bedrock, one element of $103.5m$ size is used. For all the elements, 5 GLL points are defined (corresponding to the 4th polynomial order). Thus, the minimum grid size

overall the model is $0.525m$. The time step is set to $2.10^{-4}s$.

Table 2.3 Soil properties at the Volvi model.

Layer	Thickness $[m]$	$V_s[m/s]$	$V_p[m/s]$	$\rho[kg/m^3]$	Q_s	Q_p
1	7	130	1500	2050	15	75
2	13	200	1500	2150	20	75
3	34	300	1650	2075	30	83
4	23.5	450	2050	2100	40	103
5	50	600	2450	2155	60	123
6	59	700	2550	2200	70	140
7	10	1250	3500	2500	100	200
Bedrock	103.5	2600	4500	2600	50000	50000

Figure 2.9 displays surface velocities (top panel) and transfer functions (bottom panel) up to 14 Hz where enough energy lies on for elasticity calculated with SEM and HT methods. Same comparison is made for viscoelasticity in Figure 2.10. For both elasticity and viscoelasticity, two methods give identical results on temporal and frequency plans. The introduction of viscoelastic damping in the media results in approximately 2 times smaller values of resonance peaks. Also, in surface velocity outputs, motion is weaker in viscoelasticity.
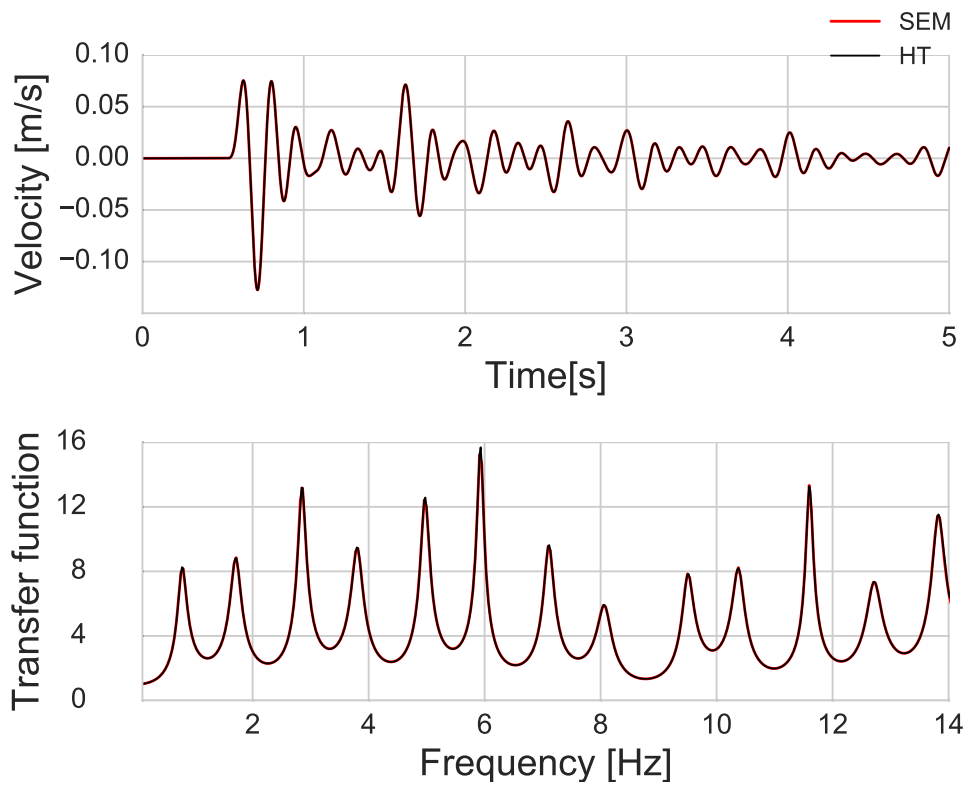
Fig. 2.9 Comparison between velocity time histories at surface obtained with SEM (in red) and HT (in black) (top); transfer functions obtained with SEM (in red) and HT (in black) (bottom) for elasticity.
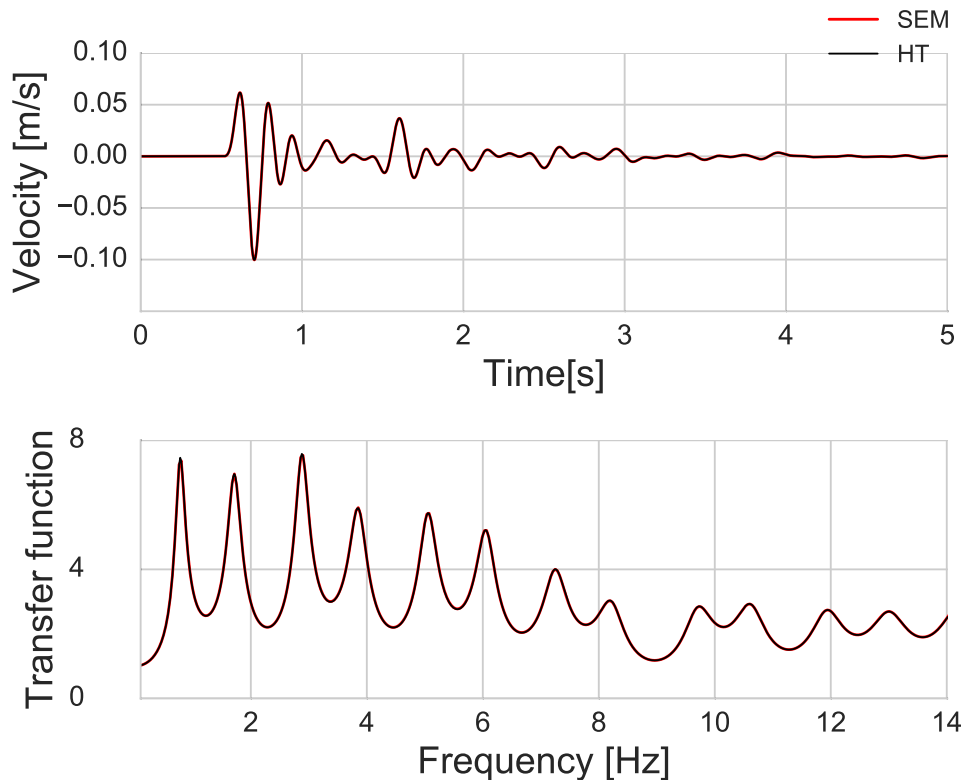
Fig. 2.10 Comparison between surface velocities obtained with SEM (in red) and HT (in black) (top); transfer functions obtained with SEM (in red) and HT (in black) (bottom) for viscoelasticity.

We show that 1D SEM code gives compatible results with different numerical methods for different real models. By taking into consideration the good agreement between the spectral element method and other methods for all the simulated models presented in this section, it can be concluded that viscoelasticity is successfully implemented in 1D SEM code.

2.3   Nonlinearity verification

2.3.1   Numerical algorithm

In 1D nonlinear site response analysis, the soil behavior is approximated by a three-dimensional constitutive model, which takes part in the family of MPII model (See Chapter 1.3.3 for more details). The MPII model is implemented in the 1D SEM code as a subroutine (IWAN in Figure 2.1) that takes strain increment at each GLL point and returns

the corresponding total stress increment based on deviatoric stress and strain parameters. Regarding to Figure 2.1, for elastoplastic soil rheology consideration in the medium, the strain rate $\dot{\varepsilon}$ is directly used for calculation of corresponding stress $\sigma_{elastoplastic}$ inside the nonlinearity subroutine. On the other hand, for visco-elastoplasticity, first, the degradation in strain rate $\dot{\varepsilon}$ due to viscoelastic damping in the medium is computed, so that the resultant strain rate term $\dot{\varepsilon}_{viscoelastic}$ is employed in the nonlinearity subroutine, where the resultant stress $\sigma_{visco-elastoplastic}$ is calculated for the given strain rate at the point.

2.3.2   Benchmarking of the 1D SEM code on nonlinearity

In order to verify the nonlinearity implementation in our code, we use one of the results obtained within the PRENOLIN project (part of the SINAPS@ project) (Régnier et al., 2016 [129]). This project aims at comparing 1D numerical wave propagation codes, developed by 21 international participating teams that model the soil nonlinearity using canonical and real cases. One of the canonical cases of the project, the so-called P1 model, is taken into consideration for this verification test. In the P1 model, a single layer of soil defined with a thickness of $20m$ and a velocity of $300m/s$ is overlying a bedrock with a shear velocity of $1000m/s$ (Table 2.4). For surface level, free surface boundary condition is defined, while for bottom boundary, borehole boundary condition is used (See Chapter 1.2.3). It should be noted that although the model is hypothetical and there is no borehole record at the model bottom, borehole condition is used for defining incident wave field in a medium where no energy loss is allowed. A fourth-order polynomial degree (5 GLL points) is chosen for this model. A simple Ricker signal with a PGA of $0.93m/s^2$ and duration of $1s$, which is provided by the project, is imposed as input motion at the bottom of the discretisized domain. In order to remove potential numerical noise with minimal loss of signal components, an acausal low pass frequency-domain filtering is applied below $10Hz$ by using a Butterworth filter before and after the simulation. Figure 2.11 displays the velocity time history and Fourier amplitude of the filtered input motion. The time step is set to $5.10^{-5}s$. Elements of $5m$ size are used in the model. As nonlinearity properties of the medium, reference strain equal to $3.65.10^{-4}$ is used for 50 plasticity surfaces (Iwan springs) (See Chapter 1.3.3). The soil rheology defined in the model is elastoplasticity, such that no viscoelastic damping is taken into account.

The results obtained with SEM are compared to the results of another team participating in the project, team EY, (Mercerat and Glinsky, 2015 [111]; Régnier et al., 2016 [129]), who uses discontinuous Galerkin method (DGM) code, where the MPII model is also

implemented. Figure 2.12 shows the stress-strain diagram for the point located at GL-9 m. Both methods show similar dynamic loading paths with negligible differences at the extreme values. Furthermore, due to soil nonlinearity, the material behavior is no longer elastic and experienced values of shear strain becomes important in the soil even under such simple input and site conditions. The agreement between the two methods is also seen in surface acceleration time histories in Figure 2.13. Besides the slight differences in amplitudes, nonlinear surface response is very similar in both methods and the ground motion weakens with time due to energy attenuation in nonlinear media.

Table 2.4 Soil properties at P1 model (PRENOLIN).

Layer	Thickness $[m]$	$V_s[m/s]$	$V_p[m/s]$	$\rho[kg/m^3]$	Q_s	Q_p
1	20	300	700	2000	30	70
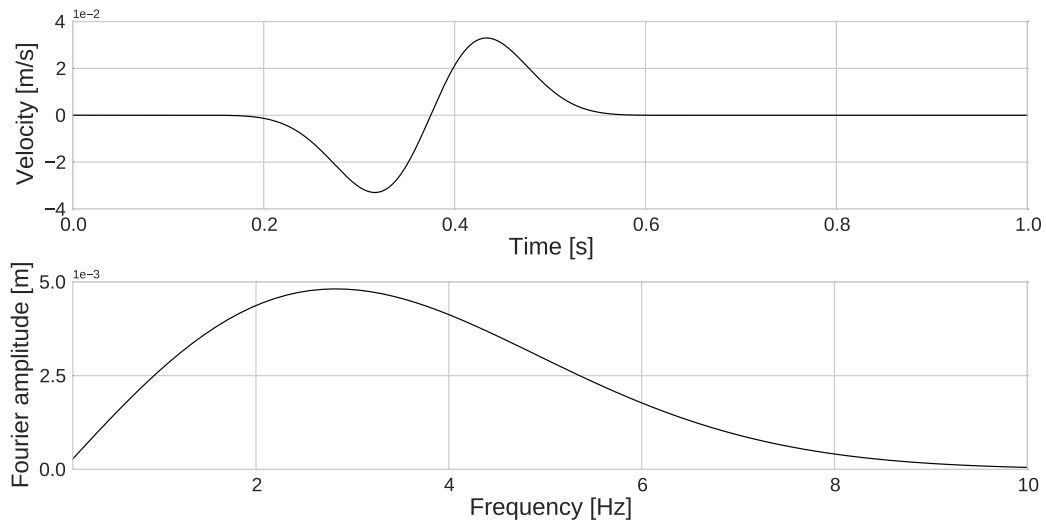
Fig. 2.11 Velocity time histories (top); Fourier amplitude (bottom) of Ricker signal used in the P1 model.
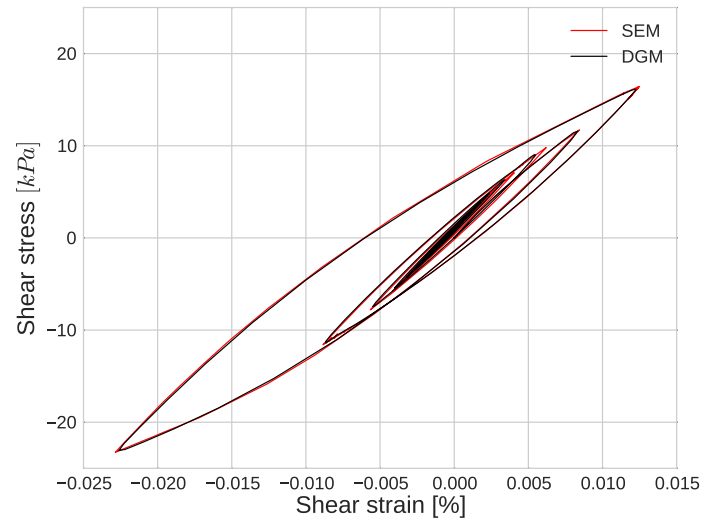
Fig. 2.12 Stress-strain curves computed with SEM (in red) and DGM (in black) for the P1 model simulation under elastoplastic conditions.
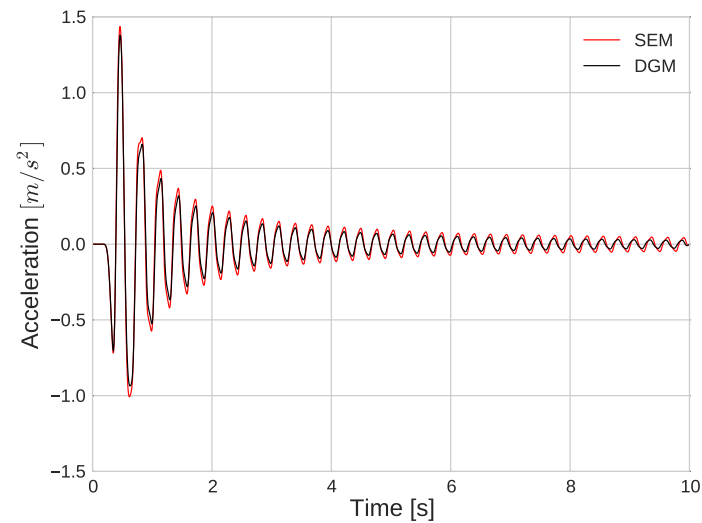
Fig. 2.13 Acceleration time histories at surface computed with SEM (in red) and DGM (in black) for the P1 model simulation under elastoplastic conditions.

In the framework of PRENOLIN project, another benchmark group (Iwan group) is organized for comparisons between different numerical schemes using MPII nonlinear model in 1D seismic wave propagation. In this benchmark, the possible numerical differences between finite-difference, finite-element, spectral-element and discontinuous Galerkin methods are investigated. Our 1D-1C spectral-element code also takes part in this group. A

number of 1D nonlinear wave propagation tests performed on canonical and realistic models are analyzed (Mercerat et al. 2015 [109]; 2016 [110]). The most recent of these studies (Mercerat et al., 2016 [110]) can be found in Annex A.

2.4   Comparison of different rheologies

Following the satisfactory verification tests of viscoelasticity and nonlinearity implementations, in this section, we focus on the influence of soil constitutive models on wave propagation under a real input signal. As input motion, one of the real data procured by PRENOLIN projet materials is used. The project makes use of the sites and recorded data within Japanese KiK-net and PARI networks (Régnier et al., 2016 [129]). For the phase of verification on 1D canonical cases, the real accelerograms are prepared after the data recorded on EW direction in IWTH17 Japanese site by scaling for PGA values of $0.5m/s^2$, $2m/s^2$ and $5m/s^2$. The signals are named as Real source #1, Real source #2 and Real source #3, respectively. In our study, the Real source #3, of which velocity time history and Fourier amplitude are shown in Figure 2.14, is employed as real input motion. It has been filtered between $0.1 - 20Hz$. Real source #3 has a peak velocity of $0.2m/s$ with a total duration of 100 seconds. Content of the signal is quite complicated that it can trigger successive loading-unloading cycles in soil. Simulations are performed on the 1D nonlinear P1 model, which is used for the nonlinearity verification in Chapter 2.3.2. The mesh and soil nonlinearity properties remain the same as well as the boundary conditions. Moreover, we recall that for nonlinearity verification in Chapter 2.3.2, elastoplasticity is considered as soil rheology in the P1 model. In this section, for viscoelastic and visco-elastoplastic models, we use a reference frequency of $1Hz$ and quality factors of shear and pressure waves are set to a tenth of velocity values (Q_s and Q_p in Table 2.4).
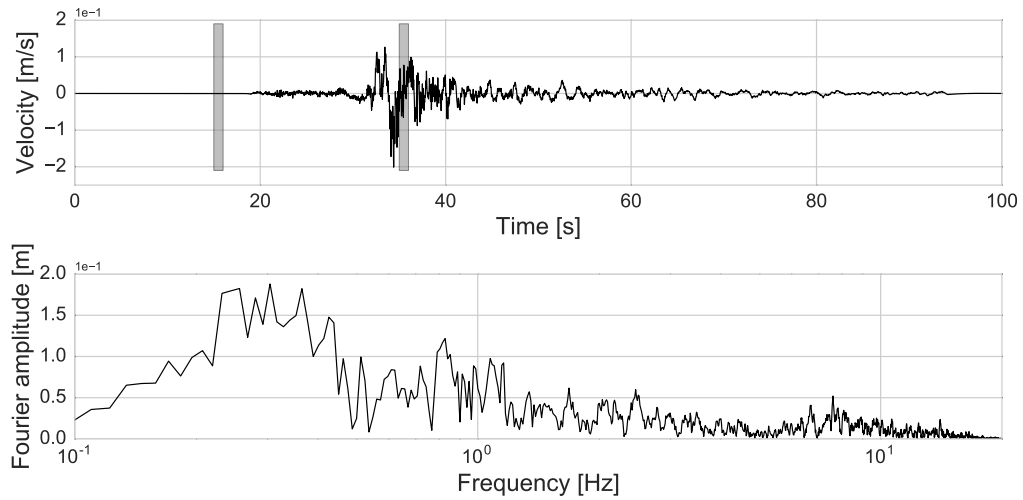
Fig. 2.14 Velocity time histories of Real source #3 signal where $[15 - 16]s$ and $[35 - 36]s$ time intervals are shaded (top); Fourier amplitude (bottom) of Real source #3 signal.

Figure 2.15 illustrates the attenuation effects of viscoelastic, elastoplastic and visco-elastoplastic behaviors by comparing surface acceleration outputs of each rheological model under Real source #3 loading. For elasticity model, propagating waves are trapped in the medium due to rigid boundary condition at bottom. As a result, the surface motion calculated in elasticity model is significantly strong (peak ground acceleration over $20m/s^2$). There exists a significant attenuation of the elastic acceleration field with occurrence of viscoelasticity since the initial seconds. This attenuation is larger for plasticity compared to viscoelasticity and becomes even larger in visco-elastoplastic model with the existence of both mechanisms together.
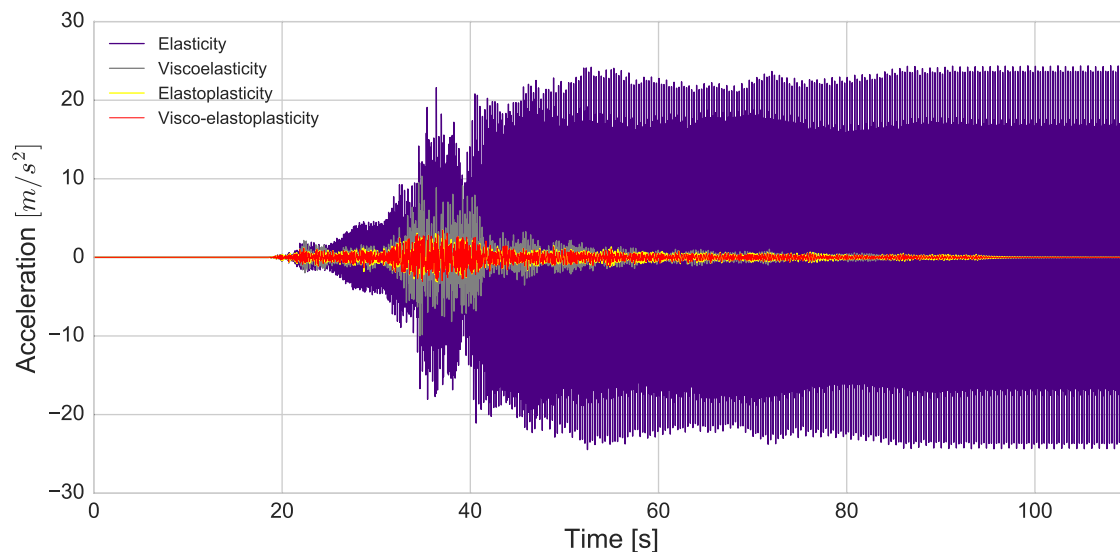
Fig. 2.15 Acceleration time histories for elasticity (in purple), viscoelasticity (in yellow), elastoplasticity (in blue) and visco-elastoplasticity (in red) for simulations under Real source #3 signal in the P1 model.

Moreover, in Figure 2.16 , the model results are analyzed in frequency domain by fast Fourier amplitudes in the frequency band of $[0.1 - 20]$ Hz for simulations with Real source #3 signal. For the elastic case, we see peaks that correspond to resonance frequencies of the soil model (3.75, 11.25 and 18.75 Hz). These peaks are apparent in viscoelastic model with deamplified values. When nonlinearity is considered (elastoplasticity and visco-elastoplasticity), a significant drop in the amplitudes of these peaks is seen with frequency shift towards lower frequencies. The shift under nonlinearity is a result of the weakening of soil rigidity. In other words, for higher strains, the shear modulus of the soil becomes smaller than the initial shear modulus. In consequence, shear wave velocity in the medium is lowered such that natural frequency and harmonics are shifted to lower values. Also, these shifts and nonlinear damping are not homogeneous overall the frequency band. Under the loading of a real input signal which consists of successive loading-unloading trend, soil becomes strongly nonlinear and frequency shifts with energy damping become prominent. This indicates that wave propagation and resultant ground motion are influenced by soil nonlinearity in terms of energy and frequency content.
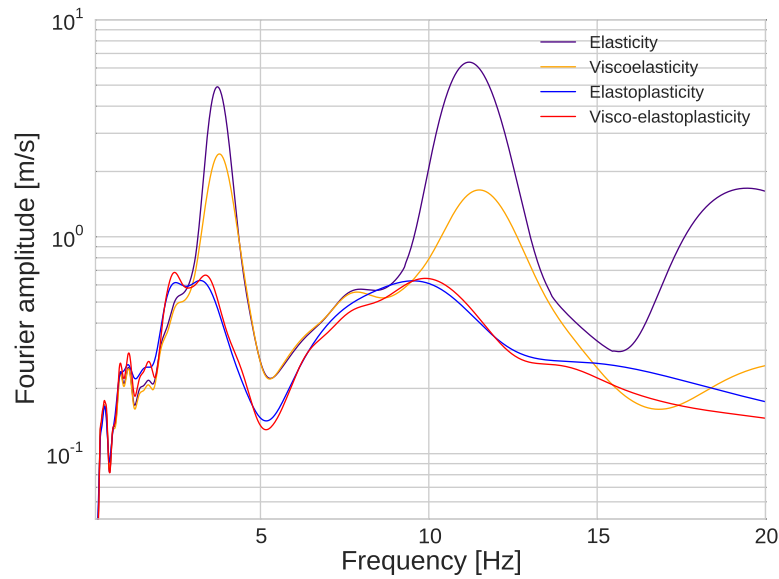
Fig. 2.16 Fourier amplitudes of surface velocities for elasticity (in purple), viscoelasticity (in yellow), elastoplasticity (in blue) and visco-elastoplasticity (in red) for simulations under Real source #3 signal in the P1 model.

We recall that for very small deformations, elasticity is assumed to occur for the most of the engineering materials. This elastic limit is generally considered as 10^{-6}, which may be less or higher depending on soil rigidity (Ishihara, 1996) [75] (See Chapter 1.3.1). Based on this observation, elastic and elastoplastic model results are expected to be equal for small deformations. Similarly, viscoelastic and visco-elastoplastic model results are expected not to differ significantly. With respect to this aspect, surface motion is analyzed for different time intervals in order to verify the nonlinearity implementation in 1D SEM code. For this purpose, surface acceleration time histories on time intervals of $15 - 16$ seconds and $35 - 36$ seconds are compared between elasticity and elastoplasticity. The same comparison is made between the cases of viscoelasticity and visco-elastoplasticity for the same purpose by taking into account the viscoelastic attenuation. The input motion corresponding to these time intervals are shown by shaded zones in Figure 2.14.

Figure 2.17 displays the comparison of elastic and elastoplastic models (top panel) and viscoelastic and visco-elastoplastic models (bottom panel) on [15-16] s time interval for surface acceleration outputs. In both comparisons, compared models result in identical surface acceleration. For elasticity and elastoplasticity models, the peak ground acceleration (PGA) is $9.8.10^{-4}$ and for viscoelasticity and visco-elastoplasticity, it is $8.6.10^{-4}$. For this interval, maximum strain at the middle of soil layer (GL-10 m) in elastic and elastoplastic

models is 7.10^{-8} which is smaller than the elastic limit mentioned above. For viscoelasticity and visco-elastoplasticity, maximum strain is slightly smaller as 6.10^{-8}. The soil response is the same for elastic and nonlinear models. The same comparison for time interval [35-36] s is shown in Figure 2.18. In this interval, PGA is very strong for elasticity with $19.08 m/s^2$ and maximum strain is 10^{-3}, which is much higher than the [15-16] s interval. On the other hand, for elastoplastic model, the PGA is $2.81 m/s^2$ and maximum strain is 7.10^{-4}. We see that although maximum strain levels are close in elastic and elastoplastic models, resultant surface motion differs significantly, which is an effect of increase in soil nonlinearity. Similarly, when viscoelastic and visco-elastoplastic models are compared (bottom of the same figure), there exists a remarkable difference between two models. PGA is equal to $7.27 m/s^2$ for viscoelasticity, while it is $2.77 m/s^2$. The viscoelastic attenuation reduces the PGA of elasticity by a factor of 2.5 approximately. Yet, the surface motion is further damped under higher soil nonlinearity such that PGA is $2.77 m/s^2$. The maximum strain for viscoelastic and visco-elastoplastic models in this time interval is equal to 6.10^{-4}. Again, despite the slight difference of strain, nonlinearity leads to a considerable attenuation of wave motion at surface. Also, a time delay is noted in nonlinear surface acceleration time histories due to the weakening of soil rigidity (decrease of shear modulus).
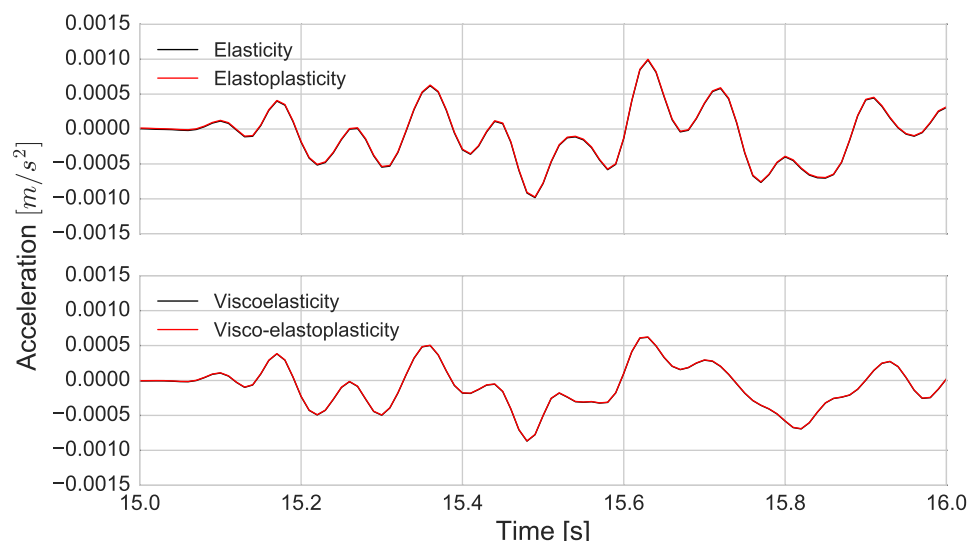
Fig. 2.17 Acceleration time histories for elasticity (in black) and elastoplasticity (in red) (top); Acceleration time histories for viscoelasticity (in black) and visco-elastoplasticity (in red) (bottom) on [15-16] s time interval for simulations under Real source #3 signal in the P1 model.
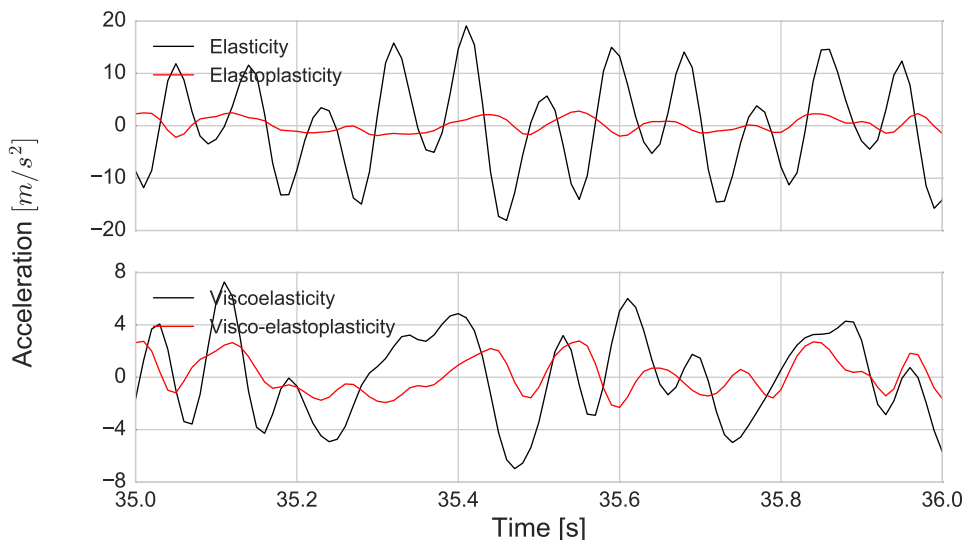
Fig. 2.18 Acceleration time histories for elasticity (in black) and elastoplasticity (in red) (top); Acceleration time histories for viscoelasticity (in black) and visco-elastoplasticity (in red) (bottom) on [35-36] s time interval for simulations under Real source #3 signal in the P1 model.

For the simulations with Real source #3, the stress-strain diagrams obtained for the elastic, viscoelastic, elastoplastic and visco-elastoplastic models at midlayer are shown in Figure 2.19. The linearity between stress and strain is valid only for the elastic and viscoelastic cases. Yet, energy attenuation in viscoelastic medium results in smaller stress and strain values. The viscoelastic and visco-elastoplastic curves initially follow the same slope for the range of small deformations. On the other hand, although the viscoelastic deformation range is very close to that of nonlinear curves, the stress differs considerably between viscoelasticity and nonlinearity. Consistently, the visco-elastoplasic model leads to slightly more attenuation than the elastoplastic model. For the nonlinear cases, a factor of reduction is observed in maximum strain and stress values experienced by the material throughout the simulation. Moreover, a slope change in the diagram is clearly seen due to nonlinearity. As a result, the loading-unloading path is more cyclic due to the hysteresis (continuous decrease of shear modulus) in nonlinearity and the soil undergoes permanent deformation under nonlinearity.
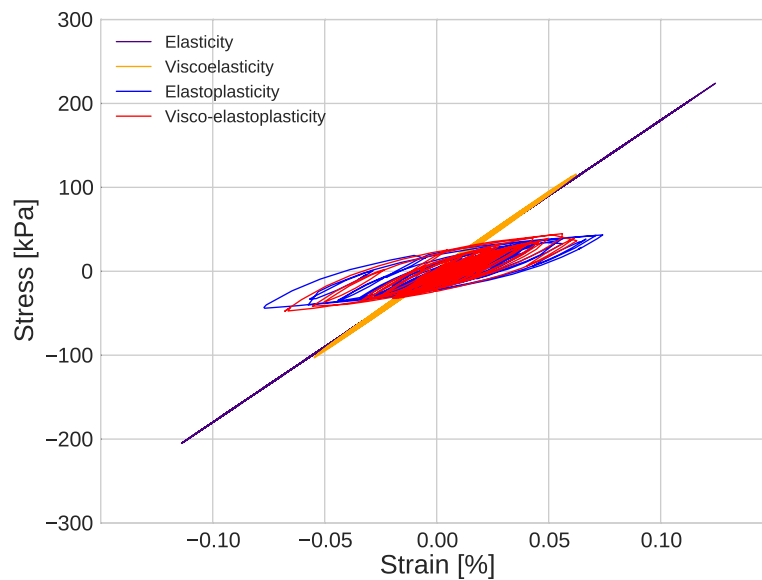
Fig. 2.19 Stress-strain curves for elasticity (in purple), viscoelasticity (in yellow), elastoplasticity (in blue) and visco-elastoplasticity (in red) for simulations under Real source #3 signal in the P1 model.

Lastly, in Figure 2.20, maximum PGA, stress and strain values throughout the soil profile are compared between elasticity and elastoplasticity. The nonlinearity effect leads to a strong damping in PGA all over the model so that surface motion has an approximate PGA of $4m/s^2$ in elastoplastic soil rheology consideration while it has a PGA of $25m/s^2$ in elastic conditions. This energy loss is also present in ultimate strength values reached by the soil. Soil rigidity weakens in nonlinearity by a factor more than 5 for each depth of the P1 model. As a result, strain values are much stronger in elasticity for each point whereas in nonlinear model strain increases with depth and superficial layers have less deformation. The same comparison is made between viscoelastic and visco-elastoplastic soil conditions in Figure 2.21. In viscoelastic P1 model, surface PGA is approximately 2 times smaller than elasticity. With the introduction of soil nonlinearity, this value reduces to $3.2m/s^2$ which is slightly smaller than surface PGA in elastoplasticity. The same effect is seen in maximum strength values of the soil in mid-panel of the figure. Soil becomes less rigid under nonlinearity as seen by maximum stress decrease. Also, maximum strain values demonstrate that for viscoelasticity an overall damping in deformation takes place while under nonlinearity soil layers closer to surface have more attenuation in strain and middle part of the soil is concerned more by nonlinearity and experiences higher level of strain.
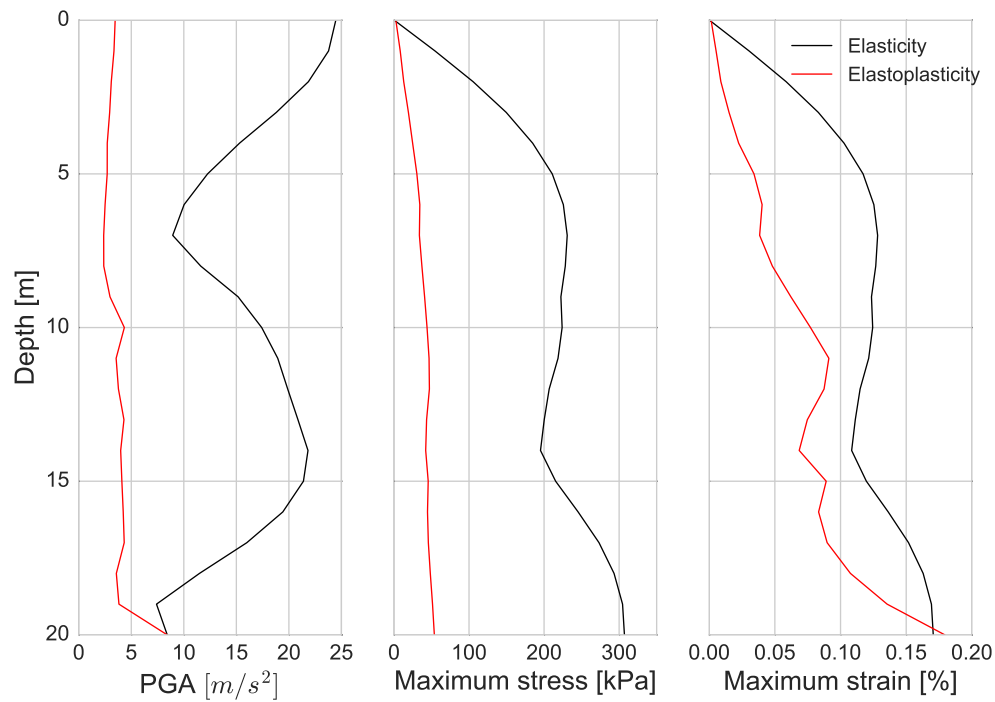
Fig. 2.20 Maximum PGA profile of P1 model under Real source #3 signal for elasticity (in black) and elastoplasticity (in red) (left); Maximum stress profile of P1 model under Real source #3 signal for elasticity (in black) and elastoplasticity (in red) (middle);Maximum strain profile of P1 model under Real source #3 signal for elasticity (in black) and elastoplasticity (in red) (right).
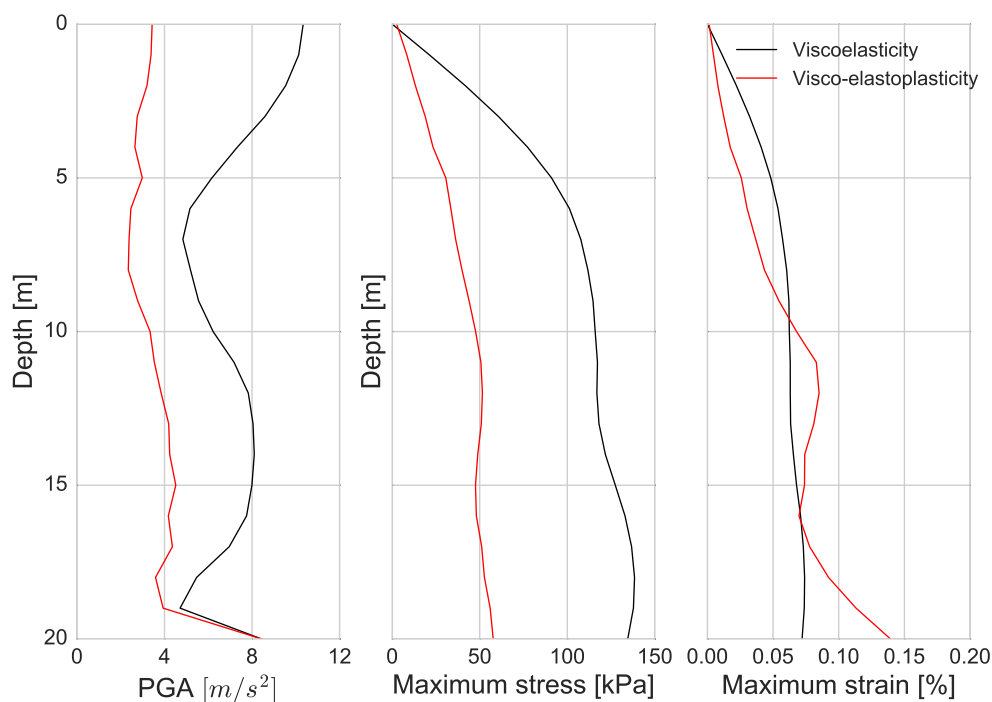
Fig. 2.21 Maximum PGA profile of P1 model under Real source #3 signal for viscoelasticity (in black) and visco-elastoplasticity (in red) (left); Maximum stress profile of P1 model under Real source #3 signal for viscoelasticity (in black) and visco-elastoplasticity (in red) (middle);Maximum strain profile of P1 model under Real source #3 signal for viscoelasticity (in black) and visco-elastoplasticity (in red) (right).

2.5   Sensitivity analysis on different numerical aspects

Thus far, the verification of viscoelasticity and nonlinearity in 1D wave propagation has been shown. For all the performed tests, we need to prepare numerical models of which the properties are precisely defined. In this aspect, it is necessary to highlight the selection of certain numerical parameters for the studied model. For this purpose, in this section, a sensitivity analysis is performed on a precise model and the effect of different aspects on precision and computation time cost is explained. As numerical model, the Volvi model (See Chapter 2.2.3) is chosen given the reasonable time of computation.

In previous applications in Volvi model, an elastic rock boundary at bottom of the model is defined with C-PML elements (See Chapter 1.2.3). In the applications of this section, bottom

boundary is defined with borehole condition in order to keep the numerical model the same as physical model so that no additional element is used for C-PML. First, the influence of spectral element polynomial degree on precision and computation time is explored for Volvi model with elastic rheology. Second, a similar study is realized to see the effect of Iwan spring numbers for elastoplastic models. Lastly, computation time is compared for different assumptions of soil constitutive model in Volvi model.

2.5.1   Effect of polynomial order

Effect on numerical precision and dispersion

In order to see the effect of spectral element polynomial degree on computation precision, a series of tests are performed for models with different number of polynomial degree ($N = 2, 4, 6, 8$). In the study of Seriani and Priolo (1991 [144]; 1993 [127]), necessary number of points per wavelength (ppw) is calculated in function of polynomial degree (Figure 2.22). Referring to mean element size curve (dx mean) of this graph, we see that for a correct wave propagation the use of $ppw = 5 - 6$ is needed for $N = 5$ polynomial order. For comparison purposes, a reference solution is created for a resolution of $50Hz$ by considering 6 points per wavelength with $N = 5$. For all the models in this section, soil rheology is defined as elastic. Among these models, for $N = 2$ and $N = 4$, the use of different number of ppw (number of points per wavelength) is tested. In the simulations below, the same signal that is shown in Figure 2.4 for Volvi model is used after having been filtered by low pass filter below $20Hz$. All the models are created for a resolution of $20Hz$ except for the reference model. Total simulation duration is defined as 30 seconds. Table 2.5 shows the polynomial degree N of each model with number of grid points per wavelength ppw, resultant minimum ratio of minimum grid distance to element size (dx_{min} factor), time step determined for the model (Δt) and total computational time (t_{total}). It should be noted that all the computations are performed on a machine of Dell Precision T5610 with four dual cores of Intel Xeon E5-2609V2 2.5GHz processor features.
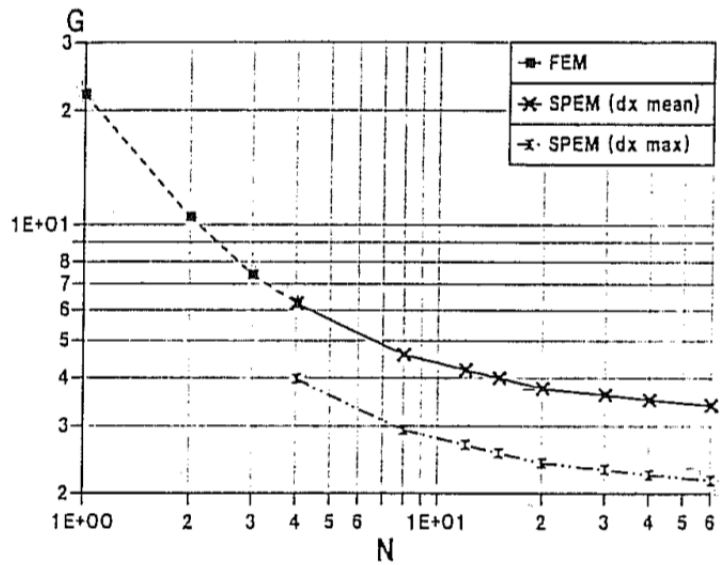
Fig. 2.22 Values for the minimum number of points per wavelength (G) versus the polynomial order (N) for FEM and SEM, at a distance of 960 grid points. Estimations of G were done, taking into account the mean value of element size (dx mean) (solid line) and the maximum element size (dx max) (dashed line) (after Seriani and Priolo 1991[144]; 1993 [127]).

Model	Element number	N	dx_{min} factor	Δt [s]	t_{total} [min]
Reference	38	5	0.235	1.10^{-4}	1.097
1 (ppw=5)	33	2	0.500	1.10^{-3}	0.120
2 (ppw=40)	245	2	0.500	2.10^{-4}	2.430
3 (ppw=5)	17	4	0.175	2.10^{-4}	0.215
4 (ppw=6)	19	4	0.175	2.10^{-4}	0.244
5 (ppw=5)	12	6	0.085	2.10^{-4}	0.392
6 (ppw=5)	11	8	0.101	5.10^{-5}	0.681

Table 2.5 Element number, time step and computation time in polynomial order effect test models.

Figure 2.23 demonstrates the error percentage on transfer function for each model with reference model solution $TF(reference)$ at top panel. At top of each figure, mean arithmetic error value over the whole frequency band is shown. The error percentage is calculated based on following formula:

$$Error = \left| \frac{TF(model) - TF(reference)}{TF(reference)} \right| * 100 \qquad (2.2)$$

where $TF(model)$ is the transfer function of the studied model and $TF(reference)$ is the transfer function of reference solution.

Firstly, the models 1 and 2 that have 2nd order polynomial degree ($N = 2$) are compared with the reference solution in terms of precision. Use of a 2nd order polynomial degree attributes 3 GLL points on each spectral element. The points are equidistant so that the minimum grid size on element is half of the element size (dx_{min} factor = 0.5). In this sense, it is similar to elements of finite element numerical method that assigns 3 points on a finite element (See Chapter 1.2.1 for more details on grid point distribution). Referring to the curve of Figure 2.23 (left of top panel), use of $ppw = 5$ is not sufficient to obtain accurate solution. For low frequency motion, maximum error is close to 30 % and for high frequency motion ($> 10Hz$) over 10 %. In order to see the difference of ppw, we define different number of ppw on $N = 2$. Model 1 element sizes are calculated based on the assumption of 5 points per wavelength, whereas Model 2 has 40 points per wavelength. With the use of $ppw = 40$ in $N = 2$, error in Model 1 is reduced significantly in all frequency band. In the study of De Martin (2010), finite element and spectral element methods are compared for different number of points per wavelength. It is shown that the use of $ppw = 40$ in finite element method does not provide sufficiently accurate solution and the solution becomes better by increasing ppw up to 120. This comparison reveals that for $N = 2$ in spectral element method, in order to acquire precision in results, the use of $ppw = 5$ is not sufficient while increasing this number to 40 improves the solution by requiring significantly more elements. Despite of the increase in computational time cost, spectral element solution results in higher precision compared to finite element method.
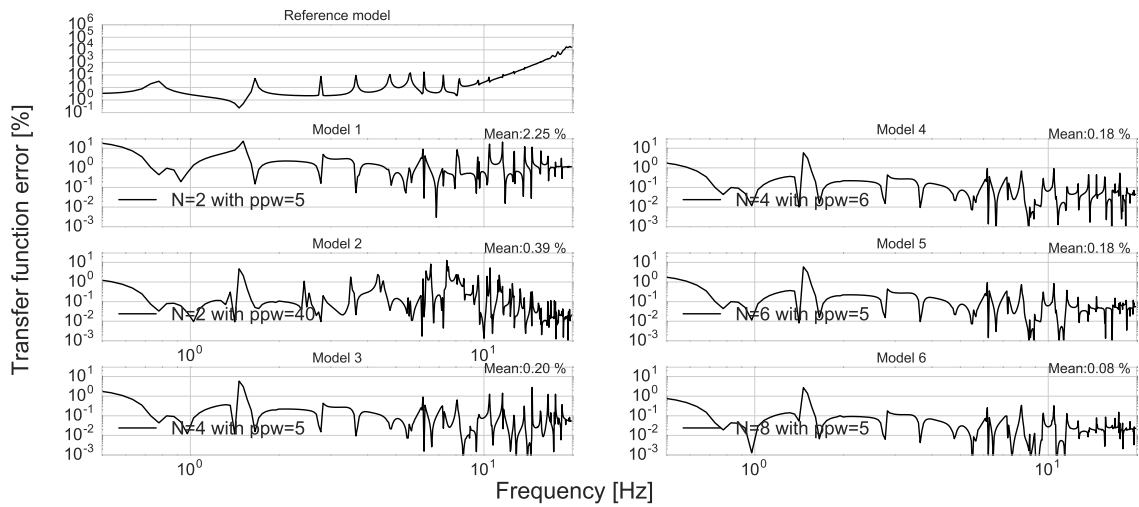
Fig. 2.23 Relative error in frequency domain for the solutions of all the models.

Referring to the dx mean curve of Figure 2.22, $ppw = 5$ corresponds to polynomial orders $N \geq 5$ and for $N = 4$, we would like to verify whether the use of $ppw = 5$ gives satisfactorily precise results. For this purpose, Model 3 is created for $ppw = 5$ and Model 4 for $ppw = 6$. In Figure 2.23 (left of bottom panel and right of top panel), the error percentages for Model 3 and Model 4 are shown. Two models give very close results with very slight differences in high frequency range where dispersion effects are expected. Overall errors in both models are less than 1 %. Mean error values are very close between two models (0.20 % is reduced to 0.18 % in Model 4). This ensures the accuracy of using $ppw = 5$ for $N = 4$. Comparing the errors of Model 2, Model 3 and Model 4, using higher order polynomial degree mostly decreases the error in the solution for frequencies over 2 Hz. Following the satisfactory results obtained with 4th order of polynomial degree, we make additional comparisons for models with higher order polynomial degree.

When Model 3 and Model 5 are compared, it is seen that increasing the polynomial degree from 4 to 6 does not change the precision significantly for low and moderate frequencies. For very high frequencies ($> 10Hz$), solution with higher polynomial degree reduces the error. At last panel of the same figure, error percentage is shown for Model 6. Additional decrease in error is seen in high frequency band.

Figure 2.24 shows the peak ground velocity errors for Model 2 ($N = 2$), Model 3 ($N = 4$), Model 5 ($N = 6$) and Model 6 ($N = 8$). Higher polynomial order gives better fit to the reference solution at free surface. On the other hand, for all the models this error on PGV remains small (less than 1%).
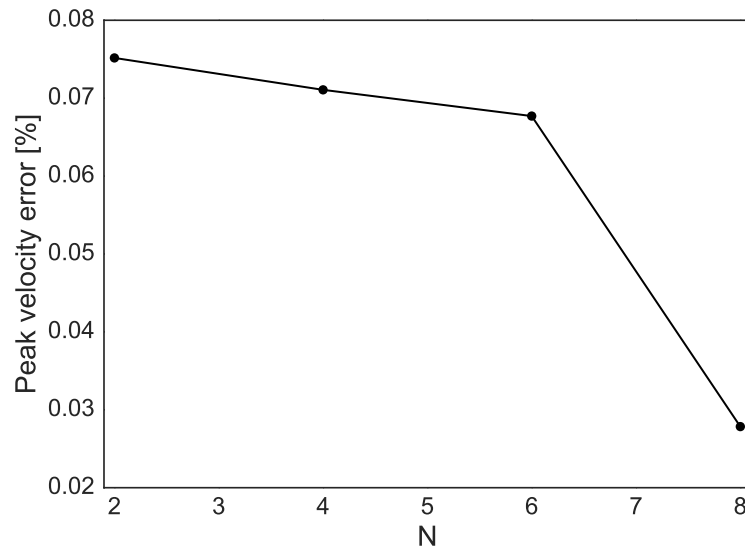
Fig. 2.24 Peak velocity error percentage for the solutions of Model 2 ($N = 2$), Model 3 ($N = 4$), Model 5 ($N = 6$) and Model 6 ($N = 8$).

Effect on computational cost

In this section, we show the influence of increase of polynomial degree on computation time. For all the models, total time of computation is shown in Table 2.5. First, Model 1 (N=2 with ppw=5) and Model 2 (N=2 with ppw=40) are compared. In order to obtain the precision of Model 1, element number that is 33 for Model 1 is increased to 245. In consequence, due to smaller element size in Model 2 the time step is 5 times smaller and computation time cost is approximately 20 times higher.

By using 4th polynomial order, the solution is found to be more precise in Model 3 compared to Model 2. In addition, computation is approximately 10 times faster with Model 3 than Model 2. When Model 3 and Model 4 are compared with respect to computational cost, total time of computation is very close for both models (0.215 and 0.244 minutes), similarly to

precision.

Increasing the polynomial degree from 4 to 6, we compare Model 3 and Model 5. Even though the allowed maximum element size increases for the models of higher order polynomial degree, given the thickness of the 7th layer of Volvi model, element sizes for layers in Model 5 do not differ much from Model 3. For this reason, time step is the same in Model 3 and Model 5. Since the GLL point number increases with polynomial degree, minimum grid size on element decreases from factor 0.175 to 0.085 and the computation time is longer than Model 5. In other words, selection of higher order polynomial degree may not be always computationally efficient depending on model properties.

When Model 5 (N=6) and Model 6 (N=8) are compared, we can draw the same conclusions also for this model. Element number in Model 6 decreases only by one element compared to Model 5 and due to smaller minimum grid size, time step decreases by a factor of 4 and total computation time is approximately 2 times longer.

Regarding the comparisons above, we can conclude that using higher polynomial degree increases the precision. On the other hand, depending on the model properties, the selection of higher order polynomials may not always correspond to the optimal case in sense of computational time. For Volvi model, the use of $N = 4$ with $ppw = 5$ results in sufficient precision and advantageous time cost.

Thus far, we have considered only elasticity as soil constitutive model. In our study, for nonlinear media, we refer to the same equations for selection of element size. However, in the equations, medium velocity taken into account is decreased by a given factor due to softening with nonlinearity. For instance, a factor 4 of softening is assumed in the beginning while determining the element sizes in the media. At the end of simulations, it is checked whether the initial assumption of factor 4 is exceeded or not. In case of higher softening than factor 4, a new mesh with a higher factor of softening assumption is created and computations are repeated with the new mesh. If the softening is less than factor 4, solution is considered as acceptable in terms of mesh choice. In the following section, the influence of using different number of Iwan springs on precision and computational time is shown for nonlinear media.

2.5.2   Effect of Iwan spring number for elastoplastic models

The nonlinear model that we use is MPII model which is based on Iwan (1967) [76] formulations. In the model, the plasticity levels are described by so-called Iwan springs (See Chapter 1.3.3). In order to see the effect of Iwan spring number on precision and computational time cost, we prepared six models with different number of Iwan springs. As numerical model, we still use the Volvi model with borehole boundary condition similarly to previous section. Regarding the conclusions drawn in the preceding section, in all the models, a polynomial degree of $N = 4$ with $ppw = 5$ is used. The soil constitutive model is defined as elastoplastic where the nonlinearity is pressure-dependent all over the model. Element sizes are calculated for a consideration of maximum 4 times weakening in shear wave velocity. For comparisons, the reference model is considered to have 250 springs, while other models have $10, 30, 50, 100$ and 200 Iwan springs (See Table 2.6).

Figure 2.25 shows the PGA, maximum strain and maximum stress distribution throughout the soil profile for reference solution. Maximum PGA is calculated as $3.75 m/s^2$ and it is reduced towards the ground surface under nonlinearity. In very superficial layers ($< 20m$ depth), it is increased by an approximate factor of 1.5. Towards the surface, maximum stress is lowered and maximum strain increases, which could be interpreted as higher nonlinearity effect.
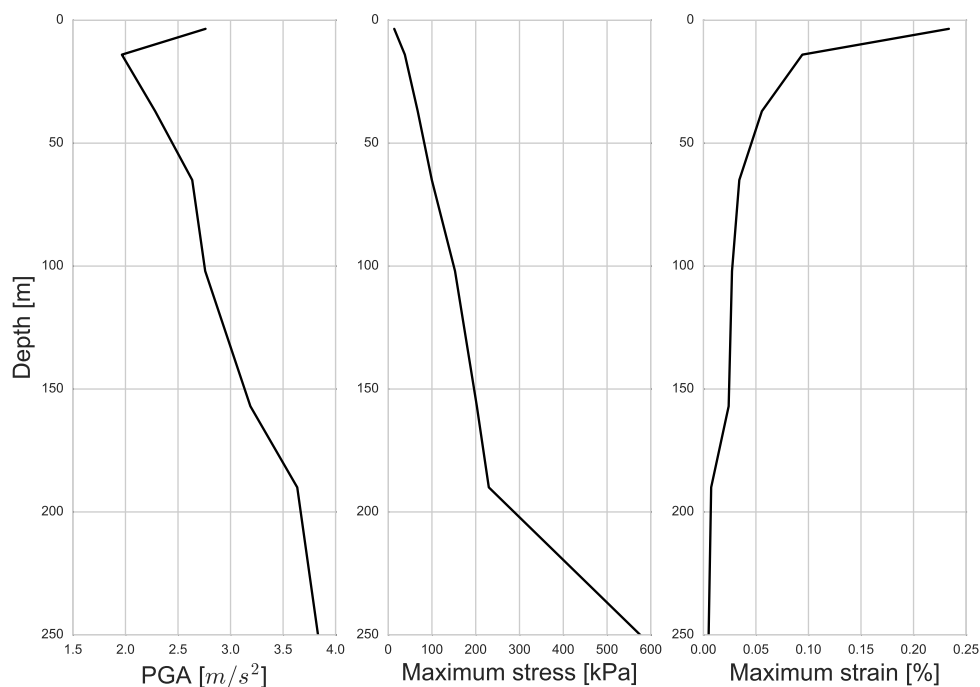
Fig. 2.25 Peak ground acceleration (left), maximum stress (middle) and maximum strain (right) distribution on soil model of Volvi model.

In Figure 2.26, the maximum surface velocity, strain and stress error percentages for the models are shown. For maximum strain and stress parameters, values at 37 meters (middle of layer 3) are used since the nonlinearity is relatively more apparent. By using 10 springs, solution is significantly different than the reference so that maximum error percentages of all parameters are over 2 %. Increasing the spring number from 10 to 30, the solution error decreases remarkably. While the peak velocity error is approximately 6% with 10 springs, this error reduces by a factor of 5 with 30 springs. Similarly in stress and strain limits, the error exhibits a strong decay that the error which is over 2% for 10 springs decreases to values below 1% with 30 spring use. Use of 50 springs results in relatively small errors ($< 1\%$), while for models with 100 and 200 springs, solutions are even closer to reference solutions. Figure 2.27 displays the comparison of stress-strain curves of each model to the solution of reference model at 37 meters. Model 1 differs from the reference stress-strain curve significantly and overestimates nonlinear attenuation as seen from extremity strain values and lower slope. These differences become smaller with the use of 30 springs. The differences are small and the solution becomes very close to reference solution for Model 3,

Model 4 and Model 5.

Table 2.6 displays the computational time for each model. Although the precision is satisfactory for the models with 50 springs and more (Models 3,4 and 5), cost of computation time differs considerably much. While total time of computation is around 50 minutes for Model 3, increasing the spring number to 250 leads to 2.5 times longer simulations. Also, it must be noted that these results concern directly the simulations on elastoplastic model of Volvi site under a simple source excitation. In case of loading with a motion that can lead soil to higher nonlinearity by means of intensive loading-unloading cycles, the factor of increase could be greater. Under the light of results above, the use of 50 Iwan springs could be considered as optimum choice in terms of precision and computational time cost. Thus, in Joyner (1975) [78], cyclic behavior of a single soil element is presented for a nonlinear model with 50 springs and friction units. In next section, different hypotheses of soil constitutive models are compared in terms of computational time cost. For nonlinear models, use of 50 springs is considered.

Table 2.6 Spring number and computation time in Iwan spring number effect test models.

Model	Spring number	t_{total} [min]
Reference	250	160.15
1	10	27.56
2	30	38.75
3	50	49.57
4	100	78.57
5	200	133.91
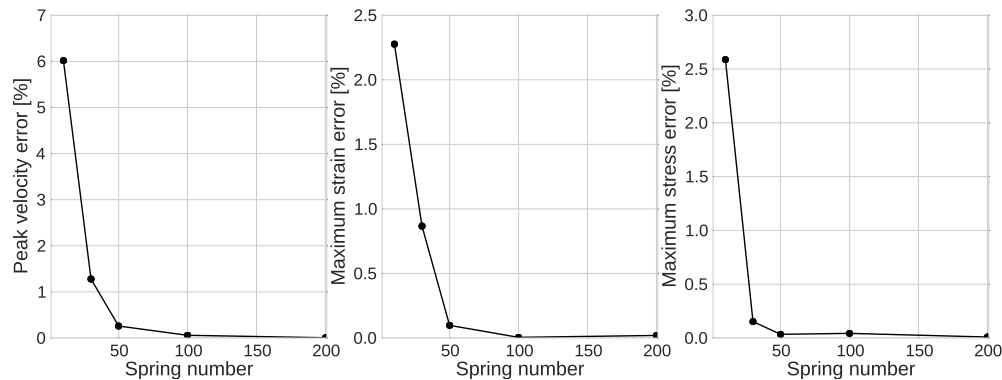
Fig. 2.26 Peak velocity error percentage (left); Maximum strain error percentage (middle); Maximum stress error (right) for the solutions of all the models.
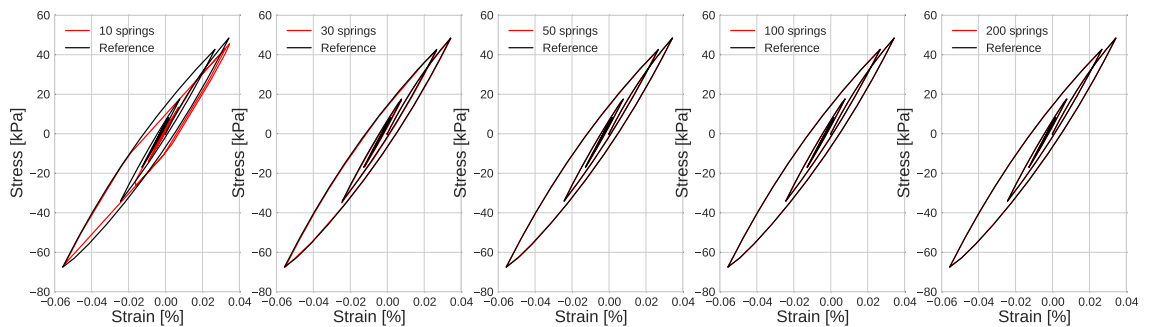
Fig. 2.27 Stress-strain curves for all the models with reference model solution (in black).

2.5.3 Effect of soil rheology

As a last sensitivity analysis, we compare the computational time costs of different constitutive model considerations in Volvi model. In all the models, simulation is performed for 30 seconds and a polynomial degree of $N = 4$ with $ppw = 5$ is used. Table 2.7 demonstrates the total computational time for each rheological model. For all the nonlinear models, 50 springs are defined on the whole model. It should be noted that the resolution of nonlinear models are prepared for 4 times of shear wave velocity weakening in the media.

For this reason, the comparisons in this section do not substitute for the fastest model but for relatively conservative conditions used in practice. In addition, for effective stress analysis, layers 3, 5 and 6 are conditioned to excess pore pressure generation. Such an assumption is not based on a physical aspect, yet used only for numerical comparison purposes in this section. As dilatancy parameters, $sin\phi_p = 0.4067$, $p_1 = 0.5$, $p_2 = 0.4$, $S_1 = 0.01$, $w_1 = 2.0$ are used for all the layers, whereas $sin\phi_f = 0.5$ for layer 3 and $sin\phi_f = 0.5299$ for layers 5 and 6.

The elastic model simulation takes 7.24 minutes. With viscoelasticity, total time cost increases by a factor of 2 approximately and with elastoplasticity, by a factor of 7. Visco-elastoplastic model computation is slightly longer than elastoplastic model and the introduction of pore pressure excess in three layers results in 1.5 times longer computation compared to total stress analysis with visco-elastoplastic rheology.

Table 2.7 Computational time costs for each rheological model.

Model	t_{total} [min]
Elasticity	7.24
Viscoelasticity	15.78
Elastoplasticity	48.71
Visco-elastoplasticity (T.S.A.)	50.85
Visco-elastoplasticity (E.S.A.)	78.24

2.6 Conclusions

A one-dimensional, one-component (1D-1C) geomechanical model has been implemented in the framework of the spectral element method. Soil rheologies may vary from linear, viscoelastic to nonlinear models for seismic wave propagation studies. The 1D-1C SEM has been benchmarked with known numerical solutions and the obtained results give satisfactory fit. Very good matches are obtained with 1D-1C SEM code on realistic viscoelastic models that differ in terms of soil properties. In addition, the importance of selection of reference frequency in viscoelastic media has been pointed (cf. Peyrusse et al., 2014 [124]). For

nonlinearity, a benchmark on a canonical model is performed and soil strength weakening due to soil hysteresis under nonlinearity is shown. In addition, among different soil constitutive models, significant energy damping is observed in viscoelastic and nonlinear models. In nonlinearity, strength weakening and deformation increase are noted additionally to viscoelasticity. Due to rigidity loss in soil nonlinearity, phase delays are observed in surface motion time histories and resonance frequency shifts towards lower frequencies are noted in frequency plan. It has been shown that soil becomes highly nonlinear under a real input motion which exerts successive loading-unloading cycles on the soil. With high nonlinearity, soil strength weakens and higher level of deformations are noted in the middle for soil column compared to superficial layers. Gélis and Bonilla (2012) have shown the effect of input frequency content on location of higher strain at depth. Lastly, a sensitivity analysis is performed on the 1D SEM code for a realistic layered 1D model in order to see the influence of number of SEM polynomial order, number of Iwan springs in nonlinearity and soil constitutive behavior on precision and/or computational cost. The use of higher order polynomial degree increases the precision of solution, but in order to avoid unnecessary computational cost, an optimal selection should be made depending on the model properties. In nonlinearity, use of 50 springs is shown to be advantageous in terms of computational time cost without compromising precision. Also, it is shown that computation time increases for models using effective stress analysis, nonlinearity and viscoelasticity compared to elastic model.

Chapter 3

1D-3C SEM wave propagation modeling: Code validation

1D-3C SEM wave propagation modeling: Code validation

3.1 Introduction

In this chapter, the 1D-1C SEM code is extended to one-dimensional (1D) three-component (3C) form. First, the effect of different loading conditions is studied by comparing uniaxial, biaxial and triaxial loading applied on a simple soil model. Then, the 1D-3C SEM code is applied on three real site models Wildlife Refuge Liquefaction Array (WRLA), Kushiro Port (KP) and Onahama Port (OP), which are affected by 1987 Superstition Hills, the 1993 Kushiro-Oki and The 2011 off the Pacific coast of Tohoku earthquakes, respectively. The three sites present differences in terms of initial consolidation condition (isotropic or anisotropic consolidation), soil to borehole depth (deep or surficial model) and the tendency of dilatant/contractive behavior (dense/loose soil behavior detailed in Chapter 1.3.4). We investigate the influence of pore pressure development in soil behavior and wave propagation in these three models. The ground motion is recorded on three directions by surface and borehole accelerometers during the earthquake. The simulations with the 1D-3C SEM code are performed by using the recorded borehole data as input. For each site, soil behavior is studied by effective stress analyses. Use of different constitutive models and different loading conditions (uniaxial and triaxial loading) is analyzed and the results are discussed in detail. Lastly, conclusions regarding the importance of taking into account

pore pressure excess and of determining the soil properties of a site under study are developed.

3.2   One-component vs three-component in nonlinearity

In the 1D-3C SEM code, the propagation of a vertical incident plane wave can be computed using two shear components (x,y) and one compression component through the vertical axis (z), so that all the three components (x, y, z) can be considered in the calculations. In other words, it is possible to take into account the interaction between shear and pressure components during the wave propagation. Within multiaxial stress state, the loading is likely to lead to more energy dissipation and to result in a consequent plastification effect in the soil (Santisi d'Avila et al., 2013 [38]; Santisi d'Avila and Semblat, 2014 [138]). In this section, we compare the nonlinear soil behavior under uniaxial, biaxial and triaxial loading without pore pressure excess modeling. For this purpose, the previously used P1 model is used with the same input signal (See Chapter 2.3.2). As a first analysis, the soil column is loaded only on x direction, so that the propagation is done for one shear component. For biaxial loading test, the same input signal is defined for all the horizontal components (x, y), so that double shearing is applied to the soil column. Indeed, such input configuration corresponds to the input signal implemented on the diagonal of (x,y). For triaxial loading test, the same input signal is defined for all the components (x, y, z), even though such a composition is not realistic. It mimics an input signal put on the diagonal axis of a cube. Figure 3.1 (left) shows that in uniaxial loading, stress-strain curve at the middle of the soil follows the backbone curve; while at middle of the figure, the same soil deviates from the backbone curve under biaxial loading. Such behavior indicates higher plastification that leads to loss of strength and change in deformation values in the soil with higher damping. Moreover, at right of the figure, stress-strain curve for triaxial loading results is displayed. Additional plastification under triaxial loading could be neglected compared to biaxial loading, so that stress-strain curves under biaxial and triaxial loadings are very similar. In consequence, at the surface, resultant motion is stronger for uniaxial loading than biaxial and triaxial loadings (top of Figure 3.2). Starting from initial seconds of simulation, the increase in attenuation is noticeable with multiaxial loading. Also, a slight time shift of multi-component simulation with respect to one-component simulation is observed. This is a consequence of higher nonlinearity corresponding to a lower shear modulus under multiaxial loading. The transfer functions depict the impact of this higher nonlinearity by attenuation of maximum values (bottom of Figure 3.2). Indeed, with the nonlinearity under uniaxial loading, the strong peak is slightly shifted from the fundamental frequency of the soil model ($3.75 Hz$) towards $3.5 Hz$.

Under triaxial loading, this peak is attenuated and shifted even more (approximately $3.4Hz$).

We can conclude that soil becomes more plastic due to multiaxial loading even in cases where propagation is modeled for simple input motion, showing the interdependence of motion components even for the 1D case. Additional energy attenuation with higher nonlinearity due to multiaxial loading should be taken into account for realistic seismic wave propagation modeling. However, this numerical test used the same amplitude on the three components of the input motion, which is not the case for real ground motions.
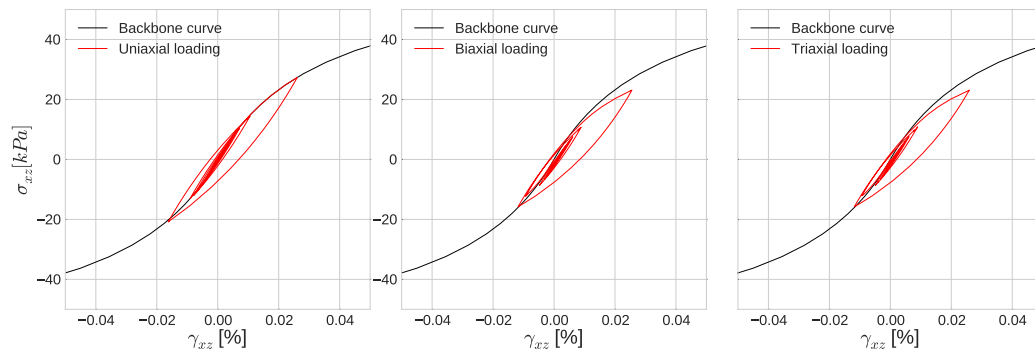
Fig. 3.1 Comparison of stress-strain curve for the P1 model under uniaxial loading (left), biaxial loading (middle) and triaxial loading (right). The backbone curve is shown in black.
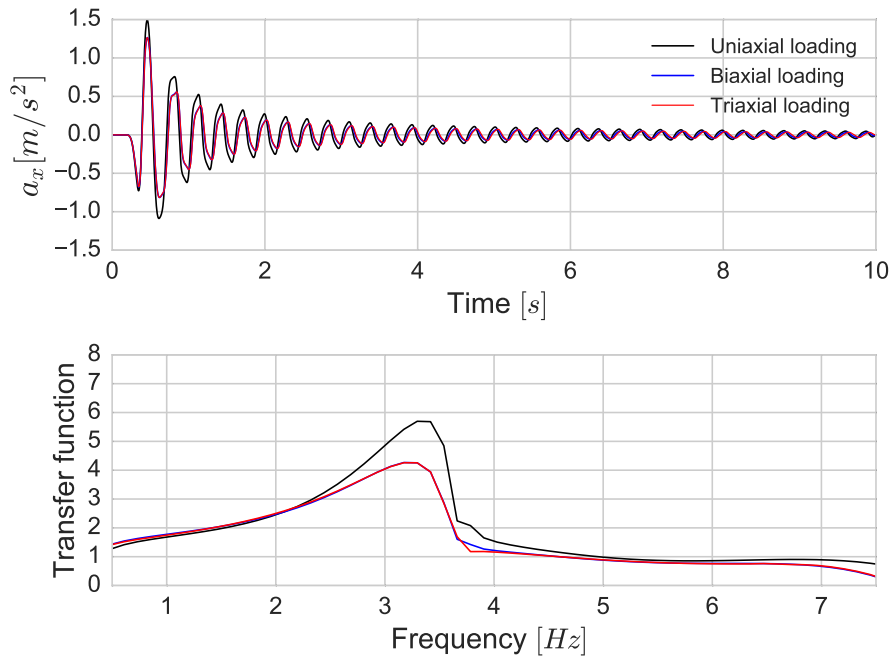
Fig. 3.2 Surface acceleration time histories (top); Fourier amplitudes of surface acceleration for uniaxial loading (in black), biaxial loading (blue) and triaxial loading (in red) for P1 model (bottom).

3.3 Validation of the 1D-3C SEM code

In previous section, the importance of consideration of three components is highlighted by comparison of 1C and 3C approaches with the 1D nonlinear SEM code on a canonical model under simple conditions. In this section, we would like to further investigate the influence of soil nonlinearity on wave propagation by using real site models, where nonlinear soil behavior and pore pressure effects are observed. Recorded data on the studied sites are used as input motion. In the following, first, the soil nonlinearity is studied on Wildlife Refuge Liquefaction Array (USA) site by performing wave propagation analyses under different hypotheses of soil constitutive models. Then, another comparative study between uniaxial and triaxial loading conditions is realized. Afterwards, similar analyses are performed on two Japanese sites, Kushiro Port and Onahama Port sites. For each studied site, obtained results are discussed in detail and conclusions are drawn at the end.

3.3.1   The 1987 Superstition Hills Earthquake

In order to validate the 1D-3C approach, we compute ground motion recorded at a real liquefaction site Wildlife Refuge Liquefaction Array (WRLA), which is located on floodplain of Alamo River in the Imperial Valley of California. The array is investigated under the study conducted by the United States Geological Survey (USGS) in 1987 by uphole and downhole accelerometers and pore pressure transducers at different depths. WRLA recorded several earthquakes on the 23-24 November 1987. Pore pressure changes are recorded together with the seismic motion generated by the ML 6.6 main shock of Superstition Hills on the 24 November 1987 (Holzer et al., 1989 [68]). In our study, we follow the soil model of Bonilla et al. (2005) [16]. The velocity profile is composed of 4 soil layers as seen in Table 3.1. In the table, V_s and V_p correspond to shear and pressure wave velocities respectively; ρ for density, ϕ_f for failure line angle and K_0 for coefficient of Eart at rest that allows to compute initial stress conditions. The water table is set at 2 meters depth. The site is assumed to be initially isotropically consolidated and dilatancy parameters (ϕ_p, w_1, p_1, p_2 and S_1) are used for the third layer as proposed by Bonilla et al. (2005) [16] as shown in Table 3.2.

Table 3.1 Soil properties at Wildlife Refuge Liquefaction Array after Bonilla et al. (2005) [16].

Layer	Description	Thickness $[m]$	$V_s[m/s]$	$V_p[m/s]$	$\rho[kg/m^3]$	$\phi_f[degree]$	K_0
1	Silt	1.5	99	249	1600	28	1.0
2	Silt	1.0	99	281	1928	28	1.0
3	Silty sand	4.3	116	1019	2000	32	1.0
4	Silty sand	0.7	116	1591	2000	32	1.0

Table 3.2 Dilatancy parameters for the loose silty sand layer at the Wildlife Refuge Liquefaction Array after Bonilla et al. (2005) [16].

$\phi_p[degree]$	w_1	p_1	p_2	S_1
24.0	4.0	0.4	0.9	0.01

In next section, we present the model for the seismic wave propagation in the WRLA by considering the changes of pore pressure in the third layer and using the 1987 Superstition Hills earthquake records. Then, the obtained results are discussed in detail.

Numerical model

Recorded waves in the borehole at GL-7.5 m depth are used as input of our simulations whereas recorded waves at free surface are compared to the results of the simulations. Figure 3.3 shows the acceleration time histories of the Superstition Hills earthquake at the borehole sensor located at 7.5 m depth. The strongest motion is on the north-south direction with an amplitude of 1.60 m/s^2, while the weakest motion is 0.54 m/s^2 on the vertical direction. Hereafter, north-south component is symbolized by (NS), east-west component by (EW) and vertical component by (UD).
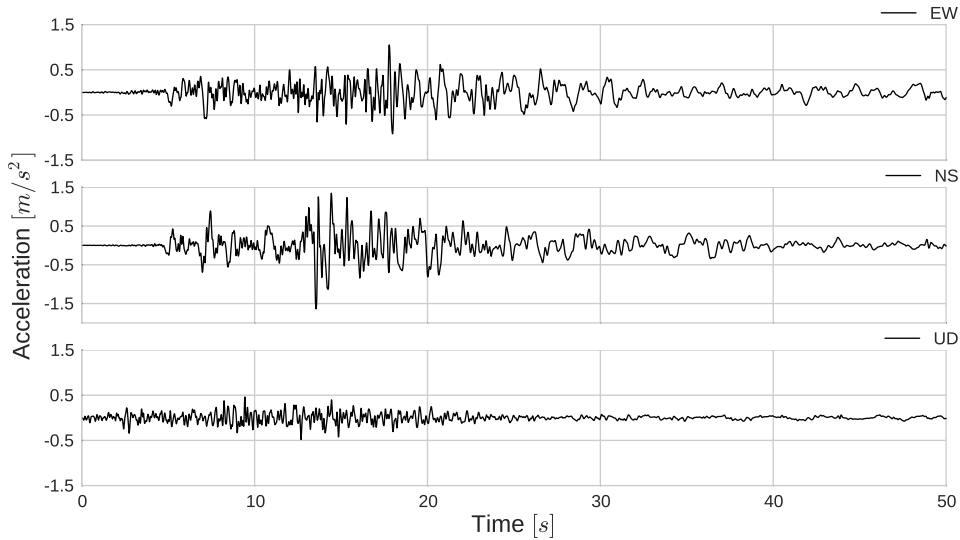
Fig. 3.3 Acceleration time histories at GL-7.5 m depth in east-west (EW), north-south (NS) and vertical (UD) directions recorded at WRLA.

The computation is done for a resolution of 10Hz where the minimum element size changes in range of $[0.5 - 0.7]m$, each spectral element has 5 GLL points (4th polynomial order). Time step $\Delta t = 1.0 \times 10^{-5}s$ and total simulation time is 50s. Minimum grid distance on elements changes in $[0.0875 - 0.1225]m$. The mesh is created for a maximum 4 factor of softening of each soil layer. For all the defined integration points in the model, the reference strain γ_{ref} is computed by Equation (1.30). The quality factors for shear and pressure waves are assumed as $V_s/10$ and $V_p/10$, respectively and reference frequency is set to 1Hz.

Results

Figure 3.4 shows the resulting accelerations at the surface of this simulation on the three directions. After the first 13 seconds, acceleration is damped in all the shear components and large span dilation pulses are observed. Except for the slight phase differences on NS component and amplitude variability in all the components, simulation is able to reproduce quite well the observed ground motion at surface.
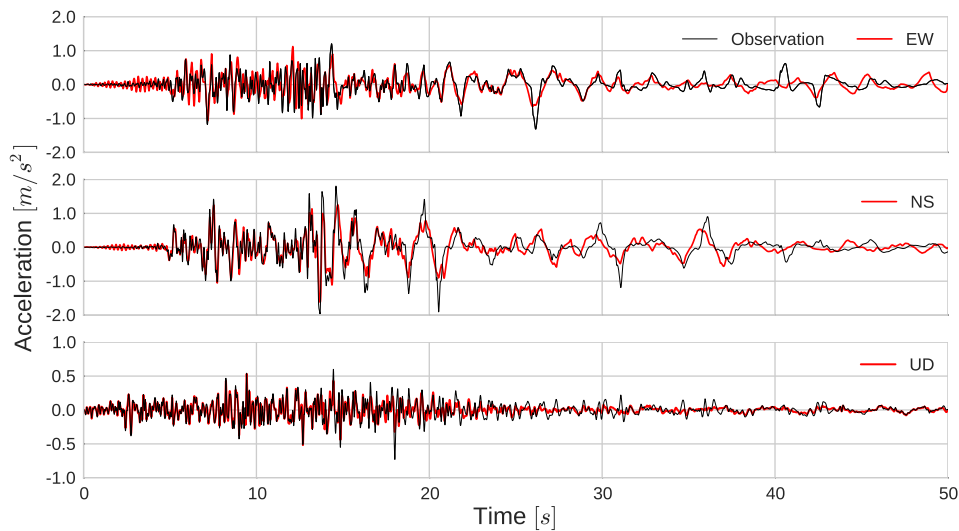
Fig. 3.4 Surface acceleration time histories calculated using the visco-elastoplastic model with pore pressure effects (in red) and real records (in black) for the WRLA site.

The long period pulses in acceleration time histories of shear components can be explained by the dilatancy change in liquefiable silty sand layer. In order to see the changes in liquefiable soil layer, two points at different depths are chosen, one close to upper layer and where pore pressure temporal record is available (GL-2.9 m) and another point at the middle of the layer (GL-4 m). In Figure 3.5, the deviatoric plans for GL-2.9 m (left) and for GL-4 m (right) are given. In these figures, deviatoric stress normalized by initial effective stress (r) is related to current effective stress normalized by initial effective stress (S). A continuous decrease in effective stress is observed. Conversely, at right of the same figure, at GL-4.0 m depth corresponding to the middle of the third layer, the soil experiences initial decrease in effective stress. When the effective stress is halved, soil exhibits instantaneously dilatant behavior by reaching the phase transformation line. The stress-strain curves are considered for the same points in Figures 3.6-3.7. For each point, the decrease in effective

stress can be remarked by sharp slope changes in shear stress-strain curve. Differently than GL-2.9 m, dilatancy at GL-4.0 m results in stress-strain loops for shear components having classical banana shape, which is typical of weakening and partial regain of soil strength due to successive changes in soil dilatancy. Maximum strain reached by the soil at this depth is close to 5 %. Strain values at depth GL-2.9 m are small due to high attenuation of waves propagating upwards at this depth. Conversely, in vertical component at either depth, the rigidity is close to initial state. This comes from the bulk modulus being held independent of soil dilatancy changes in our model. Such an assumption should be ameliorated in future studies, yet it makes it possible to model the vertical wave propagation in this case.

Figure 3.8 displays the recorded pore pressure excess at GL-2.9 m (left) and calculated pore pressure excess as a function of time at GL-2.9 m and GL-4.0 m (right), respectively. At both depths, a sudden increase in pore pressure is seen after 13 seconds. Since the effective stress decreases more at GL-4.0 m, the pore pressure excess reaches higher values than GL-2.9 m. Continuous changes in contractive-dilatant behavior of the soil at GL-4.0 m is seen in this figure by successive oscillations in pore pressure values. As soil becomes contractive, pore pressure decreases and increases for dilatant behavior. These sudden changes in dilatancy, where stress path changes direction and effective stress increases with dilatant behavior, could be related to partial strength gain and consequent spiky values in surface acceleration which take place after 13 seconds.
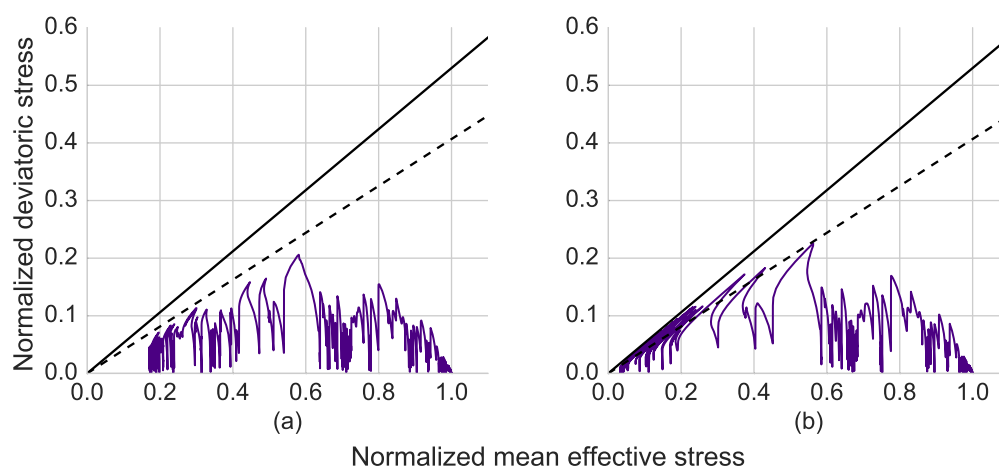
Fig. 3.5 (a) Deviatoric plan for point at GL-2.9 m, (b) Deviatoric plan for point at GL-4.0 m of the WRLA model with failure line (solid line) and phase transformation line (dashed line).
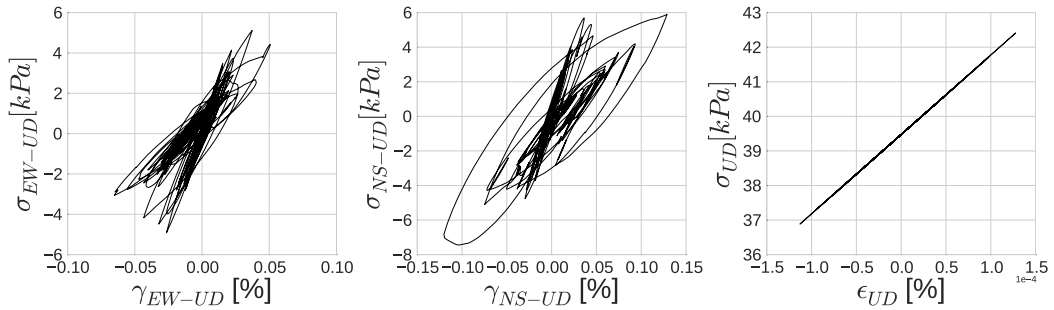
Fig. 3.6 Stress-strain curves on EW-UD component (left), NS-UD component (middle) and UD component (right) for point at GL-2.9 m of the WRLA.
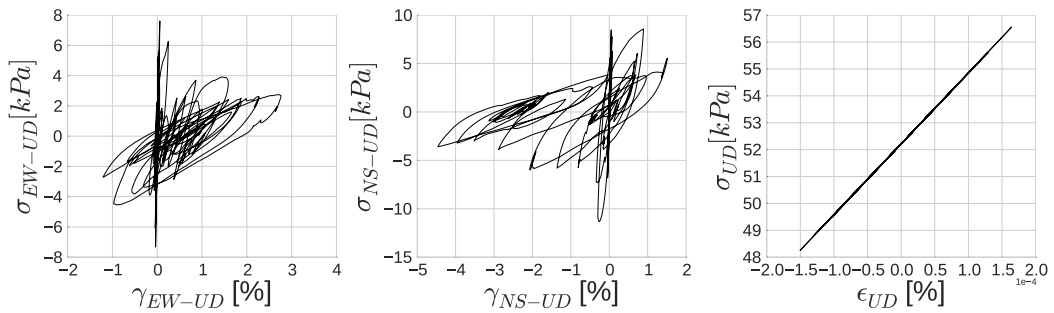
Fig. 3.7 Stress-strain curves on EW-UD component (left), NS-UD component (middle) and UD component (right) for point at GL-4.0 m of the WRLA.
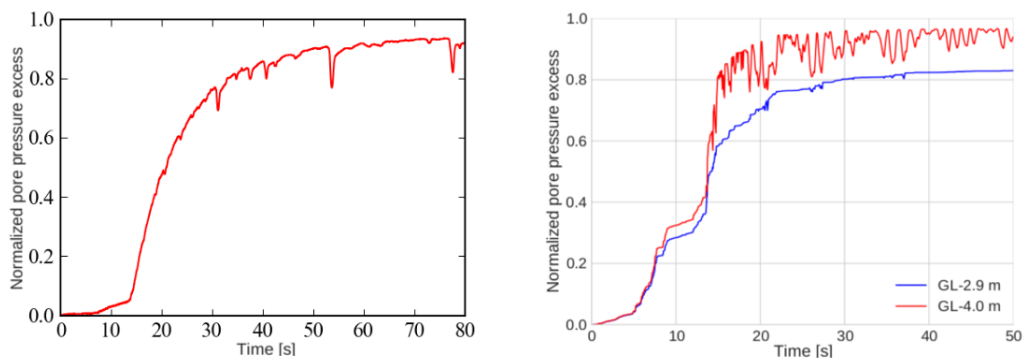
Fig. 3.8 Recorded pore pressure change at GL-2.9 m of the WRLA (left) (extracted from Holzer and Youd, 2007 [67] and modified after Pham, 2013); Pore pressure excess temporal change for the point at GL-2.9 m (in blue) and for the point at GL-4.0 m (in red) of the WRLA (right).

Thus far the influence of cyclic mobility phenomenon in the 4.3 m thick silty sand layer is demonstrated and the spiky-form wavelets at surface is explained with the sudden changes in pore pressure due to dilatancy of the silty sand layer. All these conclusions drawn by excess pore pressure development are consistent with the in-situ records of acceleration and pore pressure temporal changes. The good agreement between observed and calculated accelerations at the surface supports the understanding of observations with the nonlinear soil rheology including pore pressure effects used in this model. In the next section, a sensitivity study is performed to study the effect of soil rheology on the accelerations at the free surface and to compare one-component and three-component approaches at the WRLA site.

Influence of material rheology on wave propagation

In this section, we investigate the influence of ignoring pore pressure development on the soil column response using a visco-elastoplastic analysis of WRLA model. Figure 3.9 shows the computed 3C acceleration time histories at the surface. In both shear components, signal is dominated by high frequency motion and the particular wave forms observed after first 13 seconds cannot be reproduced. Conversely, in the vertical component, there is few difference, which is expected since the constitutive equations lead to material nonlinearity development on the deviatoric plan only. This is, however, a drawback of the model since it will not be able to correctly model volumetric changes during cyclic loading. This has to be improved in the future and it is important to correctly predict vertical settlements.
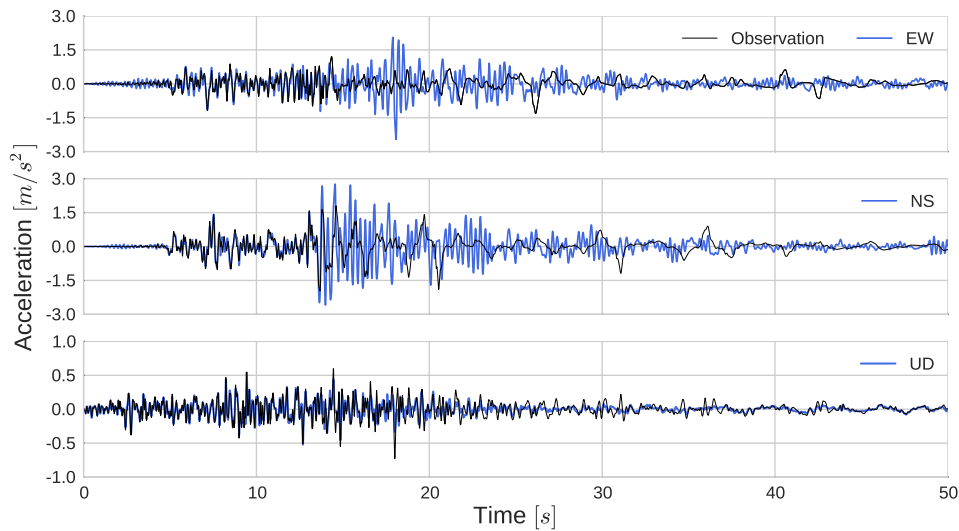
Fig. 3.9 Surface acceleration time histories on three directions for the simulation without pore pressure effects (in blue) and observation (in black) at the WRLA.

Figure 3.10 displays the 5% acceleration response spectra for the three components when pore pressure (in red) and dry conditions (in blue) are taken into account. A very strong peak around $3Hz$ in visco-elastoplastic analysis without pore pressure excess is noted in both shear directions. This peak is significantly damped with the introduction of cyclic mobility in the third layer so that the results become much closer to observations. Also, for low frequencies ($< 1Hz$), the spectrum is amplified under the effect of excess pore pressure development, which indeed results in a better fit to the observation. As expected, on the vertical component, these two models give similar results. With these results, we see that taking into account only one layer with a different soil constitutive model plays an important role on surface motion. The response spectra in the frequency band of interest for structural modeling (0.1-10 Hz) are strongly influenced. Thus, for certain structures whose resonance frequencies fall into the low frequency band, the design could exceed the safety limit if the rheological characteristics of the underlying media are not correctly taken into account. Such considerations enhance the importance of realistic hypothesis and good knowledge of soil behavior and properties for site specific studies.

In addition, Figure 3.11 shows maximum strain profiles obtained on the three components for the two analyses. On the shear components, a significant increase in strain values of the third layer is noted for the simulation with excess pore pressure development. On NS-UD component of shear strain (γ_{NS-UD}), the soil strain reaches to 5% while without

pore pressure excess the maximum strain does not exceed 0.2%. While the strain increases in the third layer, in other layers, an overall strain decrease is seen. Increasing deformations on a soil layer means that the incoming waves can be trapped inside the layer and excite higher nonlinearity. As a consequence, upward propagating waves could be damped or amplified more before entering into layers located above. Strength loss in the soil could result in large-span pulses in the transmitted waves. Also, due to the changes in the behavior of dilatant soil in only one layer, high peaks could follow low amplitude motion.
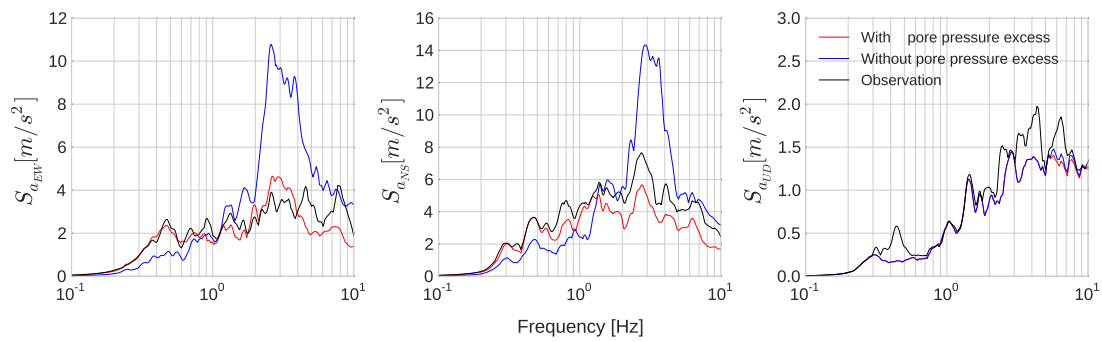
Fig. 3.10 Acceleration spectra of recorded surface acceleration (in black), visco-elastoplastic SEM simulation with excess pore pressure development (in red) and without excess pore pressure development (in blue) for EW component (left); for NS component (middle); for UD component (right).
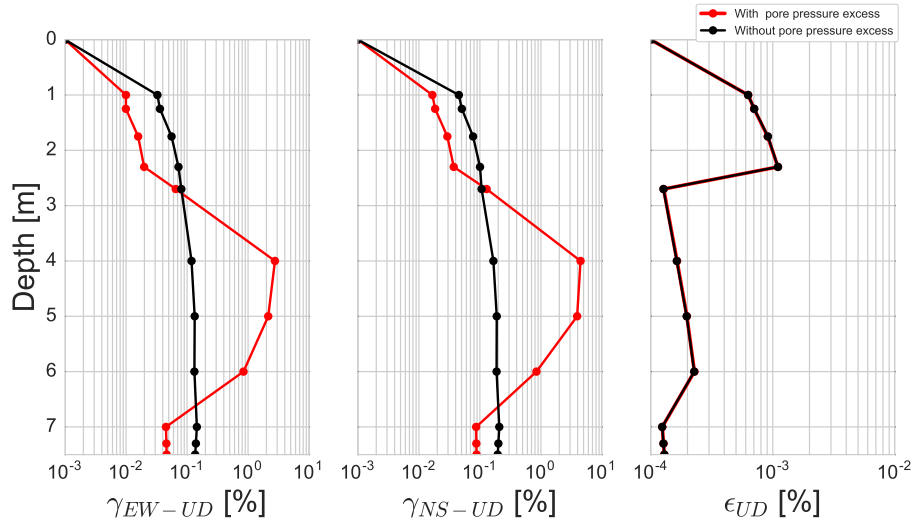
Fig. 3.11 Comparison of maximum strain profiles as a function of depth between visco-elastoplastic simulations with excess pore pressure development (in red) and without excess pore pressure development (in black) for EW-UD (left), NS-UD (middle) and UD (right) components.

We have shown the influence of pore pressure development in visco-elastoplastic rheological model. Lastly, in order to see the possible changes with other rheological assumptions, we perform similar tests for elastic, viscoelastic and elastoplastic models. Figure 3.12 displays the response spectra of the all the models on three directions. In elasticity, there is a very strong peak amplification at fundamental frequency of the model. This amplification is damped in viscoelasticity on each direction. By introduction of nonlinearity in elastoplasticity, we see that there is additional damping in the spectrum similarly to viscoelastic damping with a peak shift towards lower frequency. By means of this comparison, we see that under real input motion, soil nonlinearity and related frequency shift becomes prominent besides the effect of pore pressure development and consideration of an elastic or visco-elastic may lead to unrealistic computations.

Figure 3.13 demonstrates maximum strain profiles for all the rheological models on three directions. We can see the attenuation of elastic behavior due to the damping by plasticity and/or viscosity. In elastoplasticity, the maximum strain is higher overall the model compared to viscoelasticity, in particular for shear components. On the other hand,

in visco-elastoplasticity attenuation increases and solution becomes closer to viscoelasticity. This indicates that the viscous damping is significant in total stress analysis in this case.
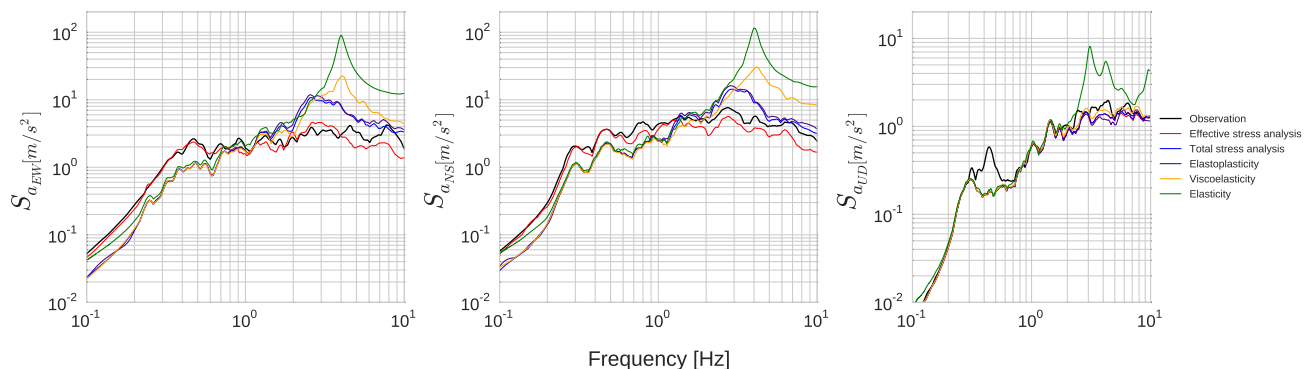
Fig. 3.12 Spectral acceleration comparison between elastic (in green), viscoelastic (in orange), elastoplastic (in purple), visco-elastoplastic with no excess pore pressure development (in blue) and visco-elastoplastic with excess pore pressure development (in red) models for three components.
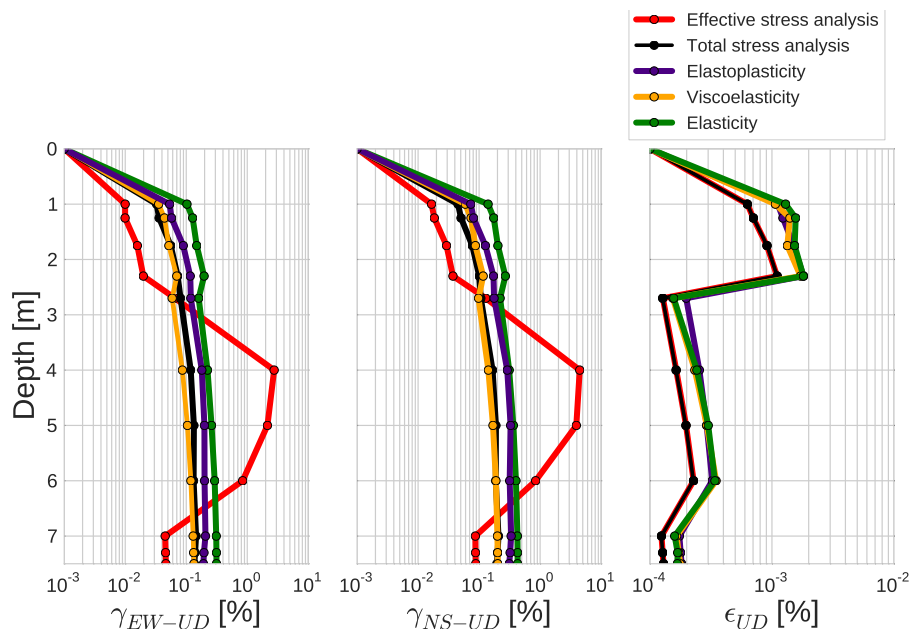
Fig. 3.13 Maximum strain profile of elastic (in green), viscoelastic (in orange), elastoplastic (in purple), visco-elastoplastic with no excess pore pressure development (in blue) and visco-elastoplastic with excess pore pressure development (in red) models for three components.

Uniaxial vs Triaxial loading

We also compare results obtained with uniaxial and triaxial loadings on WRLA model. Previously (See Chapter 3.2), we have shown that the soil becomes more nonlinear due to multi-component loading. We investigate here this effect on a real model in which pore pressure excess plays an important role using the real records for the site. For this purpose, in uniaxial loading case, we propagate only the NS component. Figure 3.14 shows the comparison of the two approaches on acceleration, velocity and displacement for the NS component.
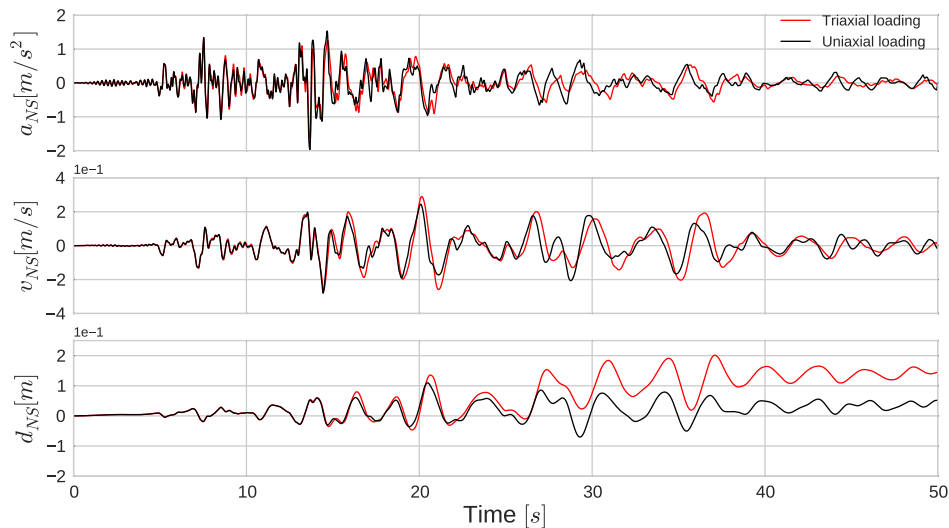
Fig. 3.14 Surface acceleration (top), velocity (middle) and displacement (bottom) comparison between uniaxial (in black) and triaxial (in red) loading for NS component.

In the initial part of the simulation (first 13 seconds) the results are very similar between uniaxial and triaxial loading. Then, waves in triaxial loading arrive later than the uniaxial loading. This indicates that the velocity of the media has further decreased under triaxial loading. Indeed, 3C behavior exhibits higher amplitudes and presents larger permanent

displacements. At right of Figure 3.15, the rise in pore pressure modeled with triaxial loading is earlier than in uniaxial loading. Given the fact that in triaxial loading soil is more nonlinear, the effective stress decreases more rapidly which results in earlier and stronger pore pressure excess rise. In consequence, the soil under triaxial loading undergoes more oscillations in the second half of the simulation (after 13 seconds). At left of the same figure, stress-strain loops are shown for both approaches. More nonlinear and dilatant behavior in triaxial loading leads the soil to undergo higher deformations. Under triaxial loading, although the loading on other directions is not as strong as NS direction, EW and possibly UD have an undeniable influence on soil nonlinearity and consequently on soil dilatancy. Indeed, soil becomes more nonlinear and more dilatant under the effect of loading on other directions and this may result in higher displacement at surface. For a realistic analysis on seismic wave propagation studies, the multiaxial interaction should therefore be considered.
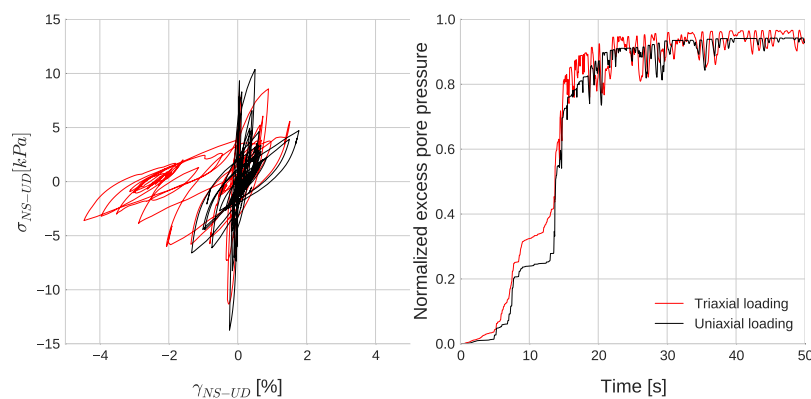
Fig. 3.15 (a) Stress-strain curve comparison between uniaxial (in black) and triaxial (in red) loading results for NS-UD component at GL-4.0 m; (b) Pore pressure excess temporal change comparison between uniaxial (in black) and triaxial (in red) loading results at GL-4.0 m.

Conclusions

The developed 1D-3C SEM code is validated on a real liquefaction site Wildlife Refuge Liquefaction Array (WRLA), which is affected by 1987 Superstition Hills earthquake. The simulated ground motion acceleration on three directions allow to reproduce the observations. Spiky behavior of the acceleration is reproduced successfully and related to pore pressure changes in the liquefiable soil layer. Following the validation, we used the 1D-3C SEM code for further exploration of the soil behavior under different conditions. We have shown that neglecting pore pressure effects in soil may result in ground motion with very different

frequency content. Calculated motion without including pore pressure effects overestimates high frequency motion and underestimates amplification of low frequency motion. Under excess pore pressure development effect, waves could be trapped in liquefiable soils where the soil strength changes continuously and the medium velocity decreases. As a result of rigidity loss, such soils can undergo very large deformations. The outgoing waves could be attenuated more with higher nonlinearity in liquefiable soils and can have highly damped large-span forms. Moreover, with strength hardening due to dilatant behavior, sudden strong peaks can be seen in transmitted waves. Additionally, we have compared uniaxial and triaxial loading approaches on WRLA model for the strongest ground motion direction. It is concluded that the soil becomes more nonlinear under triaxial loading and higher nonlinearity results in more rapid rise in pore pressure excess. Soil becomes more dilatant due to this increase in nonlinearity and resultant displacement at surface is much higher under triaxial loading. For this reason, consideration of multiaxial interaction is required for a realistic modeling of seismic wave propagation.

3.3.2   The 1993 Kushiro-Oki earthquake

On 15 January 1993, an earthquake of magnitude 7.8 with epicenter in south of Kushiro City was recorded by Japan Meteorological Agency (JMA). The focal depth of the event is determined to be 107 km. The ground motion during the earthquake is recorded by surface and borehole seismographs (GL-77 m) at central Kushiro Port (Figure 3.16). The fault activity is reported in NS direction and consistently the strongest motion of the surface records is observed in NS component. Around the stations, no evidence of ground failure such as soil boils, cracking and water spouting is reported. After the analyses on main shock and aftershock (4 February), the natural frequency of the sand deposit which is approximately $1Hz$ for the aftershock is found to have decreased during the main shock to lower frequencies. This is considered as a nonlinearity indication for the site Kushiro Port (KP). In ground surface records of NS and EW components, motion is found to be damped for high frequencies and a cyclic motion with a period of $1.5s$ and a spike after each peak is noted around $30s$ (Iai et al. 1995 [71]).

The soil parameters of the site KP is determined following a series of in-situ and laboratory tests by Iai et al. (1995) [71]. In the same study, the wave propagation is performed only on one direction (NS) and an additional analysis is devoted to the dilatancy parameter effects. Pham et al. (2013) [125] and Roten et al. (2014) [132] have also studied 1C shear wave propagation in KP site by considering soil nonlinearity and excess pore pressure generation

considering the Iai et al. (1990) [69] and Bonilla et al. (2005) [16] models. In this latter, dilatancy parameters are inverted numerically for a better fit of the computed surface motion to the observed one. For this site, the soil parameters are taken by the study of Iai et al. (1995) [71] as shown in Table 3.3. Kushiro Port site is composed of eight different soil layers. The second and third layers are susceptible to develop excess pore pressure. In Iai et al. (1995) [71], the wave propagation is performed on the NS component only. In spite of a careful site characterization of the shear wave speed, there is no information about the P wave velocity at this site. We decided to use a Poisson ratio equal to 0.48. This assumption is made based on average Poisson ratio values near KP site after the data provided by PARI network (See http://www.eq.pari.go.jp/kyosin/data/pnt/kushiro-g.htm). Dilatancy parameters of the liquefiable sand layers are given in Table 3.4. Moreover, all layers are initially anisotropically consolidated and water table is set at 2 meters depth.
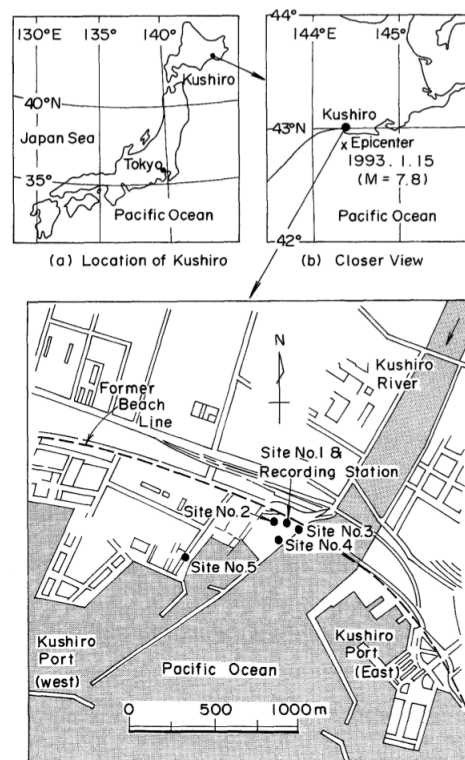
Fig. 3.16 Locations of epicenter of the earthquake, Kushiro City, recording station and boring sites (after Iai et al. 1995 [71]).

Table 3.3 Soil properties at Kushiro Port vertical array (after Iai et al. 1995 [71]). V_p values are calculated by assumption of Poisson ratio equal to 0.48.

Layer	Description	Thickness $[m]$	$V_s[m/s]$	$V_p[m/s]$	$\rho[kg/m^3]$	$\phi_f[degree]$	K_0
1	Fill soil	2.0	249	1270	1540	40	0.5
2	Sand	7.0	249	1270	1720	40	0.5
3	Sand	14.0	326	1662	1980	48	0.5
4	Silt	9.0	265	1351	1730	37	0.5
5	Silt	4.0	341	1739	1760	44	0.5
6	Silt	8.0	286	1458	1700	44	0.5
7	Silt	8.0	302	1540	2000	45	0.5
8	Silt	25.0	341	1739	1730	44	0.5

Table 3.4 Dilatancy parameters for the sand layers at Kushiro Port vertical array (after Iai et al. 1995 [71]).

Layer	$\phi_p[degree]$	w_1	p_1	p_2	S_1
2	28	7.0	0.50	0.65	0.01
3	28	3.5	0.50	0.40	0.01

In next section, we model the seismic wave propagation in the KP with consideration of pore pressure changes in the second and third layers by using the 1993 Kushiro-Oki earthquake records. Then, the obtained results are discussed in detail.

Numerical model

The input data that is used in this study is obtained by the borehole accelerometer records at GL-77 m of KP site. The data is filtered on the frequency interval $0.1 - 10 \; Hz$ before simulations. Figure 3.17 displays the borehole acceleration records on three directions. The maximum values of the filtered input data are approximately 1.83 m/s^2 in EW direction, 1.72 m/s^2 in NS direction and 0.49 m/s^2 in vertical direction. Accordingly, the input motion is defined at 77 m depth of the created model in borehole condition. The model is composed of spectral elements of which the sizes range between 1.0 and 1.5 m overall the model and 5 GLL points are defined on each element. The time step is $2x10^{-5}$ s that allows to have a resolution of 10 Hz with the consideration of V_s softening due to nonlinearity by a factor

of 4. Total time of simulation is set to 60s. A visco-elastoplastic soil rheology is defined all over the model by taking into account pore pressure effects in the second and third soil layers. The quality factors for shear and pressure waves are assumed as $V_s/10$ and $V_p/10$, respectively and reference frequency is set to 1Hz.
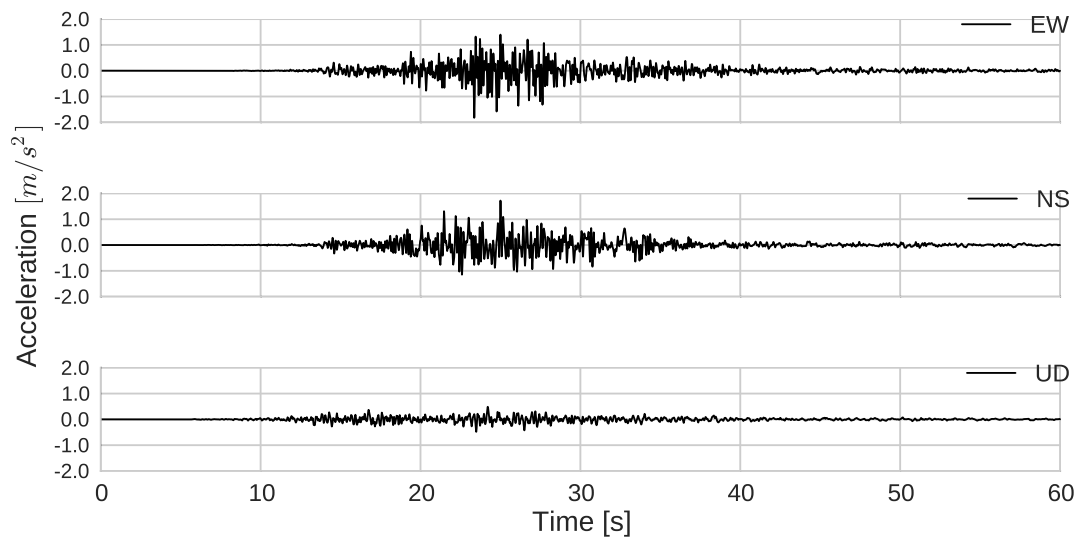
Fig. 3.17 Acceleration time histories at GL-77 m depth in east-west (EW), north-south (NS) and vertical (UD) directions recorded at KP.

Results

Figure 3.18 shows the comparison of computed surface acceleration and observations in three directions. While we see a reasonable fit for the horizontal components, the vertical one is completely missed. Considering that we were able to fit well the Wildlife Refuge Liquefaction Array model for all three components of the Superstition Hill earthquake, this result suggests the importance of site characterization in three-component studies.
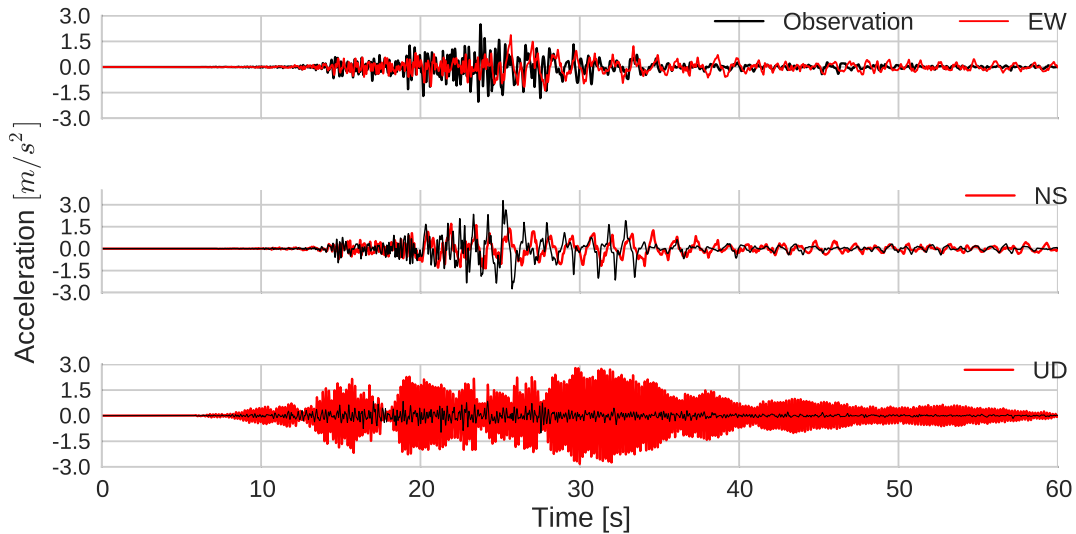
Fig. 3.18 Surface acceleration time histories calculated using the visco-elastoplastic model (in red) and real records (in black) for the KP site.

Besides, the EW and NS components show the peaks related to dilatancy effects. The simulated ground motion is in phase with the observed data, yet there are some differences in amplitude. In order to better understand the origin of these differences, we look at pore pressure changes in the second and third layers in Figure 3.19. For both depths, the sudden increase in pore pressure is seen starting from 15th seconds. After approximately 25 seconds when normalized pore pressure reaches to 0.4, oscillations appear on the curves, which indicates that dilatant behavior takes place in 25 seconds. Figure 3.20 displays the deviatoric plans for both depths. Since the layers are initially anisotropically consolidated, initial deviatoric stress is non-zero. Continuous decrease in effective stress is noted until $S = 0.6$. This corresponds to remarkable oscillations in pore pressure development. In observations, large-span wave forms that are followed by high peaks start at 30 seconds, while in our simulations, this behavior is developed towards 25 seconds. Due to this earlier pore pressure generation in liquefiable soils, surface motion between 25-30 seconds have relatively larger period content than observations on EW and NS directions. The absence of high peaks at 25 seconds could be related to this fact as well given the resultant higher nonlinearity from early pore pressure development. On the other hand, the calculated surface motion after 30 seconds demonstrates a considerable agreement between observations in terms of phase and wave forms. Figures 3.21-3.22 display the stress-strain curves for EW-UD and NS-UD components. For both depths, expansion in stress-strain loops due to pore pressure changes is more apparent in NS-UD component. Maximum strain values are around 0.25 % in the second layer (GL-4 m) and 0.15

% in the third layer (GL-15 m). These strain values are considerably low compared to WRLA.
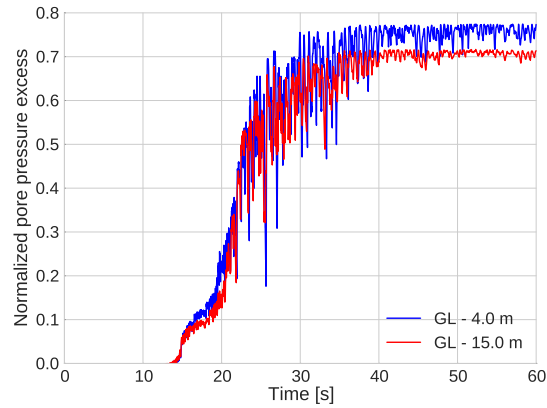
Fig. 3.19 Pore pressure excess temporal change for the point at GL-4.0 m (in blue) and for the point at GL-15.0 m (in red) of the KP.
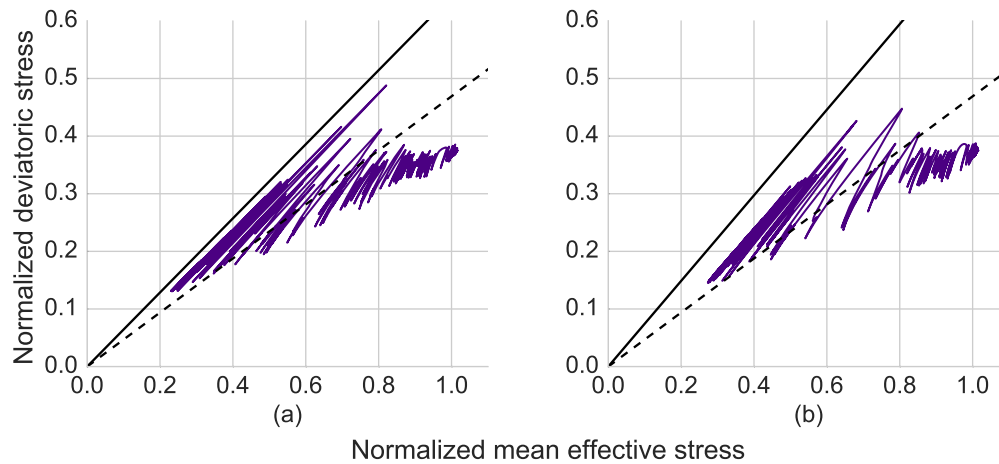
Fig. 3.20 (a) Deviatoric plan for point at GL-4 m, (b) Deviatoric plan for point at GL-15 m of the KP model with failure line (solid line) and phase transformation line (dashed line).
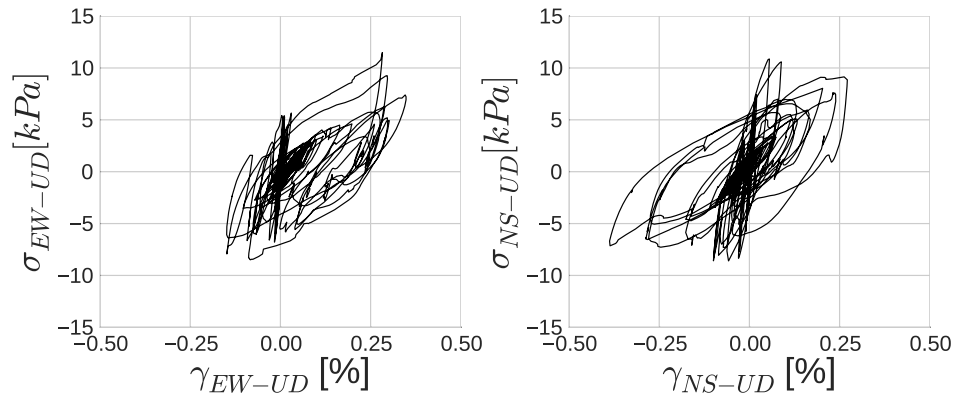
Fig. 3.21 Stress-strain curves on EW-UD component (left) and NS-UD component (right) for point at GL-4 m of the KP.
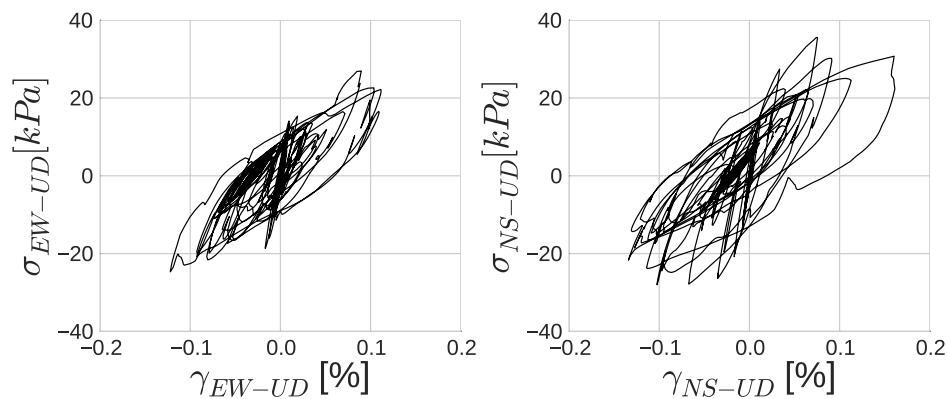
Fig. 3.22 Stress-strain curves on EW-UD component (left) and NS-UD component (right) for point at GL-15 m of the KP.

A satisfactory similitude in comparison of the ground motion calculated by the 1D-3C SEM code with observations on horizontal directions is obtained for the Kushiro Port model. Inconsistency in vertical motion is probably associated with the lack of data on P velocity profile of the media and it reveals the importance of a complete site characterization in wave propagation studies using three components. With the 1D-3C SEM code analyses, we are

able to explain the relation between temporal change in pore pressure and surface motion also for initially anisotropically consolidated sites such as Kushiro Port. In next section, further analyses are performed in order to see the effect of different rheological assumptions on the Kushiro Port model.

Influence of material rheology on wave propagation

In this section, we explore possible outcomes of using a material rheology different than visco-elasticity including pore pressure effects. First, the pore pressure development in the second and third layers is neglected. Figure 3.23 demonstrates the resultant surface acceleration on three directions compared to observations. As explained in previous section, at KP site, long period motion followed by high peaks starts at 30 seconds. In our effective stress analysis, these traits are seen starting from 25th second. Coherently, in total stress analysis, the resultant acceleration on EW and NS directions is dominated by high frequency motion beyond 25 seconds. In Figure 3.24, this high frequency attenuation in effective stress analysis can be seen on both directions. Although the effect of excess pore pressure generation figures by high frequency attenuation and low frequency amplification similarly to Wildlife Refuge Liquefaction Array (See Chapter 3.3.1), in KP model two approaches do not differentiate dramatically. Such differences of pore pressure excess influence on the surface wave motion highlight the necessity of site-specific studies. In Figure 3.25, maximum strain profiles are shown for two components. Even though the maximum strain is below 1 % in effective stress analysis, it is approximately 8 times greater than total stress analysis in liquefiable soil layers.
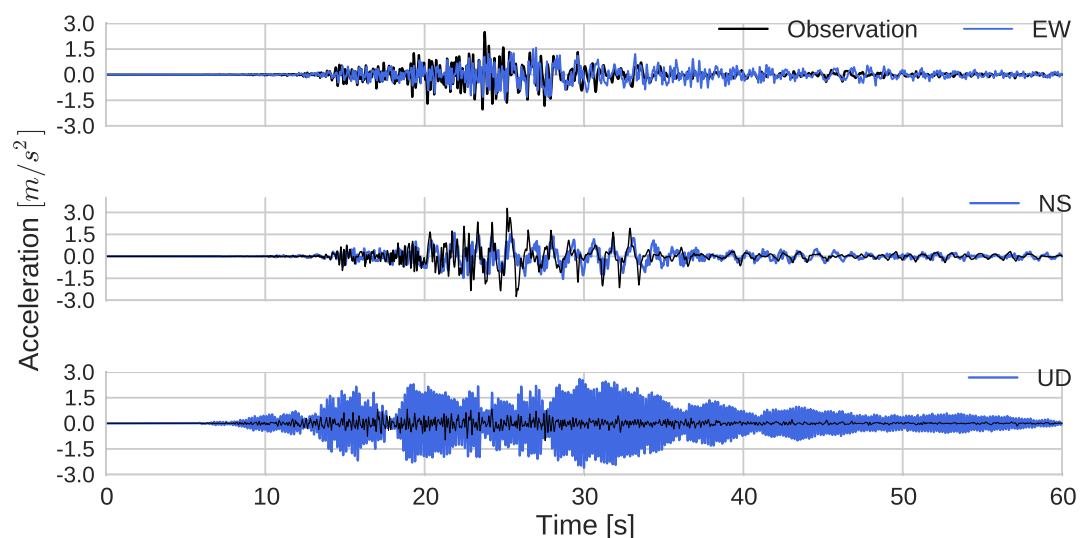
Fig. 3.23 Surface acceleration time histories on three directions for the simulation without pore pressure effects (in blue) and observation (in black) at the KP.
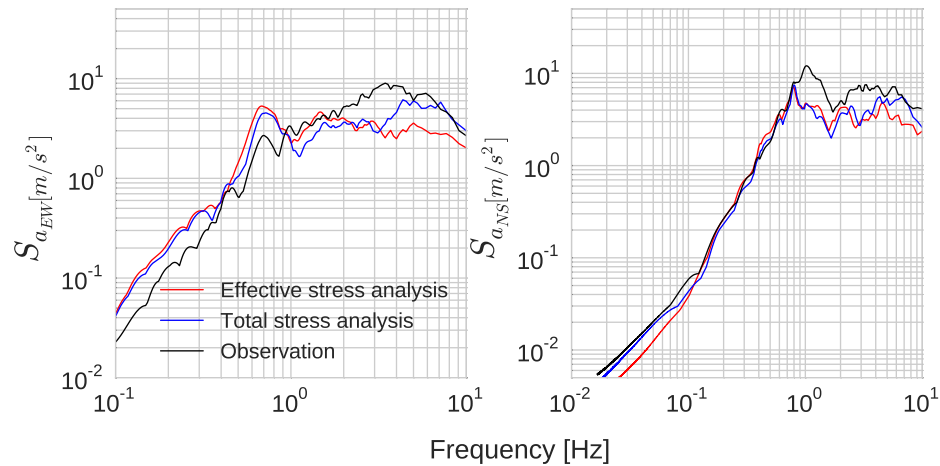

Fig. 3.24 Acceleration spectra of recorded surface acceleration (in black), visco-elastoplastic SEM simulation with excess pore pressure development (in red) and without excess pore pressure development (in blue) for EW component (left); for NS component (right)
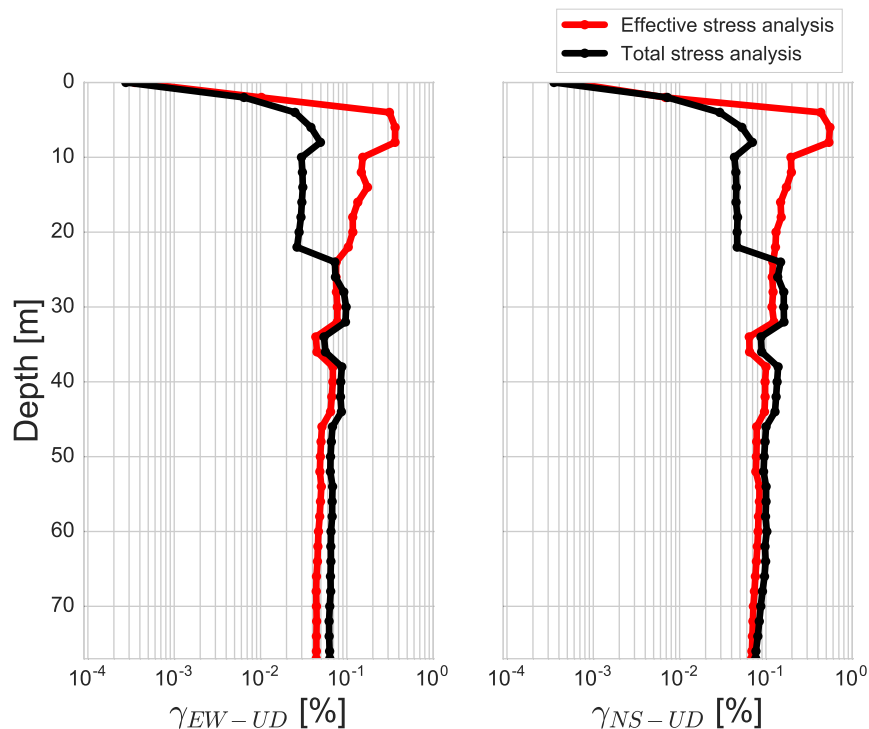
Fig. 3.25 Comparison of maximum strain profiles as a function of depth between visco-elastoplastic simulations with excess pore pressure development (in red) and without excess pore pressure development (in black) for EW-UD (left) and NS-UD (right) components.

All the rheological assumptions are compared in response spectra graphs (Figure 3.26). Similarly to Wildlife Refuge Liquefaction Array model, in elasticity, there is high energy peak which is attenuated in viscoelasticity, elastoplasticity and visco-elastoplasticity without pore pressure development. In nonlinear rheologies, the frequency is shifted towards lower frequencies with respect to the other ones. On the other hand, it must be noted that nonlinear effect is not seen in the same way all over the frequency band. While elastic/viscoelastic peaks are highly damped over 3 Hz, the attenuation is less around 1 Hz. Thus, frequency shift is more visible at 1 Hz for both directions. In addition, in effective stress analysis, there is more attenuation in high frequencies. Compared to observation, the calculated motion is slightly more nonlinear with more frequency shift and more attenuation. Yet, the general trend in effective stress analysis is in accordance with observations. We see that for a site

of 77 meters depth, the nonlinearity of the surficial layers have similar impact on resultant ground motion as another site of 7.5 meters depth (Wildlife Refuge Liquefaction Array) where deformation limit is much higher. We are able to model these effects by using the same nonlinear model. Lastly, in Figure 3.27, maximum strain profiles are shown for all the rheologies on two components. With viscoelasticity and nonlinearity, energy attenuation results in lower strain level throughout the 23 meters of surficial zone. In effective stress analysis, a strong increase in deformation on the same zone is noticed on both directions.
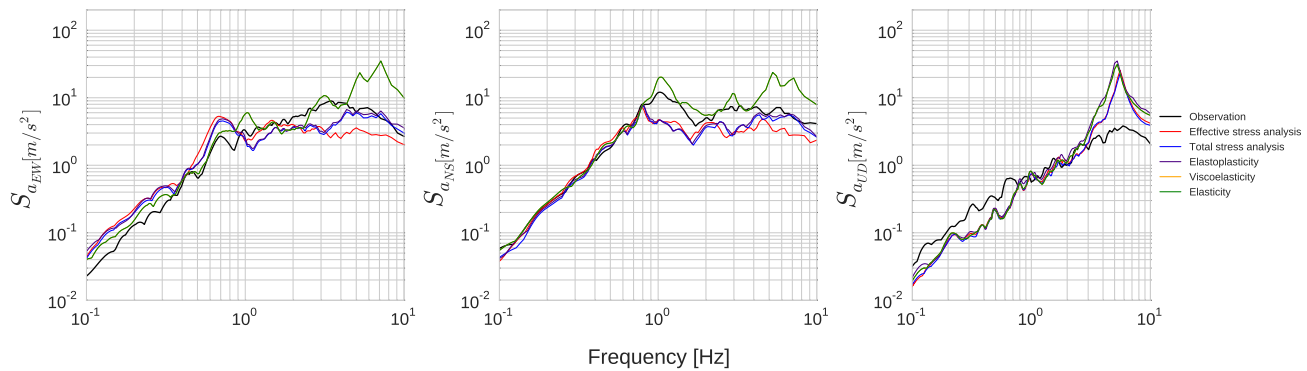
Fig. 3.26 Spectral acceleration comparison between elastic (in green), viscoelastic (in orange), elastoplastic (in purple), visco-elastoplastic with no excess pore pressure development (in blue) and visco-elastoplastic with excess pore pressure development (in red) models for three components of Kushiro Port site.
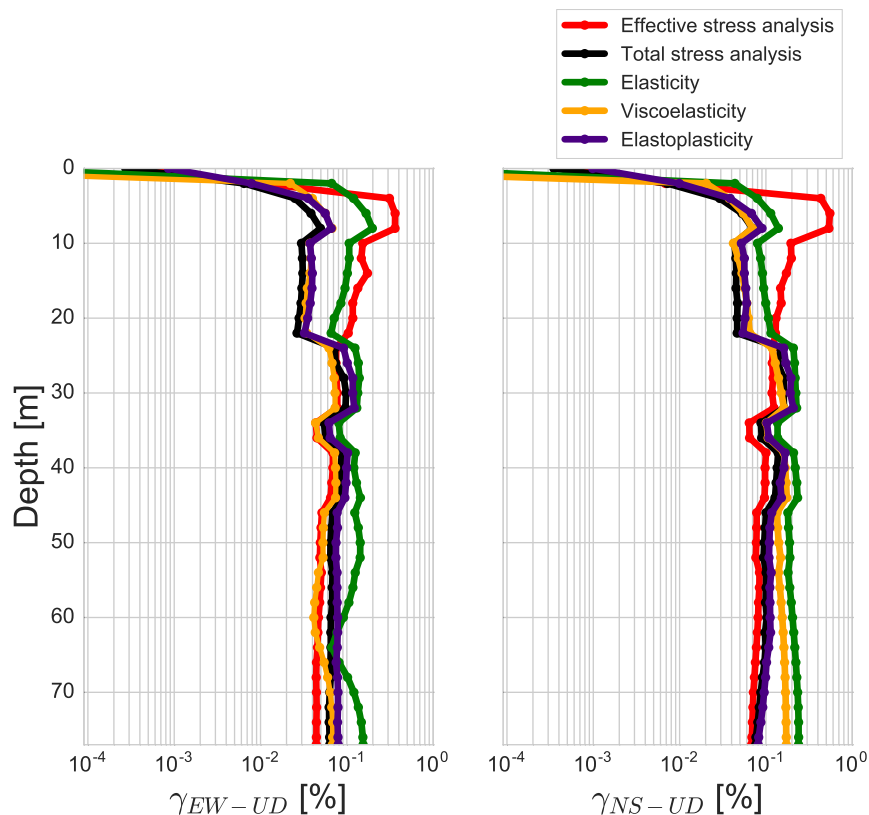
Fig. 3.27 Maximum strain profile of elastic (in green), viscoelastic (in orange), elastoplastic (in purple), visco-elastoplastic with no excess pore pressure development (in blue) and visco-elastoplastic with excess pore pressure development (in red) models for three components of Kushiro Port site.

Uniaxial vs Triaxial loading

In this section, the soil behavior in KP site is analyzed for propagation on NS direction (where the strongest PGA is recorded) under uniaxial and triaxial loading conditions. Figure 3.28 shows surface acceleration, velocity and displacement time histories for both conditions. In all variables, the resultant values are very close. However, in previous section where we made the same comparison for Wildlife Refuge Liquefaction Array (See Chapter 3.3.1), displacement in triaxial loading was shown to be much greater than uniaxial loading due to higher nonlinearity and dilatancy. Although acceleration and velocity range share very similar values in KP and WRLA, we do not obtain the same conclusion at KP model. In

order to better understand the reason, we look at stress-strain curves (left of Figure 3.29) and pore pressure generation (right of Figure 3.29) at middle of the second layer (GL-4 m). Under triaxial loading, soil is slightly more nonlinear. Strength weakening is higher and maximum strain is larger. In pore pressure change, more oscillations are seen under triaxial loading, which indicates higher dilatancy under triaxial loading. Nevertheless, dilatancy does not lead the soil to reach much higher deformations and strain distribution is considerably symmetrical under both loading conditions. In other words, strain does not accumulate on one side. As a result, transmitted wave velocity content at surface has very close values on positive and negative directions and surface displacement is close to zero for both conditions. This test shows the strong influence of the dilatancy level and resultant strain in a liquefiable soil on the ground surface motion. The level of ultimate nonlinearity and dilatancy evoked in the model is very determinant on the difference between uniaxial and triaxial loading approaches. We see again the importance of site-specific analysis, given the fact that KP and WRLA surface motion content differ despite of the similitude in their surface motion amplitude.
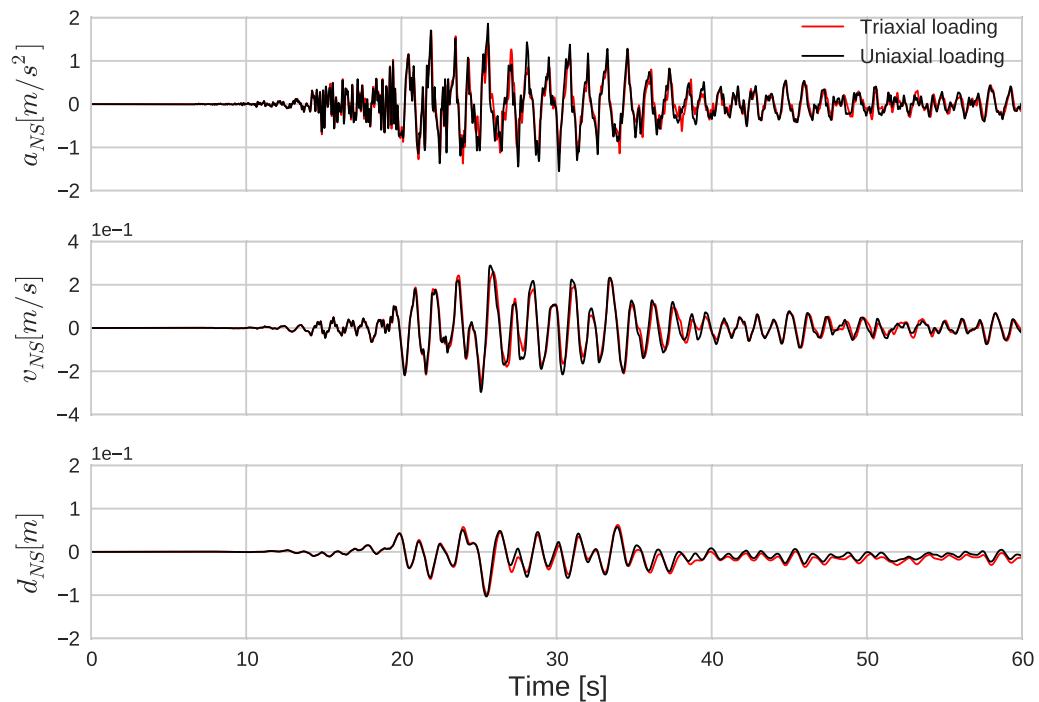
Fig. 3.28 Surface acceleration (top), velocity (middle) and displacement (bottom) comparison between uniaxial (in black) and triaxial (in red) loading for NS component.
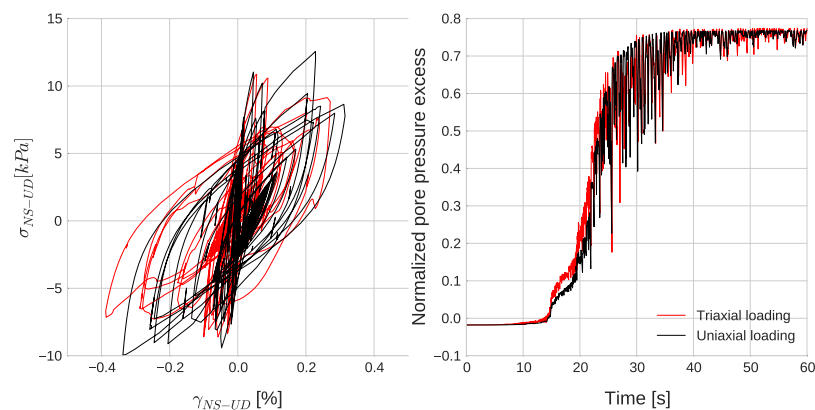
Fig. 3.29 (a) Stress-strain curve comparison between uniaxial (in black) and triaxial (in red) loading results for NS-UD component at GL-4 m, (b) Excess pore pressure vs time comparison between uniaxial (in black) and triaxial (in red) loading results at GL-4 m.

Conclusions

The validated 1D-3C SEM code on the WRLA site is used in modeling of Kushiro Port (KP) site where the ground motion is recorded during the 1993 Kushiro-Oki earthquake. KP site consists of eight different soft soil layers and extends to a depth of 77 meters. In observations, pore pressure effect is observed by long period motion followed by large peaks. By the 1D-3C SEM code, we produced these pore pressure effects on horizontal directions surface motion by means of effective stress analysis. On the other hand, due to the lack of data for P velocity profile, inconsistency is induced on vertical direction. While we are able to model the vertical motion in Wildlife Refuge Liquefaction Array where soil properties are determined comprehensively, the irrelevancy in the results of KP site reveals the importance of a complete site characterization in wave propagation studies using three components. Moreover, by comparing different rheological models at KP site, nonlinearity is shown to bring up more attenuation and frequency shifts in surface motion energy content on horizontal directions. Yet, these nonlinearity-related changes are not homogeneous all over the concerned frequency band. Also, with effective stress analysis, high frequency damping and low frequency amplification are obtained similarly to Wildlife Refuge Liquefaction Array model. However, the tendency of such behavior is highly dependent on soil properties and input motion. Also, despite the fact that actual strain level is low in KP site, effective stress analysis results in nearly 8 times higher strain than total strain analysis. This shows the importance of pore pressure effects in superficial layers on wave propagation in a deep model. Lastly, differences in uniaxial and triaxial loading approaches highly depend on the ultimate level of nonlinearity triggered in soil.

3.3.3 The 2011 off the Pacific coast of Tohoku earthquake

On 11 March 2011, one of the largest earthquake of the world and the largest earthquake for Japan since the installation of the recording systems occurred off the Pacific coast of Japan with a magnitude of $M_w = 9$. The 2011 off the Pacific coast of Tohoku earthquake, or the Great East Japan earthquake caused vast damages due to seismic force and tsunami following the main shock. Tsunami stroke all the Pacific coast of Japan and waves of 9.3 *m* and higher are observed close to Fukushima where a nuclear crisis has risen after the severe accidents in the Daiichi Nuclear Power Plant. The intensity of the event led to by more than 23000 people killed or missing (Hayashi et al., 2011 [65]; Kurahashi and Irikura, 2011 [92]; Kazama and Noda, 2012 [84]). The focal mechanism of the earthquake is defined by reverse fault activity on WNW - ESE direction on the boundary between the continental plates and the Pacific plate. The epicenter of the earthquake is the southeast of Sendai city (Miyagi prefecture). The rupture area is extended over an area with a length of 450 km and a width of 200 km approximately. Numerous aftershocks over magnitude 5 are recorded on following days. Figure 3.30 displays the locations of recorded main shocks and aftershocks.

According to the geotechnical field reports, liquefaction-induced damages are observed over an area of approximately 500 km along the coast extending from Iwate region (south of Ibaraki prefecture) to Kanagawa region (north of Miyagi prefecture). Extensive damages are observed in residential, commercial structures and public facilities. The typical liquefaction-related traces are recorded such as sand boils, lateral spreading, tilted buildings, uplift and settlement on structures, offset in tunnels and slope deformations. It is noted that additional damages in many places are recurred but their traces are washed away by aftershock tsunamis. On the other hand, in many areas where ground improvement had been carried out, no significant damage of liquefaction is observed. For many buildings which adopt highly rigid and spread type of foundations such as mat and sand compaction foundations, less damages are recorded. Also, on the underground subway structures working with 'Urgent Earthquake Detection and Alarm System', excessive damages were avoided (Ashford et al. 2011 [7]; Kazama and Noda, 2011 [84]; Tokimatsu et al. 2012 [153]).

Thanks to the station networks distributed across Japan belonging to various Japanese institutes and organizations, the strong ground motion has been well recorded by a number of stations at surface (K-NET and KiK-net) and in borehole (KiK-net) (Kinoshita, 1998 [85]; Aoi et al. 2000 [5]). In Bonilla et al. (2011) [18], by use of K-NET and KiK-net station data, a large variety of nonlinearity is shown after the 2011 off the Pacific coast of Tohoku earthquake. In the same study, by use of K-NET station data, it is shown that some soils

have higher PGA values compared to relatively softer soils. This has been considered as a nonlinearity indication given the fact that the nonlinearity results in deamplification of higher frequencies and resonance frequency shift towards lower frequencies (Beresnev and Wen, 1996 [12]). Another nonlinearity finding is the recorded high acceleration peaks at surface following a low frequency carrier, contrarily to the typical nonlinearity effect deamplification. This has been explained by partial shear strength gain of cohesionless soils during wave propagation due to their dilant nature (Iai et al. 1995 [71]; Archuleta, 1998 [6]; Bonilla et al., 2005 [16]).

Roten et al. (2013) [131] studied the Onahama Port site (near Iwaki, Fukushima prefecture) operated by the Port and Airport Research Institute where amplification of high frequency motion is observed (See Figure 3.30). In the same study, using the surface and borehole data, the 1D wave propagation is performed by considering the excess pore pressure development in the model. For this purpose, the 1D finite-difference code of NOAH (Bonilla et al. 2005 [16]) which employs the front saturation model (Iai et al., 1990 [69]) has been used. The soil model is composed of a fill soil layer of a thickness of $1.25m$ overlying the water table, two cohesionless sand layers and a silt layer at the bottom. The details are shown in Table 3.5. The front saturation model parameters are obtained by inversion method based on misfit technique between the observation and calculated horizontal surface motion (Roten et al., 2013 [131]).
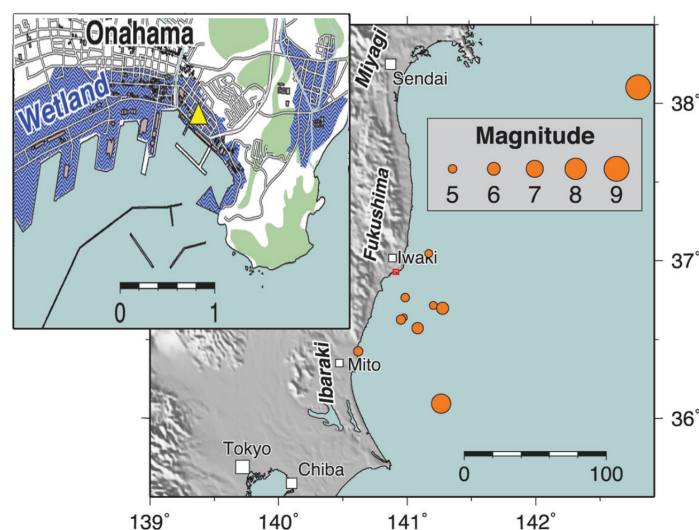
Fig. 3.30 Map of the epicenters of the main shocks and aftershocks in eastern Japan and the location of the Onahama Port vertical array in red rectangle and with detailed zoom on the inset map in yellow triangle (after Roten et al. 2013 [131]).

Table 3.5 Soil properties at Onahama Port vertical array (after Roten et al. 2013 [131]).

Layer	Description	Thickness $[m]$	V_s $[m/s]$	V_p $[m/s]$	ρ $[kg/m^3]$	ϕ_f $[degree]$	K_0	Cohesion $[Pa]$
1	Fill soil	1.25	100	510	1800	30	1.0	10E+06.04
2	Sand	2.25	124	632	2000	30	1.0	-
3	Sand	3.50	215	1096	2000	40	1.0	-
4	Silt	4.00	950	4844	2000	20	1.0	10E+03

Table 3.6 Dilatancy parameters for the sand layers at Kushiro Port vertical array (after Roten et al. 2013 [131]).

Layer	$\phi_p[degree]$	w_1	p_1	p_2	S_1
2	20	114.815	0.6	1.2	0.01
3	28	1000.000	0.6	1.2	0.01

In the following section, the Onahama Port site (OP) is modeled with the 1D-3C SEM code by considering pore pressure effects in the second and third layers.

Numerical model

The input data that is used in this study is obtained by borehole accelerometer records at GL-11 m of OP site (See Figure 3.31). The data is filtered on the frequency interval $0.1 - 10$ *Hz*. The maximum values of the filtered input data are approximately 1.51 m/s^2 in EW direction, 1.72 m/s^2 in NS direction and 1.58 m/s^2 in vertical direction. Accordingly, the input motion is defined at GL-11 m depth of the created model with borehole condition. The model is composed of spectral elements which range between 0.25 and 1.5 m overall the model and 5 GLL points are defined on each element. The time step is 1.10^{-5} *s* that allows to have a resolution of 10 Hz with the consideration of V_s softening due to nonlinearity by a factor of 4. The rheology for the whole model is set as visco-elastoplasticity. Only the second and third layers are susceptible to excess pore pressure generation. The quality factors for shear and pressure waves are assumed as $V_s/10$ and $V_p/10$, respectively and reference frequency is set to $1Hz$.
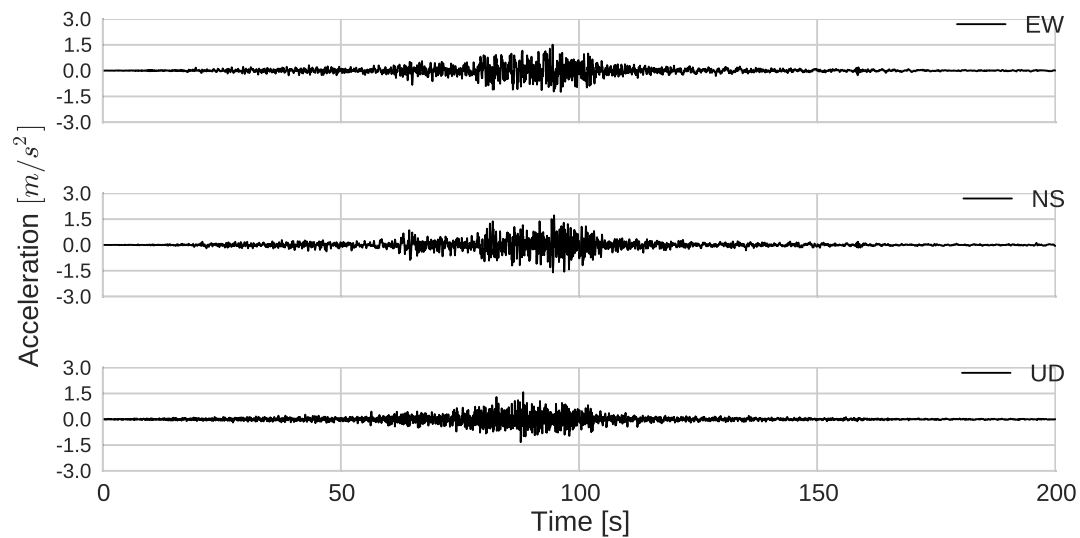
Fig. 3.31 Acceleration time histories at GL-11 m depth in east-west (EW), north-south (NS) and vertical (UD) directions recorded at OP.

Results

Figure 3.32 demonstrates the comparison of calculated and observed surface acceleration on three directions. Strongest motion is recorded in EW component with an amplitude of $6m/s^2$ in acceleration. Calculated signals are generally in agreement with observations throughout the simulation in terms of amplitude and phase. Yet, on horizontal directions, some differences in amplitude can be remarked around 100 seconds. Since the duration of signals is considerably long (200 seconds), a detailed window between 90-100 seconds where the highest peaks appear is shown in Figure 3.33. It is seen that on both horizontal directions, signals are in phase and wave forms are quite similar. At about 100 seconds, the effect of dilatancy starts to intervene by larger-span wave forms followed by high peaks. These large-span wave forms correspond to longer period of motion due to rigidity change in liquefiable soil layers. On the other hand, sudden peaks in recorded data, particularly in EW component, cannot be modeled with same amplitude. Such discrepancies could be related to the fact that dilatancy parameters used in the model are inverted numerically to obtain best-fit between EW component of observation and another code that uses a different model for nonlinearity. Therefore, it may be possible to ameliorate the results in terms of amplitude by use of different parameters. Besides this point, the 1D-3C SEM code models satisfactorily the surface motion by taking into account the changes due to dilatancy in underlying layers. On vertical direction, computed motion is consistent with observed motion despite of higher

level of high-frequency content. This indicates that observed motion is more nonlinear than computed motion even though it is of low-level nonlinearity. As explained in preceding sections, this is one of the aspects to improve in future by a detailed knowledge of soil nonlinearity on vertical direction as well as a better characterization of pressure wave velocity profile.
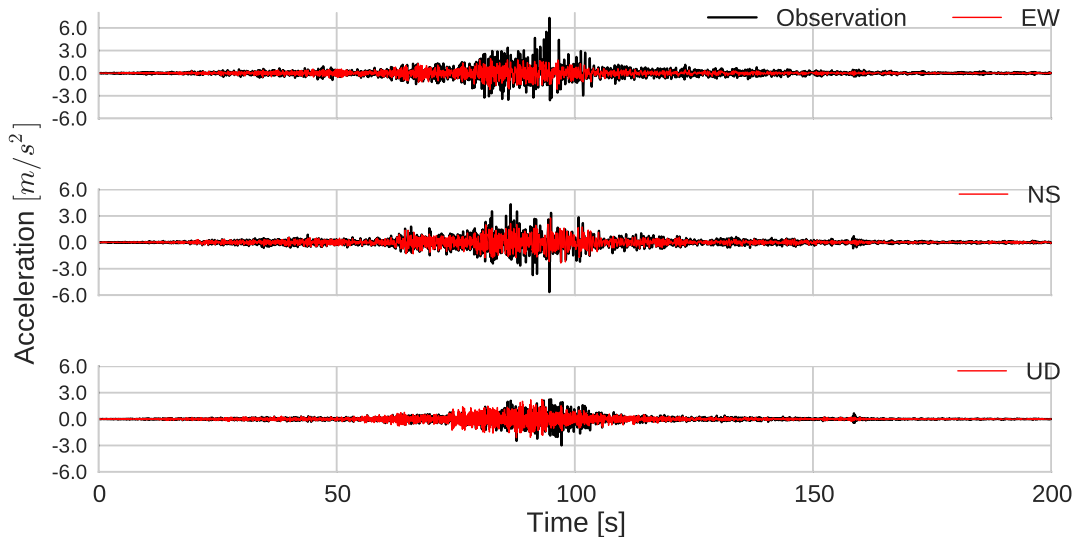
Fig. 3.32 Output acceleration time histories calculated in visco-elastoplastic model with excess pore pressure generation (in red) and real records (in black) of OP.
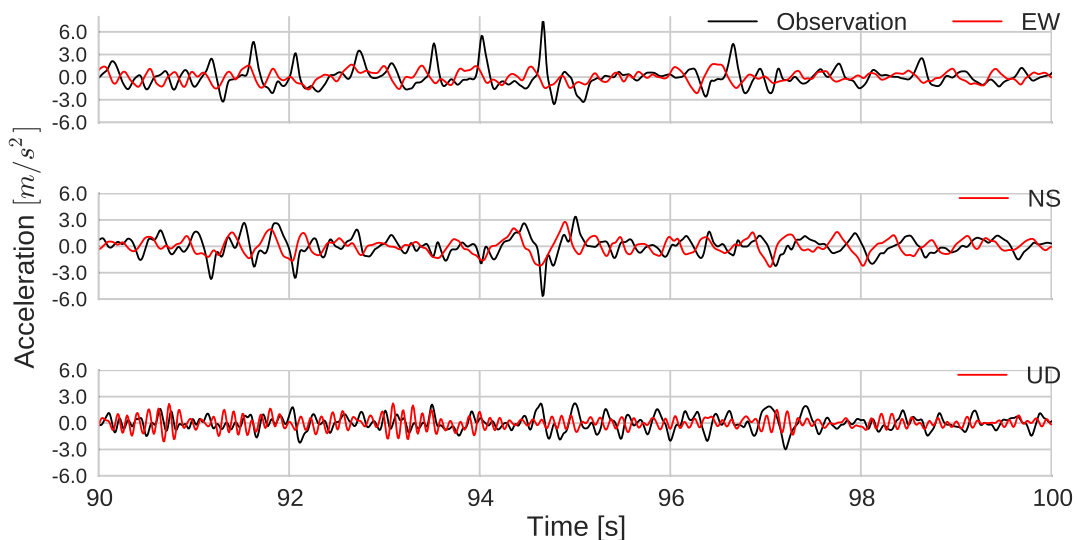
Fig. 3.33 Output acceleration time histories on [90-100] seconds time interval calculated in visco-elastoplastic model with excess pore pressure generation (in red) and real records (in black) of OP.

Evolution of pore pressure along 200 seconds is shown in Figure 3.34 for midpoints of the second and third layers. Pore pressure augmentation starts around 60 seconds and oscillations take place starting from 75 seconds at GL-2.75 m (2nd layer). However, for the third layer, increase in pore pressure is very limited, so that significant changes in soil strength at third layer is not expected. This is coherent with the conclusions in Roten et al. (2013) [131] that dilatant behavior in the third layer does not play an important role on wave propagation in the model. In Figure 3.35, deviatoric plans are shown for the two layers. Difference in stress path between the layers is noticed. At GL-2.75 m, soil is highly dilatant and continuous changes in effective stress are seen by extension of loading path parallel to failure line. Nevertheless, at GL-5 m, soil strength is very close to initial state. In consequence, stress-strain curves for two depth levels are quite different (Figures 3.36-3.37). At GL-2.75 m, dilatant behavior is seen by slight expansion in shear components. Since the soil is highly dilatant throughout the propagation as seen in loading path in deviatoric plan, strength loss in the soil is recovered frequently. For this reason, expansion in stress-strain loops is much less than liquefiable soil layer of Wildlife Refuge model where continuous decline in effective strength occurs. As a result, maximum strain is also limited (less than 1 % in NS-UD and EW-UD components).
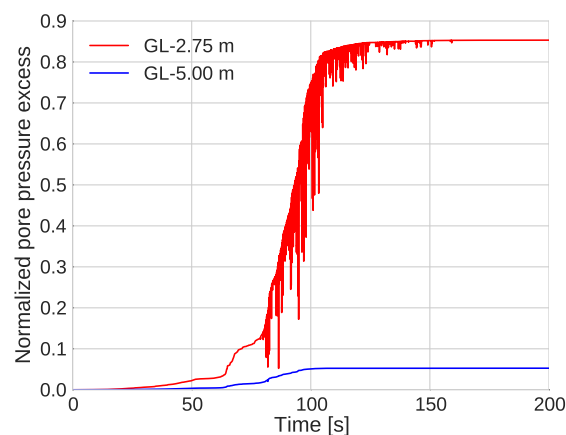
Fig. 3.34 Pore pressure excess temporal change for the point at GL-2.75 m (in blue) and for the point at GL-5 m (in red) of the OP.
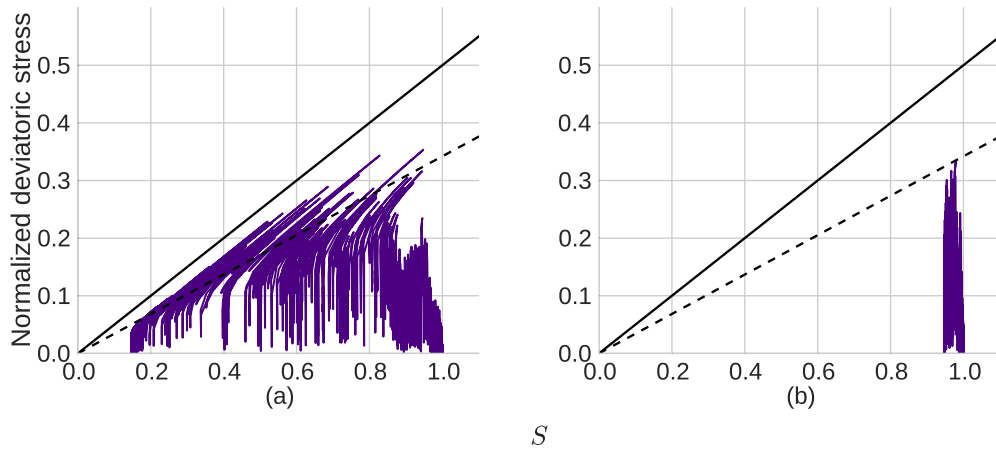
Fig. 3.35 (a) Deviatoric plan for point at GL-2.75 m, (b) Deviatoric plan for point at GL-5 m of the OP model with failure line (solid line) and phase transformation line (dashed line).
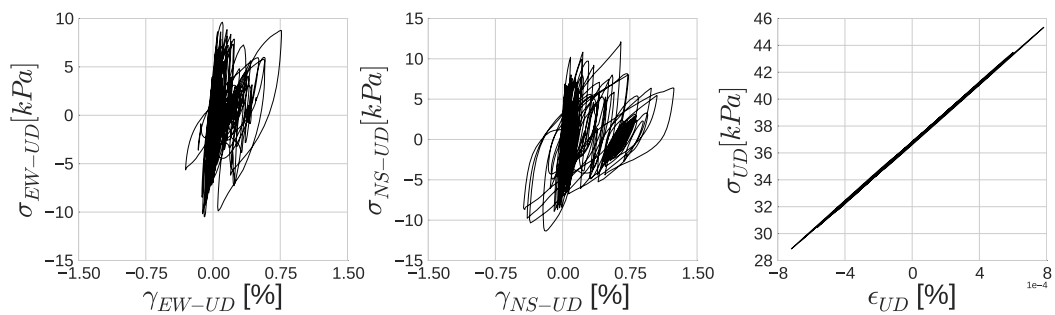
Fig. 3.36 Stress-strain curves on EW-UD component (left), NS-UD component (middle) and UD component (right) for point at GL-2.75 m of the OP.
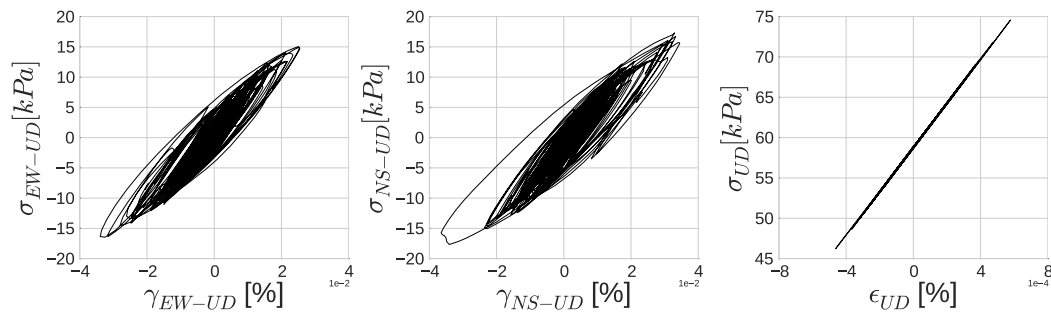
Fig. 3.37 Stress-strain curves on EW-UD component (left), NS-UD component (middle) and UD component (right) for point at GL-5 m of the OP.

In this site model, differently than other sites, we see highly dilatant soil behavior from the initial seconds to the end of loading. We show how soil behavior could change strongly on different layers in the same site. In this sense, simulations with the 1D-3C SEM code help us to explore possible differences in soil response under different loading conditions such as the input motion in OP site that leads to high shear work accumulation in the soil. In next section, we analyze the wave propagation in the OP site for different considerations of soil constitutive model.

Influence of material rheology on wave propagation

Similarly to other sites, the influence of soil rheology is analyzed comparatively on the OP site. First, total stress and effective stress analyses are compared. Figure 3.38 displays the surface acceleration on three directions for both approaches on [90-120] seconds time interval. Starting from 100 seconds where the dilatancy effect is seen in surface motion, signal is dominated by high-frequency motion in effective stress analysis on horizontal directions. In Figure 3.39, two analyses are compared in frequency plan. On horizontal directions, in effective stress analysis the motion over 4 Hz is attenuated relatively and for frequencies less than 2 Hz, a slight amplification appears. In surface motion of OP site, dilatancy is evoked rather by peaks with high amplitude and differently than other two sites studied in this chapter high period wave forms are less frequent. Accordingly, in acceleration spectra, differences are more apparent in high frequency motion. Amplification in low frequency is not significant. On vertical direction, both approaches result in a strong peak around 10 Hz whereas observed motion demonstrates more nonlinearity by the peak shifted towards 2.5

Hz and lower energy level. In Figure 3.40, maximum strain profiles corresponding to two approaches are compared. Similarly to Kushiro site where the maximum strain overall the model does not exceed 1%, in OP site effective stress analysis leads the liquefiable soil to approximately 10 times larger strain. While in the second layer both approaches differ by this amount, in the third layer, where no significant pore pressure change is noted, total and effective stress analyses give similar results. Also, outside of the second layer, in all other layers an additional damping on EW-UD and NS-UD components is seen in effective stress analysis. These conclusions are consistent with the analyses in KP and WRLA sites.
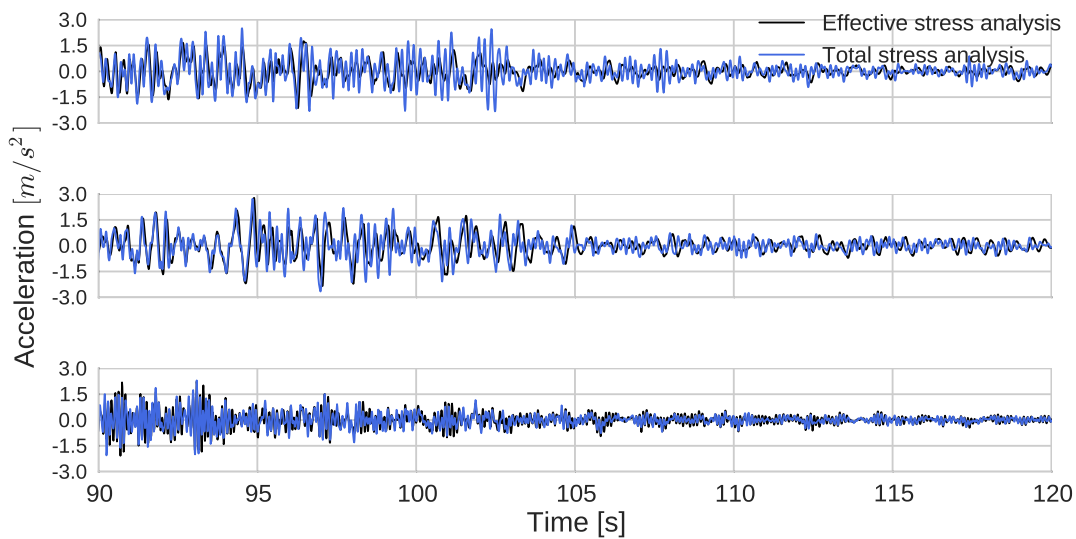
Fig. 3.38 Surface acceleration time histories on [90-120] seconds time interval for three directions for the simulation without pore pressure effects (in blue) and with pore pressure effects (in black) at the OP.
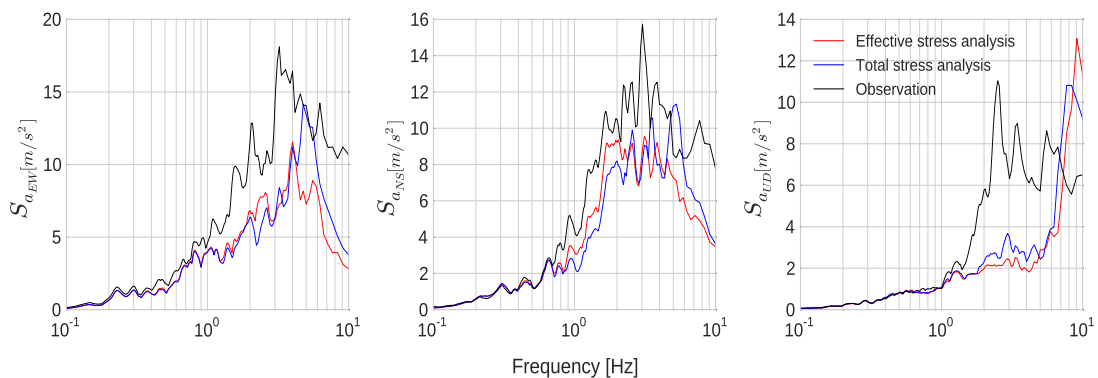
Fig. 3.39 Acceleration spectra of recorded surface acceleration (in black), visco-elastoplastic SEM simulation with excess pore pressure development (in red) and without excess pore pressure development (in blue) for EW component (left); for NS component (right)
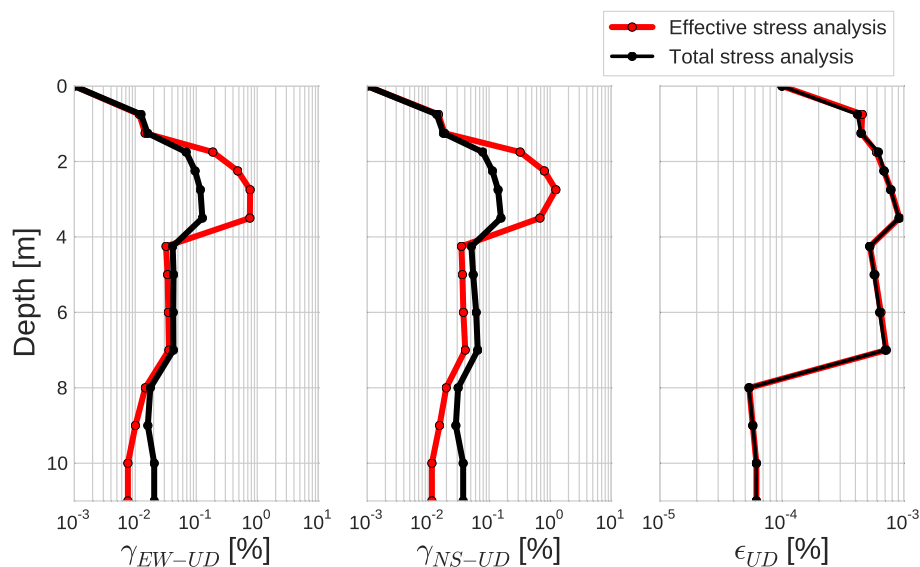
Fig. 3.40 Comparison of maximum strain profiles as a function of depth between visco-elastoplastic simulations with excess pore pressure development (in red) and without excess pore pressure development (in black) for EW-UD (left) and NS-UD (right) components.

In addition to effective and total stress analyses, elasticity, viscoelasticity and elastoplasticity models are compared by design spectra in Figure 3.41. Models differ mostly by high frequency interval where energy is damped significantly. For frequencies below 1 Hz, no remarkable difference is noted. In high frequency range, energy content is highest in elasticity and it is attenuated in viscoelasticity and in nonlinearity (elastoplasticity and visco-elastoplasticity) with shift of peak from 6.5 Hz to 5 Hz in EW and NS components. On UD, all the models attenuate the energy content in elasticity with no shift. In Figure 3.42, maximum strain profiles are shown for all models on three directions. The general tendency is to decrease strain with viscous and nonlinear damping (without pore pressure effects). Yet, in relatively more rigid soil layer (layer 4 on [GL-7 - GL-11] m depth), strain increases in nonlinearity compared to viscoelasticity. With pore pressure effects, nonlinear model results

in higher damping in non-liquefiable soil layers (layers 1 and 4) and remarkable increase in deformation of liquefiable soil layer 2 ([GL-1.25,GL-3.5] m depth) where soil behavior is influenced by pore pressure changes.
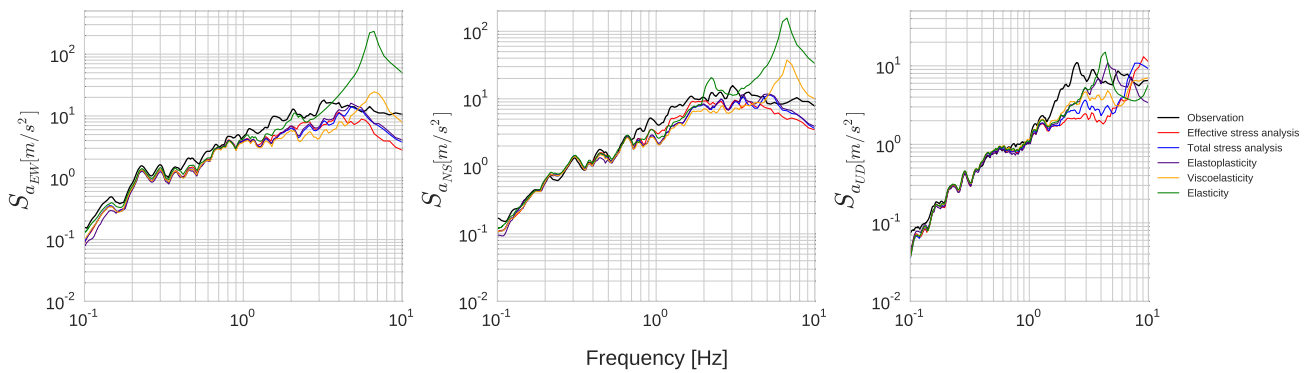
Fig. 3.41 Spectral acceleration comparison between elastic (in green), viscoelastic (in orange), elastoplastic (in purple), visco-elastoplastic with no excess pore pressure development (in blue) and visco-elastoplastic with excess pore pressure development (in red) models for three components of Kushiro Port site.
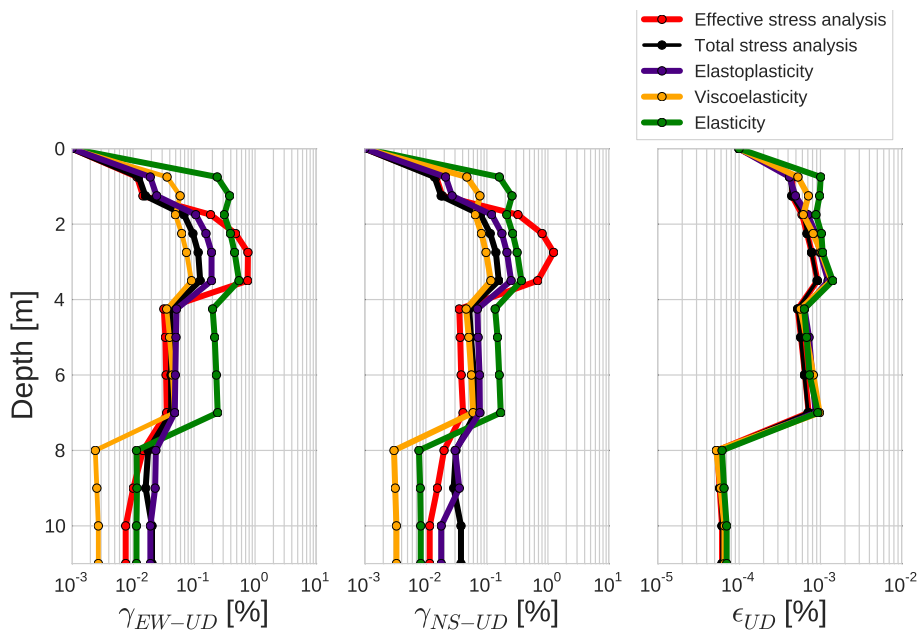
Fig. 3.42 Maximum strain profile of elastic (in green), viscoelastic (in orange), elastoplastic (in purple), visco-elastoplastic with no excess pore pressure development (in blue) and visco-elastoplastic with excess pore pressure development (in red) models for three components of Kushiro Port site.

Uniaxial vs Triaxial loading

On the strongest motion direction (EW) at OP site, soil response is compared for uniaxial and triaxial loading conditions. Figure 3.43 shows surface acceleration, velocity and displacement for two analyses. In all the variables, two approaches give very close results. When the results are displayed on [90-100] seconds time interval (See Figure 3.44), only very small differences are remarked on all variables. As in Kushiro Port model, no difference is noted in surface displacement under uniaxial and triaxial loading. In Figure 3.45, stress-strain curves and pore pressure temporal change are compared for GL-2.75 m. Under triaxial loading, actual pore pressure change is approximately 2 times higher than uniaxial loading. As a result, soil becomes more dilatant under triaxial loading and stress-strain loop expands with continuous rigidity change. However, maximum deformation with higher nonlinearity under triaxial loading is less than 1 %. Similarly to KP site, higher nonlinear behavior under triaxial loading with limited strain level in the liquefiable soil does not influence surface motion considerably. On the other hand, strain level in the liquefiable soil layer is 8 times greater under triaxial loading.
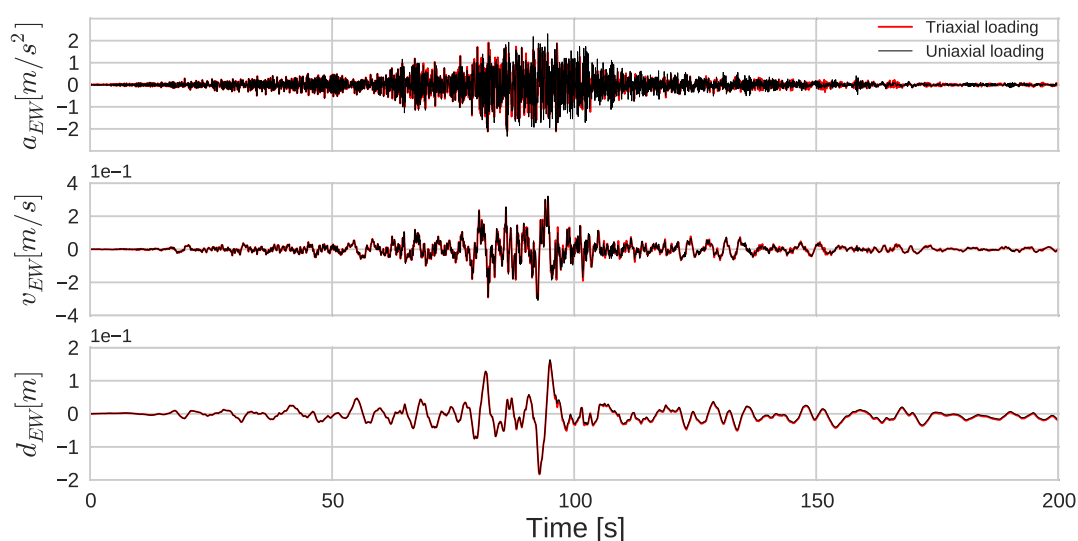
Fig. 3.43 Surface acceleration (top), velocity (middle) and displacement (bottom) comparison between uniaxial (in black) and triaxial (in red) loading for EW component.
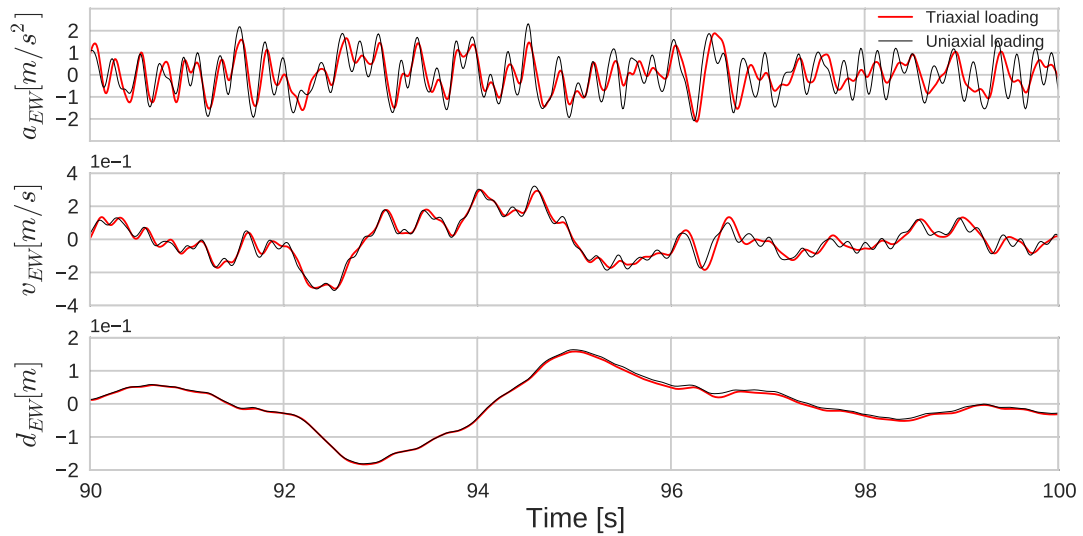
Fig. 3.44 Surface acceleration (top), velocity (middle) and displacement (bottom) comparison between uniaxial (in black) and triaxial (in red) loading for EW component.
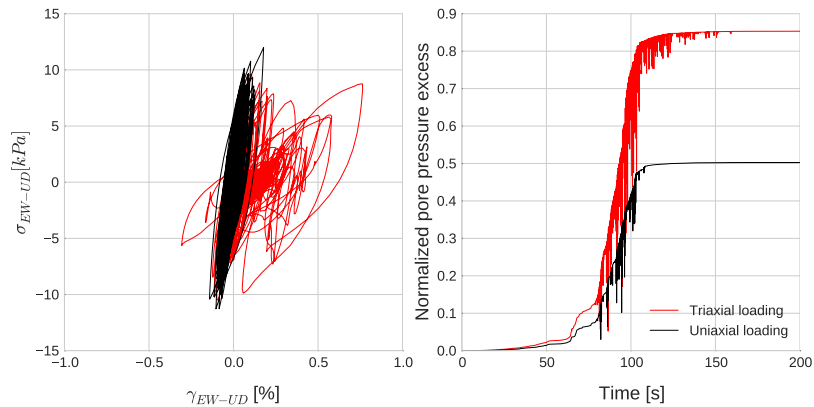
Fig. 3.45 (a) Stress-strain curve comparison between uniaxial (in black) and triaxial (in red) loading results for EW-UD component at GL-2.75 m, (b) Excess pore pressure vs time comparison between uniaxial (in black) and triaxial (in red) loading results at GL-2.75 m.

Conclusions

As last application of the 1D-3C SEM code to real models, we studied the Onahama Port, which is influenced by the 2011 off the Pacific Coast of Tohoku earthquake. OP model is

composed of 4 different soil layers where the second and third layers are liquefiable. Surface and borehole ground motion records for 200 seconds are used. In surface acceleration, motion starts to display dilatant behavior towards 100 seconds with longer period waves followed by sudden peaks with very high amplitude. Despite of some amplitude differences, observed ground motion is partially reproduced by visco-elastoplastic soil model including pore pressure generation in cohesionless soil layers. It is shown that in the third layer, pore pressure development is not very significant. Differently than other sites (WRLA and KP), in OP soil behavior in cohesionless soil is highly dilatant. For this reason, strength recovery is quite frequent and the dilatancy effect is dominant in high frequency motion of slightly large-span wave forms followed by high peaks. Effective stress analysis differs from other rheologies by strong high frequency damping and frequency shift in OP site. Also, maximum strain increases remarkably in dilatant soil layer and additional damping in other layers are obtained. Lastly, in dilatant soil layer, it is shown that pore pressure increases 2 times more under triaxial loading and soil behavior becomes more dilatant. Yet, due to limited deformation range, this dilatancy change is not seen in surface motion.

3.4   Conclusions

A one-dimensional three-component geomechanical model has been implemented under the numerical scheme of the spectral element method. Soil rheologies that can be studied by the developed 1D-3C SEM code vary from linear, viscoelastic to nonlinear models. It couples the nonlinear hysteresis of Iwan (1967) model with viscous damping. The influence of excess pore pressure development in liquefiable soils is also taken into consideration by Iai et al. (1990) [69] model which requires only few parameters.

The developed 1D-3C SEM code is applied on three real liquefaction site models: Wildlife Refuge Liquefaction Array (WRLA), Kushiro Port (KP) and Onahama Port (OP), which are affected by 1987 Superstition Hills, the The 1993 Kushiro-Oki and The 2011 off the Pacific coast of Tohoku earthquakes, respectively. The simulated ground motion acceleration on three directions matches well with the observations in WRLA. Spiky behavior of the acceleration is reproduced successfully and related to pore pressure changes in the liquefiable soil layer. Following the satisfactory results, we used the 1D-3C SEM code for further exploration of the soil behavior under different conditions. We have shown that neglecting of pore pressure effects in soil may result in ground motion with very different frequency content. Calculated motion without including pore pressure effects overestimates high frequency motion and amplification of low frequency motion is neglected. Under excess

pore pressure development effect, waves could be trapped in liquefiable soils where the soil strength changes continuously and the medium velocity gets lower. The outgoing waves could be attenuated more with higher nonlinearity in liquefiable soils. As a result of rigidity loss, such soils can undergo very large deformations. Outgoing waves can have highly damped large-span forms. On the other hand, with strength hardening due to dilatant behavior, sudden strong peaks can be seen in transmitted waves.

The same analyses are performed on KP model. In this site, due to the lack of data for P velocity profile, inconsistency is induced on vertical direction. While we are able to model the vertical motion in Wildlife Refuge Liquefaction Array where soil properties are determined comprehensively, the irrelevancy in the results of KP site reveals the importance of a complete site characterization in wave propagation studies using three components. Moreover, by comparing different rheological models at all sites, nonlinearity is shown to bring up more attenuation and frequency shifts in surface motion energy content on horizontal directions. Yet, these nonlinearity-related changes are not homogeneous all over the concerned frequency band and depends strongly on model properties. In all the sites, effective stress analysis leads to a tendency of significant increase in deformation range of liquefiable soil layers, where soil dilatancy changes continuously, and additional damping on other layers. Also, with effective stress analysis, high frequency damping and low frequency amplification are obtained at KP model similarly to Wildlife Refuge Liquefaction Array model. For OP model, the influence of effective stress analysis is seen mostly on high frequency motion. This shows that the influence of cohesionless soil behavior on wave propagation is highly dependent on model properties and loading conditions. Additionally, we have compared uniaxial and triaxial loading approaches on three models for the strongest ground motion direction. It is concluded that the soil becomes more nonlinear under triaxial loading and higher nonlinearity results in more rapid rise in pore pressure excess. Soil becomes more dilatant due to this increase in nonlinearity. For this reason, consideration of multiaxial interaction and pore pressure excess is recommended for a realistic modeling of seismic wave propagation. Also,resultant deformation at surface may be very high under triaxial loading as in case of the WRLA model. Yet, for cases with low level of ultimate strain (e.g.less than 1 %), this effect in surface displacement may not be seen.

This study shows the possibility of modeling nonlinear soil behavior including pore pressure effects in seismic wave propagation studies by coupling different models. We need three elastic parameters (pressure and shear wave velocities and density) and three parameters for nonlinearity (failure line angle, cohesion and coefficient of Earth at rest). When excess

pore pressure development is taken into account, we need five parameters that can be obtained by laboratory tests or numerical analyses (ϕ_p, w_1, p_1, p_2 and S_1). As in the real applications in this chapter, we are able to model soil behavior in different sites where soil is initially isotropically consolidated (WRLA and OP) or anisotropically consolidated (KP) and very superficial soil models (WRLA and OP) or deep models with many different soil composition (KP). It is an efficient tool for a better understanding of the influence of soil-related phenomena on 1D seismic wave propagation.

Chapter 4

2D P-SV and SH SEM wave propagation modeling: Code verification

2D P-SV and SH SEM wave propagation modeling: Code verification

4.1   Introduction

Following the satisfactory results obtained with the 1D-3C SEM code, the code is extended to a multi-dimensional case. For this purpose, the 2D spectral element method based code SEM2DPACK (version 2.3.8) is used. The code is started to be developed during the PhD theses of Dimitri Komatitsch and Jean-Paul Ampuero at the Institut de Physique du Globe de Paris (IPGP). It is open to researchers for further development and contributions. All the versions of the code are available in http://sourceforge.net/projects/sem2d/files/sem2dpack/ address. SEM2DPACK provides 2D P-SV and SH modeling of wave propagation by accounting for different source rupture in a 2D medium. Some of the applications of SEM2DPACK cover the modeling of dynamic rupture on non-planar faults and seismic wave radiation (Madariaga et al., 2006), fault reflections from fluid-infiltrated faults (Haney et al., 2007), non-linear wave propagation in damaged rocks (Lyakhovsky et al., 2009), wave propagation around a prototype nuclear waste storage tunnel (Smith and Snieder, 2010),

benchmark for wave propagation in heterogeneous media (O'Brien and Bean, 2011 [119]) and dynamic rupture model of the 2012 off-Sumatra earthquake (Meng and Ampuero, 2012 [108]).

SEM2DPACK offers to users different options of boundary conditions and source mechanics related to different fault mechanisms. It focuses on seismic wave propagation after a given source mechanism in a media without taking into account the site effects related to the soil mechanics in superficial soil layers. For a more detailed information, the reader is invited to refer to the supplied manual of SEM2DPACK. In this section, we implement the same soil rheologies presented and used in the previous chapters (Chapters 1-3 for implementation of viscoelasticity, nonlinearity and pore pressure effects) to SEM2DPACK. In addition, in order to recreate the identical conditions in 1D examples used in the previous chapters, different boundary conditions are also implemented in the 2D SEM code. It must be noted that in SEM2DPACK there exist several options for time integration schemes (explicit Newmark, explicit HHT-alpha, quasi-static and leap-frog time integration schemes). In this study, all the implementations in the code are applicable only to the models using 'leap-frog time scheme'.

In following sections, first, the implementations of borehole boundary condition, incident wave velocity field and absorbing boundary condition are explained and related verification tests are shown. Second, implementation and verification of nonlinear and viscoelastic rheologies take place. Lastly, the developed 2D SEM code is compared to the 1D-3C SEM code by means of results on the real models of Volvi (Greece) and Wildlife Refuge Liquefaction Array (USA) sites. The developed 2D SEM code is able to handle P-SV and SH wave propagation problems by considering different soil constitutive models for the media. The mesh is required to consist of quadrilateral elements in SEM2DPACK. The code provides sufficient environment for generating basic meshes and does not include a built-in unstructured mesh generator for complicated models with realistic geometries. For such models, external software (such as EMC2, GMSH, CUBIT) could be used.

4.2   Implementation of boundary conditions

4.2.1   Borehole boundary condition

The implementation of borehole condition is done in a way that the defined boundary must be horizontal or vertical. Once the boundary condition is chosen as borehole condition, the

velocity field to be imposed on the borehole condition is given by a file on which velocity values on x and z directions for P-SV wave propagation or on y direction for SH wave propagation are given with corresponding time steps.

For the purpose of verification of this implementation, the one-layered canonical model of P1 is used (detailed in Chapter 2.3.2). The two-dimensional P1 model (Figure 4.1) is created by using 4 square elements, each of which has a depth of 5 m and a width of 5 m. 5 GLL points are used on each element similarly to 1D model. Since there is no gradient on horizontal direction (x), we reanimate the one-dimensional conditions on a 2D model by choosing periodic boundaries at sides and free surface for upper boundary (for more detail about boundary conditions, See Chapter 1.2.3). Three stations are defined at each 5 meters of depth. Station coordinates can be found at Table 4.1.

As a first test, the P-SV wave propagation is performed by choosing 2 degree of freedom (ndof=2) under the Ricker signal imposed on x and z directions (same signal used in Chapter 2.3.2). In the second test, a single degree of freedom is chosen (ndof=1) so that the propagation is done only for SH waves (y direction). An elastic soil rheology is assumed for both tests to track numerical differences between studied cases. The input motion inserted at bottom of the model, on borehole condition, is propagated in the medium for 10 seconds. The results obtained with the 2D code are compared to the 1D code results.
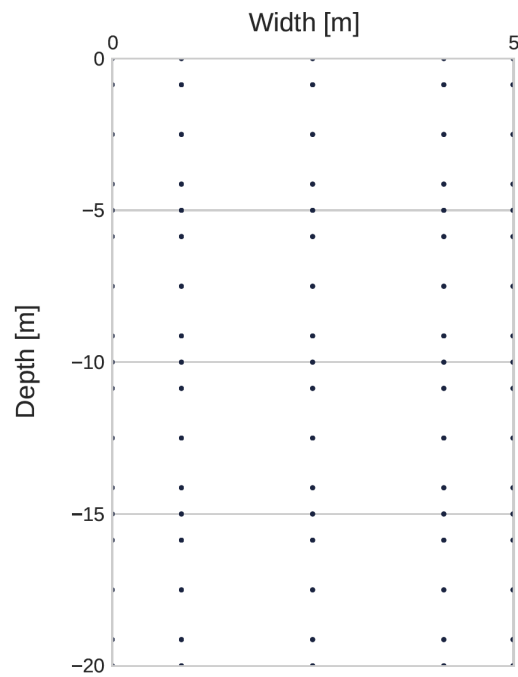
Fig. 4.1 Two-dimensional mesh used in 2D SEM code for P1 model, shown with GLL point distribution. Solid lines hold for elementary boundaries.

Table 4.1 Horizontal (x) and vertical (z) coordinates of the stations used in P1 model.

Station	x-coordinate [m]	z-coordinate [m]
S1	0.0	0.0
S2	2.5	0.0
S3	5.0	0.0
S4	0.0	-5.0
S5	2.5	-5.0
S6	5.0	-5.0
S7	0.0	-10.0
S8	2.5	-10.0
S9	5.0	-10.0
S10	0.0	-15.0
S11	2.5	-15.0
S12	5.0	-15.0
S13	0.0	-20.0
S14	2.5	-20.0
S15	5.0	-20.0

P-SV wave propagation

Figures 4.2-4.3 show velocity outputs of each station for horizontal and vertical directions, respectively. The input is inserted at GL-20 m. Under the loading on x and z directions, identical velocity values are recorded at each depth of the soil column. In horizontal component, at GL-20 m depth (Stations 13,14,15), velocity is equal to the incident wave field. The incoming energy is propagated towards the surface. Since the bottom boundary is defined as borehole condition, the waves are reflected back so that the surface motion is dominated by continuous reflections until the end of the simulation (10 seconds). On vertical component, similarly to horizontal component, wave field at GL-20 m is identical to the input motion. However, since the pressure wave velocity of the medium is greater than shear wave velocity (Table 2.4, $V_p = 700 m/s$ and $V_s = 300 m/s$), resultant amplitudes of the propagated waves with continuous reflections are different in two directions. Compared to 1D SEM code results on two directions for the same conditions on the same model, we obtain identical surface velocity values for both directions with the 2D SEM code (Figure 4.4).
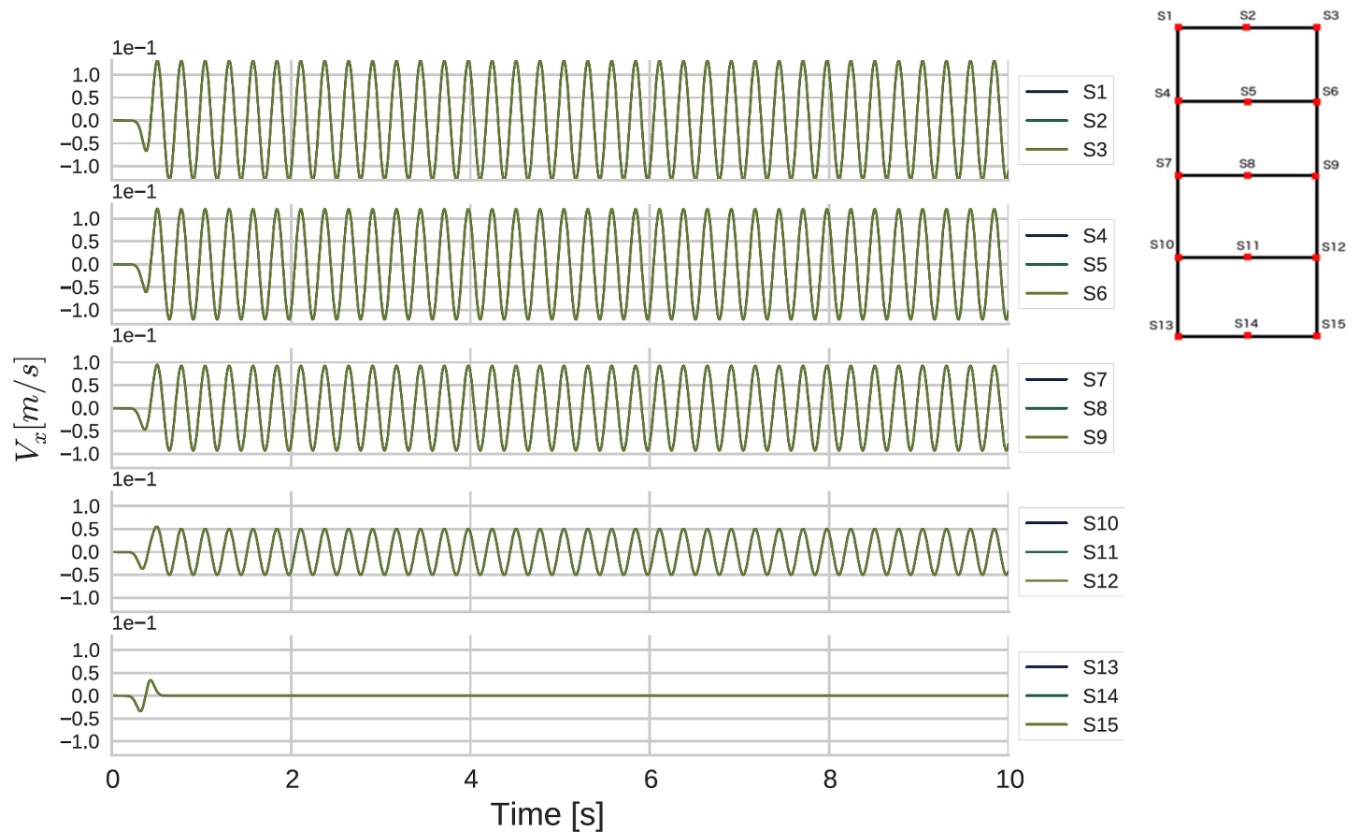
Fig. 4.2 Horizontal velocity outputs for all the stations of P-SV wave propagation model with borehole condition.
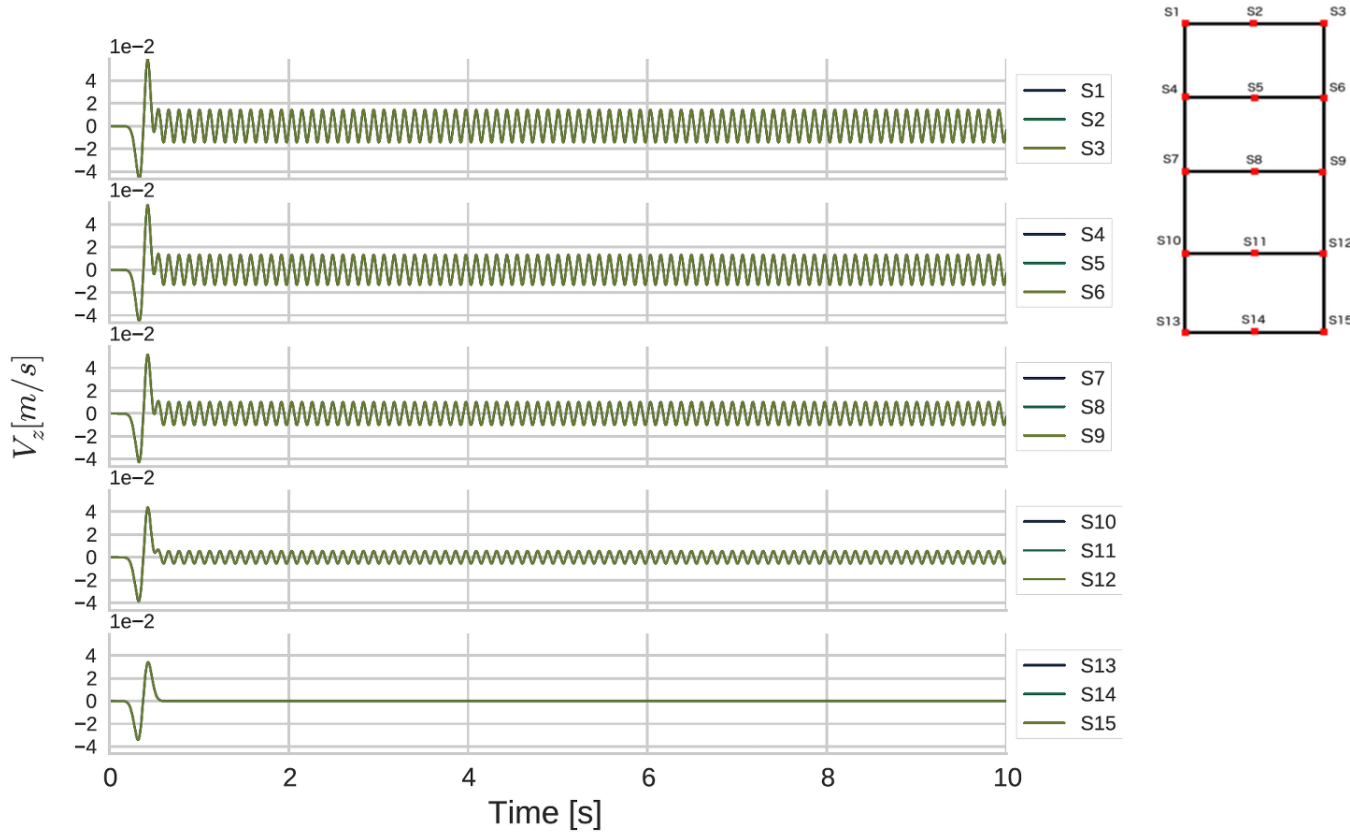
Fig. 4.3 Vertical velocity outputs for all the stations of P-SV wave propagation model with borehole condition.
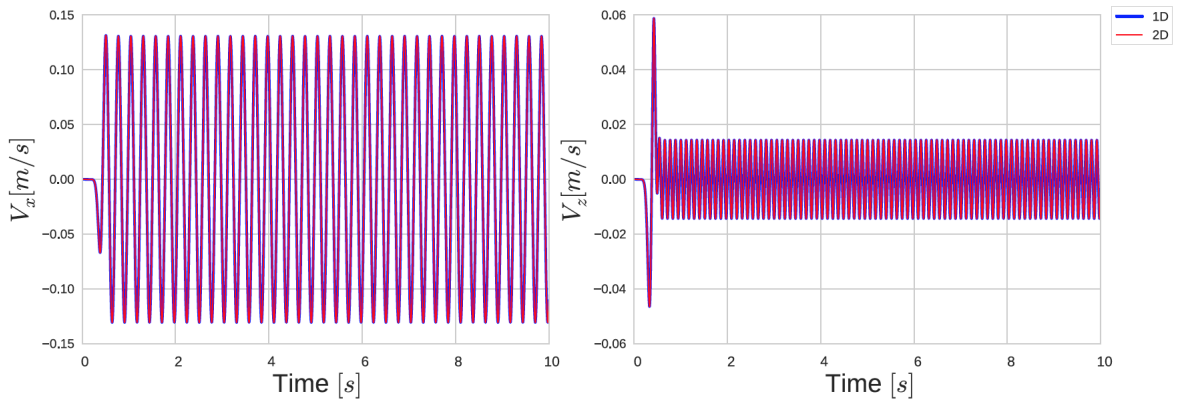
Fig. 4.4 Comparison of velocity outputs on horizontal (left) and vertical (right) directions of P-SV wave propagation model with borehole condition between 1D (in blue) and 2D (in red) SEM codes.

SH wave propagation

This test is performed for SH wave propagation by setting the degree of freedom as 1. The same input motion is imposed on y direction and propagated in the same medium for 10 seconds. The resultant motion is the same for each station at different depths (Figure 4.5). The velocity field recorded at the surface is identical to the horizontal velocity of 1D SEM code (Figure 4.6), and therefore to the SV case (horizontal direction in P-SV model) previously presented.
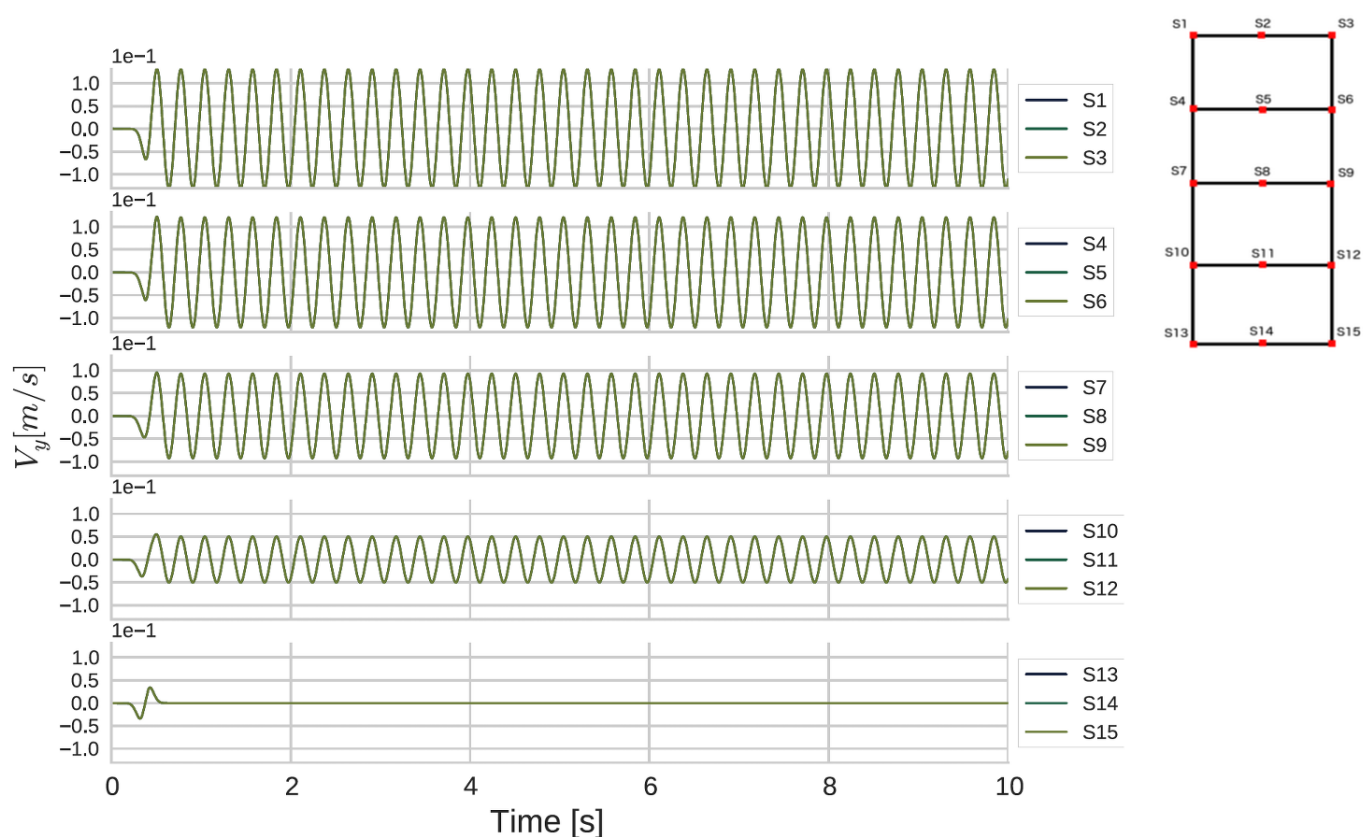
Fig. 4.5 Horizontal velocity outputs for all the stations of SH wave propagation model with borehole condition.
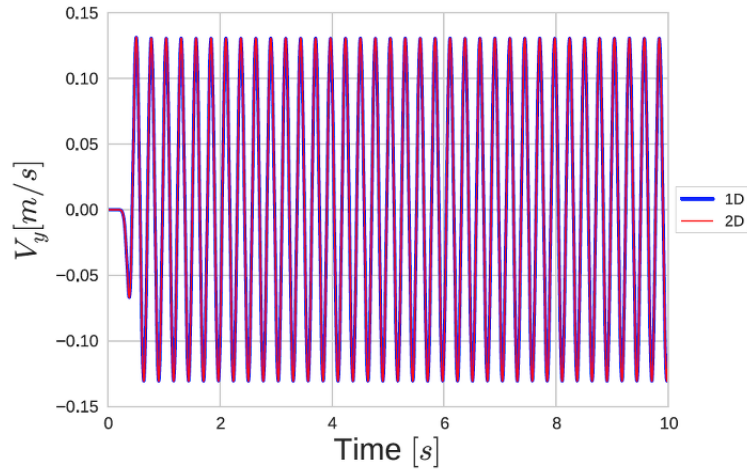
Fig. 4.6 Comparison of velocity outputs on horizontal direction of SH wave propagation model with borehole condition between 1D (in blue) and 2D (in red) SEM codes.

Based on the agreement between the 1D and 2D SEM code results, we conclude that the implementation of the borehole condition on 2D SEM code for P-SV and SH wave propagation models is verified.

4.2.2 C-PML implementation with incident wave field

In this section, the implementation of incident wave field to be used with absorbing boundaries is explained. We recall that original 2D SEM code SEM2DPACK offers different types of absorbing boundaries and it is also possible to define an incident wave field on absorbing boundaries of SEM2DPACK by source time functions. However, it is not possible to define an incident wave field directly by velocity parameter (velocity file including input velocity as a function time). Moreover, energy attenuation of propagating waves in the medium is approximated by means of C-PML (Classical Perfectly Matched Layer) type absorbing layers (C-PML is detailed in Chapter 1.2.3).

For all the constitutive models implemented in SEM2DPACK in this PhD thesis (viscoelasticity and nonlinearity), velocity is the main parameter in order to compute the corresponding force in the system (See Chapter 1.2.2). On the other hand, it must be noted that SEM2DPACK already offers elastic rheology which uses the displacement as main variable. For this reason, while the incident wave field is implemented, exceptionally for the domains with elastic rheology, source contribution by incident wave field is done by

displacement inside the code.

In the following, first, incident wave implementation by velocity field is explained and verified by comparisons with 1D SEM code results. Secondly, C-PML type absorbing layers are implemented and verified.

Incident wave field implementation

Incident wave implementation in 2D SEM code is based on the hypothesis of multiple point sources definition with identical wave field. All the points (including GLL points) at the depth by which the wave enters into the medium are defined with the same incident wave field, such that it mimics a 1D vertical plane wave incidence. Simply, the name of the file with the coordinates of those points is given in the input file.

P-SV wave propagation

A first test is done for P-SV wave propagation by using the two-dimensional P1 model. The upper and lower boundaries are defined as free surface. The lateral boundaries are again defined as periodic. The soil rheology is assumed elastic. The Ricker signal used in the previous section is used as input motion for both directions. The incident wave field is defined for all the points at 10 m depth (at the middle of soil column), so that wave propagation is upwards and downwards at the same time. Figures 4.7-4.8 display output velocities on each station for horizontal and vertical directions, respectively. All the stations located at the same depth record identical motion on both directions, so that the wave propagation is laterally identical. In horizontal direction, the incident wave field at GL-10 m is halved and one half is transmitted to upper nodes and other to lower nodes. Due to the properties of the code, two halves are inversely polarized. Therefore, the surface motion (Stations 1, 2 and 3) and the motion at bottom boundary (Stations 13, 14 and 15) are opposite. In addition, the reflected waves from upper and lower boundaries cancel out when they arrive to GL-10 m. Thus, the wave motion has zero amplitude after the first pulse at this depth and upward and downward propagating waves are reflected back. In vertical direction, the same manner of propagation (upward and downward propagation) is noted. Wave motion is canceled out with reflections due to the inverse polarization, so that each station has zero motion amplitude after 1 s.
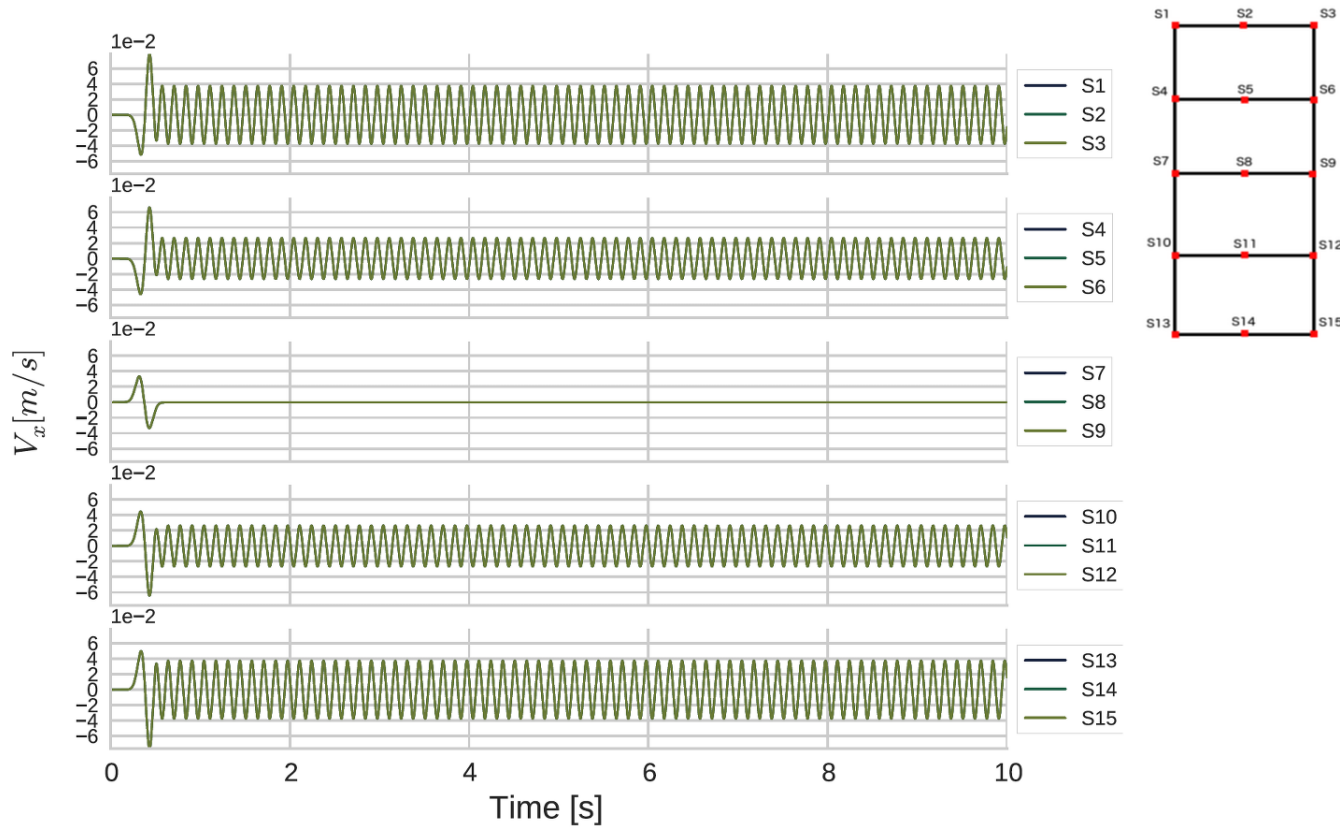
Fig. 4.7 Horizontal velocity outputs for all the stations of P-SV wave propagation model with incident wave field.
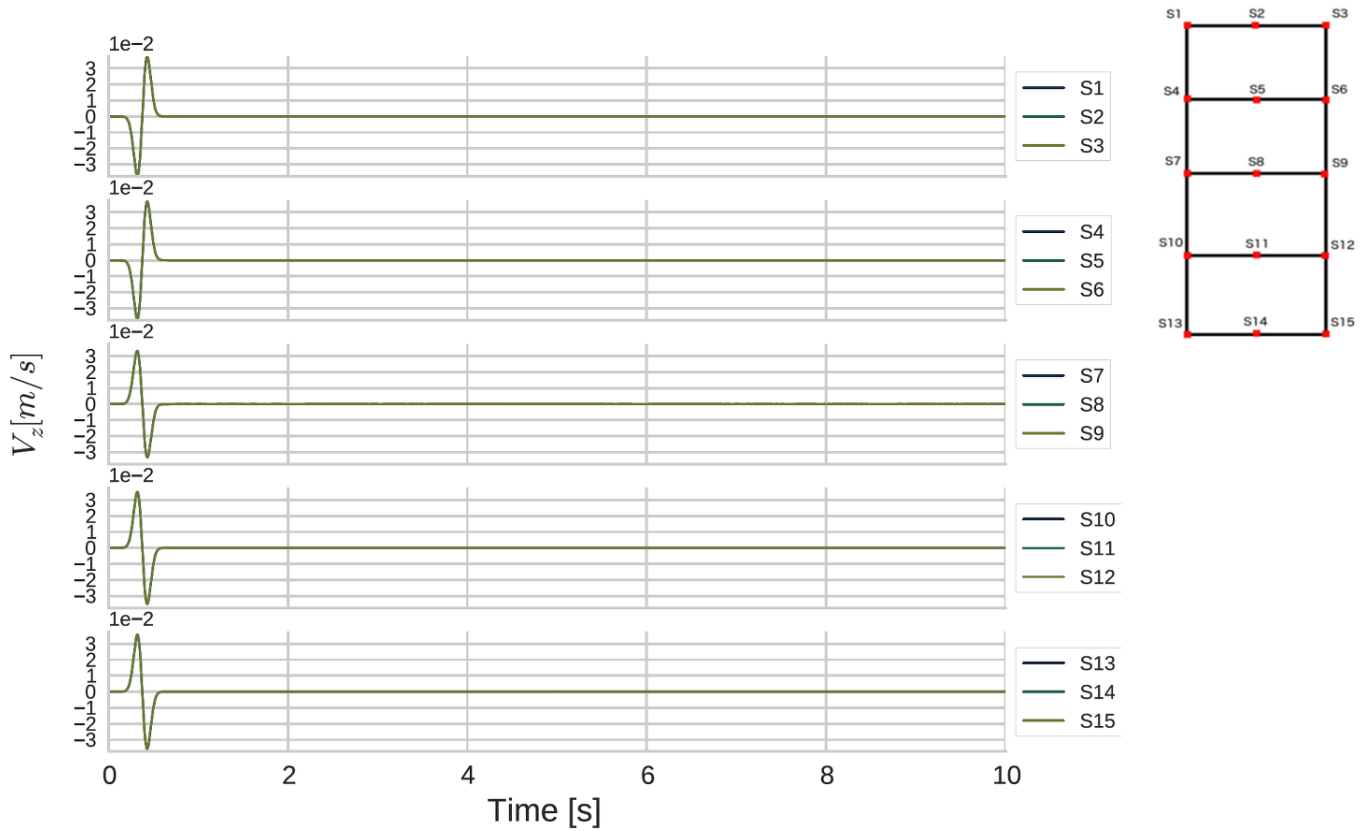
Fig. 4.8 Vertical velocity outputs for all the stations of P-SV wave propagation model with incident wave field.

In Figure 4.9, 1D and 2D SEM code surface velocity results are compared. The surface motion (z=0) in both directions is identical in 1D and 2D SEM codes.
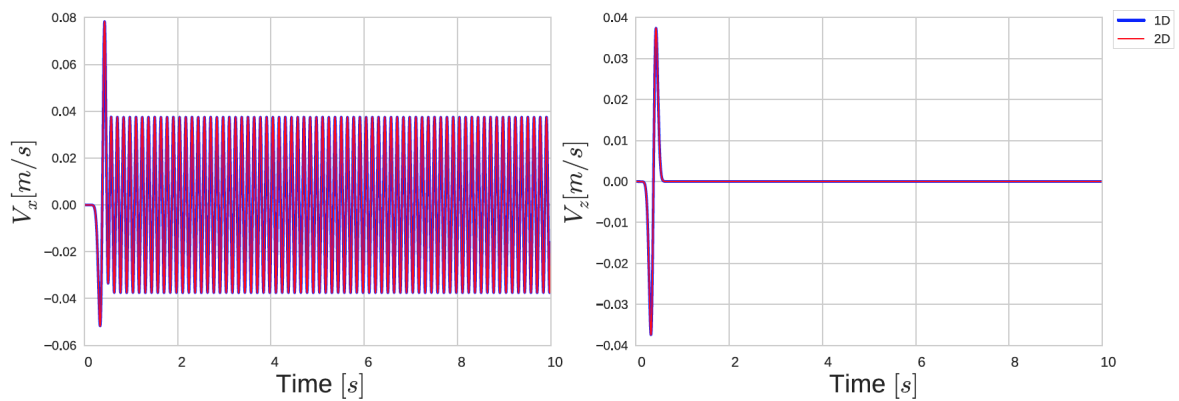
Fig. 4.9 Comparison of velocity outputs on horizontal (left) and vertical (right) directions of P-SV wave propagation model with incident wave field between 1D (in blue) and 2D (in red) SEM codes.

SH wave propagation

The previous test with free surface conditions on upper and lower boundaries is repeated for SH wave propagation. The incident wave is imposed on y direction with the same velocity values of Ricker signal. Satisfactorily, all the stations result in identical motion at each depth (Figure 4.10) and surface velocity is the same for 1D and 2D SEM codes (Figure 4.11).
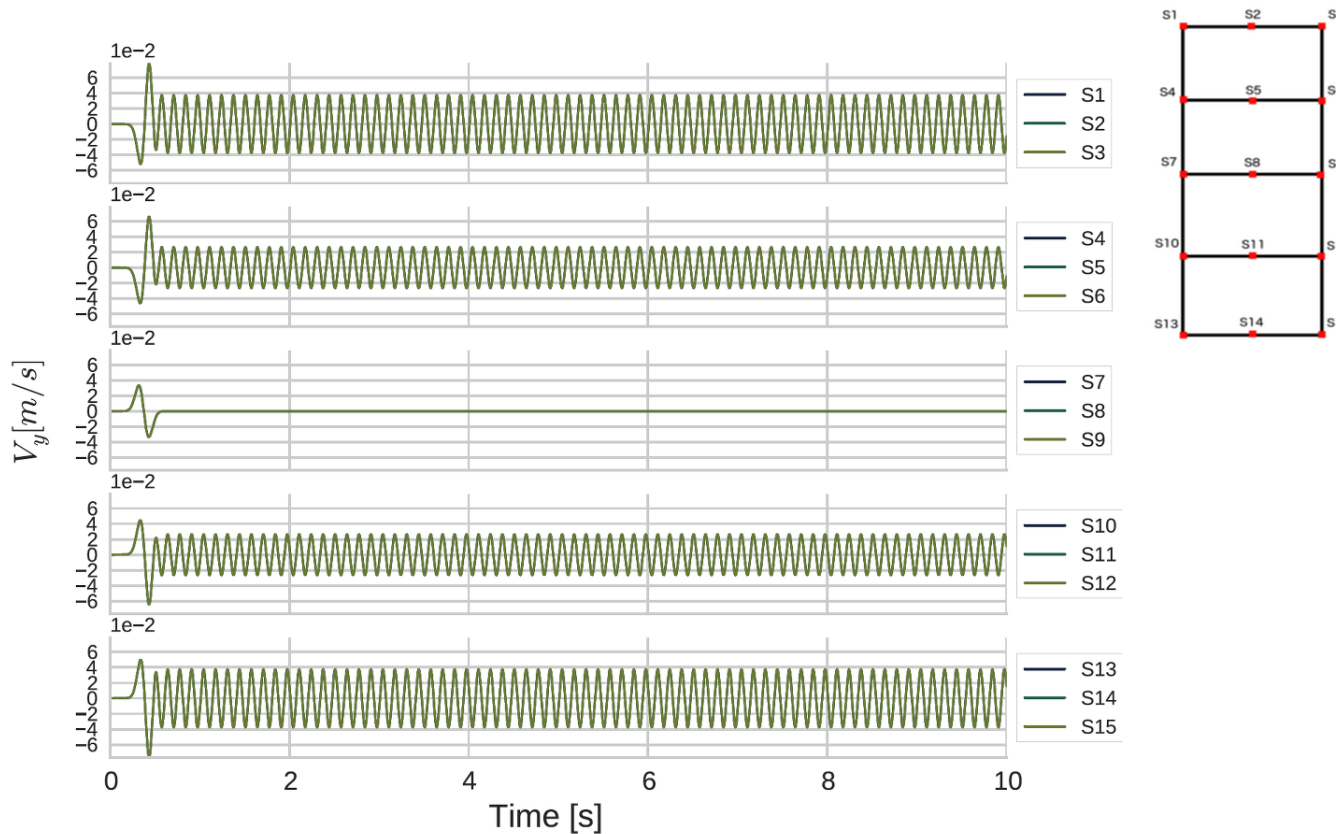
Fig. 4.10 Horizontal velocity outputs for all the stations of SH wave propagation model with incident wave field.
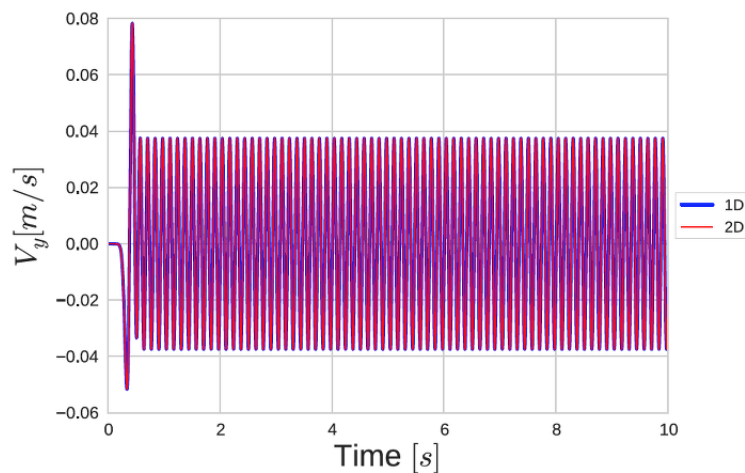
Fig. 4.11 Comparison of velocity outputs on horizontal direction of SH wave propagation model with incident wave field between 1D (in blue) and 2D (in red) SEM codes.

Under the light of these verification test results, the incident wave velocity field can be said to be well implemented in 2DSEMPACK for P-SV and SH wave propagation models.

C-PML implementation

The C-PML has been used in all the models with elastic rock wave attenuation of 1D analyses in this PhD thesis. The theory behind C-PML is briefly explained in Chapter 1.2.3. In its implementation into 2D SEM code, the attenuation is formulated only in vertical direction (z) with the possibility of selecting upward or downward orientation. Necessary parameters of A and n in Equation 1.17 are required in the input file with the orientation of attenuation. For C-PML used at bottom of the model, downward attenuation is chosen and for C-PML that overlies the model upward attenuation is used. Although we use C-PML only for elastic rock condition at bottom of the model, this option of upward/downward orientation is implemented for possible numerical uses in further studies. Moreover, it must be noted that the C-PML is not implemented as a boundary condition but as a material type. In the following sections, the verification test results are shown firstly for the use of a single C-PML element, secondly for the use of two C-PML elements.

Single-element PML analysis In this section, we use the 2D P1 model by defining the upper boundary as free surface and lower boundary as rigid. At this point, we recall that

C-PML is defined as material type and used with rigid boundary condition (See Chapter 1.2.3). An incident wave field is defined at 10 m. For the element located between 15-20 m depth, material type is defined as C-PML with parameters $n = 2$ and $A = 10$. Downward attenuation is selected. The tests are performed for P-SV and SH wave propagation models. An elastic medium is assumed.

P-SV wave propagation
In this test, the incident wave identical to previously used Ricker signal is defined at 10 m on both horizontal and vertical directions. As seen in Figures 4.12-4.13, the wave field is attenuated between 15-20 m depth and there is no oscillation at other depths for either direction. This shows the efficiency of C-PML use. Differently than Figure 4.7, since there is no reflected wave from bottom boundary, the reflected waves from surface continue to propagate to GL-15 m and they are attenuated. In vertical component, the motion is identical to horizontal component. Again, since there is no reflection from lower boundary differently than previous examples, after first reflection from free surface boundary at top of the model, waves are attenuated in 15-20 m depth interval.
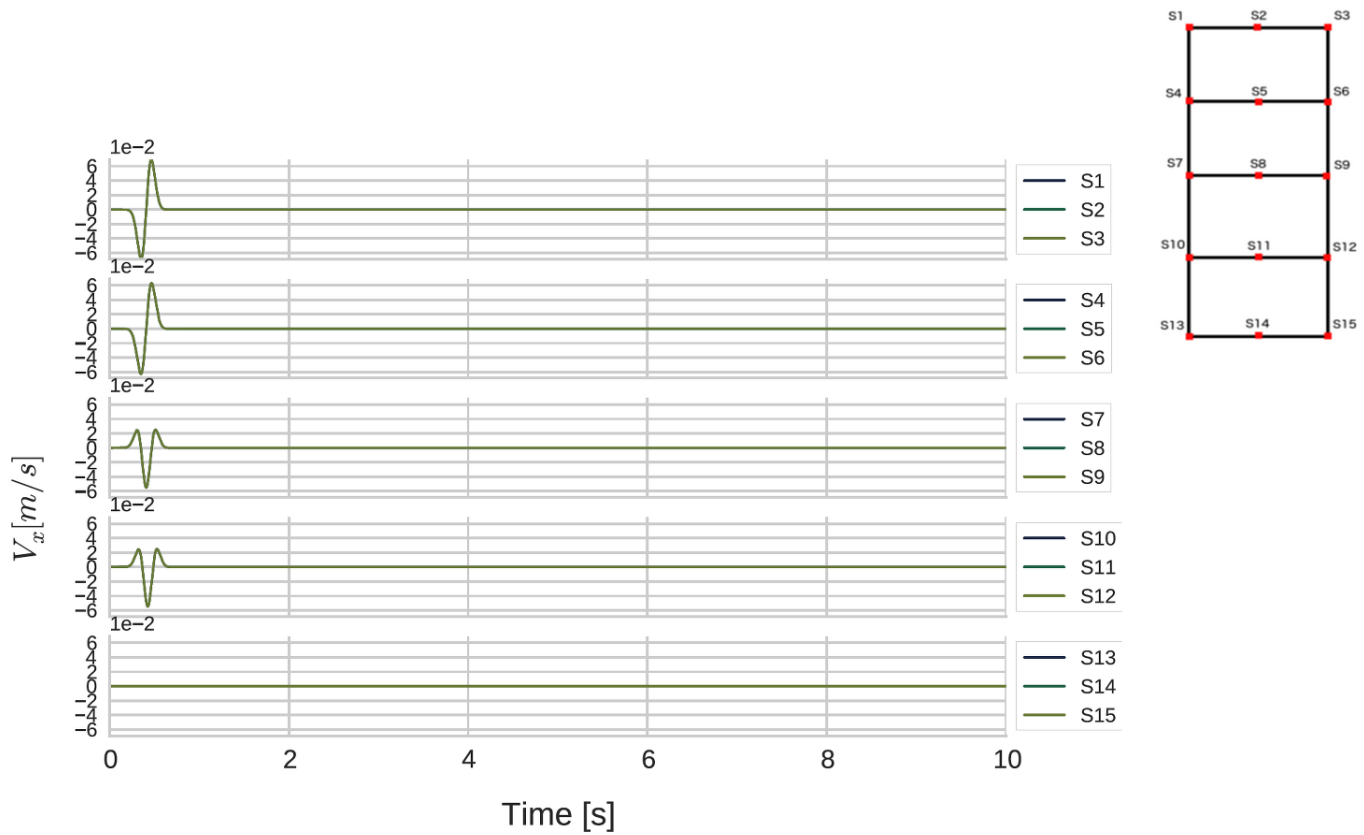
Fig. 4.12 Horizontal velocity outputs for all the stations of P-SV wave propagation model with single-element C-PML model.
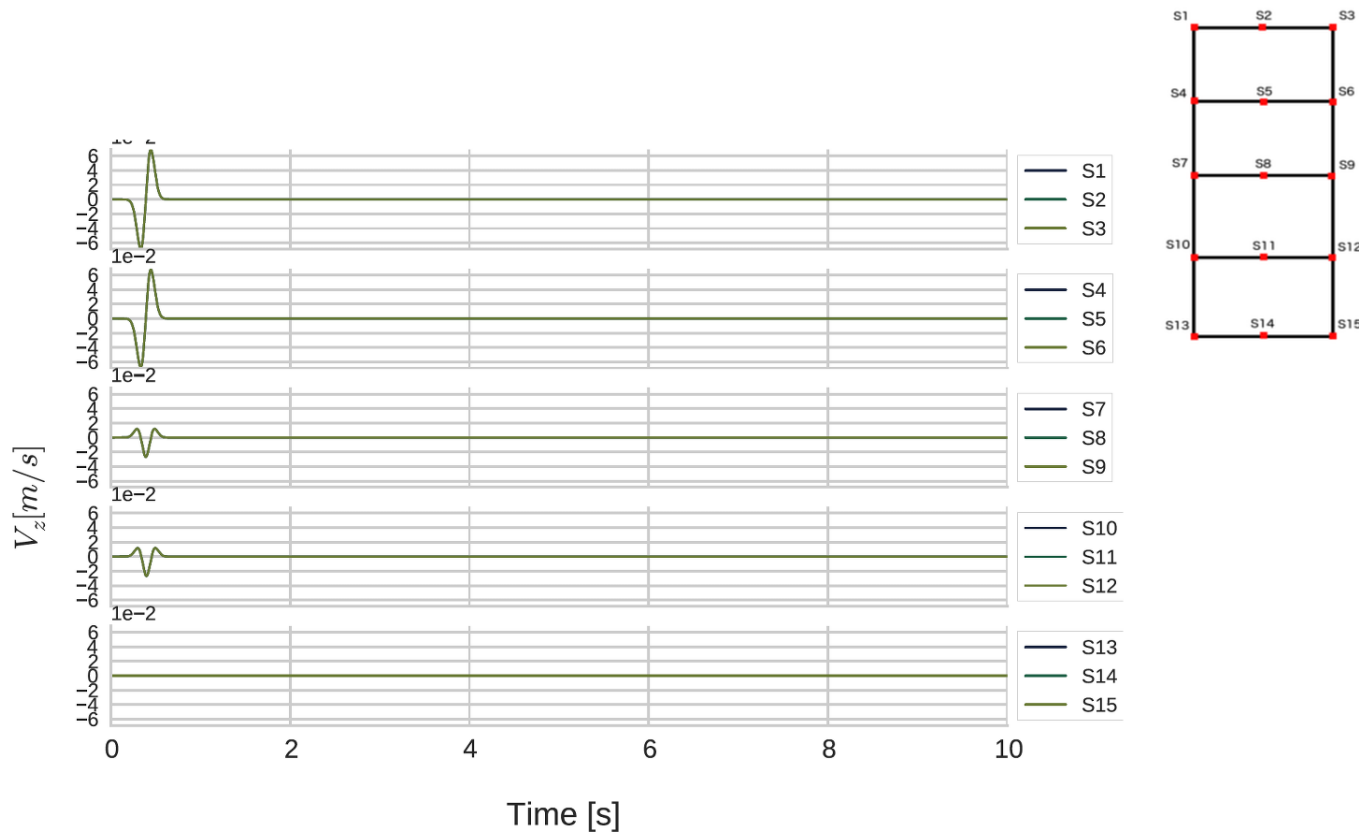
Fig. 4.13 Vertical velocity outputs for all the stations of P-SV wave propagation model with single-element C-PML model.

Additionally, comparing to 1D code outputs, 2D code results in identical surface velocity on both directions (Figure 4.14).
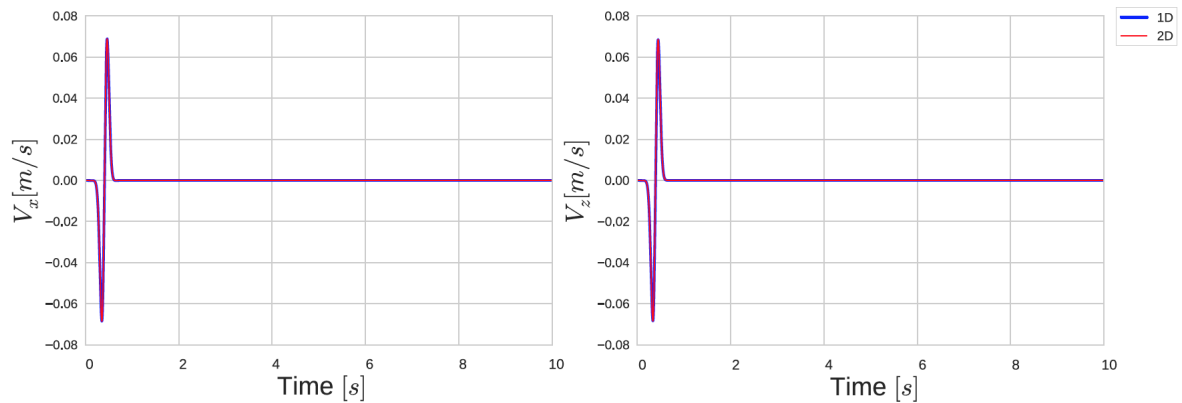
Fig. 4.14 Comparison of velocity outputs on horizontal (left) and vertical (right) directions of P-SV wave propagation model with single-element C-PML between 1D (in blue) and 2D (in red) SEM codes.

SH wave propagation

The previous test is repeated in this section for a single degree of freedom, so that the incident wave is defined on y component. In Figure 4.15, surface velocity on each station for y component is shown. The absorbing layer between 15-20 m depth attenuates the entering wave field so that the calculated surface motion is identical on 1D and 2D SEM codes in Figure 4.16.
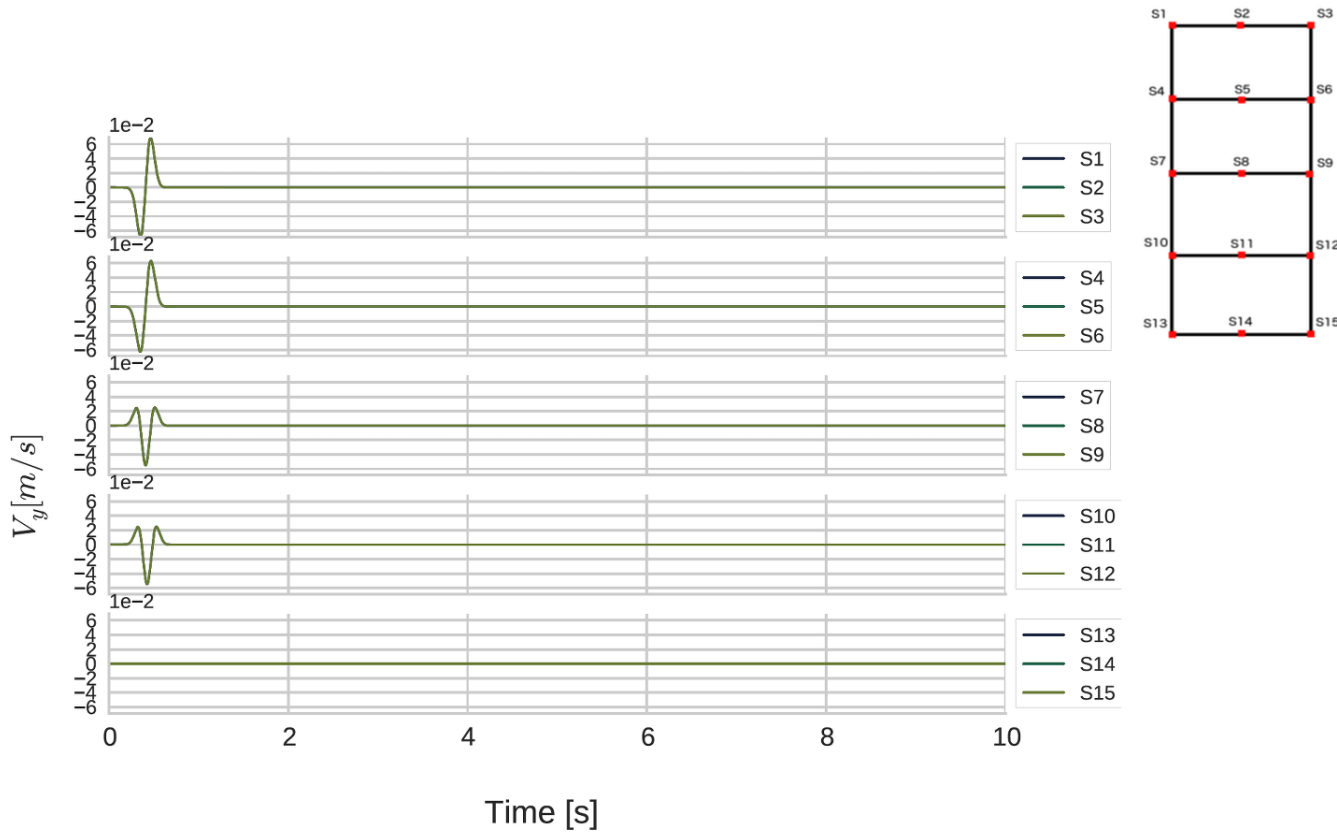
Fig. 4.15 Horizontal velocity outputs for all the stations of SH wave propagation model with single-element C-PML model.
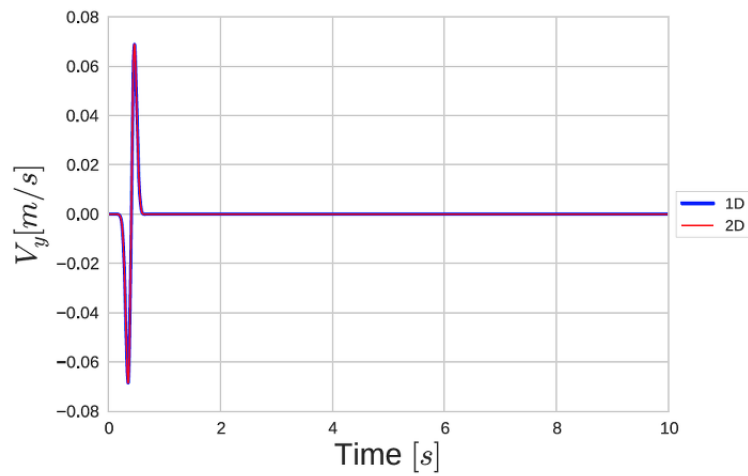
Fig. 4.16 Comparison of velocity outputs on horizontal direction of SH wave propagation model with single-element C-PML between 1D (in blue) and 2D (in red) SEM codes.

Two-element C-PML analysis   In this section, we use the two-dimensional P1 model by defining the upper boundary as free surface and lower boundary as rigid. An incident wave field is defined at 10 m. For the two elements located between 10-20 m depth, material type is defined as C-PML with parameters $n = 2$ and $A = 10$. Downward attenuation is selected. The tests are performed for P-SV and SH wave propagation models.

P-SV wave propagation

In this test, the incident wave identical to previously used Ricker signal is defined at 10 m on both horizontal and vertical directions. Figures 4.17-4.18 display velocity outputs on each station for horizontal and vertical directions, respectively. The wave field is attenuated starting from 10 m towards 20 m and there is no oscillation at other depths for either directions. The surface velocities on both directions are compared to the 1D code outputs. It must be noted that the 1D model uses a single element of C-PML between 15-20 m depth. Regarding Figure 4.19, we can conclude that the models with C-PML of single element and C-PML of two elements both attenuate incoming wave field efficiently.
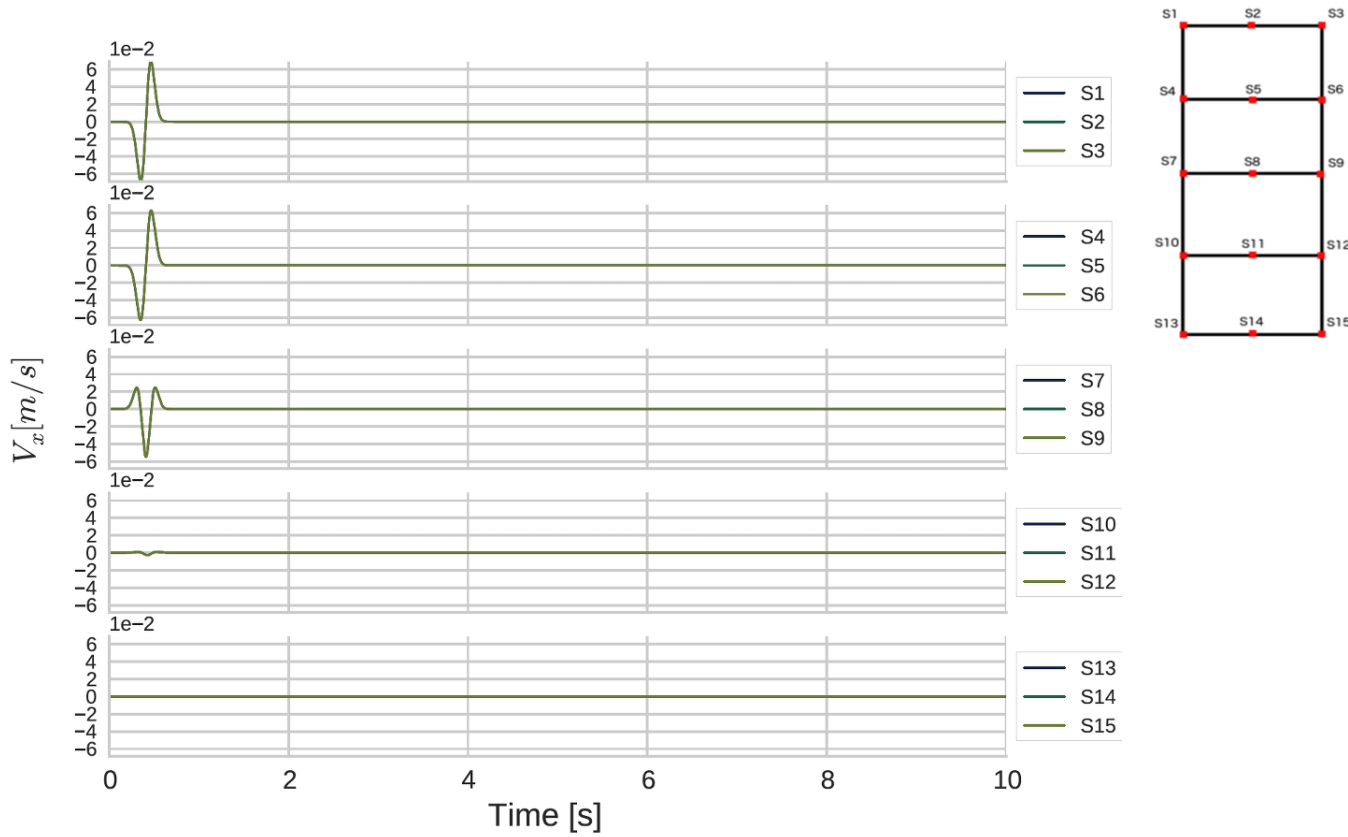
Fig. 4.17 Horizontal velocity outputs for all the stations of P-SV wave propagation model with two-element C-PML model.
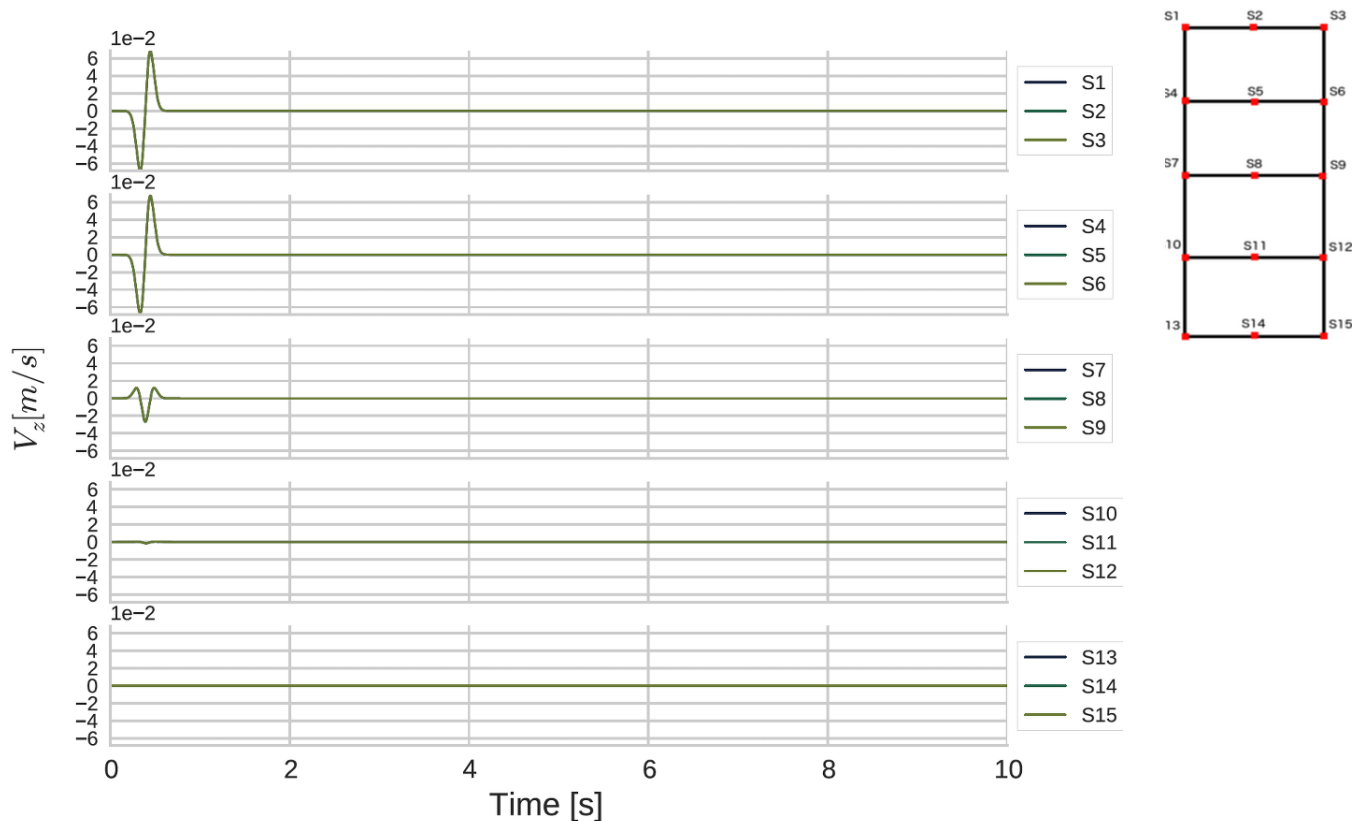
Fig. 4.18 Vertical velocity outputs for all the stations of P-SV wave propagation model with two-element C-PML model.
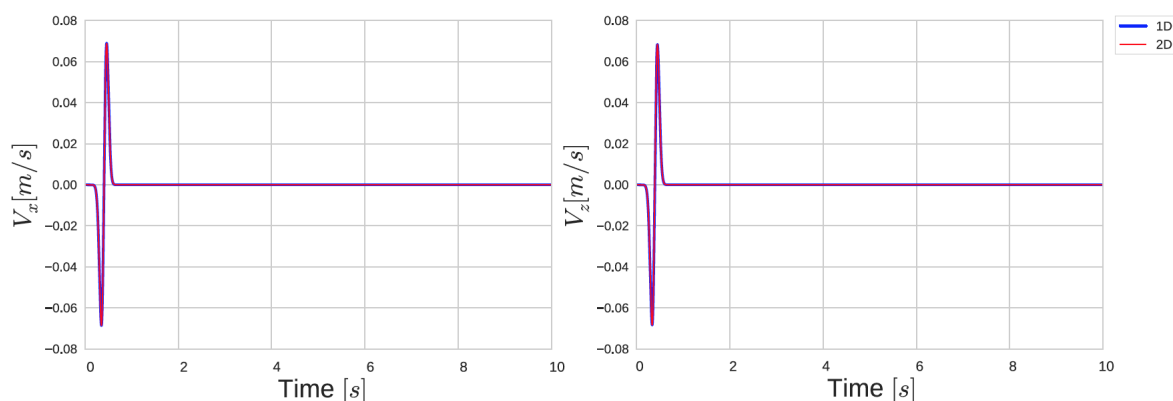
Fig. 4.19 Comparison of velocity outputs on horizontal (left) and vertical (right) directions of P-SV wave propagation model with two-element C-PML between 1D (in blue) and 2D (in red) SEM codes.

SH wave propagation

The previous test is repeated in this section for a single degree of freedom, so that the incident wave is defined on y component. In Figure 4.20, we see that the wave is attenuated between 10-20 m depth without any oscillation at other depths. Also, in Figure 4.21, 1D and 2D SEM codes give identical surface velocities. We can conclude that C-PML of single element and C-PML of two elements both attenuate incoming wave field efficiently also in SH wave propagation models.
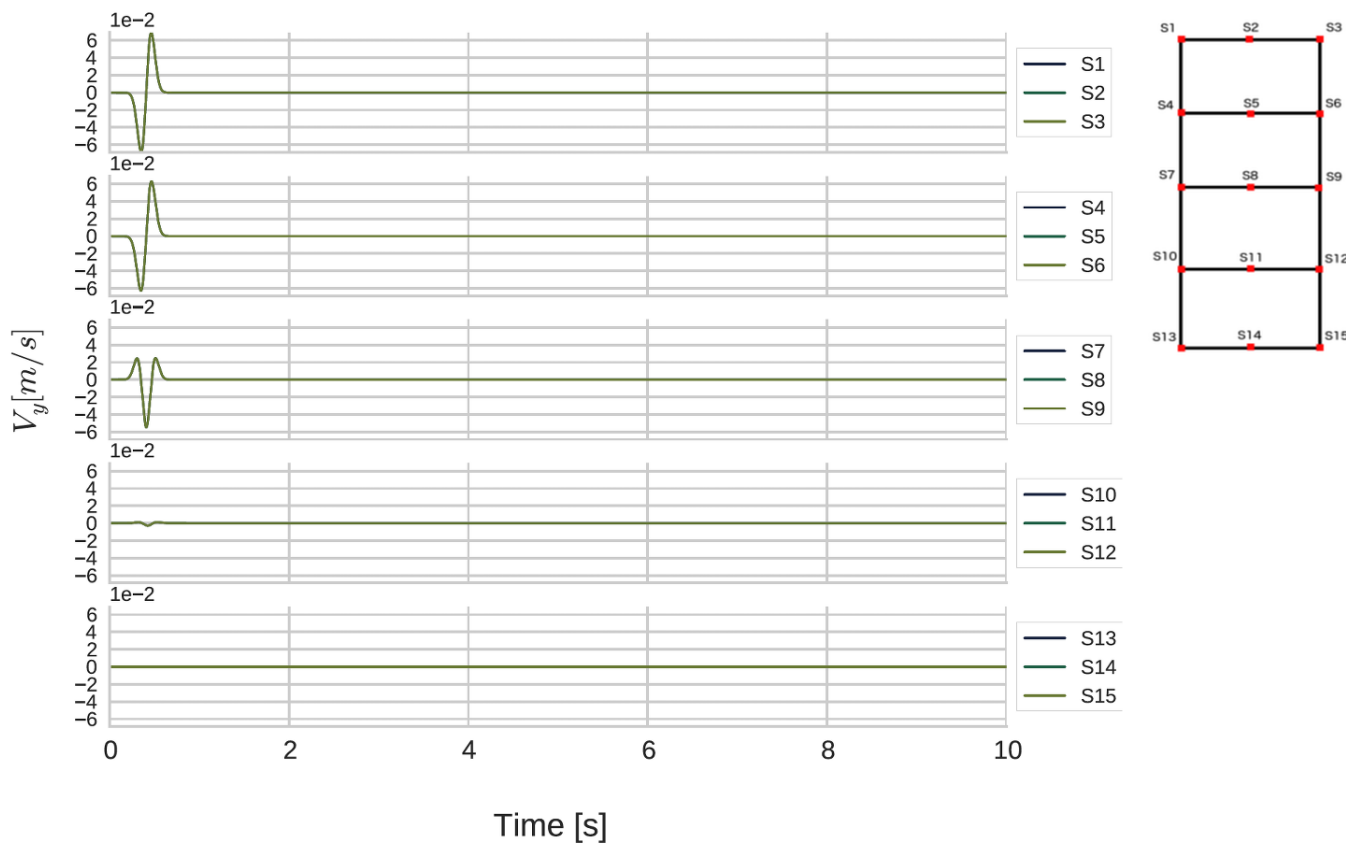
Fig. 4.20 Horizontal velocity outputs for all the stations of SH wave propagation model with two-element C-PML model.
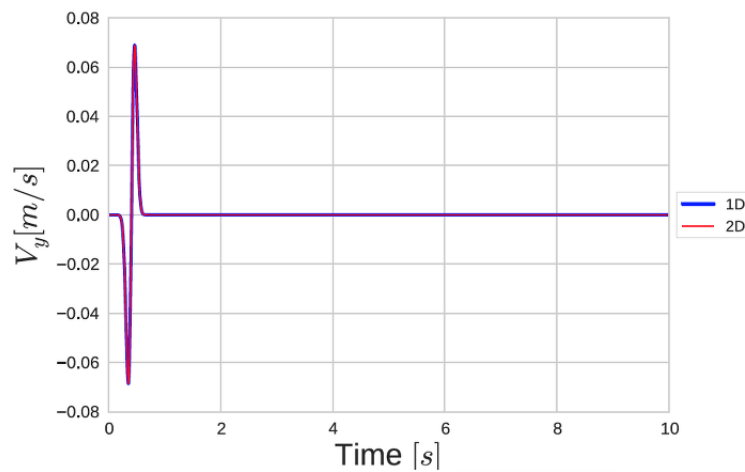
Fig. 4.21 Comparison of velocity outputs on horizontal direction of SH wave propagation model with two-element C-PML between 1D (in blue) and 2D (in red) SEM codes.

PML analysis for upward attenuation

The C-PML implementation in the SEM2DPACK makes it possible to use C-PML layer that attenuates the motion upward. In order to verify the implementation of this option, we take the two-dimensional P1 model and define the upper boundary as rigid and lower boundary as free surface. The incident wave field used in previous tests is multiplied by -1 and inserted at 10 m . For the tests in this part, we use a single element of C-PML which is located between 0-5 m depth of the P1 model. The material type is defined as C-PML with parameters $n = 2$ and $A = 10$. Upward attenuation is selected.

P-SV wave propagation

In this test, the incident wave identical to previous Ricker signal is defined at 10 m on both horizontal and vertical directions. Figures 4.22-4.23 show horizontal and vertical velocities recorded at each station. The wave field is attenuated starting from 5 m towards the surface (z=0 m) and there is no oscillation at other depths for any direction. Compared to Figures 4.12-4.13, incident wave at GL-10 m is similarly shared by two directions. Downward propagating waves have the same polarization as GL-10 m and upward propagating motion is inversely polarized. Since the input motion has opposite sign of the case of downward attenuation, we obtain same wave motion (in terms of polarization) as downward attenuation case. Also, the amplitudes of the motions are identical. The same comments can be made for vertical direction as well. For both upward and downward attenuation of C-PML, resultant

wave motion is identical.
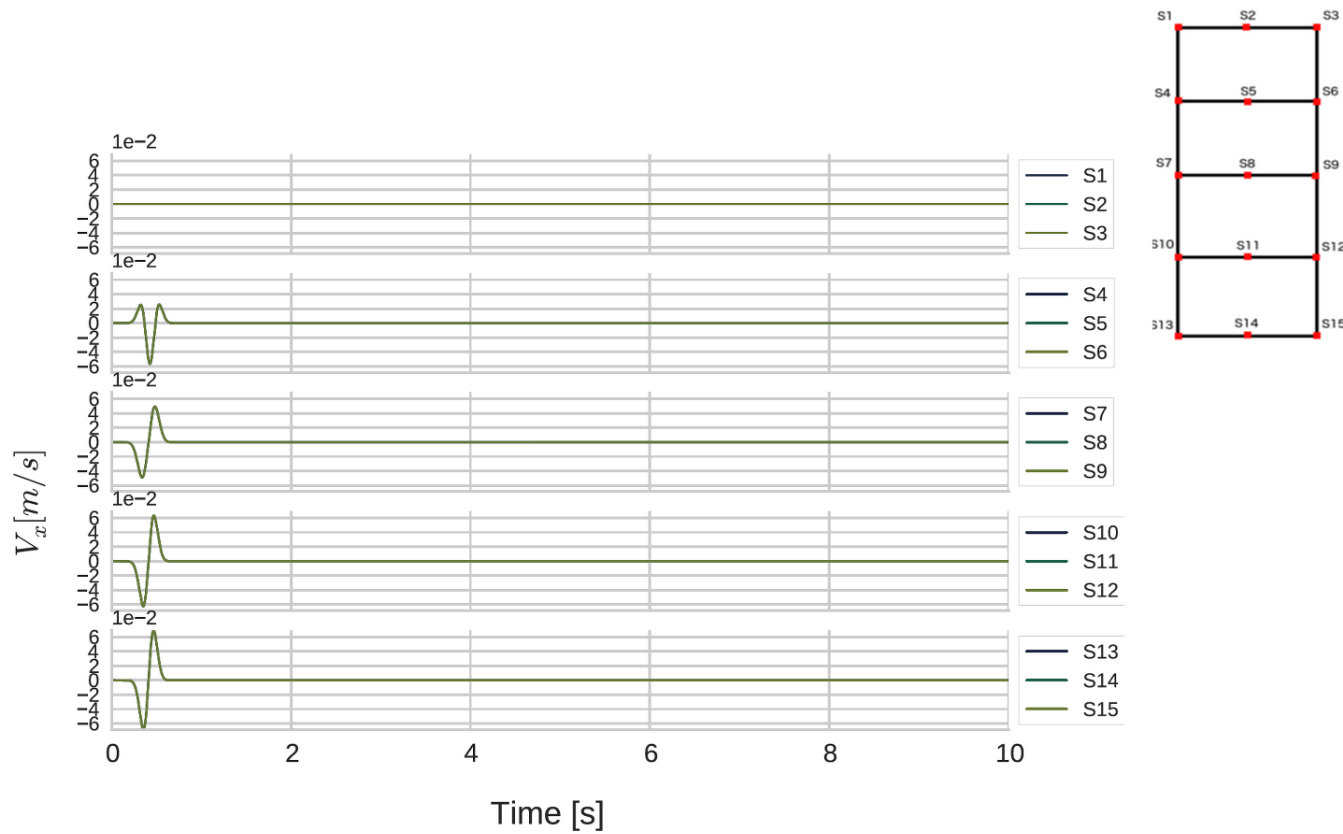
Fig. 4.22 Horizontal velocity outputs for all the stations of P-SV wave propagation model with upward attenuation C-PML element.
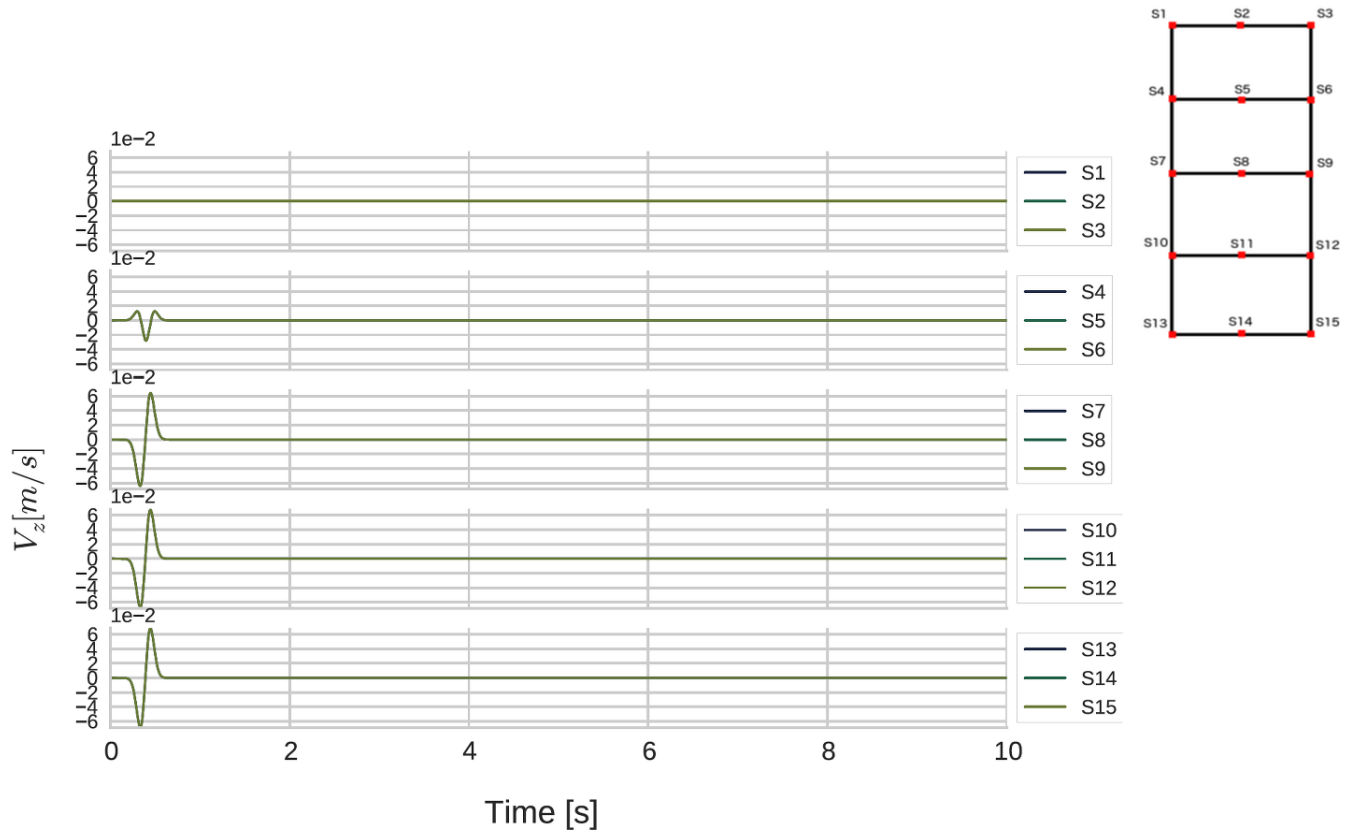
Fig. 4.23 Vertical velocity outputs for all the stations of P-SV wave propagation model with upward attenuation C-PML element.

The velocities at bottom boundary (z=20 m) on both directions are compared to the 1D code outputs in Figure 4.24. Both codes result in identical velocities at extremity. Regarding these results, we can conclude that C-PML element attenuates incoming wave field efficiently on upward direction for P-SV wave propagation models.
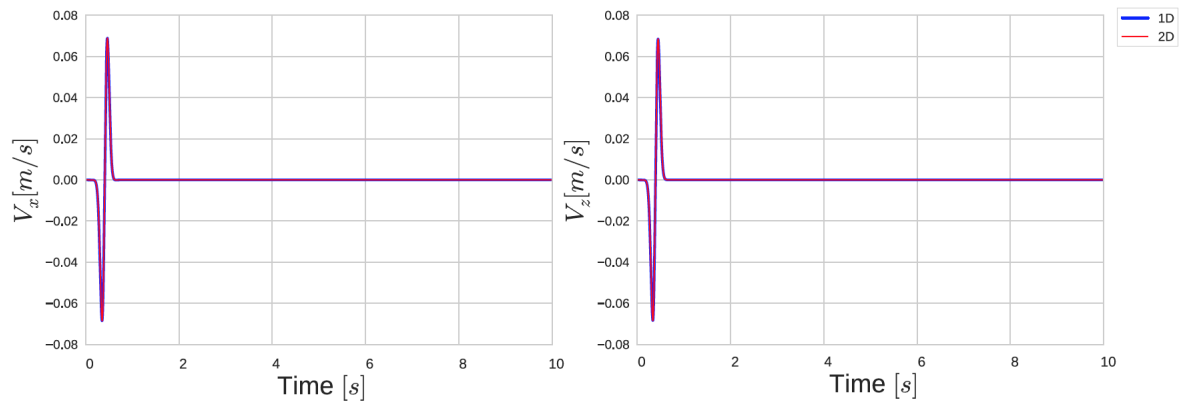
Fig. 4.24 Comparison of velocity outputs on horizontal (left) and vertical (right) directions of P-SV wave propagation model with upward attenuation C-PML element between 1D (in blue) and 2D (in red) SEM codes.

SH wave propagation

The previous test is repeated in this section for a single degree of freedom, so that the incident wave is defined on y component. In Figure 4.25, it is seen that the absorbing layer attenuates the entering wave field and the calculated surface motion shown at bottom of Figure 4.26 is identical on 1D and 2D SEM codes.
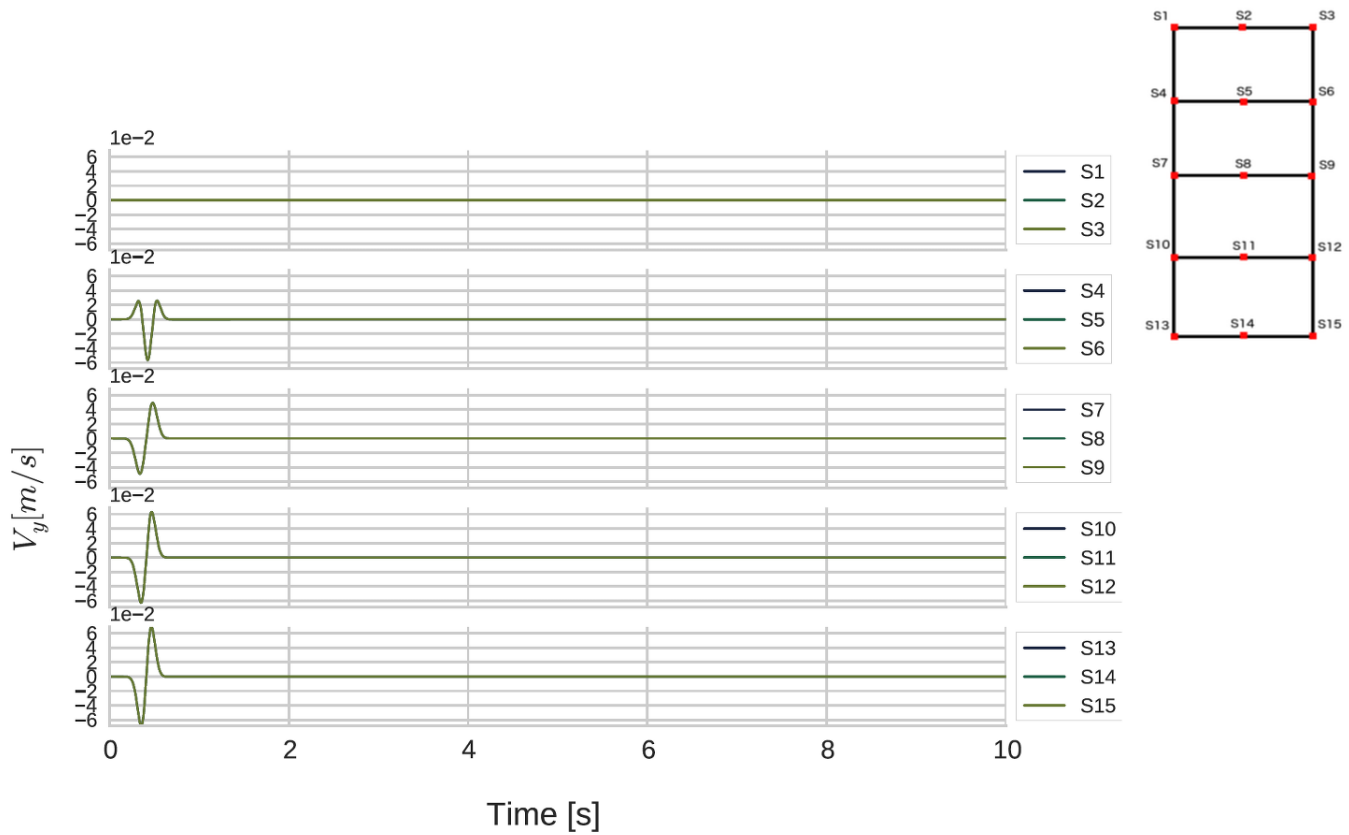
Fig. 4.25 Horizontal velocity outputs for all the stations of SH wave propagation model with upward attenuation C-PML element.
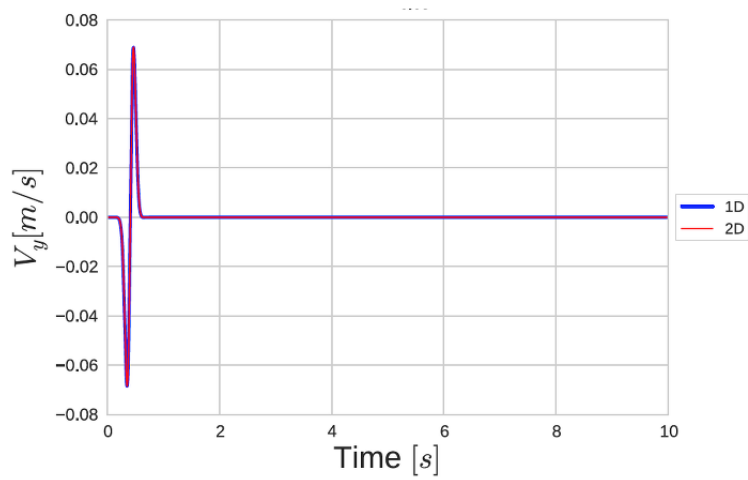
Fig. 4.26 Comparison of velocity outputs on horizontal direction of SH wave propagation model with upward attenuation C-PML element between 1D (in blue) and 2D (in red) SEM codes.

Based on the verification test results with C-PML material type, we can conclude that downward and upward attenuation on vertical direction for C-PML layer works efficiently and the use of a single C-PML layer is sufficient for attenuation without numerical oscillations.

4.3   Implementation of different rheologies

In SEM2DPACK, following the instructions of new material implementation in the manual of SEM2DPACK, viscoelastic and nonlinear rheology options are created as new material type. The work scheme of viscoelastic an nonlinear calculations is the same as 1D SEM code, for which the procedure is illustrated in Figure 2.1. For each time step, strain rate of each GLL point is computed by means of velocity. For elastoplastic models, stress is calculated by this strain rate. For the models where viscoelastic attenuation is taken into account, first, viscoelastic strain is determined and used for computation of stress. In the following, the verification of viscoelasticity and nonlinearity is shown for the developed 2D SEM code.

4.3.1   Viscoelasticity implementation

The viscoelasticity model that we refer to is Liu and Archuleta (2006) [98] model (detailed in Chapter 1.3.2). The code requires for each viscoelastic material block the quality factors for P and S waves and reference frequency to account for viscoelastic computations in addition to elastic parameters of density and P and S wave velocities of the material type.

In order to verify the implementation of viscoelasticity, the two-dimensional P1 model is used again. Viscoelasticity parameters of the P1 medium is given in Table 4.3.1. The bottom boundary is defined as borehole condition so that the input velocity field is inserted at that depth (z=20 m), while the upper boundary is defined as free surface. When the propagation in the medium terminates at the end of 10 seconds, the surface velocity outputs of 1D and

2D SEM codes are compared. This comparison is made for P-SV and SH wave propagation models and the results are shown below.

Table 4.2 Viscoelasticity properties used in 1D and 2D P1 models.

Q_p	Q_s	f_r [Hz]
70	30	1.0

P-SV wave propagation

For this test, input motion is defined by the Ricker signal, which is used in previous section. Both horizontal and vertical components are defined with this input signal. Figures 4.27-4.28 show horizontal and vertical velocity outputs at each station, respectively. We see that propagated motion is identical for each station at the same depth. Also, the attenuation in wave propagation energy due to viscoelasticity is noted for both directions compared to elasticity in section 2.1 of this chapter.
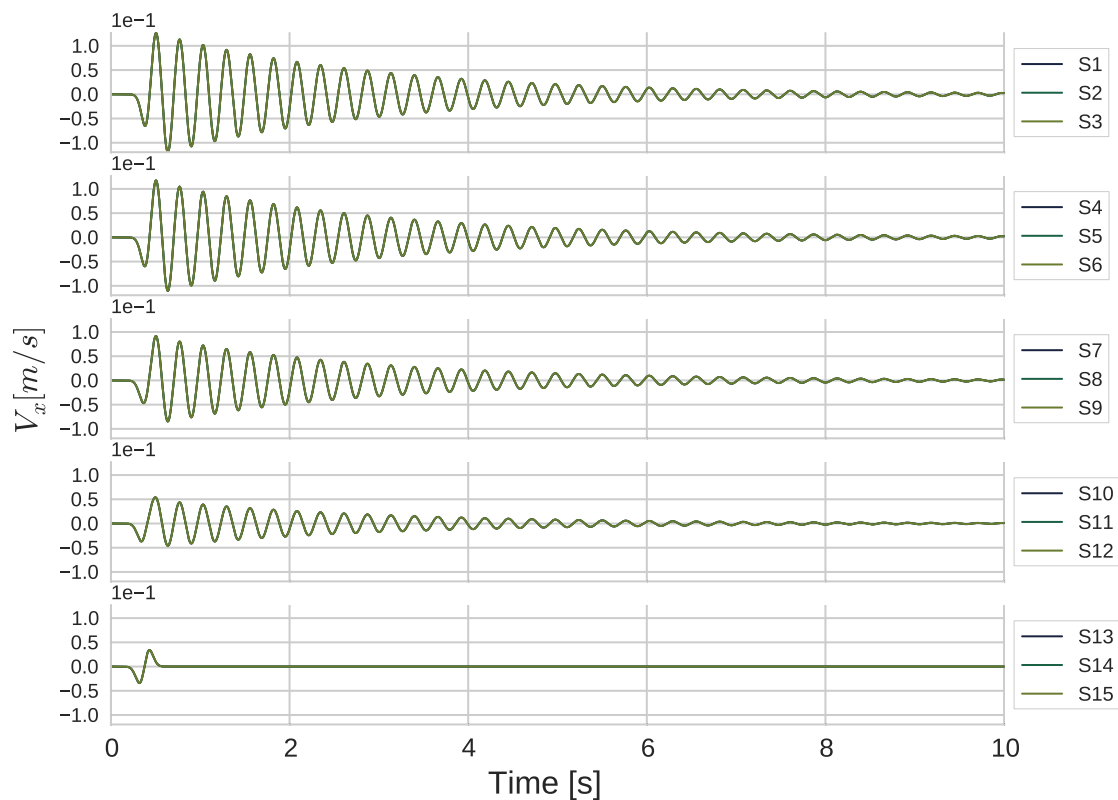
Fig. 4.27 Horizontal velocity outputs for all the stations of P-SV wave propagation model with viscoelastic rheology in P1 medium.
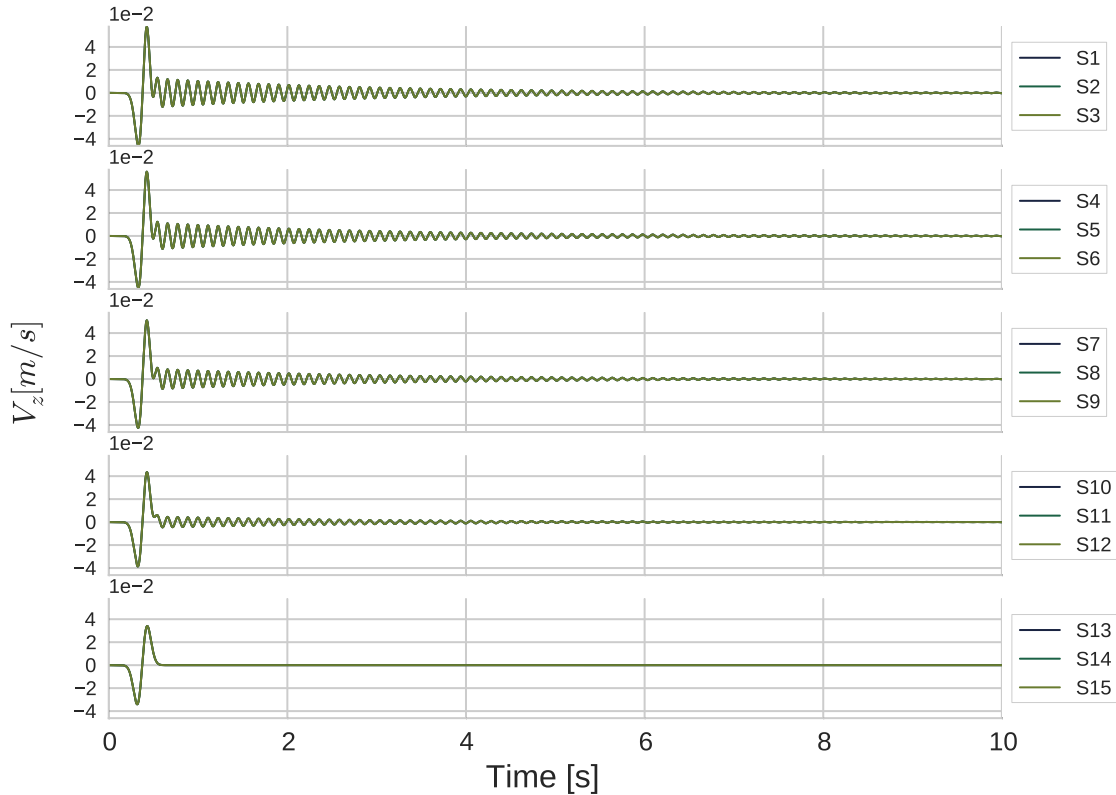
Fig. 4.28 Vertical velocity outputs for all the stations of P-SV wave propagation model with viscoelastic rheology in P1 medium.

In Figure 4.29 (top panel), the agreement between the surface motion values of 1D and 2D SEM codes for both components can be seen.
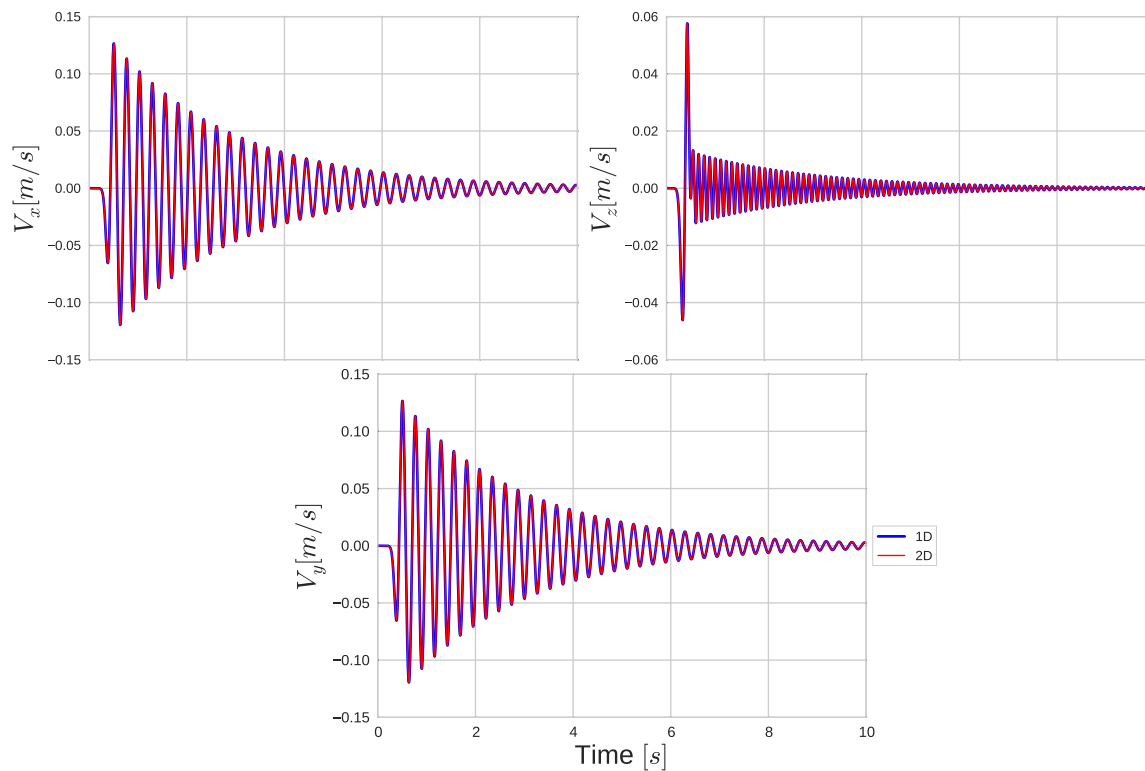
Fig. 4.29 Comparison of velocity outputs on horizontal (top left) and vertical (top right) directions of P-SV wave propagation model with viscoelastic rheology; on horizontal direction (bottom) of SH wave propagation model with viscoelastic rheology between 1D (in blue) and 2D (in red) SEM codes.

SH wave propagation

The previous test is repeated in this section for a single degree of freedom, so that the same incident wave is defined on y component. In Figure 4.30, it is seen that the propagation along the soil column is the same everywhere in the medium. Also, the results on y component are identical to the horizontal component of 1D SEM code (bottom panel of Figure 4.29).
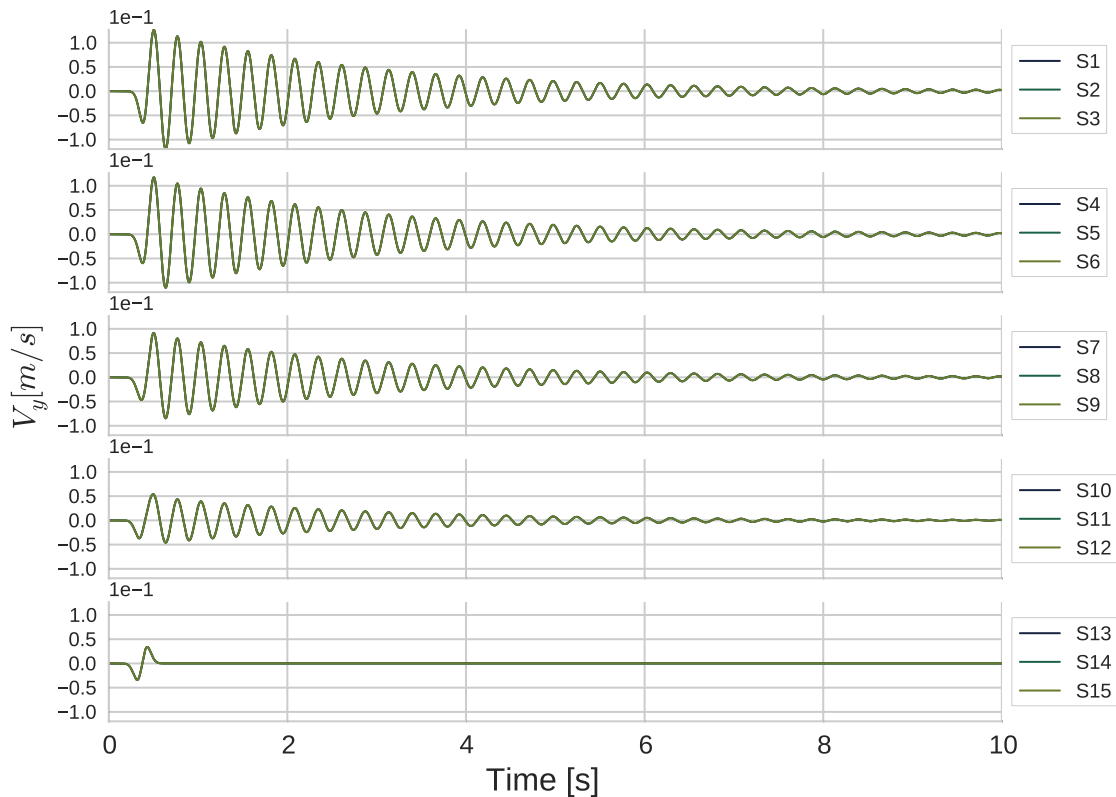
Fig. 4.30 Horizontal velocity outputs for all the stations of SH wave propagation model with viscoelastic rheology in P1 medium.

Given the similitude in 1D and 2D SEM codes results for viscoelastic P1 medium, the viscoelasticity can be said to be well implemented in SEM2DPACK for both P-SV and SH wave propagation models.

4.3.2   Nonlinearity implementation

For nonlinearity implementation in 2D, we refer to MPII model of Iwan (1967) [76] (detailed in Chapter 1.3.3). Similarly to viscoelasticity implementation, the nonlinear rheology is implemented as a new material block. There are two types of nonlinear model that can be analyzed with the developed 2D SEM code. The nonlinearity of the soil is represented by a hyperbolic backbone curve (Equations 1.32-1.35). This curve is constructed either by the reference strain parameter γ_{ref} specified in input file or by the failure line slope of the soil $sin\phi_f$. In the input file, if γ_{ref} is given for the material then all the points in the material block

are defined with this value of γ_{ref} and a common characteristic backbone curve is constructed for all the points in the same domain. If γ_{ref} parameter is not given, then $sin\phi_f$ must be defined. In such a case, the characteristic backbone curve of each point is constructed by the initial confining stress at that point and the model is said to be pressure-dependent. For pressure-dependent nonlinear models, it is possible to perform undrained effective stress analysis. For the materials in which excess pore pressure development is expected, Iai et al. (1990) [69] model is referred to. For such materials, in the input file *Par.inp*, the model parameters $sin\phi_p$, S_1, p_1, p_2 and w_1 must be given.

In the following sections, verification tests of these different nonlinear model types under different conditions are shown. All the tests are performed on the 2D P1 model for P-SV and SH wave propagation models. For the simplicity of verification, viscoelastic attenuation of the media is ignored so that the considered soil constitutive model is elastoplasticity.

Pressure-independent nonlinearity

In this section, the P1 model is defined with borehole condition at lower boundary while the upper boundary is defined as free surface and lateral boundaries are considered as periodic. For the whole domain, $\gamma_{ref} = 0.000365$ is used with 50 Iwan springs. In the following tests, the soil column is firstly loaded only on x direction with the previously used Ricker signal. Secondly, the same signal is applied on both directions. Lastly, the uniaxial loading is applied on a single degree of freedom model in order to test the efficiency of SH wave propagation model with nonlinearity.

P-SV wave propagation under uniaxial loading

In this test, the Ricker signal is inserted only on x direction. Waves are propagated in the medium for 10 seconds. Compared to 1D code result of surface velocity, 2D SEM code results in identical outputs. Since the loading is applied on only one horizontal component, the stress-strain curves are expected to follow the backbone curve. In Figure 4.31, 1D and 2D SEM codes are compared by surface velocity outputs (left) and in stress-strain curves at midlayer (z=10 m)(right). As expected, under uniaxial loading both code give stress-strain curves that follow the backbone curve of the medium. Hysteresis due to nonlinearity is clearly seen.
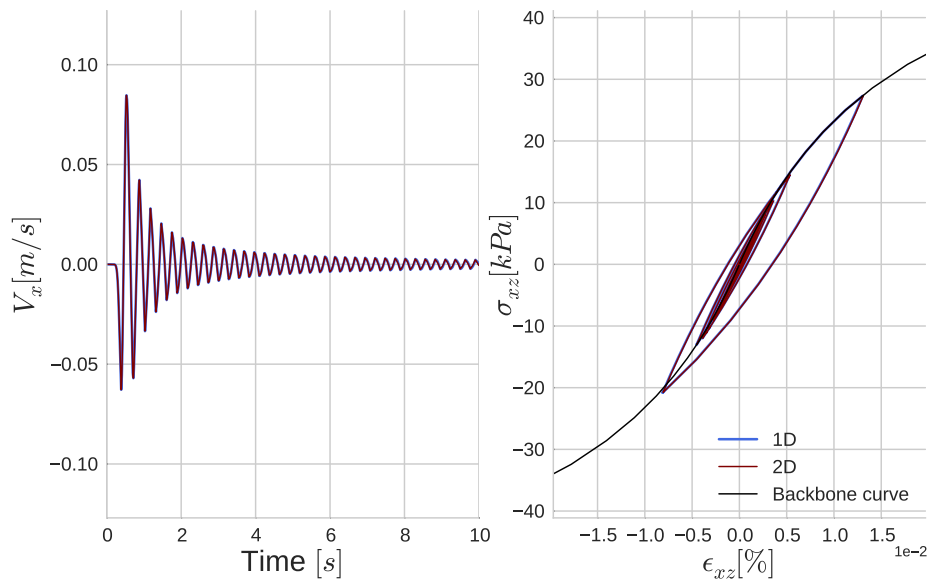
Fig. 4.31 Comparison of velocity outputs on x direction (left); comparison of stress-strain curves of *xz* component (right) at midlayer for 1D (in blue) and 2D (in red) SEM codes for pressure-independent nonlinear P1 model under uniaxial loading.

P-SV wave propagation under biaxial loading

In this test, the Ricker signal is inserted on x and z directions. Waves are propagated in the medium for 10 seconds. In Figure 4.32, 1D and 2D SEM codes are compared by surface velocity outputs on horizontal component (left) and in stress-strain curves at midlayer (z=10 m)(right). In 2D SEM code, it is not possible to apply double shearing with a vertical incident plane wave since only one horizontal component is involved. Compared to uniaxial loading, the extra loading on vertical component does not do the same plastification effect as in double shearing. Thus, there is a very slight deviation from the backbone curve under this loading. Figure 4.33 shows vertical surface velocities for 1D and 2D SEM codes. Compared to 1D code results of surface velocity, 2D SEM code results in identical outputs.
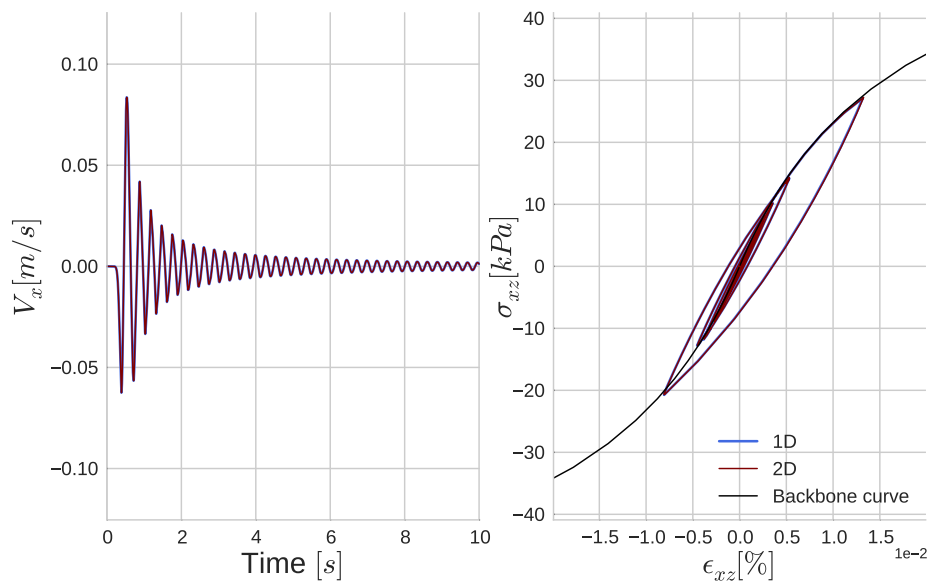
Fig. 4.32 Comparison of velocity outputs on x direction (left); comparison of stress-strain curves of *xz* component at midlayer (right) for 1D (in blue) and 2D (in red) SEM codes for pressure-independent nonlinear P1 model under biaxial loading.
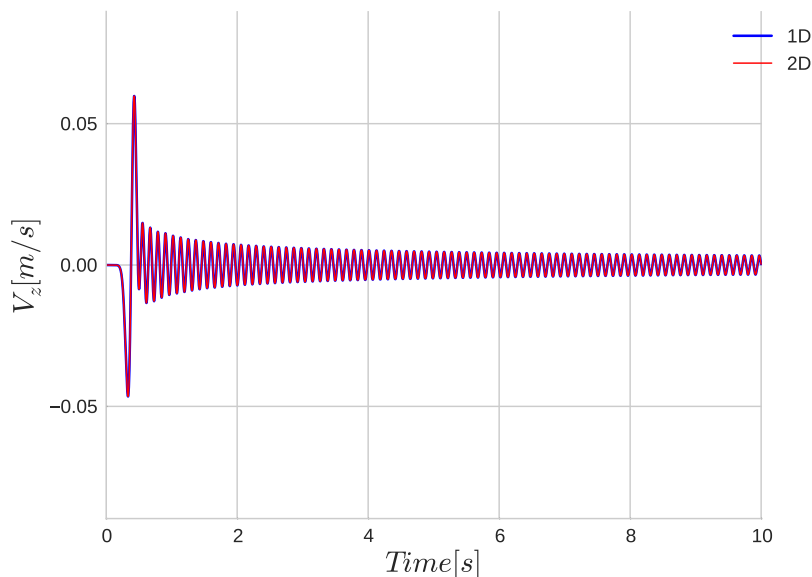
Fig. 4.33 Comparison of velocity outputs on z direction for 1D (in blue) and 2D (in red) SEM codes for pressure-independent nonlinear P1 model under biaxial loading.

SH wave propagation

In this test, the Ricker signal is inserted on y direction. Waves are propagated in the medium for 10 seconds. Simulation outputs are compared to 1D SEM code results under uniaxial loading in Figure 4.34 by surface velocity (left) and stress-strain curves (right). Both codes give the same results on surface velocity and mid-layer stress-strain curve outputs.
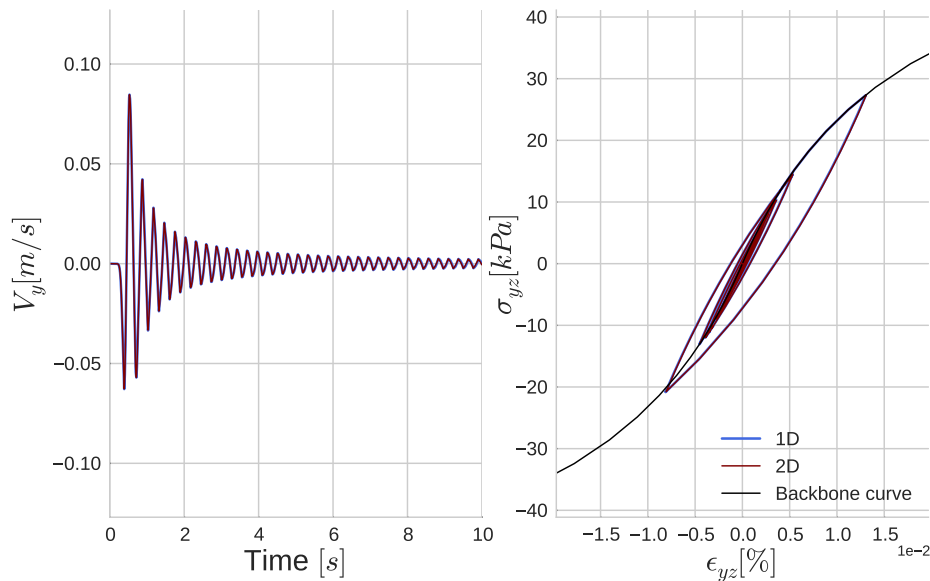
Fig. 4.34 Comparison of velocity outputs on y direction (at left); comparison of stress-strain curves of *yz* component at midlayer (at right) for 1D (in blue) and 2D (in red) SEM codes for stress-independent nonlinear P1 model under uniaxial loading.

Based on the agreement between 1D and 2D SEM code results, it is possible to conclude that the nonlinearity for pressure-independent models are well implemented for P-SV and SH wave propagation.

Pressure-dependent nonlinearity

In this section, the P1 model is defined similarly to preceding section with borehole condition at lower boundary and free surface at upper boundary. The failure line slope of the soil is defined by $sin\phi_f = 0.5299$ while the Iwan spring number is kept the same as 50. Soil is assumed to be cohesionless and initially isotropically consolidated. In the following section,

P-SV and SH wave propagation models are analyzed firstly for a consideration of water table at surface level and secondly for a consideration of water table at mid-layer (z=10 m).

P-SV wave propagation with water table at surface level

In this test, the Ricker signal is inserted on x and z directions so that the soil column is loaded biaxially. Waves are propagated in the medium for 10 seconds. Resultant surface velocity on horizontal component and stress-strain curves are compared to 1D SEM code results in Figure 4.35. A similar comparison is made on vertical surface velocity in Figure 4.36. Both codes give identical surface velocity on two directions and stress-strain curve at midlayer.
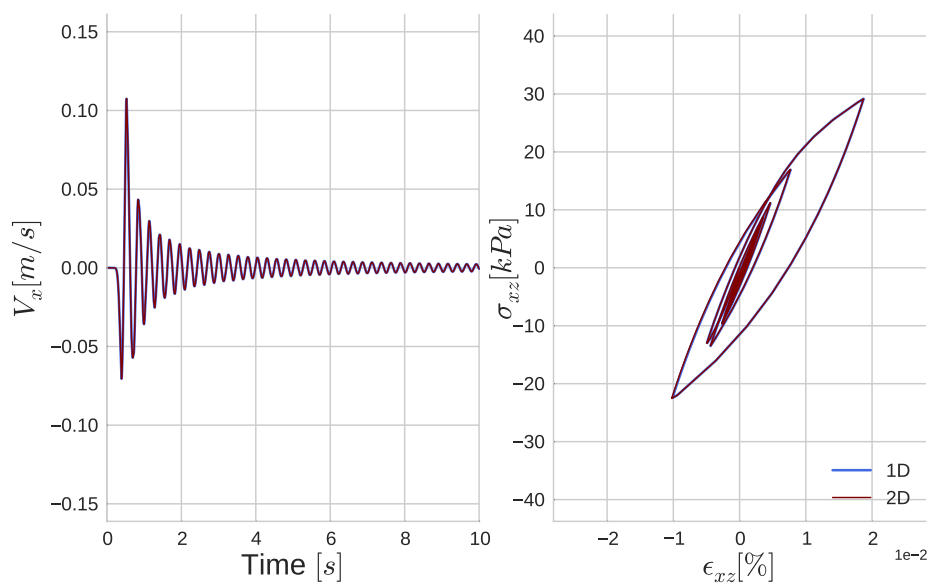
Fig. 4.35 Comparison of velocity outputs on x direction (left); comparison of stress-strain curves of *xz* component at midlayer (right) for 1D (in blue) and 2D (in red) SEM codes for pressure-dependent nonlinear P1 model with water table at surface level under biaxial loading.
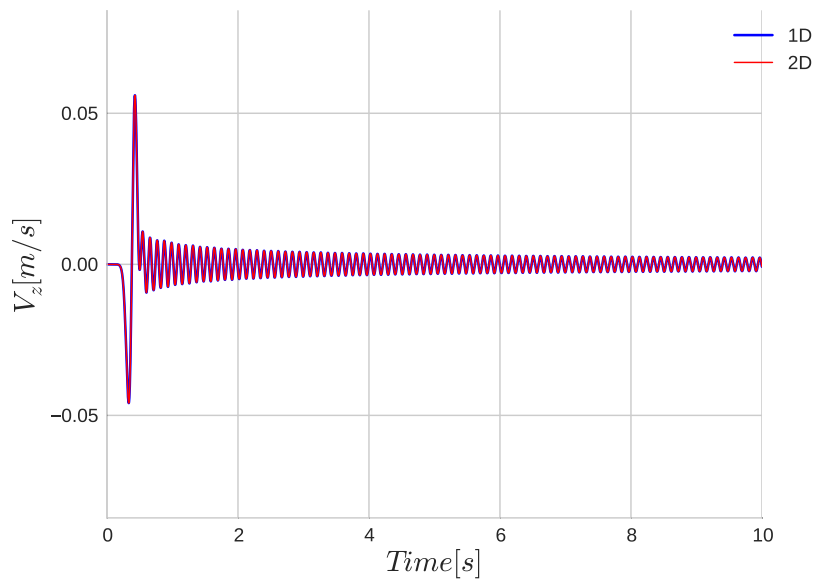
Fig. 4.36 Comparison of velocity outputs on z direction for 1D (in blue) and 2D (in red) SEM codes for pressure-dependent nonlinear P1 model with water table at surface level under biaxial loading.

SH wave propagation with water table at surface level

In this test, the Ricker signal is inserted on y direction. Waves are propagated in the medium for 10 seconds. Simulation outputs are compared to 1D SEM code results under uniaxial loading. In Figure 4.37, comparison of surface velocity and stress-strain curves at mid-layer is shown. Both codes give the same results on surface velocity and mid-layer stress-strain curve outputs.
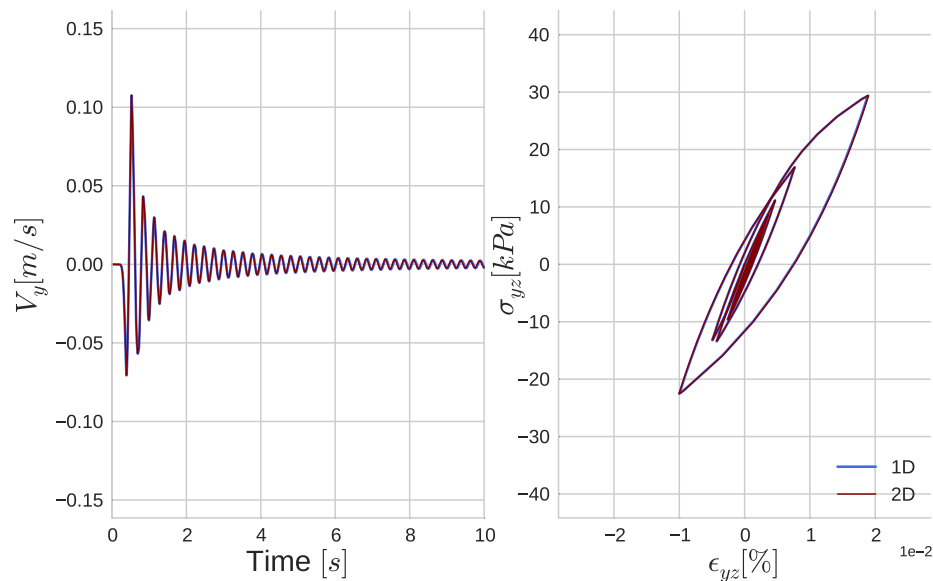
Fig. 4.37 Comparison of velocity outputs on y direction (left); comparison of stress-strain curves of *yz* component at midlayer (right) for 1D (in blue) and 2D (in red) SEM codes for pressure-dependent nonlinear P1 model with water table at surface level under uniaxial loading.

In all the verification tests for pressure-dependent nonlinear model, satisfactory results are obtained with 2D SEM code for P-SV and SH wave propagation. In order to verify the code for materials in which the water table is not located at extremities, following tests are performed.

P-SV wave propagation with water table at midlayer

In this test, the Ricker signal is inserted on x and z directions so that the soil column is loaded biaxially. Water table is defined at midlayer (z=10 m). Waves are propagated in the medium for 10 seconds. Resultant surface velocity on horizontal component and stress-strain curves are compared to 1D SEM code results in Figure 4.39. A similar comparison is made on vertical surface velocity in Figure 4.40. Compared to 1D code result of surface velocity, 2D SEM code results in identical outputs of surface velocity and stress-strain curve at midlayer. Compared to preceding section results where the water table is situated at surface level, the stress-strain curve is more rigid. Since the half of the soil column is not under water table, due to higher confining stress the strength of the soil is higher. Thus, under the same loading at the same depth, the soil has less deformation. This shows the importance of knowing

water table depth for a realistic simulation.
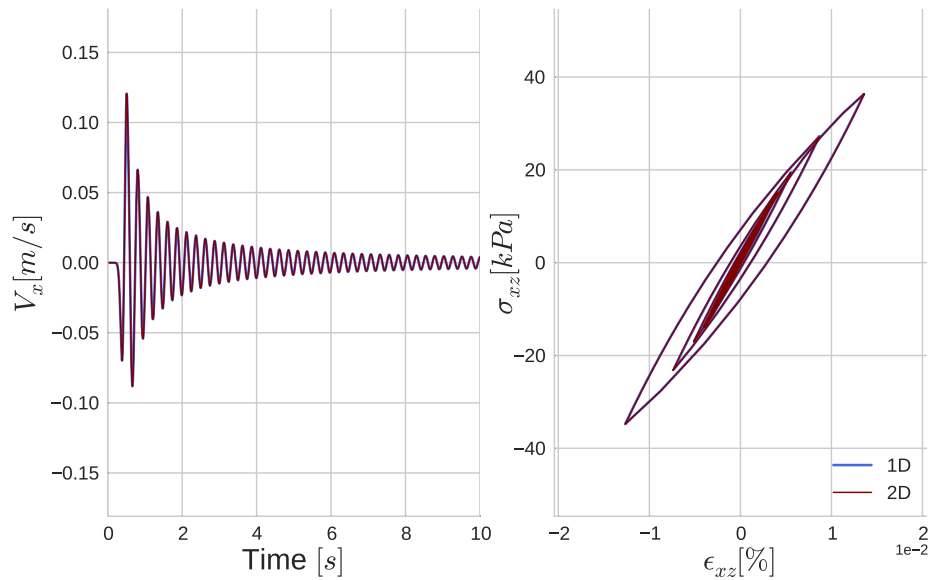
Fig. 4.38 Comparison of velocity outputs on x direction (left); comparison of stress-strain curves of *xz* component at midlayer (right) for 1D (in blue) and 2D (in red) SEM codes for pressure-dependent nonlinear P1 model with water table at midlayer under biaxial loading.
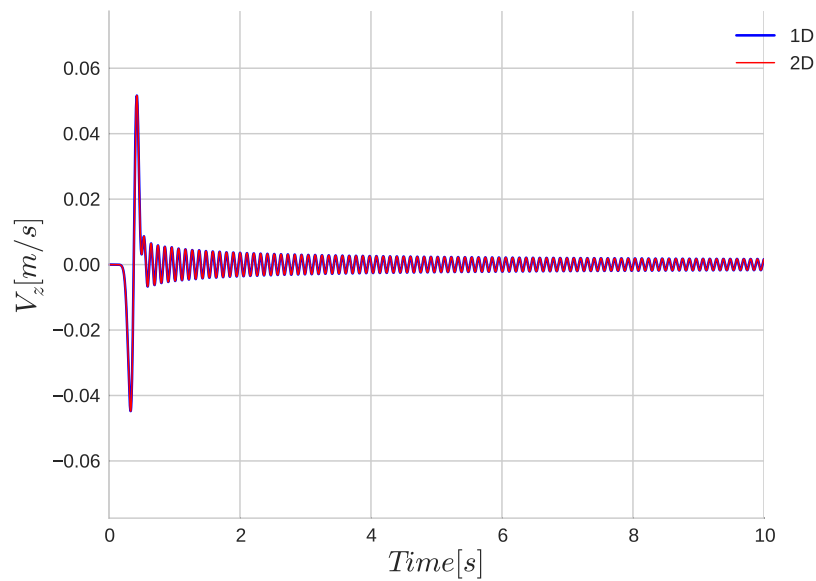
Fig. 4.39 Comparison of velocity outputs on z direction for 1D (in blue) and 2D (in red) SEM codes for pressure-dependent nonlinear P1 model with water table at midlayer under biaxial loading.

SH wave propagation with water table at midlayer

In this test, the Ricker signal is inserted on y direction. Waves are propagated in the medium for 10 seconds. Simulation outputs are compared to 1D SEM code results under uniaxial loading for surface velocity and stress-strain curves at mid-layer. Both codes give the same results as seen in Figure 4.40.
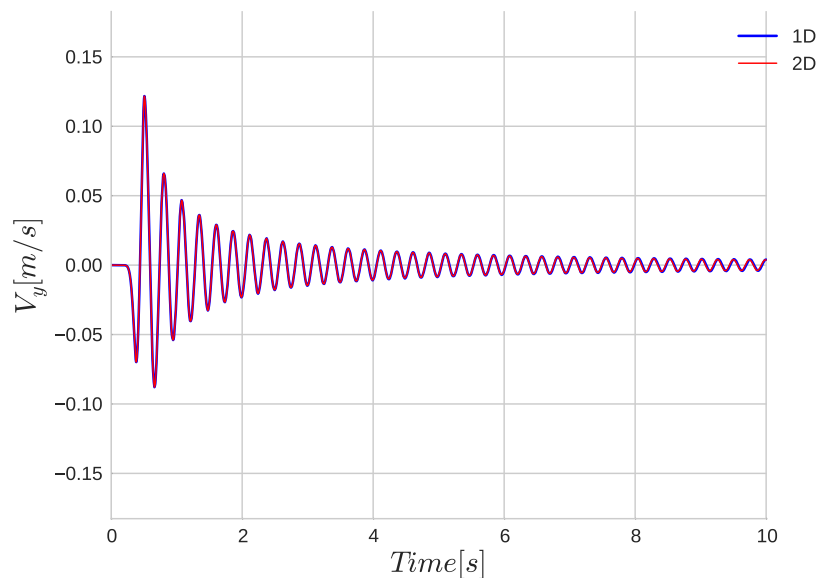
Fig. 4.40 Comparison of velocity outputs on y direction (at left); comparison of stress-strain curves of *yz* component at midlayer (at right) for 1D (in blue) and 2D (in red) SEM codes for pressure-dependent nonlinear P1 model with water table at midlayer under uniaxial loading.

The verification test results above show the efficiency of the 2D SEM code for pressure-dependent soil models where water table locates at different depths for P-SV and SH wave propagation models.

Nonlinearity with excess pore pressure development

In this section, the efficiency of the 2D SEM code for nonlinear soil models with excess pore pressure development is tested for P-SV and SH wave propagation models. As in the preceding section, the 2D P1 model is used with borehole condition at lower boundary and free surface at upper boundary. The front saturation model parameters used for the soil layer is given in Table 4.3. Since this test is performed for numerical purposes, front saturation model parameters are taken directly from Wildlife Refuge Liquefaction Array model in Chapter 3.3.1.

Table 4.3 Front saturation model parameters used in 1D and 2D P1 models for undrained effective stress analysis.

m_2	S_1	p_1	p_2	w_1
0.4067	0.01	0.4	0.9	4.0

P-SV wave propagation

In this test, the Ricker signal is inserted on x and z directions so that the soil column is loaded biaxially. Water table is defined at surface (z=0 m). Waves are propagated in the medium for 10 seconds. Figure 4.41 displays the comparison of surface velocity on horizontal direction and stress-strain curves at mid-layer between 1D and 2D SEM codes. With the effect of excess pore pressure development, the expansion in stress-strain curve and consequent plastification are remarked compared to stress-strain curve in Figure 4.35. Also, in Figure 4.42, same comparison is made for vertical surface velocities. We obtain identical results with two codes.
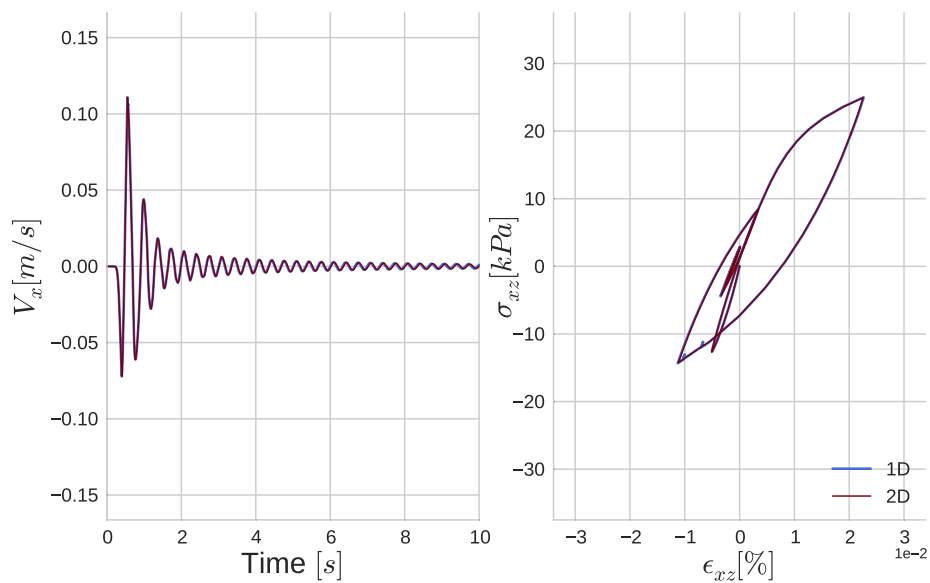
Fig. 4.41 Comparison of velocity outputs on x direction (left); comparison of stress-strain curves of *xz* component at midlayer (right) for 1D (in blue) and 2D (in red) SEM codes for pressure-dependent nonlinear P1 model under biaxial loading effective stress analysis.
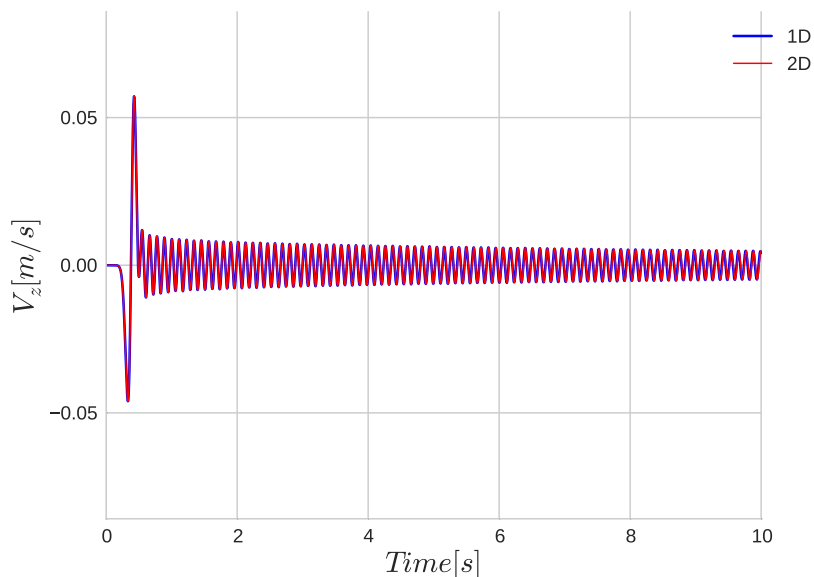
Fig. 4.42 Comparison of velocity outputs on z direction for 1D (in blue) and 2D (in red) SEM codes for pressure-dependent nonlinear P1 model under biaxial loading effective stress analysis.

SH wave propagation

In this test, the Ricker signal is inserted on y direction. Water table is defined at surface (z=0 m). Waves are propagated in the medium for 10 seconds. Simulation outputs are compared to 1D SEM code results under uniaxial loading in Figure 4.43 by surface velocity and stress-strain curves at mid-layer. Both codes give the same results of surface velocity and stress-strain curve at midlayer.
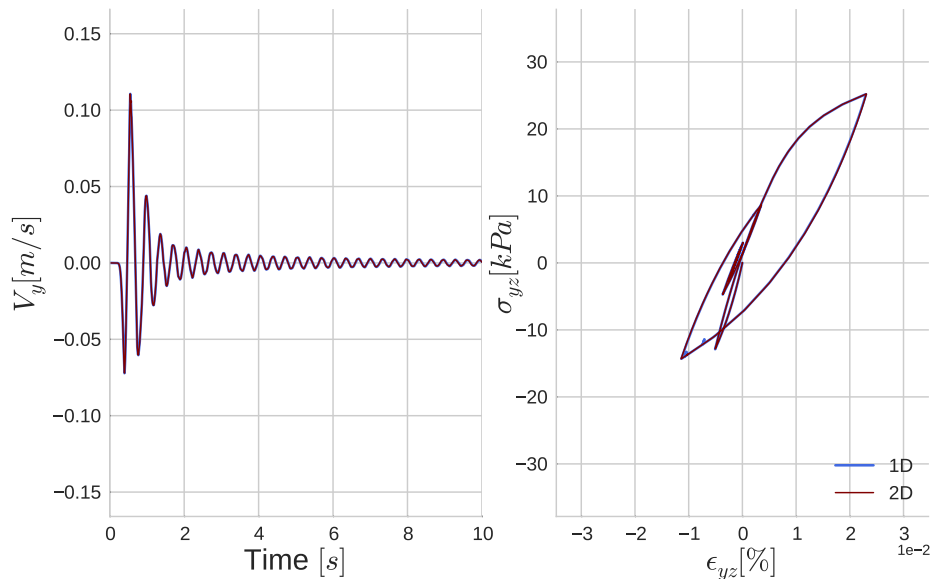
Fig. 4.43 Comparison of velocity outputs on y direction (left); comparison of stress-strain curves of *yz* component at midlayer (right) for 1D (in blue) and 2D (in red) SEM codes for pressure-dependent nonlinear P1 model under uniaxial loading effective stress analysis.

When the consequent displacements on horizontal and vertical directions at ground surface level are compared in effective and total stress analyses in Figure 4.44, it is remarked that in particular for horizontal component the displacement is accumulating in effective stress analysis due to the higher rigidity loss in underlying soil layer, whereas in vertical component the difference between two analyses is not significant. This comparison in a canonical simplified model highlights in a sense the importance of consideration of excess pore pressure development in soils.
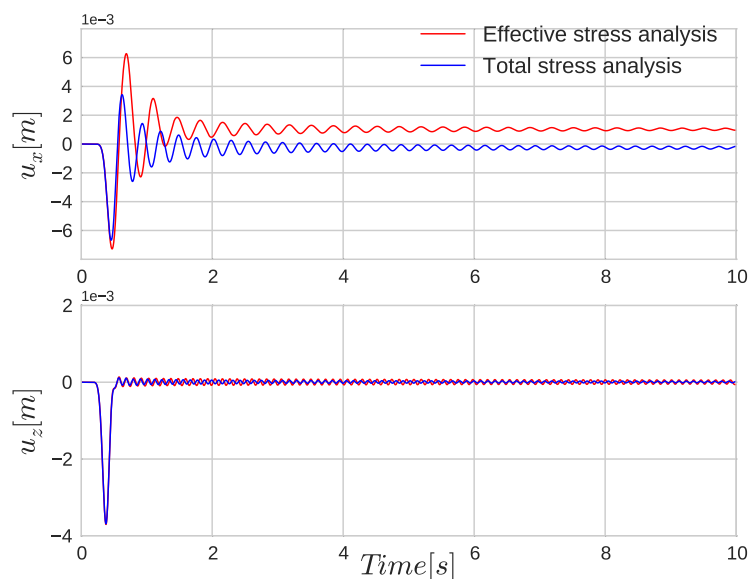
Fig. 4.44 Comparison of ground surface displacements on x direction (top) and on z direction (bottom) for total stress analysis (in blue) and effective stress analysis (in red) in 2D P1 nonlinear model.

Given the agreement between 1D and 2D SEM code results in these verification tests, the implementation of viscoelasticity and nonlinearity for effective and total stress analysis models is verified.

4.4   Verification on real models

Thus far, the verification of the developed 2D SEM code for P-SV and SH wave propagation modeling in viscoelastic and nonlinear media have been shown. The verification tests are performed on the P1 model which is a canonical model with a single soil layer. In this section, as an additional verification of the 2D SEM code, we refer to the realistic models that have been studied in previous chapters with the 1D SEM code. The first model is Volvi, Greece model (detailed in Chapter 3.3.1), in which the soil rheology is defined with viscoelasticity all over the domain. The second model is Wildlife Refuge Liquefaction Array (WRLA) (See Chapter 3.3.1) for which visco-elastoplastic rheology is used and effective stress analysis is performed.

4.4.1 Volvi model

Volvi model, which is presented in Chapter 3.3.1, contains seven different soil layers overlying bedrock at 300 m. This model is used for verification of viscoelasticity in 1D SEM code. Input motion is defined at horizontal direction at 300 m under which incoming wave fields are attenuated by C-PML layer. In this section, we create a 2D model by defining a single lateral element of 5 m size. As in 1D SEM code simulation, 5 GLL points are defined on each element and time step of $2.10^{-4}s$ is used. In the following sections, the elastic and viscoelastic response of the Volvi model is compared with 1D analyses and the efficiency of C-PML layer is tested by using single-element and two-element absorbing layers. All the tests with Volvi model in this section use a single degree of freedom (ndof=1).

Single-element C-PML model

In this section, bedrock is meshed up to a depth of 310 m. C-PML layer of Volvi model is defined for the last element located between 310-320 m. Input motion is inserted at 300 m. In Figure 4.45, 2D SEM code results on this Volvi model is compared to 1D SEM code results on Volvi model with a single-element C-PML for elasticity (top) and for viscoelasticity (bottom). As seen in the figure, both codes result in identical velocity outputs at surface.
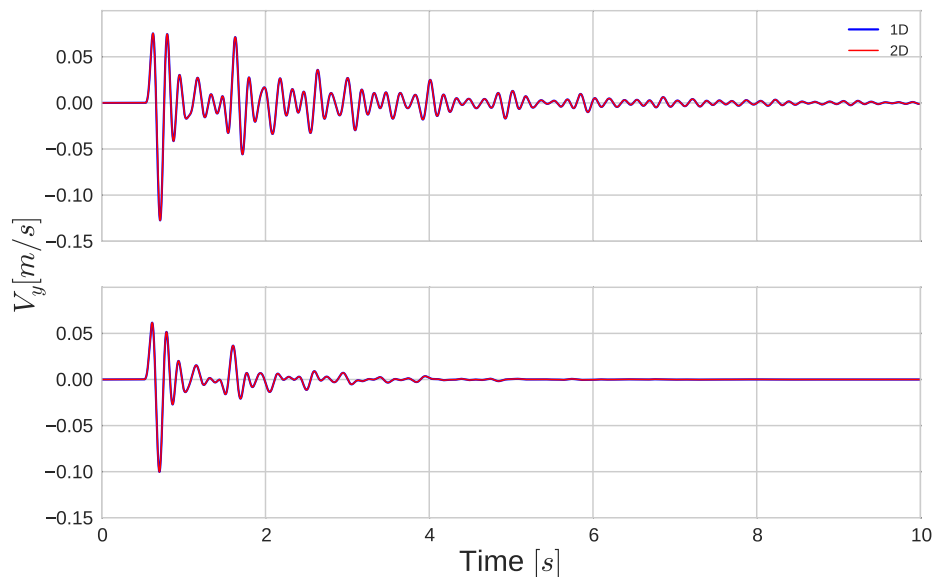
Fig. 4.45 Comparison of velocity outputs of Volvi model with single-element C-PML for elasticity (top) and for viscoelasticity (bottom) between 1D (in blue) and 2D (in red) SEM codes.

Two-element C-PML model

In this section, bedrock is meshed up to a depth of 300 m. C-PML layer of Volvi model is defined for the last two elements located between 300-310 m and 310-320 m. Input motion is inserted at 300 m. In Figure 4.46, 2D SEM code results on this Volvi model is compared to 1D SEM code results on Volvi model with a single-element of C-PML for elasticity (top) and for viscoelasticity (bottom). As seen in the figure, both codes result in identical velocity outputs at surface for elasticity and viscoelasticity. Using single-element C-PML and two-element C-PML on a real model both result in the same way in terms of incoming wave field attenuation.
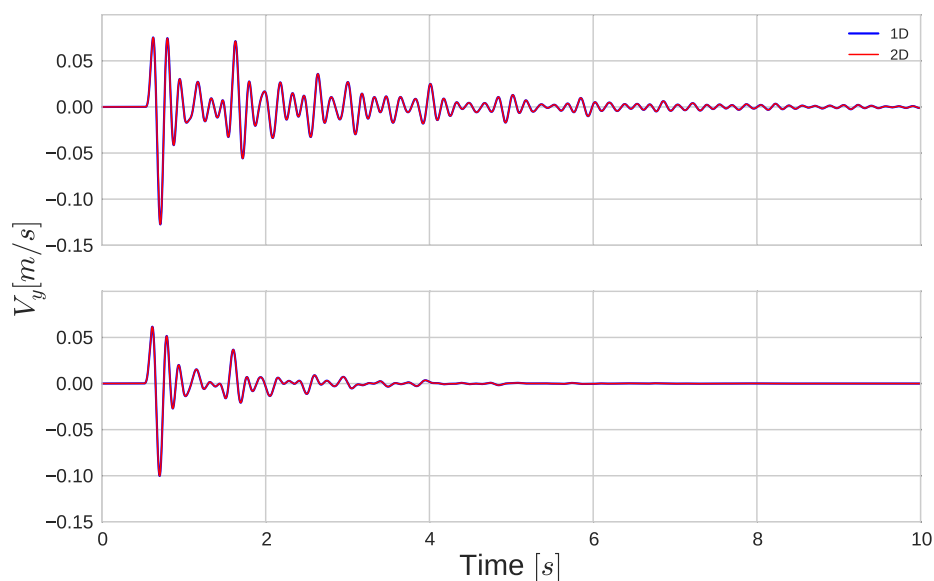
Fig. 4.46 Comparison of velocity outputs of Volvi model with two-element C-PML for elasticity (top) and for viscoelasticity (bottom) between 1D (in blue) and 2D (in red) SEM codes.

4.4.2   Wildlife Refuge Liquefaction Array model

Wildlife Refuge Liquefaction Array (WRLA), which is presented in Chapter 3.3.1 has been used for validation of the 1D-3C SEM code for nonlinear effective stress analysis.

In the third layer of WRLA, soil is expected to develop pore pressure excess. Since the input motion is recorded by borehole stations, the bottom boundary at 7.5 m is defined by borehole condition. Input motion is inserted at that depth by NS (north-south) and UD (vertical) directions in 2D SEM code. The soil rheology all over the model is defined as visco-elastoplastic. Two different meshes are created for the WRLA model, The first one has a single lateral element of 1 m size and the second one with two lateral elements each of which is of 1 m size. Thus, we also verify the 2D solution for different width.

In Figure 4.47, surface velocities on two directions are compared between 1D and 2D SEM code results for the first model (with one lateral element). The results are identical between two codes.
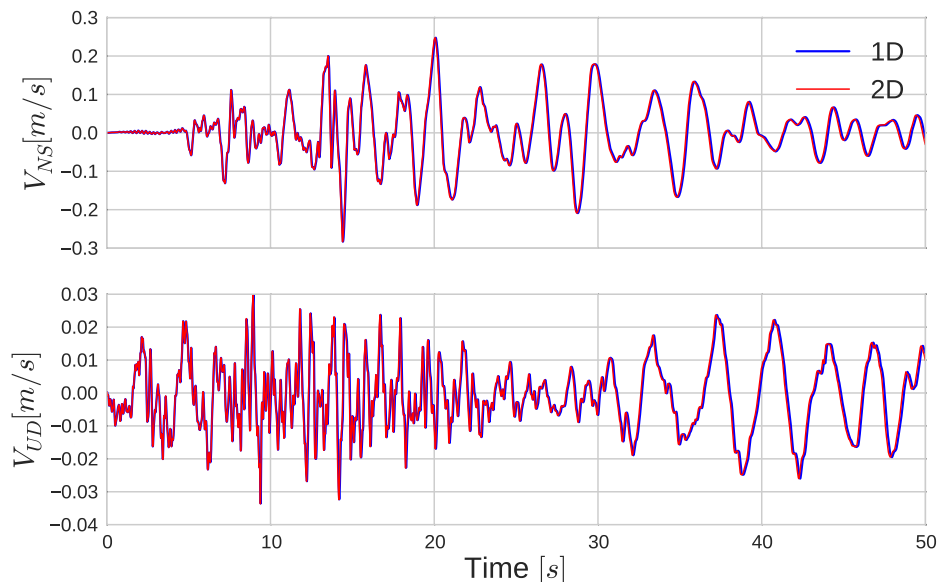
Fig. 4.47 Comparison of surface velocity outputs of WRLA model with single lateral element for NS (top) and for UD (bottom) directions between 1D (in blue) and 2D (in red) SEM codes.

In Figure 4.48, surface velocities on two directions are compared between 1D and 2D SEM codes for the second model (with two lateral elements). The results are still identical, which demonstrates the independence of the solution from 2D model thickness and the efficiency of periodic lateral boundary conditions.
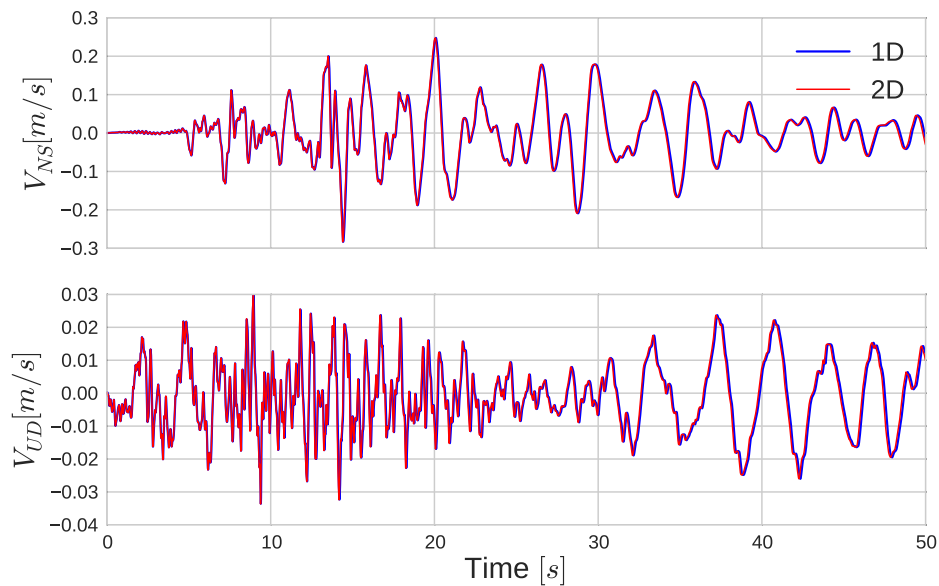
Fig. 4.48 Comparison of surface velocity outputs of WRLA model with two lateral elements for NS (top) and for UD (bottom) direction between 1D (in blue) and 2D (in red) SEM codes.

Lastly, when stress-strain curves at 4 m are compared in Figure 4.49, by using single lateral element (left) and two lateral elements (right), the solution is always identical to 1D SEM code solution for both approaches.
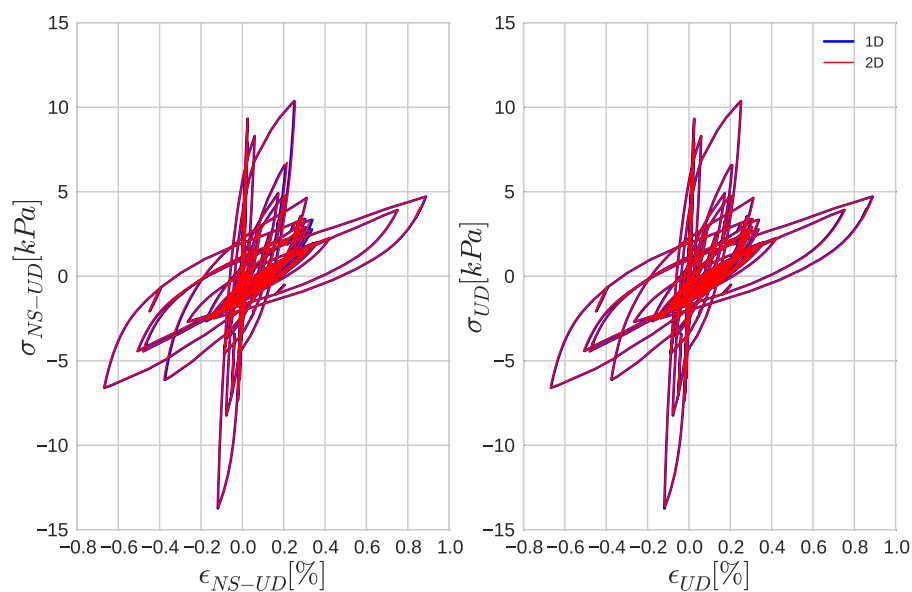
Fig. 4.49 Comparison of stress-strain curves of WRLA model with single lateral element (left) and with two lateral elements (right) for *xz* component between 1D (in blue) and 2D (in red) SEM codes.

Based on the comparison of 1D and 2D SEM codes in two real models, which are defined with different soil constitutive models and boundary conditions, it can be said that the implementations of viscoelastic and nonlinear models and the implementations of borehole and C-PML layer are verified satisfactorily. The developed 2D SEM code is intended to be used in two-dimensional problems of different aspects in next chapter.

4.5   Conclusions

In this chapter, the implementations of new boundary conditions and rheologies into SEM2DPACK are explained and verification tests for each new property are shown. As boundary conditions, borehole condition with incident wave velocity field and C-PML (Classical Perfectly Matched Layer) type absorbing layer are implemented. The verification tests of these conditions are performed by using two-dimensional P1 model which is composed of a single soil layer. C-PML condition is implemented in the code as a new material block, since the attenuation is done through a chosen soil block differently than the pre-existing absorbing boundary conditions in SEM2DPACK. Both boundary conditions are verified successfully for P-SV and SH wave propagation models.

As new material constitutive model, firstly, viscoelasticity model of Liu and Archuleta (2006) [98] is implemented and verified on the 2D P1 model for P-SV and SH wave propagation conditions. Another rheology is the nonlinearity, which is the MPII model based on Iwan (1967) [76]. For this type of material, it is possible to perform analyses for different kinds of nonlinear soil. As a first option, pressure-independent models can be used. For pressure-independent models, a certain value of reference strain parameter for the material can be set so that all the points inside the material domain refers to the same characteristic backbone curve. As another option, pressure-dependent models can be used. For pressure-dependent models, the backbone curve for any point in the nonlinear model can be calculated by means of initial confining stress. For such a model, the code requires only the failure line slope and cohesion of the soil. This type of soil model is verified by tests on P1 model for different water table levels. Lastly,

for pressure-dependent model, it is possible to perform effective stress analyses for soils that can develop pore pressure excess. For this purpose, the Iai et al. (1990) [69] model is implemented. The code requires five necessary parameters of the model additionally.

Following the satisfactory verification tests on P1 model, two real models which have been used in 1D SEM code analyses in previous chapters are studied with the 2D SEM code. One of them is Volvi model that is composed of several soil layers with different properties. This model utilizes C-PML material underlying the bedrock layer. By using single and two C-PML elements in 2D SEM code for elastic and viscoelastic rheology assumptions in the media, identical results are obtained with 1D SEM code. The second real model is Wildlife Refuge Liquefaction Array (WRLA) which has been used in validation tests of 1D-3C SEM code. The rheology is defined as visco-elastoplasticity in this model. The 2D mesh of this site is created by using first a single lateral element, second two lateral elements. With both meshes, a very good agreement between 1D and 2D SEM codes is acquired.

Chapter 5

Application of the 2D SEM code to a sedimentary basin

Application of the 2D SEM code to a sedimentary basin

5.1   Introduction

In the previous chapter, different soil constitutive models and boundary conditions implemented in the 2D SEM code have been verified. No horizontal geometrical variation neither physical variations were present in the studied models, so that wave propagation is dependent only on model properties in the vertical direction. In this chapter, we investigate different aspects of wave propagation on a two-dimensional media where material properties vary both horizontally and vertically. The influence of soil rheology and input motion is studied on P-SV and SH waves propagating in a two-dimensional sedimentary layered basin model. Indeed, this work is a follow-up of Gélis and Bonilla (2014) [53] who studied only P-SV wave propagation without taking into account pore pressure excess. Here, this study is extended to the SH case and effective stress analysis with pore water pressure effects. This study is limited to the propagation of impulse input motions with different PGA and a real input motion with more complicated energy content. In the following, first, the 2D model that is used in the analyses of this chapter is presented in detail. Then, the obtained results for all the simulations are analyzed and discussed. In particular, the effect of effective stress

analysis with pore water pressure vs total stress is discussed, as well as the influence of wave polarization (P-SV vs SH) and the effect of input motion energy content. Lastly, conclusions are developed.

5.2   2D sedimentary basin model characteristics

5.2.1   Model geometry

The 2D basin model that we refer to has been used in Gélis and Bonilla (2014) [53] for the understanding of the effect of basin properties on basin response. The model has a length of 2000 meters and a height of 250 meters, as shown in Figure 5.1. In the model, sedimentary basin with soft soil layers has a depth of 225 meters. It is located between $662.25 - 1225.25$ m at surface and between $890.50 - 1000$ m at bottom (at $225m$ depth), so that the basin width varies from 563 m to 110 m from surface to bottom of the basin. Left boundary of the basin that separates sedimentary soil layers from bedrock presents a straight slope which gives rise to sharp changes along this basin edge, particularly close to the surface. The basin has an elliptic slope at right boundary that results in smoother changes in boundary coordinates. With this aspect, the basin is asymmetrical and follows the general shape of Alpine basins (Lacave and Lemeille, 2006 [19]) as presented in Gélis and Bonilla (2014) [53].
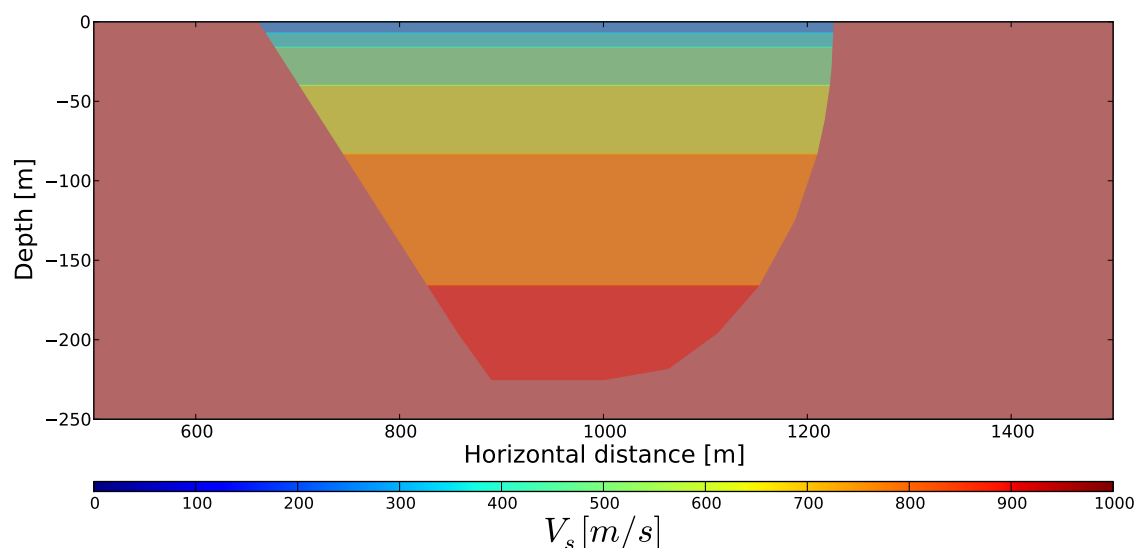
Fig. 5.1 Shear wave velocity profile of the 2D sedimentary basin model where bedrock shear velocity is 2000 m/s.

5.2.2   Material properties

The 2D model consists of six soft layers inside the sedimentary basin which is surrounded by bedrock. Inside the basin, shear velocity increases gradually towards the basin bottom. In Gélis and Bonilla (2014) [53], two different velocity models are compared in order to see the influence of model structure on basin response. In the first model, velocity changes gradually inside a soil layer so that each point at different depth is defined with a different velocity. In the second model, the basin is divided into layers of constant velocities, each one being defined by velocities of the first model. In their study, the basin response at the surface (not maximum strain distribution in the basin) is weakly sensitive to constant vs gradually increasing velocities in each layer. For this reason and simplicity, in our 2D model, we use homogeneous soil layers in terms of shear velocity profile.

In addition, Gélis and Bonilla (2012 [52], 2014 [53]) have shown the strong dependency basin response of such type on soil constitutive model on the same 2D model (same asymmetrical structure with slight differences on width and depth) by comparing viscoelastic and visco-elastoplastic models under different levels of input motion. In their models, nonlinear soil model is held pressure-independent and for each layer in the basin, nonlinear curves from EPRI (1993) [39] with different level of nonlinearity have been used. In our study, we consider pressure-dependent soil nonlinearity (See Chapter 1.3.3) so that nonlinearity changes with depth inside the same layer (due to the effect of confining stress). Water table is set to GL-2 meters inside the first layer. Although in reality water table depth is likely to differ in horizontal distance, for these initial analyses on a two-dimensional model with the 2D SEM code in this chapter, we consider a water table level which is equal everywhere in the model. Table 5.1 displays the shear and pressure velocities (V_s and V_p), density ρ, thickness, failure line angle ϕ_f and coefficient of Earth at rest K_0 for all the soil layers. All the values except for ϕ_f are taken from Gélis and Bonilla (2014) [53]. While selecting failure line angles for soft soil layers in the basin, an assumption of soil type is made even though the model is hypothetical (See Table 5.1). Based on this assumption, failure line angle is greater for deeper soils. Following Gélis and Bonilla (2014) [53], quality factors for pressure and shear wave propagation (Q_p and Q_s) are set to 40 and 20 inside the basin; 400 and 200 in bedrock respectively. Reference frequency is taken as $1Hz$ (See Table 5.2).

Table 5.1 Soil properties at 2D sedimentary basin model. V_p values are calculated by assumption of Poisson ratio equal to 0.45 for basin 0.35 for bedrock (after Gélis and Bonilla, 2014 [53]).

Layer	Depth [m]	Description	Thickness [m]	$V_s[m/s]$	$V_p[m/s]$	$\rho[kg/m^3]$	$\phi_f[degree]$	K_0
1	7	Sand	7	278.5	923.7	1800	28	1.0
2	16	Sand	9	362.4	1202.0	1800	30	1.0
3	40	Sandy silt	24	456.9	1515.4	1800	32	1.0
4	83	Sandy silt	43	585.2	1940.9	1800	32	1.0
5	166	Sandy silt	83	749.8	2486.8	1800	38	1.0
6	225	Gravelly sand	59	897.5	2976.7	1800	40	1.0
7	-	Bedrock	-	2000.0	4163.3	2200	-	1.0

Table 5.2 Quality factors for pressure waves Q_p, shear waves Q_s and reference frequency w_r for the 2D sedimentary basin model (after Gélis and Bonilla, 2014 [53]).

Layer	Q_p	Q_s	$w_r [Hz]$
1	40	20	1.0
2	40	20	1.0
3	40	20	1.0
4	40	20	1.0
5	40	20	1.0
6	40	20	1.0
7	400	200	1.0

In Bard and Bouchon (1985) [10], the nature of specific resonance patterns in 2D sedimentary deposits are investigated. 2D resonance is found to result in considerably large amplifications and longer propagation duration compared to 1D. The authors have shown that the existence of resonance modes (for P, SV and SH waves) of 2D models are strongly dependent on basin shape and velocity contrast, based on a series of analyses on 2D sinusoidal homogeneous (one type of sediment inside the basin) models. This dependency is represented by Figure 5.2, with shape factor and velocity contrast parameters. Shape factor is equal to the ratio of sediment thickness to the half of basin width (h/l in the figure) and velocity contrast c_v is the ratio of velocities of bedrock and sediment. The plotted curve is obtained after fitting five experimental points. Referring to the figure, the model which remains beyond the curve, 2D

resonance modes are expected to occur, while for other case, 1D resonance is dominant with lateral propagation effects of surface waves.
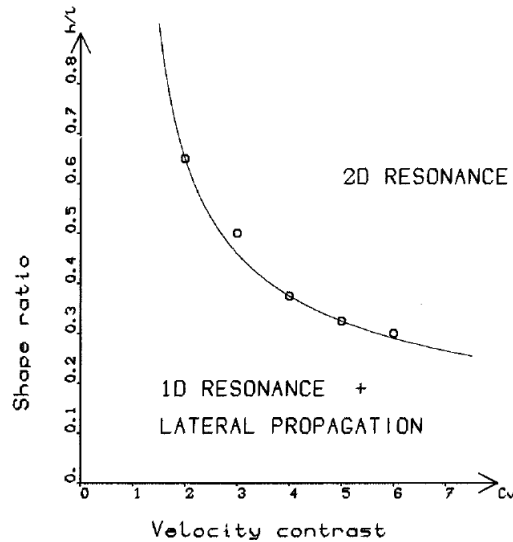
Fig. 5.2 Existence conditions of the two-dimensional (2D) resonance in the SH case (after Bard and Bouchon, 1985 [10]).

Our 2D sedimentary basin model is not homogeneous in terms of basin layer velocities and lateral boundaries do not correspond to a sinusoidal shape. Although the basin properties are not identical, we locate the position of our basin model in this figure in order to determine the tendency of resonance (whether 1D or 2D mainly). By calculating shape ratio (0.79) and minimum and maximum velocity contrasts (278.5/2000 and 897.5/2000 respectively, such that minimum velocity contrast is 2.2 and maximum 7.1), the resultant point remains in 2D resonance zone for both minimum and maximum limits of velocity contrast given high shape ratio. This indicates that SH wave propagation in our 2D model is dominated by 2D resonance mode of the basin.

Moreover, since we would like to explore the effects of pore pressure changes in 2D wave propagation, we define the first two superficial layers of the basin as liquefiable soil layers. In other words, these two layers are susceptible to excess pore pressure development. The susceptibility of liquefaction in a soil layer is represented by liquefaction resistance curve. This curve is determined by a series of stress-controlled tests (similar to the stress-controlled tests in Chapter 1.3.4). In the tests, soil is loaded under different cyclic stress ratios (Cyclic

stress ratio is equal to the ratio of applied deviatoric stress and effective mean stress of the soil). Liquefaction limit is considered to be the number of loading cycles triggering 5 % of shear strain (axial strain $\varepsilon = 2.5\%$). For each test, the number of loading cycles is noted for the applied cyclic stress ratio, such that the liquefaction resistance curve is fitted to the experimental points.

In Figure 5.3, liquefaction resistance curves of different frozen soil samples of several locations in Kushiro Port site are shown from the study of Iai et al. (1995) [71]. In this figure, C-8 and D-3 curves belong to coarse sand at GL-3.5 m and fine sand at GL-8 m depths for the same cross-section of the site. The curve depends on confining pressure applied at soil and also soil properties such as relative density.
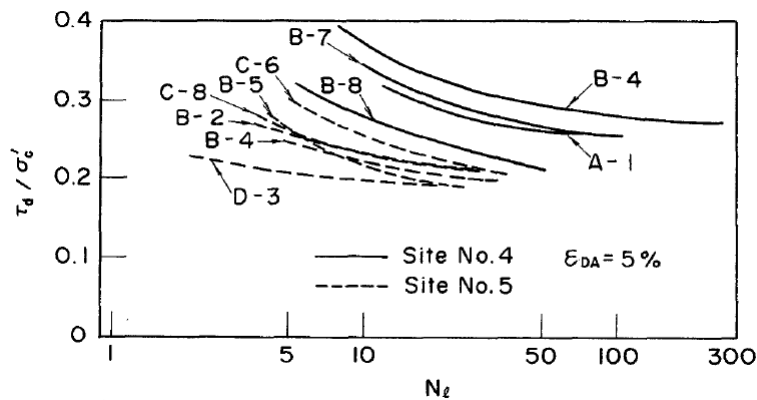
Fig. 5.3 Liquefaction resistance curves for different soil samples in Kushiro Port site (after Iai et al. 1995 [71]).

We constructed two target liquefaction curves based on the curves in Figure 5.3, for the two liquefiable layers of our model (See Figure 5.4). In the figure, number of loading cycles triggering 5 % of shear strain (axial strain $\varepsilon = 2.5\%$) under three different levels of loading (cyclic stress ratios) are plotted. For the middle of layers 1 and 2, the initial effective mean stress is calculated as $47.040kPa$ and $109.760kPa$, respectively. Given the fact that in the 2D model layer 2 is supposed to be stiffer than layer 1, under the same loading level, more loading cycles are necessary for the soil to reach 5% strain. For instance, under a stress ratio of 0.25, 6 loading cycles initiate liquefaction in layer 1 whereas approximately 10 cycles are necessary in layer 2.
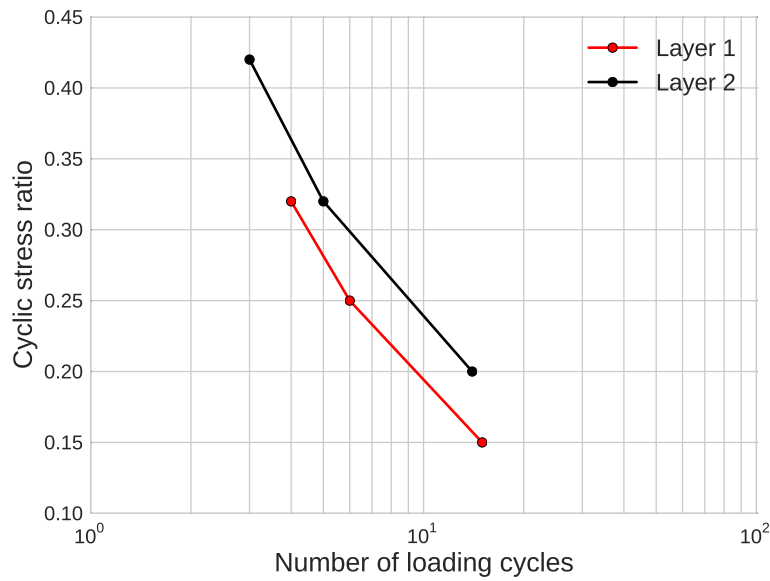
Fig. 5.4 Target liquefaction resistance curves for layer 1 (in red) and layer 2 (in black) of the 2D model.

In order to achieve to plot these curves, three stress-controlled tests are performed for different cyclic stress ratios. For example, in the middle of layer 1, the initial mean effective stress is equal to $47.040kPa$. For a cyclic ratio of 0.15, the applied deviatoric stress is calculated by multiplication of cyclic ratio with initial effective mean stress such that it is equal to $7.056kPa$. In stress-controlled test, the applied deviatoric stress is a sinusoidal function where the maximum value is equal to $7.056kPa$. Figure 5.5 displays the applied deviatoric stress on the middle of layer 1 for this example (left of the figure). The corresponding strain evolution in the soil is also plotted as a function of applied loading cycle number (right of the figure). Liquefaction limit is considered to be the number of loading cycles triggering 5 % of shear strain (axial strain $\varepsilon = 2.5\%$). For this example, the soil in the middle of layer 1 reaches to liquefaction limit under 15 loading cycles.
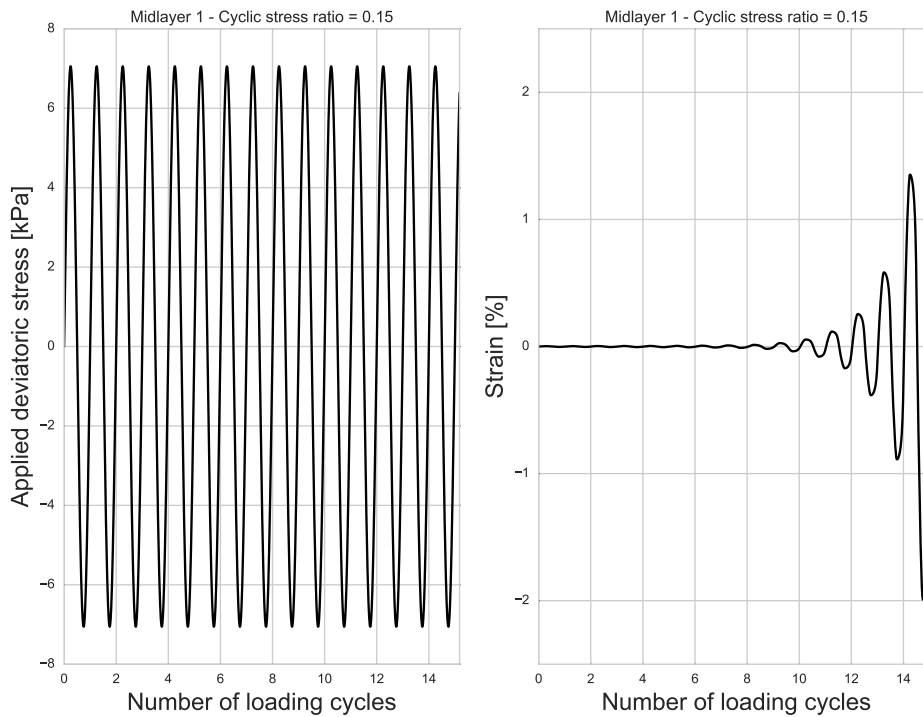
Fig. 5.5 Deviatoric stress applied on the middle of soil layer 1 (left) and strain (right) as a function of number of loading cycle.

The values for liquefaction front model parameters (detailed in Chapter 1.3.4) and friction angle (or failure line angle) ϕ_f are determined by trial-error procedure in order to obtain the target liquefaction curves for the mid-points of layers 1 and 2. Table 5.3 shows the liquefaction front model parameters used in two layers.

Table 5.3 Dilatancy parameters for layers 1 and 2 of the 2D model.

Layer	$sin\phi_p$	w_1	p_1	p_2	S_1
1	0.28	3.0	0.6	1.2	0.01
2	0.30	5.0	0.6	1.2	0.01

5.2.3 Numerical model

The default version of SEM2DPACK offers many different features for two-dimensional mesh generation (cartesian mesh, layered mesh, MESH2D Matlab utility) and compatible for

several mesh generators such as CUBIT, EMC2, EZ4U. In our study, we use GMSH mesh generator in order to create the mesh file of the 2D sedimentary basin model. GMSH is a free multi-dimensional (2D and 3D) finite element grid generator. It is built around four modules: geometry, mesh, solver and post-processing. The specification of any input to these modules is created either interactively by using the graphical user interface or in ASCII text files using GMSH's own scripting language (Geuzaine and Remacle, 2009 [54]). GMSH provides a mesh file for the created mesh in extension of *.msh*. In order to adapt this type of mesh files to SEM2DPACK, a Python-based script is written accordingly to SEM2DPACK meshfile format during this thesis.

The 2D SEM code uses only quadrangular elements. For meshing the model only with quadrangular elements, the built-in option in GMSH is chosen. The created mesh for 2D SEM code is determined to be structured mesh (defined in Chapter 1.2.3) in order to create a mesh with only quadrangular elements in GMSH. For this purpose, 'Transfinite Surface' and 'Recombine Surface' commands are used in GMSH, which forces the mesh generator to create structured meshes. Resultant basin model is not identical to the 2D model of Gélis and Bonilla (2014) [53] in terms of boundary shape. For example, corner points of last basin elements on right boundary result in less smooth boundary curve than Gélis and Bonilla (2014) [53]. This difference should be recalled while comparing two studies. Moreover, since the mesh is structured and consists of only quadrangular elements, the element size selection of one layer influences other connected layers as well. For example, if the surface spacing is divided by 10 elements, then the bottom spacing of the basin is also forced to have 10 elements. This is a restriction of using structured meshes in terms of computational time (due to the small grid size which requires small time step) and as a perspective, an unstructured mesh could be created in order to reduce the computational cost.

In mesh generation for the 2D model, we referred to minimum element size restrictions for each soil layer (See Chapter 1.2.2). Since the soil nonlinearity is taken into account in all the analyses in this chapter, a maximum eight-times softening of V_s is considered for determination of minimum element size. Table 5.4 displays the vertical element number factors for each soil layer. Similarly, in Table 5.5, horizontal element factors are given. For example, layer 1 is divided into 3 vertically and the basin surface width is divided into 253, so that $3*253$ quadrangular elements are created for layer 1.

Table 5.4 Vertical element number factor of the 2D model. Bedrock layer is the bottom layer of 25 m height that underlies the sedimentary basin.

Layer	Vertical factor
1	3
2	4
3	4
4	6
5	8
6	6
Bedrock	1

Table 5.5 Horizontal element number factor basin opening, left and right bedrock sides in the 2D model.

Layer	Horizontal factor
Basin opening	253
Left bedrock	9
Right bedrock	10

Resultant two-dimensional grid is shown in Figure 5.6 and in Figure 5.7 in a more detailed window. In the 2D SEM code, left and right vertical extremities are defined with 'periodic' boundary condition. Upper boundary is set as free surface. In all the analyses, absorbing boundary condition is used at the bottom of the 2D model so that beyond the depth of GL-250 m (between $250 - 300m$), elements are defined with C-PML material by respecting the implementation of C-PML in the 2D SEM code (See Chapter 4.2.2). In all simulations, input motion is inserted as incident wave motion condition by multiple point sources all along the GL-250 m depth level. In other words, all the GLL points at GL-250 m are defined with the same incident motion imposed as input signal. Total element number in the media is 7326 and total node number is 7582.
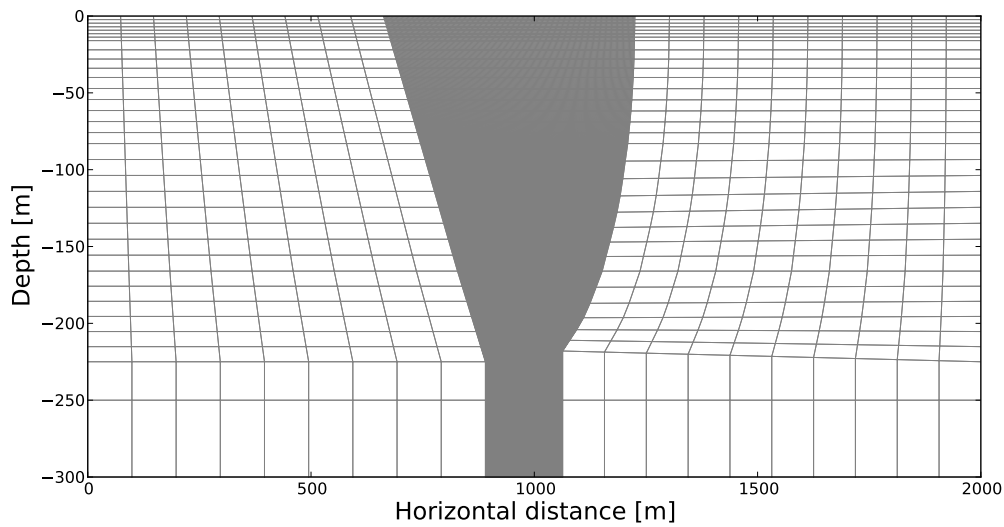
Fig. 5.6 2D mesh grid of the 2D model.
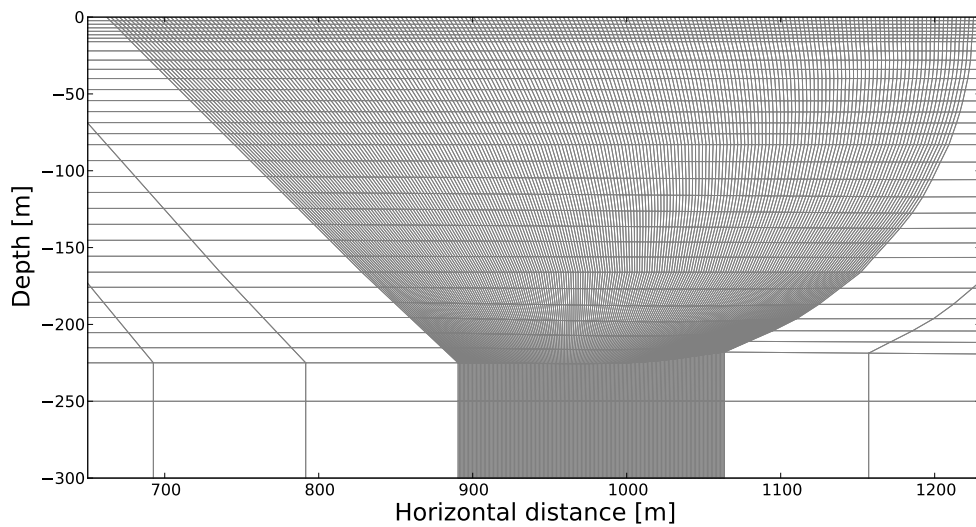
Fig. 5.7 2D mesh grid of the basin section of the 2D model .

For the evaluation of simulations, a number of receivers are defined at several depth levels. Table 5.6 displays the vertical coordinates of receiver distribution with the range of horizontal coordinates. In the same table, corresponding soil layer and total number of receivers at each depth are also specified. To save velocity values, receivers are defined at each 10

meters on the specified horizontal range for the corresponding depth level (See Figure 5.8). Subsurface receivers are disposed inside the basin in the middle of soil layers and close to layer boundaries.

Table 5.6 Vertical coordinates, horizontal coordinate ranges, corresponding soil layer number and total station number at the depth for the receivers used for saving velocity parameter in the 2D sedimentary basin model.

Vertical coordinate [m]	Horizontal coordinate range [m]	Soil layer	Station number
0.0	500-1500	1	101
-1.0	680-1220	1	55
-3.5	680-1220	1	55
-6.0	680-1220	1	55
-8.0	680-1220	2	55
-11.5	680-1220	2	55
-15.0	680-1220	2	55
-17.0	680-1220	3	55
-28.0	700-1220	3	53
-39.0	720-1220	3	51
-41.0	720-1220	4	51
-61.5	740-1200	4	47
-82.0	760-1200	4	45
-84.0	760-1200	5	45
-124.5	800-1180	5	39
-165.0	840-1140	5	31
-167.0	840-1140	6	31
-195.5	860-1100	6	25
-224.0	900-1000	6	11
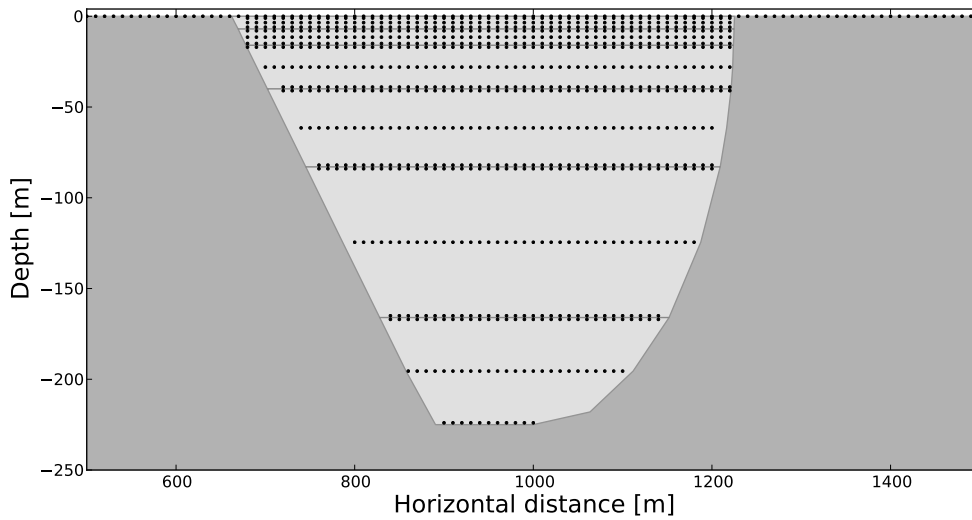
Fig. 5.8 Velocity receivers located on the 2D model.

Another feature added to the 2D SEM code is the possibility of saving stress-strain parameters for nonlinear soils and stress path parameters for liquefiable soil layers on another set of receivers. Same depth level and horizontal coordinate range are used for these receivers. Differently than velocity receivers, they are defined at each 20 meters on the specified horizontal range for the corresponding depth level as detailed in Table 5.7. The distribution of station for these stations is displayed in Figure 5.9. This choice is made based on the idea of reducing the memory burden of the code for the analyses with longer duration. The code provides currently ASCII format output files and as another perspective, saving files in binary format could allow to reducing memory burden. Also, in a further study, the limitations of the code in terms of memory and rapidity is suggested to be examined on different computers and processors. For the analyses on this chapter, we continue with this composition of receivers. Additionally, for effective stress analyses, current shear modulus, current normalized deviatoric stress and current mean effective stress are saved into file at desired time intervals (for each $0.01s$ in the analyses of this chapter) for the same receivers used to save stress and strain parameters.

Table 5.7 Vertical coordinates, horizontal coordinate ranges, corresponding soil layer number and total station number at the depth for the receivers used for saving stress-strain and stress path parameters in the 2D sedimentary basin model.

Vertical coordinate [m]	Horizontal coordinate range [m]	Soil layer	Station number
0.0	680-1220	1	28
-1.0	680-1220	1	28
-3.5	680-1220	1	28
-6.0	680-1220	1	28
-8.0	680-1220	2	28
-11.5	680-1220	2	28
-15.0	680-1220	2	28
-17.0	680-1220	3	28
-28.0	700-1220	3	27
-39.0	720-1220	3	26
-41.0	720-1220	4	26
-61.5	740-1200	4	24
-82.0	760-1200	4	23
-84.0	760-1200	5	23
-124.5	800-1180	5	20
-165.0	840-1140	5	16
-167.0	840-1140	6	16
-195.5	860-1100	6	13
-224.0	900-1000	6	6
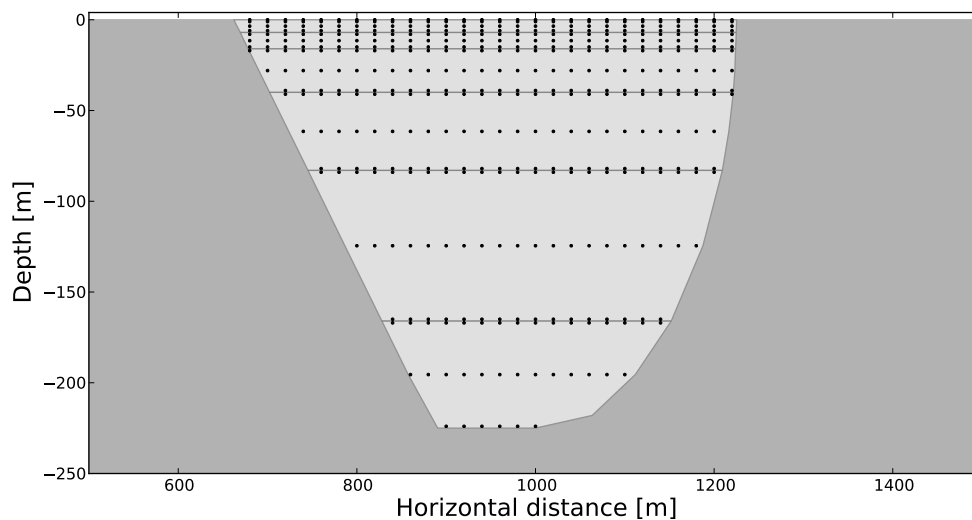
Fig. 5.9 Stress-strain and stress path parameter receivers located on the 2D model.

It should be noted that another option is added to SEM2DPACK code in order to write out the data (such as velocity, stress, strain, etc.) during the execution of the iterative analysis. In the default version of the code, data is saved at the end of last iteration. Such a feature allows saving the data before the end of all the computations. As a reminder, for the stations which do not correspond to any Gauss-Lobatto-Legendre (GLL) node of the model, an interpolation is applied on the values of the GLL nodes located in the same element as station (detailed in Chapter 1.2.3).

5.3 Simulations and results

5.3.1 Simulation models

In this section, the simulations that have been performed on the two-dimensional sedimentary basin model are presented. The 2D model is used in wave propagation analyses under different input motions and in different propagation models. As input motion, synthetic and real input motions are used. As synthetic motion, three broadband truncated Gaussian synthetic signals with different peak ground accelerations are employed. The data is provided by E2VP benchmark of EUROSEISTEST project material (Mauffroy et al., 2015 [107]). In Figure 5.10, acceleration time histories and Fourier amplitudes corresponding to these three signals are shown. The provided sources are outcrop signals so that the input motion is calculated by dividing the outcrop signals by 2. All the input motions are filtered below $10Hz$ by Butterworth lowpass filter. The PGA values associated with each impulse source amplitude correspond to PGA of the resultant elastic surface response under elastic outcrop rock conditions. For example, the first signal (top panel) has a PGA of $0.245m/s^2$ (before filtering is applied). The resultant surface motion in an elastic medium under the loading of this signal is $0.49m/s^2$, which is equal to $0.05g$. From here on, the synthetic input signals are named by these PGA values ($0.05g$, $0.10g$ and $0.25g$).
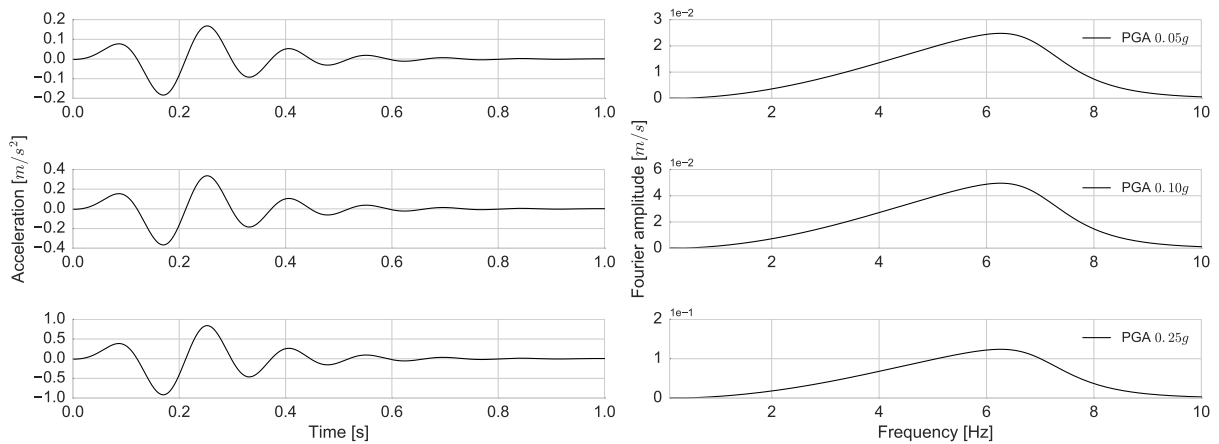
Fig. 5.10 Acceleration time histories (left column) and Fourier amplitudes (right column) of impulse sources with PGA 0.05g (top), PGA 0.10g (middle) and PGA 0.25g (bottom).

Even though we follow the study of Gélis and Bonilla (2014) [53], we do not use the same synthetic signals of their study (three Gabor signals with different PGA with energy content in [0-20] Hz). Since we model pore pressure effects in the soil as well as nonlinearity, possible higher strain levels in the media could lead the soil to higher softening (more decrease in shear velocity). In order to take into account this effect, the model requires finer mesh which reduces the time step of simulations. Thus, this study is limited to 10 Hz instead of 20 Hz and we prefer another input source in which the energy distribution is rather in [0-10] Hz.

Additionally, further analyses are performed with the 1994 Northridge earthquake records are used (Hartzell et al., 1996 [63]). For simulations with real input motion, recorded outcrop signals of past Northridge earthquake that are used in the models under uniaxial loading condition in P-SV model are shown in Figure 5.11 in time and frequency plans. Lowpass Butterworth filter below 10 Hz is applied to all the components. The strongest motion is recorded in *EW* component with a PGA of 3.68m/s^2, whereas the PGA is 2.20m/s^2 on *NS* component and 0.72m/s^2 on vertical component. The records are scaled by 0.5 such that the PGA of the real input motion is between those of the second and the third synthetic signals. In frequency plan, it is seen that the energy content is concentrated at relatively lower frequencies (< 4 Hz) compared to synthetic signals.
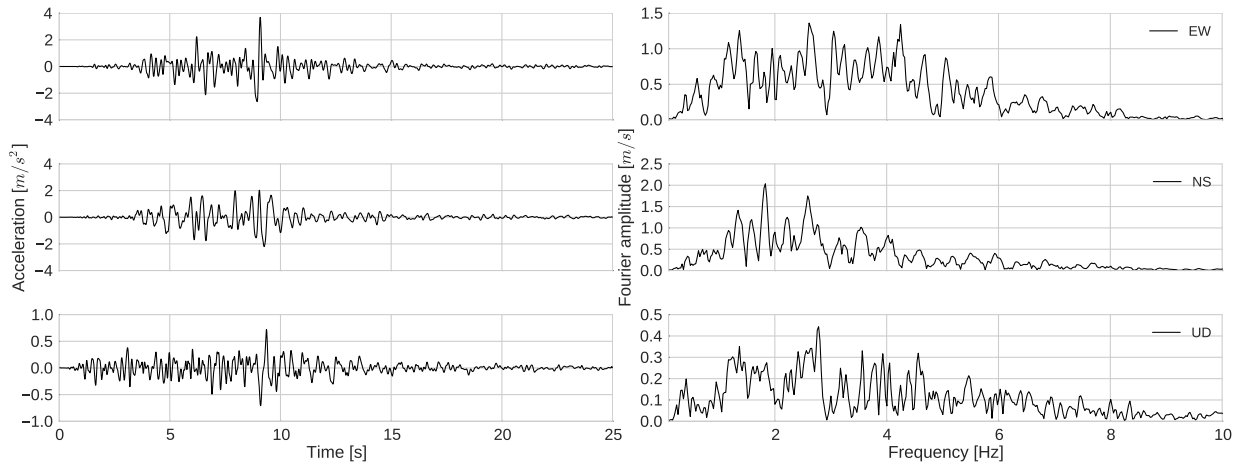
Fig. 5.11 Acceleration time histories (left column) and Fourier amplitudes (right column) of Northridge earthquake records for EW component (top), NS component (middle) and vertical component (bottom).

A representation of the simulations is given in Figure 5.12. For three loading conditions under three different synthetic signal input motions, P-SV and SH propagation models are computed. On each of these models, effective and total stress analyses are performed. The imposed input motion in SH model is the same as the input motion defined for P-SV model so that in P-SV model uniaxial loading condition is defined. For the purpose of comparison, viscoelasticity analysis is performed on SH model.

For the simulations under Northridge input motion, P-SV models with uniaxial loading conditions are created. For these models, *EW* input motion is used as input signal and effective and total stress analyses are performed.
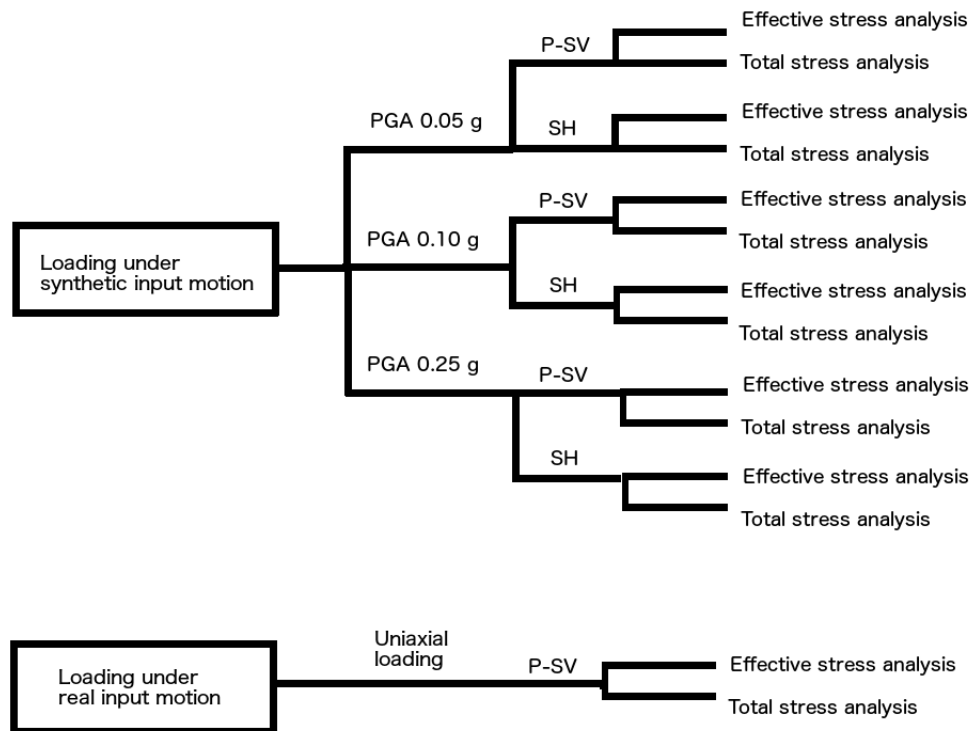
Fig. 5.12 Representation of studied test cases with the two-dimensional sedimentary basin model.

Duration of the simulations with the synthetic input signals is set to $7s$ for the total time for propagation inside the basin to be sufficient (for input motion duration of 1 s), whereas for simulations with Northridge source, it is set to $30s$. The time step used in all the models is $1.10^{-5}s$. In the following section, the results obtained in these analyses are shown and discussed in detail.

5.3.2   Results

In this section, the obtained results in P-SV and SH model effective and total stress analyses for the simulations under the loading of impulse signals are analyzed. Then, a preliminary analysis under real input motion is performed. In Gélis and Bonilla (2012 [52], 2014 [53]), a similar basin with same geometrical features as our 2D basin model has been analyzed for different assumptions of basin soil rheology. In their study, P-SV wave propagation is compared between viscoelasticity and visco-elastoplasticity models in order to clarify

the nonlinearity effects in the basin. In the same study, nonlinearity is taken into account for total stress analysis. In our study, soil nonlinearity is modeled for P-SV and SH wave propagation in total and effective stress analyses. In the following, first, the viscoelastic basin response in P-SV and SH models is presented and compared to viscoelastic basin response of P-SV model in Gélis and Bonilla (2014) [53] and SH model of the same authors. Second, the nonlinear basin response is analyzed for total and effective stress approaches under the three loading conditions in SH propagation model. Afterwards, same analyses are also performed for the P-SV model. Then, the nonlinear basin response under real input motion is analyzed for total and effective stress analyses. Lastly, the conclusions drawn from these analyses are discussed in detail.

Viscoelastic basin response of P-SV and SH models

As mentioned above, SH wave propagation modeling is not included in Gélis and Bonilla (2014 [53]. As a preliminary verification test, we create a reference model where the basin and bedrock soil constitutive model is defined with viscoelasticity for P-SV and SH wave propagation. First, the spectral ratio of basin response in this reference P-SV model is compared to the horizontal component of P-SV model in Gélis and Bonilla (2014) [53]. The spectral ratios are calculated by means of FFT values of surface acceleration time histories. FFT values of basin surface receivers are divided by the geometric mean FFT values of bedrock surface receivers. All the spectral ratios in this chapter are calculated in this way. Figure 5.13 displays this comparison. We see that in P-SV model, the fundamental frequency corresponds to 1.25 Hz. At higher frequencies, amplifications are noted in the middle of the basin. The P-SV wave propagation is seen to be influenced by the basin asymmetry such that close to right basin boundary greater values are calculated in spectral ratios. Resultant distribution patterns inside the basin are considerably close in two methods despite slightly stronger amplifications in our model. These differences could be possibly related to differences in mesh definition in two studies.
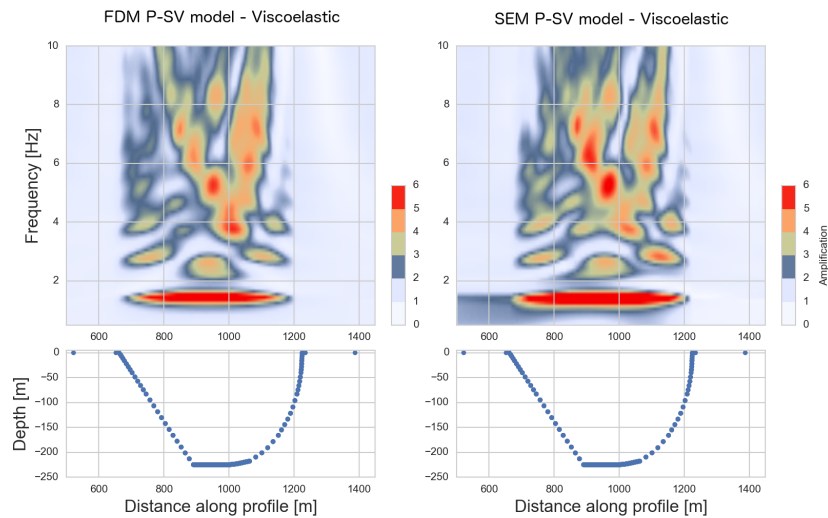
Fig. 5.13 Spectral ratio distribution of the viscoelastic basin surface response for horizontal component of P-SV model of Gélis and Bonilla (2014) [53] (top) and P-SV model of our study (bottom) on the frequency band $0.1 - 10 Hz$.

A similar comparison is made between SH models in Figure 5.14, where the SH model results are provided by Céline Gélis. The two solutions are very similar. We remark that in P-SV model, the fundamental frequency corresponds to 1.25 Hz while this value is reduced to 1 Hz in SH model. SH model distribution pattern does not exhibit the same asymmetry which is present in P-SV model. Also, in SH model, high frequency motion content is amplified close to basin edges. In Section 2.2 of this chapter, the approximate shape factor the basin is calculated and 2D resonance effects are found to be dominant than lateral effects for SH wave propagation. Stronger amplifications close to basin edges in SH model can be related to this effect.
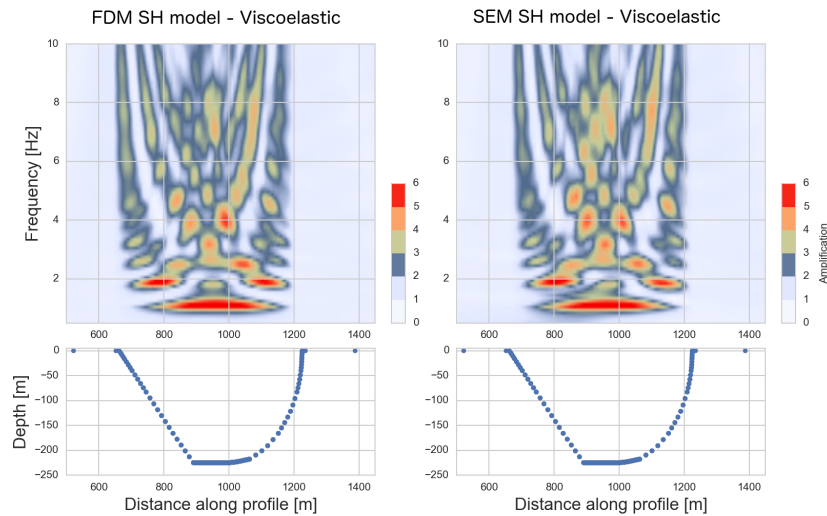
Fig. 5.14 Spectral ratio distribution of the viscoelastic basin surface response for horizontal component of SH model of Gélis and Bonilla (2014) [53] (top) and SH model of our study (bottom) on the frequency band $0.1 - 10Hz$.

In addition, Figure 5.15 displays the horizontal particle velocity components at free surface of P-SV model (top panel) and SH model (bottom panel) for viscoelasticity consideration. The first incidence of the waves from bedrock towards the basin is noted before 0.5 seconds. Following inner reflections inside the basin, on the other hand, show differences in P-SV and SH models. In P-SV model, an asymmetrical propagation results from smoother reflections from right side of the basin. The propagation in both models is attenuated in 2 seconds.
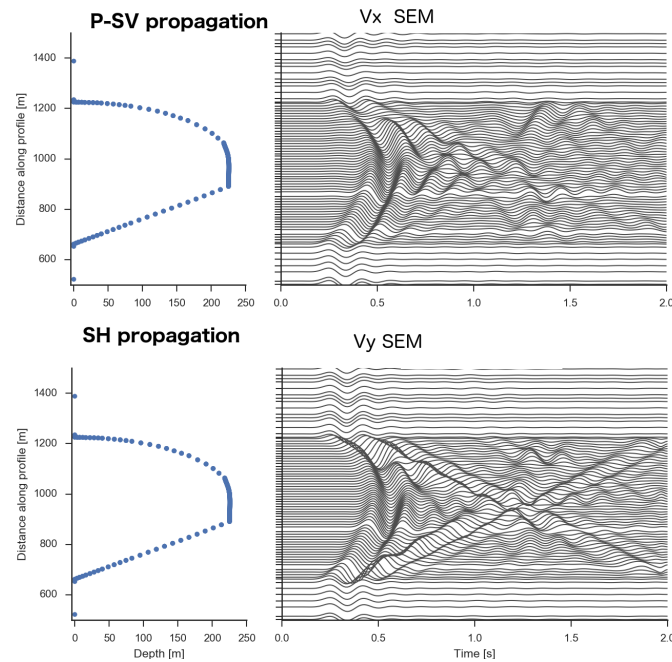
Fig. 5.15 The horizontal particle velocity components at free surface of P-SV model (top panel) and SH model (bottom panel) for viscoelasticity consideration in the 2D basin model.

In Gélis and Bonilla (2012 [52], 2014 [53]), a similar basin with same geometrical features as our 2D basin model is studied for viscoelastic and visco-elastoplastic considerations of the basin media. In this latter, nonlinear basin response is compared between loading conditions with synthetic input signal and a real input source which possess the same PGA values. The authors have shown that the content of input source plays more important role than PGA values and they propose to use peak ground velocity (PGV) as one of the key parameters to see nonlinearity effects. Also, PGV parameter has been used as strain proxy by PGV/V_{s30} in assessment of soil nonlinearity (Idriss, 2011 [72]; Chandra, 2016 [22]; Guéguen, 2016 [57]). For this reason, in this study, one of the parameters that we refer to in our comparative analyses is PGV. In Figure 5.16, we show maximum PGV distribution in the basin for viscoelasticity on SH model for the impulse source with PGA 0.05g. Highest values are concentrated in very superficial depth of the basin in the middle section and at basin edges. The maximum value of PGV all over the basin is calculated in the middle section (900-100 m) of the surface with 0.0421m/s. Underneath the superficial layers, maximum PGV values are weaker and several patches with relatively higher values are remarked. Most of these patches are concentrated on 900-1000 m range where strong vertical reverberations are expected to occur. Considering the basin in three sections consisting of left side where the effect of sharp basin boundary is seen, right side where the smooth boundary effects are dominant and

middle section where most of the reflections gather, patches are seen in the zones with more reflections. Also, in layer 3 (GL-16 - GL-40 m), close to basin edges similar patches are noted.
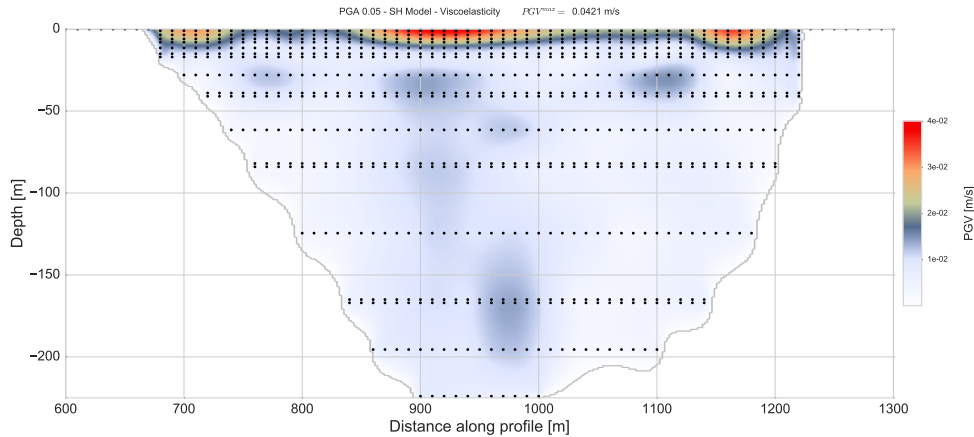
Fig. 5.16 Peak ground velocity distribution inside the viscoelastic basin media for SH model of the 2D sedimentary basin model under loading of impulse source with PGA 0.05g.

Nonlinear basin response of SH model

In this section, nonlinear response of the 2D sedimentary basin model is analyzed for total and effective stress approaches for the three loading conditions on SH model. First, for total stress analysis, the results are compared with respect to maximum strain distribution, PGV distribution and spectral ratios in the basin. Then, the same analysis is done for effective stress analysis.

Total stress analysis   Figure 5.17 displays the maximum strain distribution in the basin for total stress analyses on SH models loaded under the three input signals. The distribution is calculated by normalizing maximum strain at each point by the maximum strain in the basin. The distribution for each loading condition is very similar. Highest strain values are concentrated on basin surface and superficial layers in the basin. In particular, in the middle section of the basin surface, the highest strain values are calculated. In the first loading case (PGA 0.05g), maximum strain value overall the basin is 0.0071%. This value is increased to 0.0152% for the second case where the input motion PGA is 2 times stronger (PGA 0.10g). Under the loading with PGA 0.25g, maximum strain of the model is 0.0395%,

which is approximately 5 times greater than the first case. In SH model, the maximum strain distribution is not influenced significantly by increasing input motion intensity. Only slight damping in underlying basin layers are noted under stronger input motion. Maximum strain values overall the basin increase proportionally to PGA level.
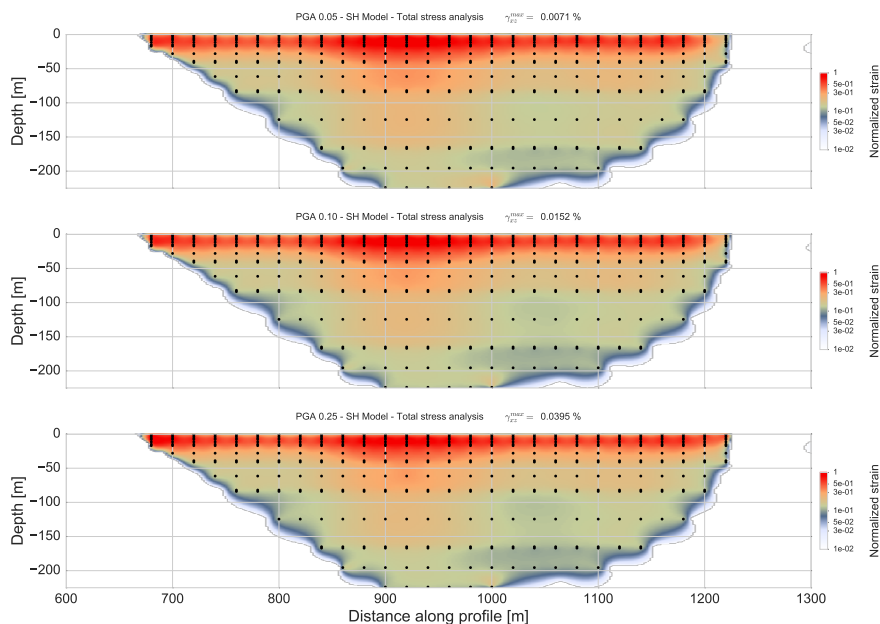
Fig. 5.17 Maximum strain distribution of the basin for *yz* component of total stress analyses on SH models on the 2D sedimentary basin model under loading of impulse source with PGA 0.05*g* (top), PGA 0.10*g* (middle) and 0.25*g* (bottom).

In Figure 5.18, PGV ratio distribution for total stress analyses on SH model is shown. PGV ratios are calculated by normalizing the PGV values by the PGV values of the first impulse source (PGA 0.05*g*), such that in top panel of the figure, the ratio is shown for the loading condition with *PGA*0.10*g* and in bottom panel for *PGA*0.25*g*. For the loading condition with *PGA*0.10*g*, the maximum ratio is 2.3 approximately. Most of the basin has stronger PGV than the loading condition of *PGA*0.05*g*. However, in surficial soil layers and in the patches close to basin edges, the PGV ratio is weaker. Also, in bottom patch which is the transition zone from deepest basin bottom and right section of the basin, weaker PGV ratios are noted. We see that under 2 times stronger input motion, everywhere in the basin PGV values increase. On the other hand, the distribution of these values is influenced by soil nonlinearity. Since under nonlinearity, shear modulus weakening takes place such that shear

wave velocity is decreased, we see slower propagation in surficial layers. By increasing the input motion PGA to $0.25g$, maximum PGV ratio is increased to more than 6. In the distribution of PGV ratio, we remark higher contrast in the basin. We also note that the distribution pattern remains the same as previous loading condition. In other words, same zones are concerned from higher nonlinearity, so that we see the same patches in the basin.
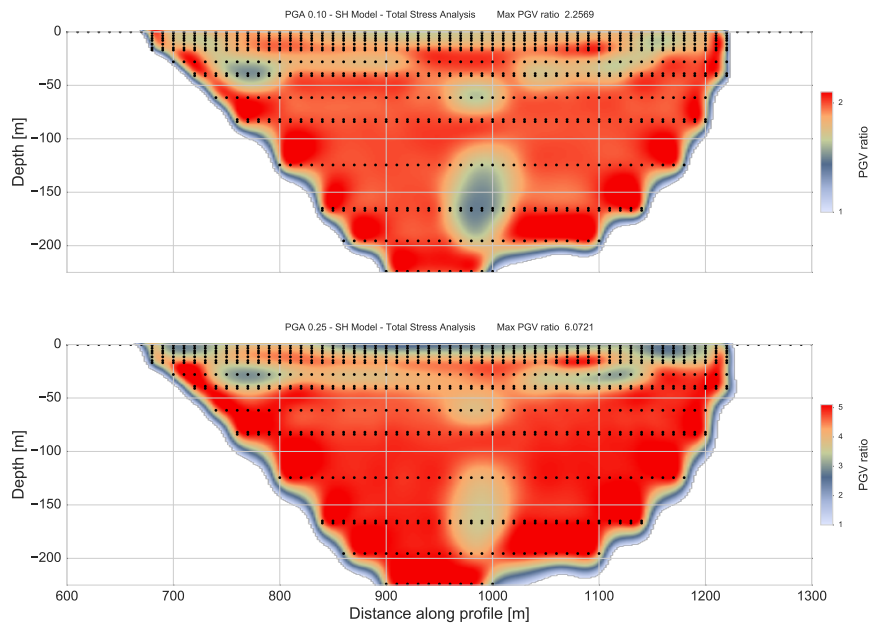
Fig. 5.18 Peak ground velocity ratio distribution of the basin for total stress analysis of SH models of the 2D sedimentary basin model under loading of impulse source with PGA $0.10g$ (top) and $0.25g$ (bottom).

In addition, the surface response is analyzed in frequency plan for three loading conditions in Figure 5.19 by spectral ratio distribution. High values above $9Hz$ are noted for the second and third loading cases. For the first loading condition, which does not result in high strain level (maximum strain calculated as 0.0071% in Figure 5.17), the spectral ratio distribution in the basin is similar to viscoelastic case of SH model. Slight attenuation of motion above $4Hz$ is noted under nonlinearity compared to viscoelasticity. Increasing nonlinearity with second loading condition intensifies this attenuation effect particularly inside the basin. For the most nonlinear case with the third loading condition, very strong damping is seen in the basin and close to basin edges. On the other hand, the fundamental frequency is not changed,

only peak values are deamplified under stronger input motion.
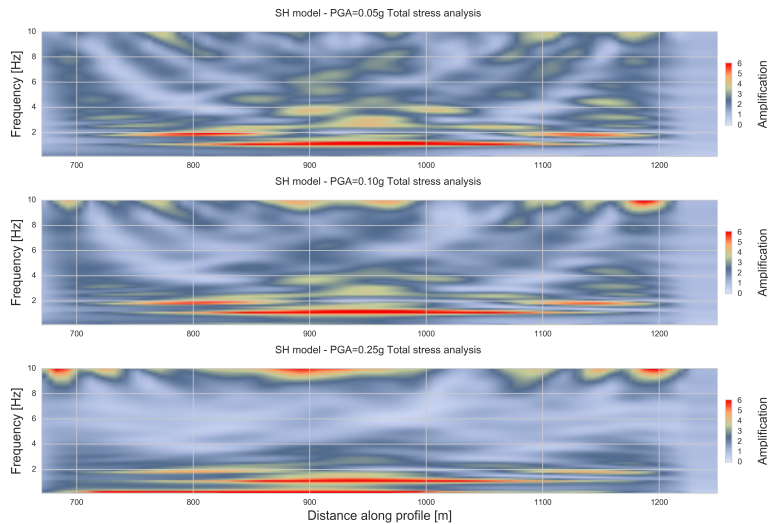
Fig. 5.19 Spectral ratios of the basin surface for total stress analysis of SH models of the 2D sedimentary basin model under loading of impulse source with PGA 0.05g (top), PGA 0.10g (middle) and 0.25g (bottom).

Effective stress analysis Figure 5.20 displays the maximum strain distribution in effective stress analyses of SH models for the three loading conditions with impulse source. For the first loading condition with PGA 0.05g (top of the figure), the maximum strain distribution is very similar to total stress analysis with slight differences. Highest strains are calculated in the superficial soil layers, in particular in middle section and in the zones close to basin edges. Also, the maximum strain value calculated in the effective stress analysis (0.0073%) is very close to total stress analysis (0.0071%). Since the nonlinearity level is very low under the input motion with PGA 0.05g, there is no significant pore pressure effects in liquefiable soil layers so that both approaches give very similar results. Under a more intense loading, attenuation throughout the basin is noted.

Points with the highest strain values remain the same. It should be noted that maximum strain values in effective and total stress values are very close (0.0152% in total stress analysis and 0.0196% in effective stress analysis). Moreover, when the input motion PGA increases to 0.25g, a significant contrast increase is remarked in the basin. Highest strain

values are concentrated in superficial layers. Maximum strain value calculated in the basin is 2 times higher than total stress analysis (0.0395% in total stress analysis and 0.0850% in effective stress analysis). We see that all the basin is concerned from nonlinearity and the distribution of maximum strain is strongly dependent on nonlinearity level, thus on input motion.

We also note that the middle section of the basin where vertical reflections occur strongly has relatively higher strain than left and right sections at the same depth. This remains the same for each loading condition. Under increasing contrast, it becomes more visible. We can conclude that basin shape influences the soil nonlinearity in the basin based on the distribution of maximum strain.
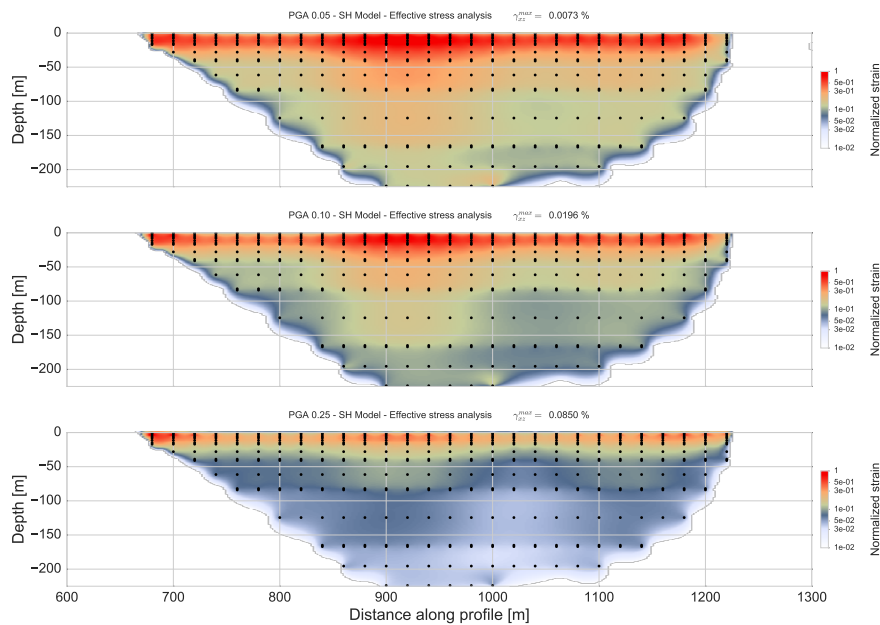
Fig. 5.20 Maximum strain distribution of the basin for *yz* component of effective stress analyses on SH models on the 2D sedimentary basin model under loading of impulse source with PGA 0.05*g* (top), PGA 0.10*g* (middle) and 0.25*g* (bottom).

In Figure 5.21, the distribution of PGV ratios between effective stress analysis of the second and third loading conditions with the first loading condition. For the second loading condition (input motion with PGA 0.10*g*), PGV ratio distribution is very similar to total stress analysis. Attenuation in surficial layers and patches are slightly increased. In other words, we do not see a strong influence of effective stress analysis in PGV ratio under this

loading. Under stronger nonlinearity with the input motion of PGA $0.25g$, pore pressure effects in superficial layers are seen here with significant increase in contrast inside the basin. The distribution manner of PGV ratio remains similar. However, relatively more nonlinear patches and surficial layers become more nonlinear compared to the rest of the basin. Also, the whole middle section of the basin is influenced by increasing nonlinearity as seen in the decrease of PGV ratio in this zone. Side sections of the basin hold the higher PGV values.

Furthermore, considering both maximum strain distribution and PGV ratio distribution, higher nonlinearity due to stronger input motion increases the pore pressure development in the first two layers of the basin. This results in higher strain values in those layers, as a result lower shear velocity. This increase in nonlinearity level of superficial layers influences the underlying layers as well such that in PGV ratio distribution, most of the basin has smaller PGV ratios.
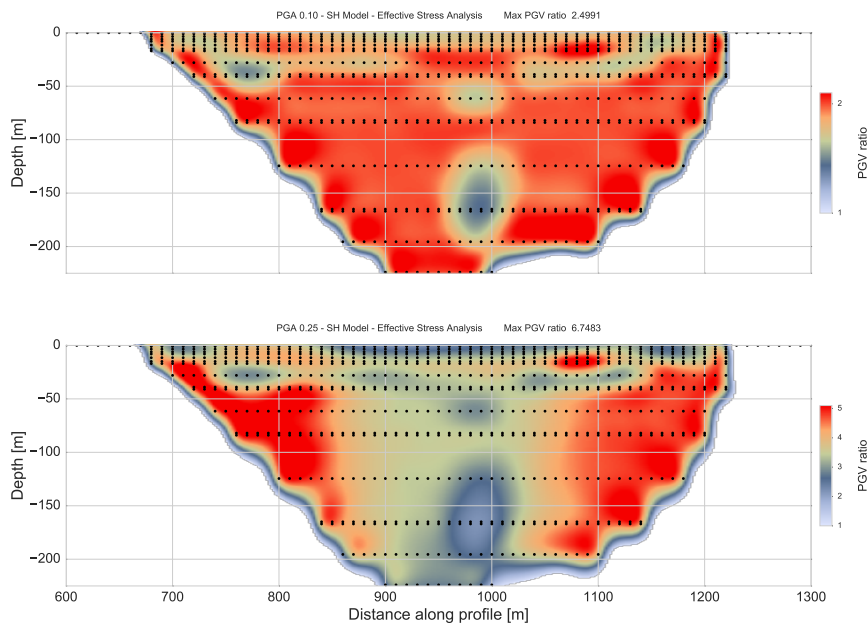
Fig. 5.21 Peak ground velocity ratio distribution of the basin for effective stress analysis of SH models of the 2D sedimentary basin model under loading of impulse source with PGA $0.10g$ (top) and $0.25g$ (bottom).

Corresponding spectral ratios of the three loading conditions are shown in Figure 5.22. The effective stress analysis in first loading condition is shown to have very slight effects

in soil nonlinearity of the basin. This can be seen in frequency plan as well. The spectral ratio distribution is very similar to total stress analysis. By increasing input PGA, the high frequency motion (> 4 Hz) is attenuated inside the basin and at basin edges. High frequency motion above 9 Hz is attenuated under pore pressure effects for the second loading condition. Under the third loading condition, the attenuation in the same locations become very strong. Low frequency motion becomes dominant everywhere in basin surface. Compared to total stress analysis, differences are more remarkable for the third loading condition. In the middle section and basin edges, the motion below 4 Hz is amplified in effective stress analysis. This can be related to the effect of pore pressure rise. For higher pore pressure level, the soil strength decreases and due to the lower velocity values of the soil, waves have longer period than total stress analysis.
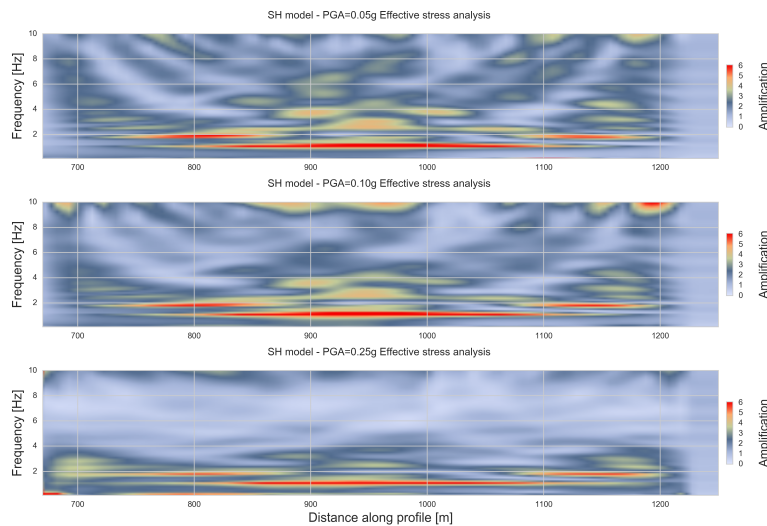
Fig. 5.22 Spectral ratios of the basin for effective stress analysis of SH models of the 2D sedimentary basin model under loading of impulse source with PGA 0.05g (top), PGA 0.10g (middle) and 0.25g (bottom).

Nonlinear basin response of P-SV model

In this section, nonlinear response of the 2D sedimentary basin model is analyzed for total and effective stress approaches for the three loading conditions on P-SV model. First, for total stress analysis, the results are compared with respect to maximum strain distribution, PGV distribution and spectral ratios in the basin. Then, the same analysis is done for

effective stress analysis.

Total stress analysis   Figure 5.23 displays the resultant maximum strain distributions of the basin for total stress analyses on P-SV model under each loading condition. The distribution is made after normalization of values by the maximal value in the basin. The maximum strain value overall the basin is 0.0074% under the first loading condition with PGA $0.05g$ (top of the figure). Surficial layers of the basin are concerned by highest values of strain the most. In particular, the middle section of the basin and basin edges have relatively higher strains than the rest of the basin. On left side of the basin, the zone with relatively higher strains extend more than the right basin edge. This can be interpreted as a result of stronger wave propagation along the left basin edge due to sharper angle of left basin boundary. Again, the stronger wave propagation in the middle of the basin results in higher strains in this zone. In Guidotti et al. (2011) [58], different considerations of model geometry and material properties are studied on 2D trapezoidal models exposed to vertically propagating SV waves. In their study, they show that the nonlinearity results in localization of 2D effects close to the edges of the model. Also, in Gélis and Bonilla (2012 [52], 2014 [53]), this amplification effect is shown in 2D asymmetrical basin models similar to our model. The increase of PGA from $0.05g$ to $0.10g$ does not lead to significant changes in maximum strain distribution of the basin (middle panel of the figure). The maximum strain overall the basin is approximately 2 times higher under the input motion that is 2 times stronger in PGA. Given the fact that such a change in input motion results only in proportional amplification of strains in the same way at each point of the basin, we can conclude that the nonlinearity level triggered by the impulse signal with PGA 0.10 is not high. On the other hand, under the loading of input motion with PGA $0.25g$, maximum strain distribution changes remarkably. The significant difference between midsection of basin surface and the rest of the basin is less pronounced. Also, the maximum strain is increased to 0.0641%, which is approximately 9 times greater than maximum strain under the input motion with PGA 0.05. Furthermore, we denote that layering is seen for each loading condition. In other words, the velocity contrast between superposed layers result in visible blocks in strain distribution of the basin. Such a result due to layering is also obtained in Gélis and Bonilla (2014) [53], in which they showed a relatively smooth distribution of maximum strain distribution in a model with gradually increasing velocity profile.

Compared to SH model, for the cases with PGA 0.05g and 0.10g, P-SV and SH model maximum strains are very close, while under PGA 0.25g the P-SV model undergoes 1.6 times higher maximum strain. Also, for this loading case, while the influence of increasing soil nonlinearity results in remarkable changes in maximum strain distribution of the basin, in SH model we do not see such a strong effect of nonlinearity. We can explain this by the fact that two models do not propagate in the same way given the physical differences. Such result indicates that nonlinear soil response is also affected by propagation model choice.
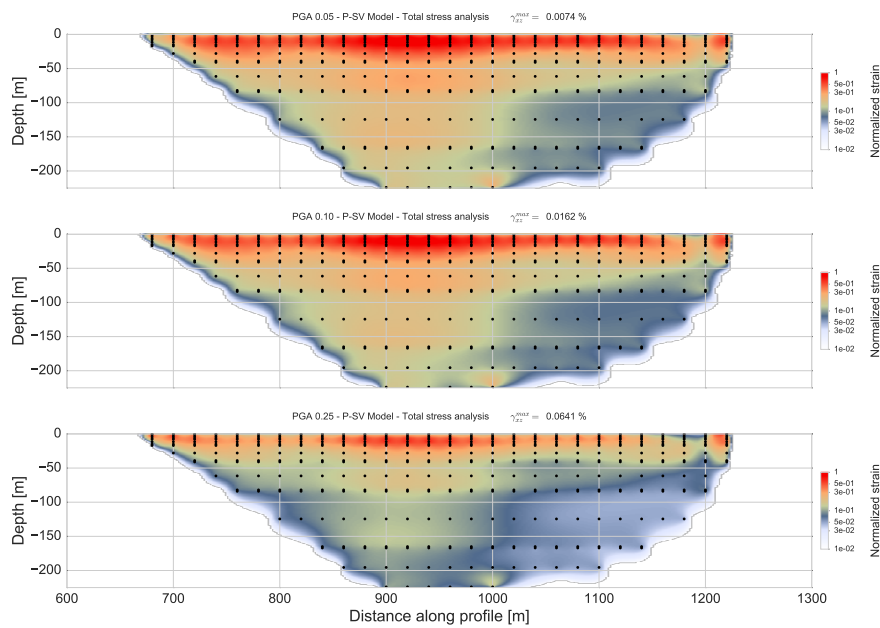
Fig. 5.23 Maximum strain distribution of the basin for *xz* component of total stress analyses on P-SV models of the 2D sedimentary basin model under loading of impulse source with PGA 0.05g (top), PGA 0.10g (middle) and 0.25g (bottom).

In Figure 5.24, total stress analyses of the second and third loading conditions are compared by means of PGV ratio distribution of the basin. for the second loading condition, the distribution of PGV ratios is similar to SH model. In basin surface and patches close to basin edges and basin bottom, the difference between the second and first loading conditions become higher. Again, similarly to SH model, the contrast between these more nonlinear zones and the rest of the basin become more apparent under stronger input motion due to higher nonlinearity level. Maximum PGV is approximately 5 times higher than the first

loading condition.
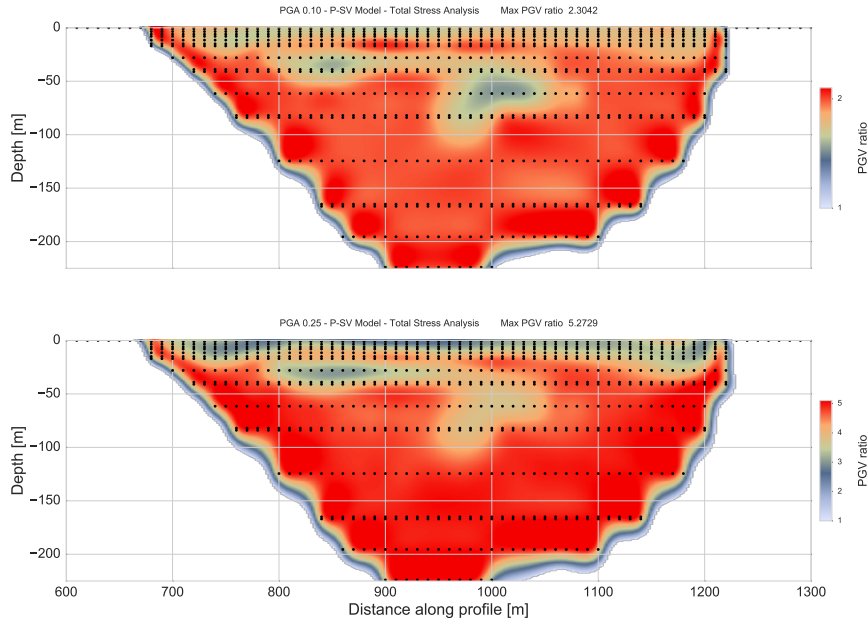
Fig. 5.24 Peak ground velocity ratio of the basin for total stress analysis on horizontal component for P-SV models of the 2D sedimentary basin model under loading of impulse source with PGA 0.05g (top), PGA 0.10g (middle) and 0.25g (bottom).

In order to analyze the results in frequency plan, spectral ratios are calculated for horizontal direction of the P-SV model. The spectral ratios on horizontal direction are calculated by means of division of spectral ratios of FFT values of basin and mean bedrock similarly to SH model analyses. In Figure 5.25, corresponding spectral ratios are shown for each loading condition. Given the fact that soil does not become very nonlinear in the first loading condition, we can compare the spectral ratio for this condition to viscoelastic spectral ratio distribution of P-SV model of Gélis and Bonilla (2014) [53] (shown at left panel of Figure 5.13). Fundamental frequency is 1.25 Hz for both models and distribution pattern is very similar in two diagrams. High frequency motion is stronger in middle section of the basin and close to right edge. Differences in amplitudes can be related to nonlinearity and to the fact that two studies have similar but not identical basin shapes. In the second loading condition, slight attenuation over 4 Hz is noted everywhere in the basin. Very high frequency motion amplification (above 10 Hz) is also seen in P-SV model similarly to SH model. This amplification is enhanced under the

third loading condition, while the attenuation inside the basin due to nonlinearity becomes more significant. On the other hand, the fundamental frequency of the model does not change.
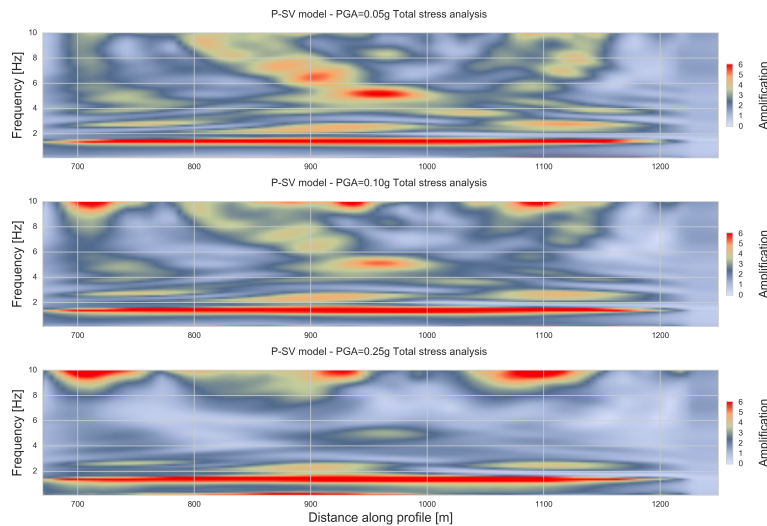
Fig. 5.25 Spectral ratios of the basin of total stress analysis on horizontal component for P-SV models of the 2D sedimentary basin model under loading of impulse source with PGA 0.05g (top), PGA 0.10g (middle) and 0.25g (bottom).

Effective stress analysis   Figure 5.26 shows the maximum strain distributions for effective stress analysis on P-SV model of each loading condition. Under the loading of impulse source with PGA 0.05g (top of the figure), Maximum value of strain is 0.0078% which is very slightly higher than total stress analysis (0.0074%). This also indicates that low level of nonlinearity under the input motion with PGA 0.05 does not trigger considerable pore pressure development in liquefiable soil layers. The middle section of the basin presents a contrast between other parts of the basin. While the input motion PGA is increased to 0.10g (middle of the figure), distribution pattern changes so that nonlinearity of superficial layers become more prominent. Maximum value of strain is approximately 1.5 times greater than total stress analysis. In other words, the input motions with PGA 0.05g and 0.10g do not result in remarkable differences in soil nonlinearity for total stress analysis, whereas in effective stress analysis the same input motion (PGA 0.10g) influences significantly the nonlinearity inside the basin. Furthermore, under stronger input motion (PGA 0.25g) as seen at bottom of the figure, attenuation in the basin becomes significant such that maximum

strain are concentrated on very superficial layers. The punctual amplification in basin corner is due to numerical interpolation. It is noted that at left basin edge, maximum strain ratio is amplified compared to the loading under the input motion with PGA 0.10g. In this example, the excess pore pressure development and consequent rigidity changes of superficial liquefiable soil layers trigger higher nonlinearity in superficial soil layers. As a result, propagating waves are rather trapped in these superficial layers (due to velocity weakening), so that soil nonlinearity close to basin edges become stronger that maximum strain increases. Also, it should be noted that maximum strain reached by the basin (0.0732%) under the loading with PGA 0.25g is not very different than total stress analysis (0.0641%). This can be interpreted as even under relatively small deformations ($< 0.1\%$), soil nonlinearity in the basin could change due to pore pressure effects.

In addition, maximum strain values are smaller than P-SV model for effective stress analysis as in total stress analysis. The distribution manner of maximum strain ratio is different in two models. In P-SV model, close to left section of the basin, maximum strain ratio is higher than the rest of the basin, while in SH model right section of the basin have higher ratios.
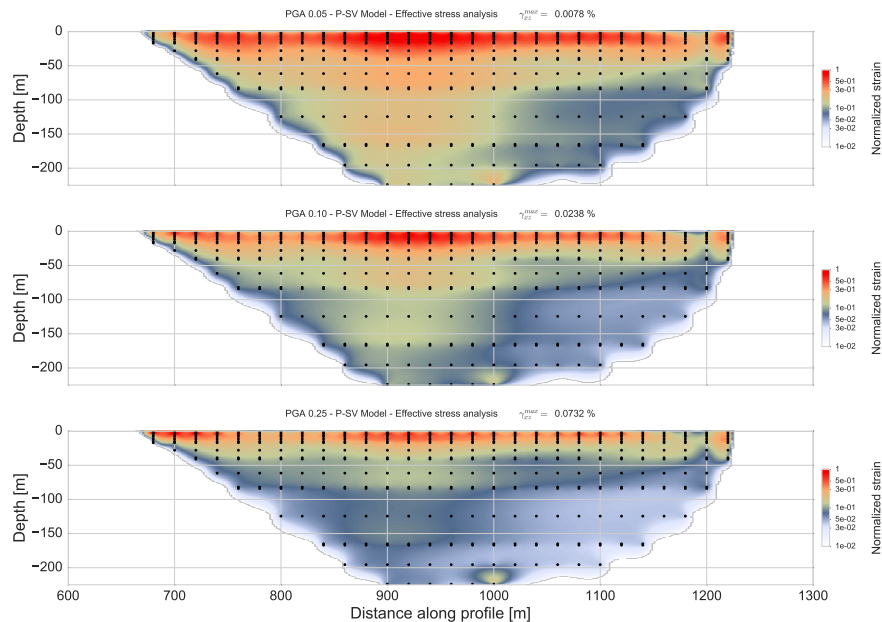
Fig. 5.26 Maximum strain distribution of the basin for *xz* component of effective stress analyses on P-SV models of the 2D sedimentary basin model under loading of impulse source with PGA 0.05g (top), PGA 0.10g (middle) and 0.25g (bottom).

Figure 5.27 displays the distribution of PGV ratio for the second and third loading conditions of effective stress analysis on P-SV model. For the second loading condition, higher PGV ratios are noted along basin boundaries, while inside the basin a slight decrease is seen. Similarly to total stress analysis, surficial layers and patches close to basin edges are more nonlinear such that the lowest PGV ratios are calculated in these zones. Under the loading of input motion with PGA 0.25g, a noticeable weakening in PGV ratios in the bottom layers of the basin is seen. The decrease of values is applied on the same patches where nonlinearity effect is more apparent under the second loading. For a 6 times stronger maximum PGV value in the third loading condition, effective stress analysis changes significantly basin nonlinearity such that the whole basin is concerned from PGV decrease compared to total stress analysis.
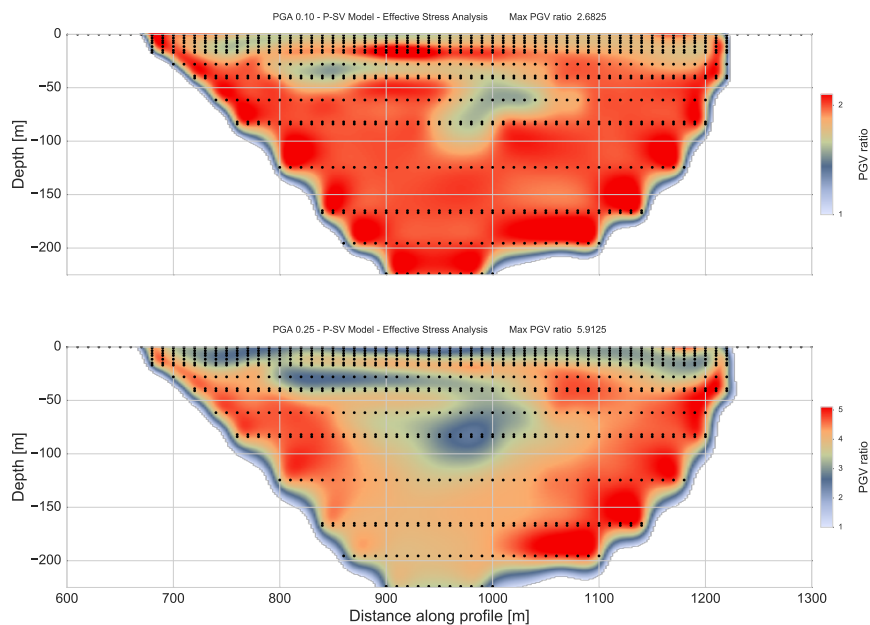
Fig. 5.27 Peak ground velocity ratio of the basin for effective stress analysis on horizontal component for P-SV models of the 2D sedimentary basin model under loading of impulse source with PGA 0.05g (top), PGA 0.10g (middle) and 0.25g (bottom).

In Figure 5.28, we compare the three loading condition in frequency plan by spectral ratio distribution. The first loading condition does not result in considerable change in spectral ratio distribution of basin response compared to total stress analysis, which is relevant considering the low level of nonlinearity and resultant poor pore pressure rise. For the

second loading condition, the surface motion above 4 Hz is damped under stronger PGA of input motion, particularly in the middle section of the basin surface. Then, the third loading condition results in a significant attenuation of the motion above 3 Hz. Below this frequency limit, the maximum values of spectral ratios are smaller for the third loading condition. Nonlinearity effect is mostly seen by attenuation of high frequency motion on basin surface. Compared to total stress analysis, low frequency motion ($< 4Hz$) is amplified at basin edges. We can associate these low frequency motion amplifications with further decrease of wave velocity under pore pressure rise.
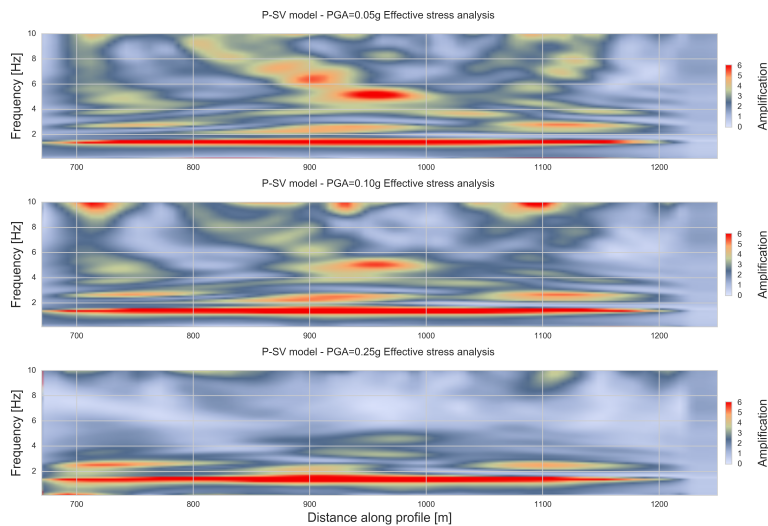
Fig. 5.28 Spectral ratios of the basin for effective stress analysis on horizontal component for P-SV models of the 2D sedimentary basin model under loading of impulse source with PGA 0.05g (top), PGA 0.10g (middle) and 0.25g (bottom).

Comparing P-SV and SH models, pore pressure effects lead to similar changes in both models by energy attenuation in surficial layers. The relative changes of PGV ratio inside the basin due to pore pressure effects are very similar in P-SV and SH models. Also, in frequency plan, the low frequency motion amplification in the basin is seen in both models.

Discussion

In previous section, total and effective stress analyses of P-SV and SH models are analyzed and evaluated for the loading conditions of input motion with different PGA values. We

have shown that the basin media becomes more nonlinear under increasing intensity of input motion. The nonlinearity of the basin leads to differences in strain distribution of the basin. As a result of higher nonlinearity, excess pore pressure development becomes more effective in wave propagation inside the basin media. Rigidity changes in liquefiable soils may result in velocity decrease in superficial soil layers and these layers become relatively more nonlinear than underlying layers. In addition, these changes in wave propagation due to total and effective stress analyses are dependent on propagation model choice (P-SV or SH model). The ultimate nonlinearity level is shown to be higher in P-SV model than SH model. Also, two models differ in terms of maximum strain distribution. However, the changes in soil nonlinearity of the basin and its effect on surface motion are found to be similar for both propagation models. In this section, we realize a further evaluation of the results. First, a comparison between total and effective stress analyses of P-SV model is made. Then, P-SV and SH models are compared based on effective stress analysis results. Lastly, a preliminary analysis is made on simulations with real input motion.

Comparison of total and effective stress analyses   In previous section, it has been shown that P-SV model results in higher maximum values in maximum strain and PGV ratios in the basin compared to SH model. For this reason, we use P-SV model for the comparison of total and effective stress analyses under the three loading conditions. Figure 5.29 displays the comparison of stress-strain curves at the middle of the first (top panel) and the second layer (bottom panel) between total and effective stress analyses of each loading condition. The values belong to the point which is located in the middle section of the surface at $x = 700m$, where strong nonlinearity effects have been calculated (See Figure 5.26).

As mentioned earlier, under the loading of impulse source with PGA $0.05g$, nonlinearity level in the basin is very low. Thus, stress-strain curves in both liquefiable layers are very similar except for small differences in layer 1. For the second case of loading (PGA $0.10g$), higher nonlinearity leads to more deformation in total stress analysis and the differences between total and effective stress analyses become more apparent in the first layer. The strength of the soil in the middle of the first layer weakens as the shear modulus (slope of the diagram) is lowered due to the rise of pore pressure excess. Even though the nonlinearity triggered under this loading condition is not very high (given the fact that ultimate deformations are 0.015% in effective stress analysis), pore pressure effects are visible in stress-strain curves. For the most nonlinear case where the input motion PGA is increased to $0.25g$, this phenomenon

becomes more evident in both layers. strength loss increases in effective stress analysis.
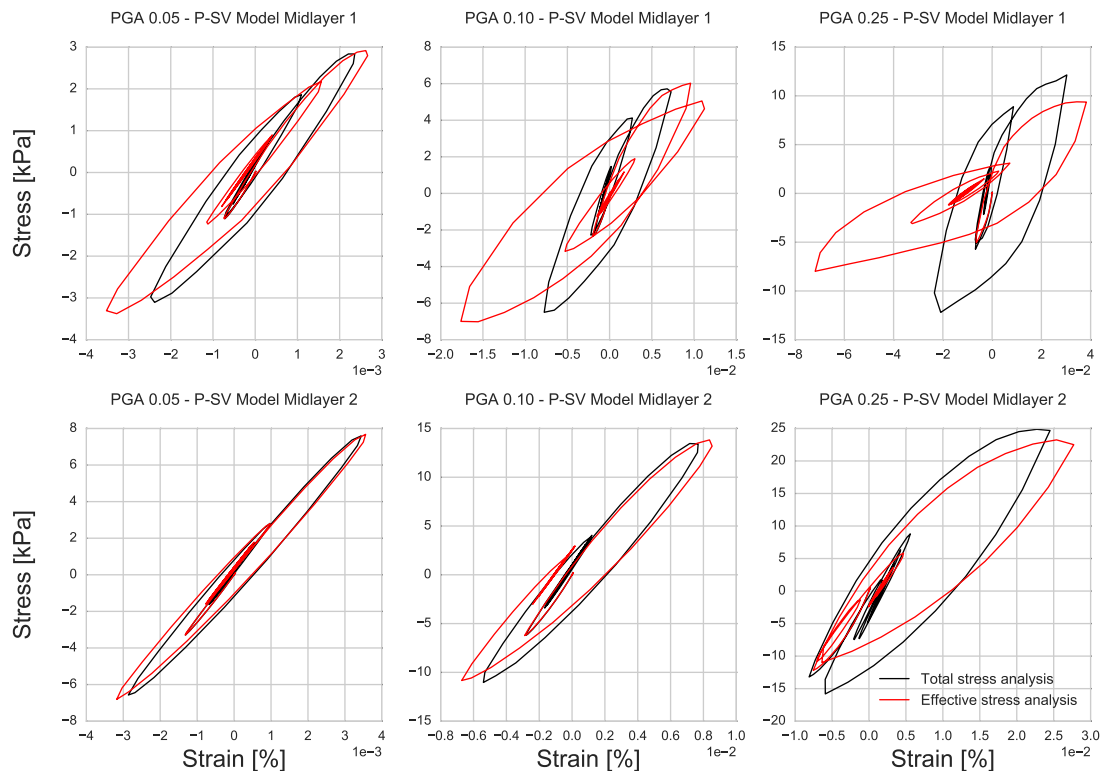
Fig. 5.29 Stress-strain curves at the middle of layer 1 (GL-3.5 m) (top) and layer 2 (GL-11.5 m) (bottom) for total stress analysis (in black) and effective stress analysis (in red) of P-SV model under loading of impulse source with PGA 0.05*g* (left), 0.10*g* (middle) and 0.25*g* (right).

Figure 5.30 shows the acceleration, velocity and displacement time histories for total and effective stress analyses on P-SV model for each loading condition. Again, the results correspond to $x = 900m$ surface location. It should be noted that acceleration and velocity values are filtered below 10 Hz with lowpass Butterworth filter. For the first case with PGA 0.05*g*, all the parameters are very similar even though stress-strain curves exhibit very slight differences. PGA for this condition is $0.8m/s^2$. While the input motion PGA is increased to PGA 0.10*g*, very slight differences in acceleration appear with initial attenuation and time shift. Although stress-strain curves for this condition represent notable differences between total and effective stress analyses at GL-3.5 m, we do not see the same level of difference in surface motion time histories. This could be related to low level of deformation that soil undergoes in this loading condition. For the last loading condition, acceleration and

velocity are damped and delayed in time under higher nonlinearity in effective stress analysis. In addition, for any of loading conditions, permanent displacement is null in total stress analysis, while in effective stress analysis the third loading condition leads to permanent displacement in the soil.
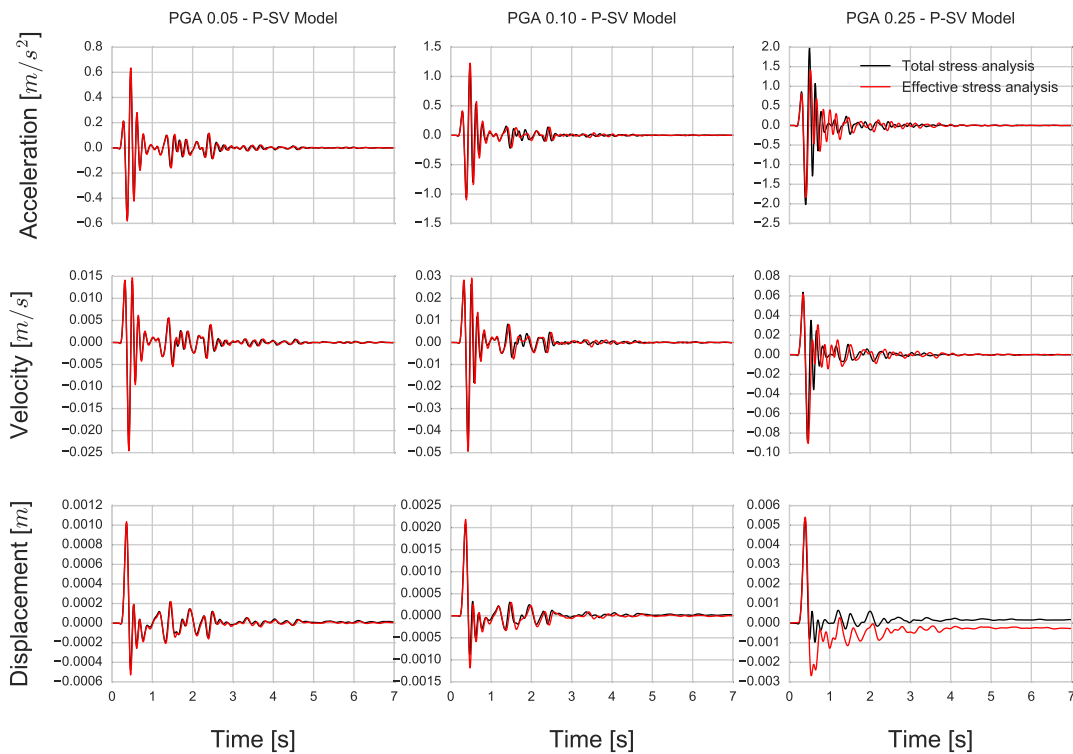
Fig. 5.30 Acceleration (top), velocity (middle) and displacement (bottom) time histories for total stress analysis (in black) and effective stress analysis (in red) of P-SV model under loading of impulse source with PGA 0.05g (left), 0.10g (middle) and 0.25g (right).

The strength changes of soil due to pore pressure development in effective stress analysis becomes more evident under increasing intensity of input motion. Therefore, the differences between total and effective stress analyses increases with the nonlinearity level of the soil triggered by the loading conditions. On the other hand, these differences are slighter in surface motion time histories, which can be related to the low level of ultimate deformation.

Comparison of P-SV and SH propagation models   In previous sections, it has been shown that P-SV and SH models exhibit differences in terms of maximum strain distribution

in different parts of the basin and ultimate level of nonlinearity. This has been related to the physical difference of propagation manners in two models. In this section, we compare P-SV and SH models based on effective stress analysis for each loading condition.

Figure 5.31 displays stress-strain curves (top panel), stress path (middle panel) and temporal change in normalized pore pressure excess (bottom) for the mid-level of the first soil layer. The comparison is made between P-SV and SH models under the three loading conditions for the left section of the basin surface ($x = 700m$). The soil behavior seen in stress-strain diagrams at this point is very similar in both models for each loading condition. For higher nonlinearity, slope change and strength loss increase. On the other hand, P-SV model exhibits higher nonlinearity at each loading condition than SH model. This is related to the fact that in the left edge of the basin (where the comparison is made), wave propagation is more intense in P-SV model, which is increases nonlinearity triggering and as a result ultimate deformation. Moreover, in stress path diagrams, under the first loading condition (PGA $0.05g$), the stress path follows continuous decrease in mean effective strength by remaining in contractive zone. The initial effective strength is reduced by approximately 20 % in P-SV model, while this value is slightly smaller in SH model. As a result of continuous contractive behavior, we see a continuous rise in pore pressure without oscillations. Corresponding to approximate 20 % decrease in effective strength, pore pressure is close to 20 % in P-SV model. In SH model, the same trend is remarked with smaller values such that pore pressure rise is 2 times lower than P-SV model (corresponding to approximately 10 % decrease in effective strength). Despite of the low level of pore pressure rise, in P-SV model stress-strain curves strength loss is apparent compared to SH model. By increasing input intensity 2 times (PGA $0.10g$), the decrease in soil strength reaches to 50 % in P-SV model whereas in SH model it is limited to 25 %. Soil behavior is contractive for both models. Accordingly, in pore pressure change, there is continuous increase until 50 % and 25 % of initial mean effective stress for P-SV and SH models, respectively. Lastly, for the case with input motion PGA $0.25g$, soil strength is reduced to 30 % of the initial mean effective stress with slight dilatant behaviors in both models. Since the applied deviatoric stress in the soil increases under this stronger loading condition, small transitions in curvature of stress path occur. This slightly dilatant behavior is seen with small and sudden decreases in pore pressure. In P-SV model, pore pressure excess reaches to 80 % of the initial mean effective strength, while in SH model it is close to 60 %. Despite high decreases in soil strength of the soil under the input motion intensity of PGA $0.10g$ and $0.25g$, resultant stress-strain curves do not lead the model to very high deformations. This is an outcome of the input motion content and monotony of the contractive soil behavior. In the study of Gélis and Bonilla (2012 [52], 2014

[53]), it has been shown that under real input motion with same PGA (0.25g) as a synthetic Gabor signal, basin becomes much more nonlinear due to successive loading-unloading cycle content in real input motion. For further investigations of this aspect on pore pressure effects, in another study, it would be of great interest to observe the possible changes under real input motion that has a more complicated content in terms of loading-unloading cycles that could trigger higher level of nonlinearity.
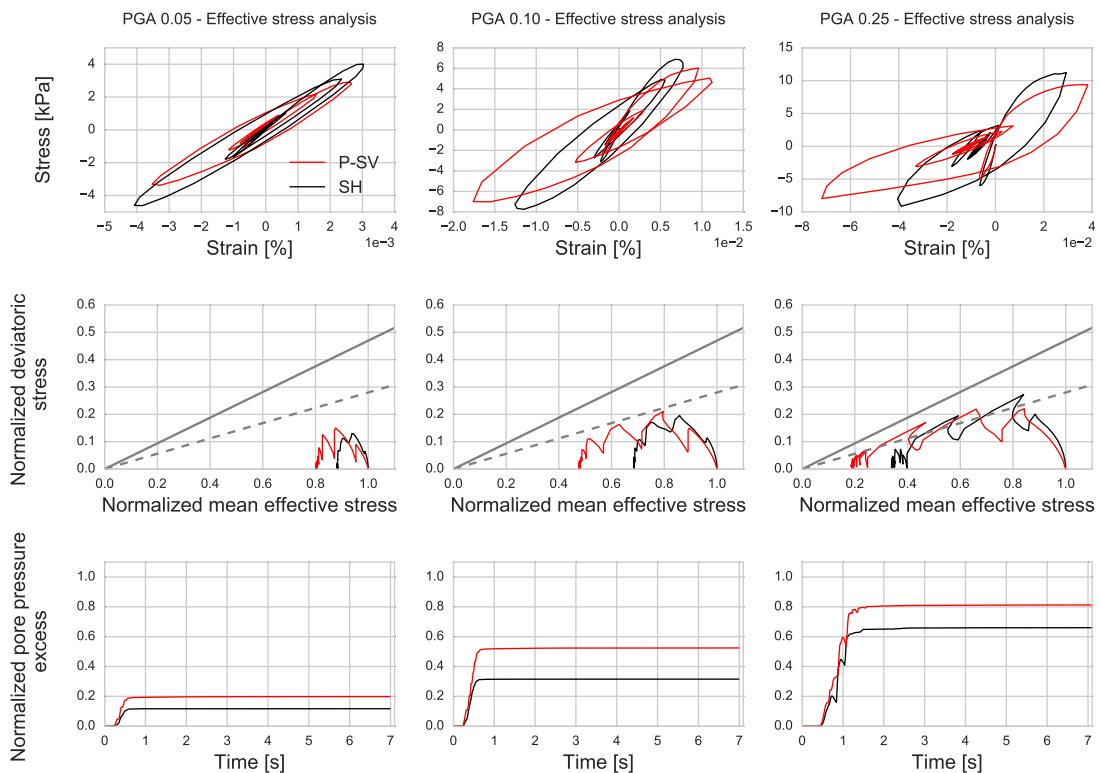
Fig. 5.31 Stress-strain curves at the middle of layer 1 ($z = -3.5m$) (top), stress path (middle) and temporal change of normalized pore pressure excess (bottom) for SH (in black) P-SV (in red) models under loading of impulse signal with PGA 0.05g (left), 0.10g (middle) and 0.25g (right).

Lastly, acceleration, velocity and time histories of effective stress analyses in P-SV and SH models are compared at basin surface for the point at $X = 700m$ in Figure 5.32. At left edge of the basin surface, ground motion is slightly stronger in P-SV model. Again, the displayed results have been filtered below 10 Hz by Butterworth lowpass filter. In acceleration time histories, higher amplitudes are calculated for P-SV model for each loading condition. Differences in velocity time histories are noted more as the pore pressure rise

is higher. Maximum displacement throughout the simulation is calculated as $6cm$ for the third case with PGA $0.25g$. Permanent displacement occurs in the P-SV model, even though it is very small. In Chapter 3.3.1, it has been shown that the permanent displacements increase considerably under higher nonlinearity in triaxial loading compared to uniaxial loading. The evolution of permanent displacement under a different loading condition which could trigger high nonlinearity (strains $> 1\%$), is another aspect to be studied as a perspective.
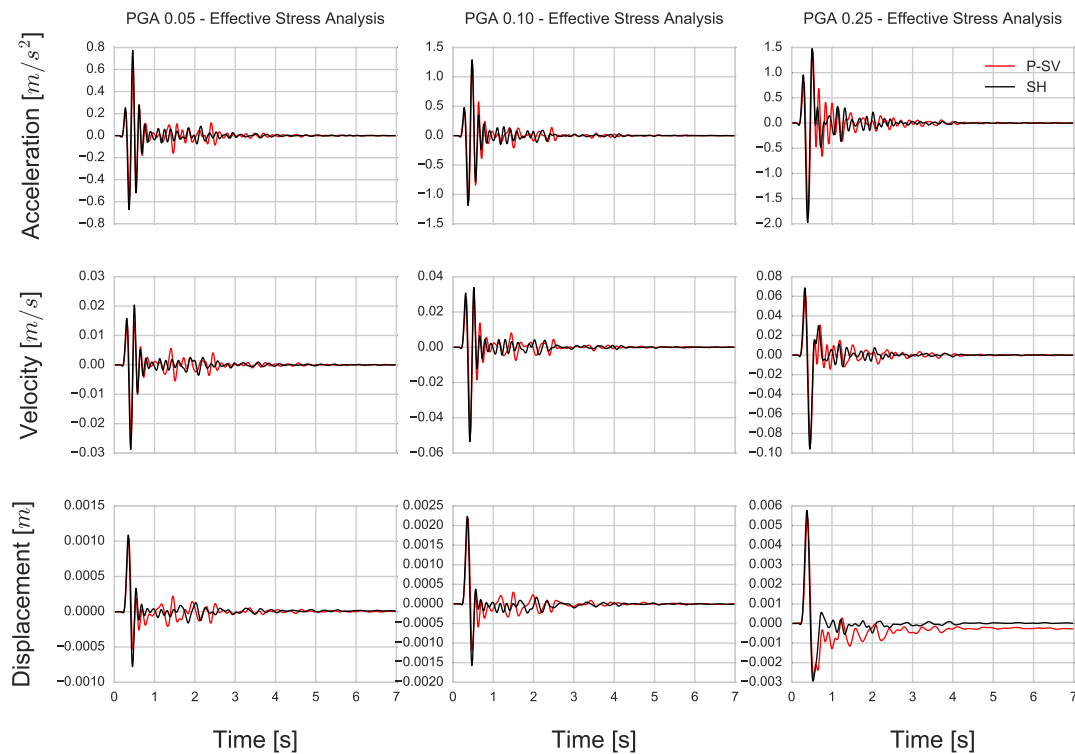
Fig. 5.32 Acceleration (top), velocity (middle) and displacement (bottom) time histories for effective stress analyses in SH (in black) and P-SV (in red) models under loading of impulse signal with PGA $0.05g$ (left), $0.10g$ (middle) and $0.25g$ (right).

We see that P-SV and SH models evoke similar soil behaviors under pore pressure effects generated on loading conditions with synthetic signals. However, the intensity of wave propagation differs in left edge of the basin for two models and resultant changes in soil strength could reach very different levels due to different pore pressure rise levels. In addition, considering the input motion simplicity related to the lack of continuous changes in loading-unloading cycle, significant changes in liquefiable soil behavior of both models do not result in great differences in acceleration and velocity time histories. On the other hand,

permanent displacement starts to takes place in the soil under high nonlinearity.

The influence of input motion energy content   In this section, we further analyze the P-SV model for effective and total stress analyses under the real input motion. We recall that the input signal is applied uniaxially on the horizontal direction of the P-SV model. Also, the input PGA is smaller than the third synthetic signal (PGA 0.25 g) used in previous sections.

First, Figure 5.33 (at left) shows the stress-strain curves in the first two mid-layers. The stations are chosen from $x = 700$ m, where the soil nonlinearity is calculated to be the highest. The influence of pore pressure excess in the model is such significant that the highest strain is 0.8% while it is less than 0.05% in total stress analysis in the middle of the first layer. Moreover, in the second layer, maximum strain is over 2.5% under pore pressure effects, which is more than 10 times higher than the case with the strongest PGA of synthetic signals. Also, we remark that the second layer is more nonlinear than the first layer, which is the opposite of the case with synthetic input motion. This could be explained by the fact that real input motion has stronger low frequency content so that the wave lengths are longer. It is more likely that longer waves are trapped in the second layer compared to high frequency wavelets in synthetic wave propagation.

The same figure (at right) displays the maximum surface displacement in the basin ($x = 1000$ m). Permanent displacement starts to occur under pore pressure effects with a value of 0.5 cm. This corresponds to more than 25 times higher permanent displacement compared to the strongest synthetic wave propagation case.
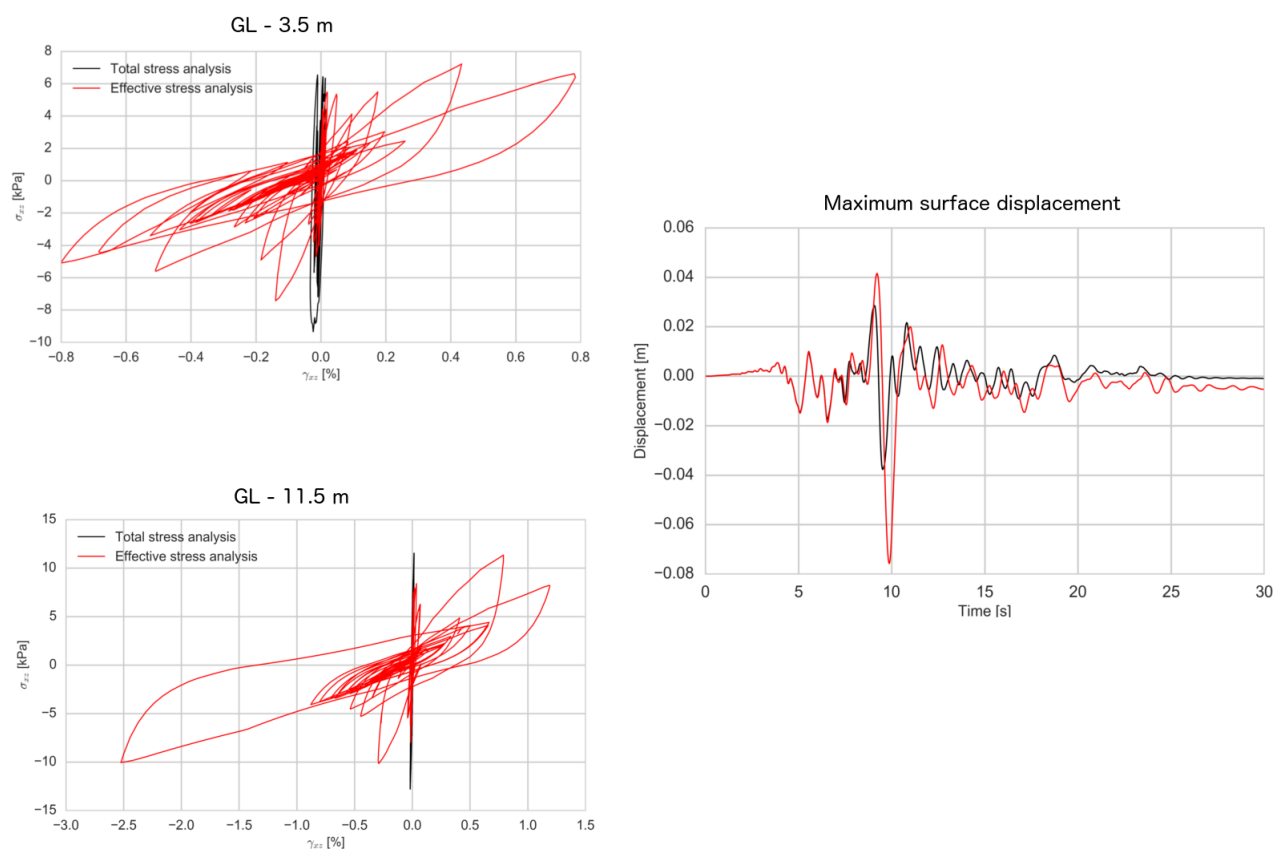
Fig. 5.33 Stress-strain curves at the middle of the first layer (top panel) and the second layer (bottom panel) (at left); Maximum surface displacement time histories (at right).

These results indicate that the nonlinearity of a basin is strongly dependent on input motion energy content. More than PGA, the content of the motion in terms of loading-unloading cycles influences the soil nonlinearity. As a result of higher nonlinearity, permanent surface displacement and maximum strain in liquefiable soil layers could reach to much higher values.

Lastly, transfer functions of total and effective stress analyses are analyzed in initial [0-18] s and last [18-30] s loading intervals of real input motion loading. Figure 5.34 displays the viscoelastic transfer function (at left) with total (at middle) and effective (at right) stress analyses. Compared to viscoelasticity, soil nonlinearity in total stress analysis leads the basin to attenuated low frequency content of surface motion and amplifications of very high frequencies (> 9 Hz). Also, a shift is remarked in fundamental frequency of the model.

Under pore pressure effects, this fundamental frequency shift becomes more prominent and low frequency motion is further amplified. On the other hand, for higher frequencies (> 2 Hz) surface motion is attenuated in the basin.
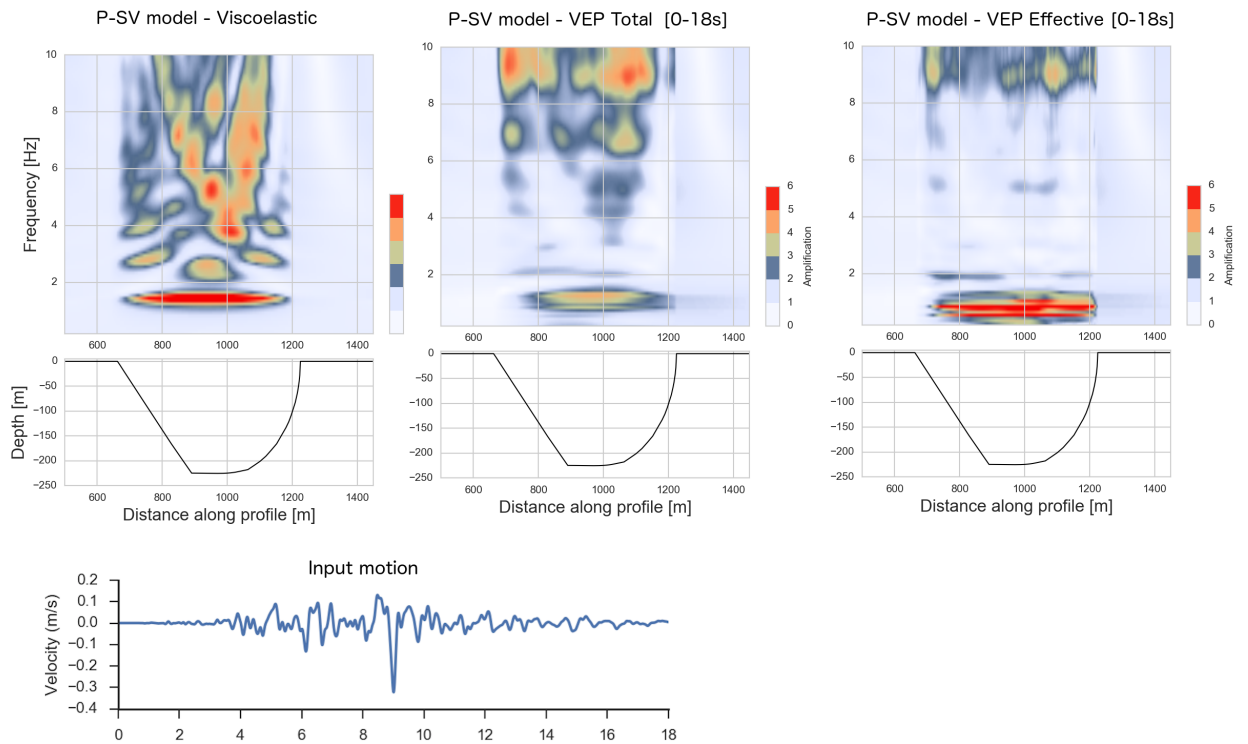
Fig. 5.34 Tranfer function of the initial interval [0-18] s of P-SV model for viscoelasticity (at left), total stress analysis (at middle) and effective stress analysis (at right) under real input motion.

In Figure 5.35, same results are shown for the second interval of the loading. Total stress analysis model exhibits very close distribution of transfer function in the basin compared to viscoelasticity. Due to initial nonlinearity, basin response is slightly stronger in high frequencies (> 6 Hz), whereas slightly more attenuated motion is noted in lower frequencies. On the other hand, in effective stress analysis, much less recovery is calculated in transfer function of the model due to excess pore pressure development. We remind that here recovery term is not meant to be the redistribution of the water in the model due to soil permeability. Compared to total stress analysis, the low frequency motion (< 2 Hz) is much stronger. Very high frequency motion is attenuated in the middle and right side of the basin, while at left side of the basin, higher values are calculated. Given these results, we can

conclude that soil nonlinearity with pore pressure effects plays a very important role on the basin response throughout the wave propagation.
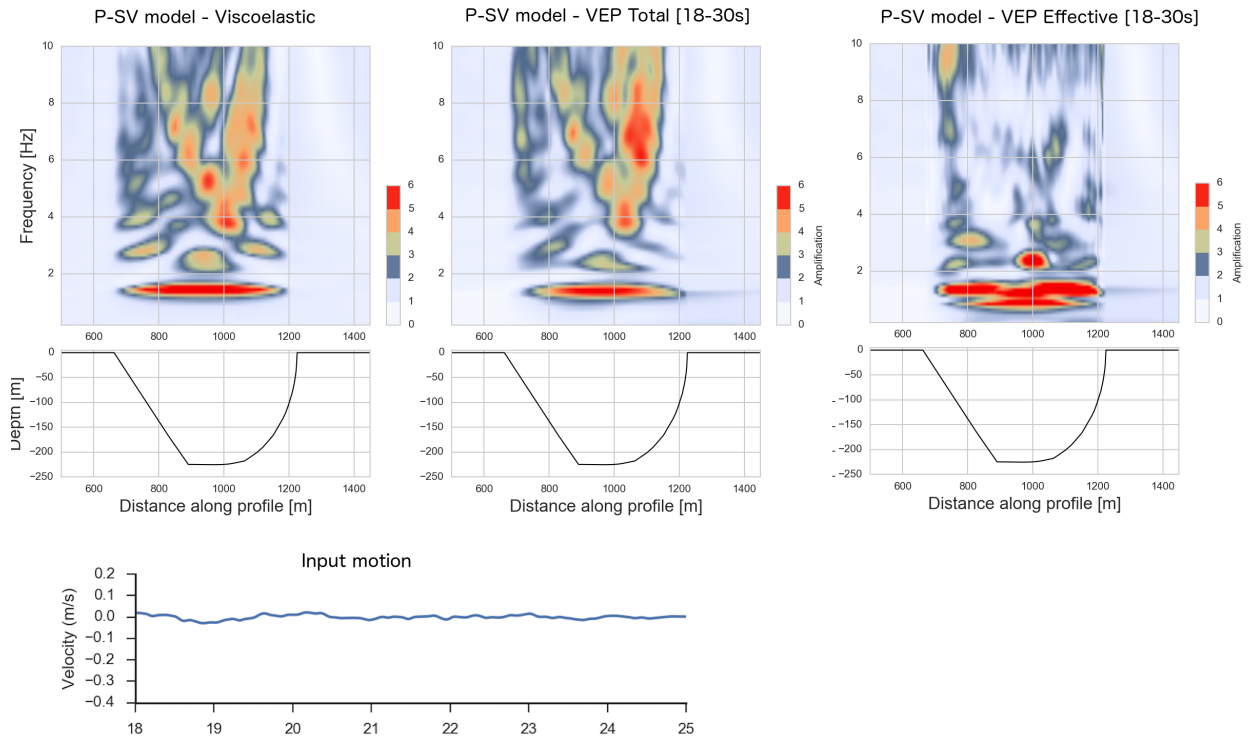
Fig. 5.35 Tranfer function of the second interval [18-30] s of P-SV model for viscoelasticity (at left), total stress analysis (at middle) and effective stress analysis (at right) under real input motion.

5.4   Conclusions and Perspectives

The developed two-dimensional spectral element code that takes into account different soil constitutive models is applied to a two-dimensional realistic sedimentary basin model in order to study the effect of soil nonlinearity on wave propagation in a more complicated medium. The 2D model, which has been studied in Gélis and Bonilla (2014) [53], consists of six soft layers situated inside a basin surrounded by bedrock. Basin and bedrock are separated by one elliptical boundary and another boundary with a sharper angle, so that the wave propagation in the model is expected to be more complicated due to complexity of basin geometry. All the soil layers inside the basin are defined with nonlinear constitutive

model and two superficial soil layers are supposed to be susceptible to excess pore pressure development. We performed effective and total stress analyses for different loading conditions on the 2D model. Three outcrop broadband truncated Gaussian signals with PGA values of 0.05, 0.10 and 0.25g are chosen as input motion. For each loading condition, wave propagation is modeled in P-SV and SH models and effective and total stress analyses are performed. Additionally, P-SV wave propagation is modeled for effective and total stress analyses under a real input motion. As input motion, EW component of outcrop records of the 1994 Northridge earthquake are used such that the basin is loaded uniaxially. The real input motion is scaled by 0.5. Thus, its PGA is less than the synthetic signal of PGA 0.25g.

The 2D sedimentary basin becomes more nonlinear under increasing intensity of input motion in both P-SV and SH wave propagation models. The distribution of high nonlinearity is localized in surficial basin layers and on patches close to basin edges which are concerned from strong reflection from basin corners. Under increasing nonlinearity, the contrast between these zones and the rest of the basin increases. This effect of localization is also seen in maximum PGV distribution of the basin. Such a correlation between maximum strain level and peak ground velocity is coherent with the studies using PGV to shear velocity ratio as a strain proxy (Idriss 2011 [72]; Chandra, 2016 [22]; Guéguen, 2016 [57]).

Moreover, the maximum strain distribution inside the basin is seen in blocks of layers due to the velocity contrasts between the superposed layers. This result is in agreement with the studies of Guidotti et al. (2011) [58] and Gélis and Bonilla (2012 [52], 2014 [53]). Also, inside the same layer, wave propagation is found to be stronger at layer boundaries as reported in Gandomzadeh (2011) [48] for another 2D nonlinear basin model.

The consideration of pore pressure development in superficial liquefiable layers reveals that the basin becomes more nonlinear under the same input motion compared to total stress analysis. Pore pressure rise in liquefiable layers could lead the propagating waves trap in superficial layers so that wave propagation in superficial layers may intensify. As a result, energy is attenuated in underlying layers of the basin and maximum strain and velocity values are concentrated close to basin surface. Pore pressure effects are easily observed in stress-strain curves, in which we see that soil strength weakens and deformations increase in effective stress analysis compared to total stress analysis. On the other hand, these pore pressure related changes in soil are not observed in surface motion such as acceleration and velocity time histories. This could be related to limited ultimate strain level triggered by the input source. As highlighted in Gélis and Bonilla (2012 [52], 2014 [53]),

the content of input motion in terms of loading-unloading cycle is a governing factor for soil nonlinearity more than PGA level. For this reason, the same basin modeled is studied under uniaxial loading of a real input motion. It has been shown that although its PGA is smaller than strongest synthetic input PGA, the complexity of the real input motion brings higher nonlinearity in the basin. Such higher nonlinearity results in stronger strain levels and higher permanent displacement values compared to a synthetic input signal with higher PGA. Also, higher low frequency content in real input motion could change the localization of maximum nonlinearity inside the basin given the stronger propagation of waves with longer wave length. Another aspect is that the higher nonlinearity under the real input motion results in remarkable fundamental frequency shift and highly attenuated high frequency content in basin surface response. Under pore pressure effects, low frequency content is significantly amplified and the more shift in fundamental frequency is noted.

Furthermore, the choice of propagation model (P-SV or SH model) shows different nonlinear basin response. Therefore, the nonlinearity level triggered under the same loading condition could differ in different sections of the basin in P-SV and SH models. In other words, the nonlinearity of a 2D basin with complex geometry is highly dependent on P-SV and SH model.

In this study, we show the possibility of multi-dimensional modeling of wave propagation by taking into account soil nonlinearity and pore pressure development in the media where geometrical complexities are present. Our 2D SEM code provides the facility of studying the influence of surficial soil behavior on wave propagation by respecting the medium properties. The study could be possibly extended to modeling nonlinear basin response for different hypotheses of source mechanism in further studies.

Chapter 6

General Conclusions and Perspectives

In this thesis, we studied seismic wave propagation in 1D and 2D complex media (layered medium with velocity contrasts, complex geometry, dense/loose soils consolidated under isotropic/anisotropic conditions) in order to better understand the influence of nonlinear soil behavior on wave propagation. For this purpose, 1D and 2D spectral element (SEM) codes which model seismic wave propagation in nonlinear media with pore pressure effects and viscoelastic attenuation are developed. For 1D, we extended the 1D - one component (1C) SEM code of Delavaud (2007) [32] to 1D - three component (3C) and coupled it with Masing-Prandtl-Ishlinskii-Iwan (MPII) model of nonlinearity (Iwan, 1967) [76], front liquefaction model of Iai et al. (1990) [70] for pore pressure effects and viscoelasticity model of Liu and Archuleta (2006) [98]. For the implementation of MPII model with pore pressure effects, the PhD work of Pham (2013) [125] has been referred to. For 2D, the open source code of SEM2DPACK (Ampuero, 2002 [2]) is used. The soil constitutive models that are implemented in 1D SEM code are also implemented in the developed 2D SEM code. We need three elastic parameters (pressure and shear wave velocities and density) and three parameters for nonlinearity (failure line angle, cohesion and coefficient of Earth at rest). When excess pore pressure development is taken into account, we need five parameters that can be obtained by laboratory tests or numerical analyses (ϕ_p, w_1, p_1, p_2 and S_1).

The developed 1D SEM code has been benchmarked for 1C wave propagation with known numerical solutions and the obtained results give satisfactory fit. Very good matches are obtained with 1D-1C SEM code on realistic viscoelastic models that differ in terms of soil properties. Further benchmarking (Iwan group in the framework of Prenolin project, Mercerat et al., 2016 [110]; Régnier et al., 2016 [129]) with various numerical methods that use the same nonlinear model verified the efficiency of the 1D SEM code for one shear component wave propagation in nonlinear models (Mercerat et al., 2015 [109]; 2016 [110]).

Moreover, the 1D SEM code is validated for 3C wave propagation in nonlinear media with pore pressure effects on real liquefaction site model of Wildlife Refuge Liquefaction Array (USA). All the implementations in the 2D SEM code has been verified by comparisons with 1D SEM code solutions.

Furthermore, a sensitivity analysis is performed on the 1D SEM code in order to see the influence of number of SEM polynomial order, number of Iwan springs in nonlinearity and soil constitutive behavior on precision and/or computational cost. The use of higher order polynomial degree increases the precision of solution, but in order to avoid unnecessary computational cost, an optimal selection should be made depending on the model properties. In nonlinearity, use of 50 springs is shown to be advantageous in terms of computational time cost without compromising precision. In Gandomzadeh (2011) [48], similar conclusion is drawn for use of 50 springs with the note that energy dissipation increases below this number of springs. Also, it is shown that computation time increases for models using effective stress analysis, nonlinearity and viscoelasticity compared to elastic model.

1D-1C wave propagation modeling in a canonical model of single soil layer revealed that significant energy damping is observed in viscoelastic and nonlinear considerations of soil rheology and soil strength weakens due to soil hysteresis in nonlinearity. Due to rigidity loss in nonlinear soil, phase delays are observed in surface motion time histories and resonance frequency shifts towards lower frequencies are noted in frequency plan. It has been shown that the canonical model becomes highly nonlinear under a real input motion which exerts successive loading-unloading cycles on the soil. With high nonlinearity, soil strength weakens and higher level of deformations are noted in the middle of soil column compared to superficial layers.

1D-3C wave propagation modeling in a nonlinear medium is found to trigger higher nonlinearity compared to 1C wave propagation modeling in the same medium. 1D-3C wave propagation is modeled with pore pressure effects on three real liquefaction site models: Wildlife Refuge Liquefaction Array (WRLA), Kushiro Port (KP) and Onahama Port (OP), which are affected by 1987 Superstition Hills, the The 1993 Kushiro-Oki and The 2011 off the Pacific coast of Tohoku earthquakes, respectively.

The simulated ground motion acceleration on three directions match well with the observations in WRLA. Spiky behavior of the acceleration is reproduced successfully and related to pore pressure changes in the liquefiable soil layer. Following the satisfactory

results, we used the 1D-3C SEM code for further exploration of the soil behavior under different conditions. We have shown that the neglecting pore pressure effects in soil may result in ground motion with very different frequency content. Calculated motion without including pore pressure effects overestimates high frequency motion and amplification of low frequency motion is neglected. Under excess pore pressure development effect, waves could be trapped in liquefiable soils where the soil strength changes continuously and the medium velocity gets lower. The outgoing waves could be attenuated more with higher nonlinearity in liquefiable soils. As a result of rigidity loss, such soils can undergo very large deformations. Outgoing waves can have highly damped large-span forms. On the other hand, with strength hardening due to dilatant behavior, sudden strong peaks can be seen in transmitted waves. The same analyses with the 1D-3C SEM code are performed on KP model. In this site, inconsistency between observed and calculated vertical acceleration may come from lack of data for P wave velocity. While we are able to model the vertical motion in Wildlife Refuge Liquefaction Array where soil properties are determined comprehensively for vertical component, the irrelevancy in the results of KP site reveals the importance of a complete site characterization in wave propagation studies using three components. Also, with effective stress analysis, high frequency damping and low frequency amplification are obtained at KP model similarly to Wildlife Refuge Liquefaction Array model. For OP model, the influence of effective stress analysis is seen mostly on high frequency motion. This shows that the influence of cohesionless soil behavior on wave propagation is highly dependent on model properties and loading conditions. Moreover, by comparing different rheological models at all sites, nonlinearity is shown to bring up more attenuation and frequency shifts in surface motion energy content on horizontal directions. Yet, these nonlinearity-related changes are not homogeneous all over the concerned frequency band and depends strongly on model properties. In all the sites, effective stress analysis leads to a tendency of significant increase in deformation range of liquefiable soil layers, where soil dilatancy changes continuously, and additional damping on other layers. Additionally, we have compared uniaxial and triaxial loading approaches on three models for the strongest ground motion direction. It is concluded that the soil becomes more nonlinear under triaxial loading and higher nonlinearity results in more rapid rise in pore pressure excess. Soil becomes more dilatant due to this increase in nonlinearity. For this reason, consideration of multiaxial interaction is suggested for a realistic modeling of seismic wave propagation. Also, resultant deformation at surface may be very high under triaxial loading as in case of the WRLA model. Yet, for cases with low level of ultimate strain (e.g. less than 1 %), this effect in surface displacement may not be seen.

The fact that this relatively simple model is able to fit the observations mean that we are able to capture the physics of nonlinear soil behavior and eventually predict the ground motion. In this sense, and to study the 2D effects on wave propagation, 2D P-SV and SH wave propagation is studied in a more complicated medium with the developed 2D SEM code. Thus, a similar 2D sedimentary basin model studied in Gélis and Bonilla (2014) [53] is used. The model consists of six soft layers situated inside a basin surrounded by bedrock. Basin and bedrock are separated by one elliptical boundary and another boundary with a sharper angle, so that the wave propagation in the model is expected to be more complicated due to complexity of basin geometry. All the soil layers inside the basin are defined with nonlinear constitutive model and two superficial soil layers are supposed to be susceptible to excess pore pressure development. We performed effective and total stress analyses for different loading conditions on the 2D model. Three outcrop broadband truncated Gaussian signals with PGA values of 0.05, 0.10 and 0.25g are chosen as input motion. For each loading condition, wave propagation is modeled in P-SV and SH models and effective and total stress analyses are performed. Additionally, P-SV wave propagation is modeled for effective and total stress analyses under a real input motion. As real input motion, EW component of outcrop records of the 1994 Northridge earthquake are used such that the basin is loaded uniaxially. The real input motion is scaled by 0.5. Thus, its PGA is less than the synthetic signal of PGA 0.25g.

The 2D sedimentary basin becomes more nonlinear under increasing intensity of input motion in both P-SV and SH wave propagation models. The distribution of high nonlinearity is localized in surficial basin layers and on patches close to basin edges which are concerned from strong reflection from basin corners. Under increasing nonlinearity, the contrast between these zones and the rest of the basin increases. This effect of localization is also seen in maximum PGV distribution of the basin. Such a correlation between maximum strain level and peak ground velocity is coherent with the studies using PGV to shear velocity ratio as a proxy (Idriss 2011 [72]; Chandra, 2016 [22]; Guéguen, 2016 [57]).

Moreover, the maximum strain distribution inside the basin is seen in blocks of layers due to the velocity contrasts between the superposed layers. This result is in agreement with the studies of Guidotti et al. (2011) and Gélis and Bonilla (2012 [52], 2014 [53]). Also, inside the same layer, wave propagation is found to be stronger at layer boundaries as reported in Gandomzadeh (2011) [48] for another 2D nonlinear basin model.

The consideration of pore pressure development in superficial liquefiable layers reveals that the basin becomes more nonlinear under the same input motion compared to total stress analysis. Pore pressure rise in liquefiable layers could lead the propagating waves trap in superficial layers so that wave propagation in superficial layers may intensify. As a result, energy is attenuated in underlying layers of the basin and maximum strain and velocity values are concentrated close to basin surface. Pore pressure effects are easily observed in stress-strain curves, in which we see that soil strength weakens and deformations increase in effective stress analysis compared to total stress analysis. On the other hand, these pore pressure related changes in soil are not observed in surface motion such as acceleration and velocity time histories. This could be related to limited ultimate strain level triggered by the input source. As highlighted in Gélis and Bonilla (2012 [52], 2014 [53]), the content of input motion in terms of loading-unloading cycle is a governing factor for soil nonlinearity more than PGA level. It has been shown that although its PGA is smaller than strongest synthetic input PGA, the complexity of the real input motion brings higher nonlinearity in the basin. Such higher nonlinearity results in stronger strain levels and higher permanent displacement values compared to a synthetic input signal with higher PGA. Another aspect is that the higher nonlinearity under the real input motion results in remarkable fundamental frequency shift and highly attenuated high frequency content in basin surface response. Under pore pressure effects, low frequency content is significantly amplified and the more shift in fundamental frequency is noted.

Furthermore, the choice of propagation model (P-SV or SH model) shows different nonlinear basin response. Therefore, the nonlinearity level triggered under the same loading condition could differ in different sections of the basin in P-SV and SH models. In other words, the nonlinearity of a 2D basin with complex geometry is highly dependent on P-SV and SH model.

The general perspectives of this study can be categorized in physical and numerical. One of the physical perspectives is further applications of the 2D SEM code on the 2D sedimentary basin model under real input source. As shown in Gélis and Bonilla (2014) [53], the 2D basin becomes more nonlinear under real input motion compared to a simple impulse which has the same PGA intensity. Also, in the 1D-3C SEM code applications on real liquefaction site models, strong oscillations in pore pressure excess and consequent dilatant/contractive soil behavior change are shown to lead the soil to significant strength loss and large deformations (e.g. > 1%). In order to investigate possible outcomes of high nonlinearity and pore pressure effects, studying the 2D sedimentary basin model with real input motion is of great interest.

Also, in our study, the 2D model that we have used is composed of uniform soil layers that does not have any lateral heterogeneity inside the basin media and water level is considered to be at same level all along the model. In a future study, the effect of such irregularities on basin response can be counted as another perspective. In addition, the SEM2DPACK offers many options for different source mechanisms. The 2D SEM code with the implemented soil constitutive models in this study allows users to model seismic wave propagation starting from fault rupture to site effects. In another study, such a modeling from source to site on large-band frequency holds great interest. Moreover, it has been shown that 3D modeling of seismic wave propagation represent better the strong reflections in models with complex geometries (e.g. Delavaud, 2007 [32]; Smerzini et al., 2011 [146]). Therefore, the development of three-dimensional (3D) SEM code that takes into account viscoelastic and nonlinear soil constitutive models is of great interest. As explained in Chapter 1.3.4, the liquefaction front model for including pore pressure effects in the media is implemented in our codes as 3D model. In this sense, our SEM code provides easiness of extension of the code to 3D form. Furthermore, in the coupled model that we use in our study for soil nonlinearity and pore pressure effects, the influence of excess pore pressure development applies directly on shear modulus of the soil. The vertical component is held independent of the changes in pore pressure of the soil. In a further study, the consideration of the effect of pore pressure excess on bulk modulus of the soil and on axial component of the strength is important in order to improve the calculations of vertical settlement in the soil.

The numerical perspectives are based on the improvement of the developed 1D and 2D SEM codes for more efficient calculations in terms of computation time. This could be done by further numerical optimization of the codes and parallel computations. The spectral element numerical method already provides the possibility of parallel computation. More information about parallel computation applications with spectral element method can be found in Fischer and Patera (1991) [46], Komatitsch and Vilotte (1998) [90], Stupazzini et al. (2009) [150]. In addition, mesh structure choice is a governing parameter for determining time step of computations. In structured mesh, the required time step can be very small given the smaller minimum grid distance in elements. For this reason, the choice of unstructured meshes could reduce the computational time. Lastly for physical perspectives, numerical inversion tests in order to obtain 5 parameters of Iai et al. (1990) [69] for 1D-3C MPII model, such that the nonlinear material behavior can be modeled better for liquefiable soil layers.

References

[1] Aguirre, J. and Irikura, K. (1997). Nonlinearity, liquefaction, and velocity variation of soft soil layers in port island, kobe, during the hyogo-ken nanbu earthquake. *Bulletin of the Seismological Society of America*, 87:1244–1258.

[2] Ampuero, J.-P. (2002). *Etude physique et numérique de la nucléation des séismes*. PhD thesis, Paris 7.

[3] Ampuero, J. P. and Vilotte, J. P. (2002). Insights on fault behaviour from the seismic nucleation phase. In *AGU Fall Meeting Abstracts*, volume 1, page 08.

[4] Angot, A. and Lemoine, P. (1910). Le tremblement de terre du 11 juin 1909 dans le sud-est de la france. In *Annales de Géographie*, volume 19, pages 8–25. JSTOR.

[5] Aoi, S. (2000). New strong-motion observation network: Kik-net. *EOS Trans. Am. Geophys. Union*.

[6] Archuleta, R. (1998). Direct observation of nonlinear soil response in acceleration time histories. *Seism. Res. Lett*, 69:149.

[7] Ashford, S. A., Boulanger, R. W., Donahue, J. L., and Stewart, J. P. (2011). Geotechnical quick report on the kanto plain region during the march 11, 2011, off pacific coast of tohoku earthquake, japan. Technical report, Geotechnical Extreme Events Reconnaissance (GEER).

[8] Assimaki, D., Gazetas, G., and Kausel, E. (2005). Effects of local soil conditions on the topographic aggravation of seismic motion: parametric investigation and recorded field evidence from the 1999 athens earthquake. *Bulletin of the Seismological Society of America*, 95(3):1059–1089.

[9] Assimaki, D., Li, W., and Kalos, A. (2011). A wavelet-based seismogram inversion algorithm for the in-situ characterization. *Pure and applied geophysics*, 168(10):1669–1691.

[10] Bard, P.-Y. and Bouchon, M. (1985). The two-dimensional resonance of sediment-filled valleys. *Bulletin of the Seismological Society of America*, 75(2):519–541.

[11] Bardet, J. P. (2000). *EERA: a computer program for equivalent–linear earthquake site response analyses of layered soil deposits*. Department of Civil Engineering, University of Southern California, Los Angeles, CA, 37 pp.

[12] Beresnev, I. A. and Wen, K.-L. (1996). Nonlinear soil response—a reality? *Bulletin of the Seismological Society of America*, 86(6):1964–1978.

[13] Bielak, J., Ghattas, O., and Kim, E. (2005). Parallel octree-based finite element method for large-scale earthquake ground motion simulation. *Computer Modeling in Engineering and Sciences*, 10(2):99–112.

[14] Bohlen, T. and Saenger, E. H. (2006). Accuracy of heterogeneous staggered-grid finite-difference modeling of rayleigh waves. *Geophysics*, 71(4):T109–T115.

[15] Bonilla, F., Giacomi, A. C., Bozzano, F., Lenti, L., Gélis, C., Martino, S., and Semblat, J.-F. (2010). Multidisciplinary study of seismic wave amplification in the historical center of rome, italy.

[16] Bonilla, L. F., Archuleta, R. J., and Lavallée (2005). Hysteretic and dilatant behavior of cohesionless soils and their effects on nonlinear site response: Field data observations and modeling. *Bulletin of the Seismological Society of America*, 95(6):2373–2395.

[17] Bonilla, L. F., Liu, P.-C., and Nielsen, S. (2006). 1d and 2d linear and nonlinear site response in the grenoble area. In *Proc. 3rd Int. Symp. on the Effects of Surface Geology on Seismic Motion (ESG2006)*.

[18] Bonilla, L. F., Tsuda, K., Régnier, J., and Laurendeau, A. (2011). Nonlinear site response evidence of k-net and kik-net records from the 2011 off the pacific coast of tohoku earthquake. *Earth, Planets and Space*, 63(7):785–789.

[19] C., L. and F., L. (2006). Seismic hazard and alpine valley response analysis : generic valley configurations. *Third international Symposium on the effects of surface geology on seismic motion. Grenoble, France, 30 August – 1 September 2006. Paper number 1.*

[20] Çelebi, M. and Hanks, T. (1986). Unique site response conditions of two major earthquakes of 1985: Chile and mexico. In *Proceedings of the International Symposium of Engineering Geology Problems in Seismic Areas*, volume 4.

[21] Chaljub, E., Moczo, P., Tsuno, S., Bard, P.-Y., Kristek, J., Käser, M., Stupazzini, M., and Kristekova, M. (2010). Quantitative comparison of four numerical predictions of 3d ground motion in the grenoble valley, france. *Bulletin of the Seismological Society of America*, 100(4):1427–1455.

[22] Chandra, J., Guéguen, P., and Bonilla, L. F. (2016). Pga-pgv/vs considered as a stress–strain proxy for predicting nonlinear soil response. *Soil Dynamics and Earthquake Engineering*, 85:146–160.

[23] Clayton, R. and Engquist, B. (1977). Absorbing boundary conditions for acoustic and elastic wave equations. *Bulletin of the seismological society of America*, 67(6):1529–1540.

[24] Dafalias, Y. F. and Popov, E. P. (1977). Cyclic loading for materials with a vanishing elastic region. *Nuclear Engineering and Design*, 41(2):293–302.

[25] Darendeli, M. B. (2001). *Development of a new family of normalized modulus reduction and material damping curves*. PhD thesis, The University of Texas at Austin.

[26] Day, S. M. and Bradley, C. R. (2001a). Memory-efficient simulation of anelastic wave propagation. *Bulletin of the Seismological Society of America*, 91(3):520–531.

[27] Day, S. M. and Bradley, C. R. (2001b). Memory-efficient simulation of anelastic wave propagation. *Bulletin of the Seismological Society of America*, 91(3):520–531.

[28] Day, S. M. and Minster, J. B. (1984). Numerical simulation of attenuated wavefields using a padé approximant method. *Geophysical Journal International*, 78(1):105–118.

[29] de la Puente, J., Ampuero, J.-P., and Käser, M. (2009). Dynamic rupture modeling on unstructured meshes using a discontinuous galerkin method. *Journal of Geophysical Research: Solid Earth*, 114(B10).

[30] de la Puente, J., Käser, M., Dumbser, M., and Igel, H. (2007). An arbitrary high-order discontinuous galerkin method for elastic waves on unstructured meshes-iv. anisotropy. *Geophysical Journal International*, 169(3):1210–1228.

[31] De Martin, F., Modaressi, H., and Aochi, H. (2007). Coupling of fdm and fem in seismic wave propagation. *in Proc. of 4th International Conference on Earthquake Geotechnical Engineering, Jun 2007, Greece.*

[32] Delavaud, E. (2007). *Simulation numérique de la propagation d'ondes en milieu géologique complexe: application à l'évaluation de la réponse sismique du bassin de Caracas (Venezuela).* PhD thesis, Institut de Physique du Globe de Paris.

[33] Delcourte, S., Fezoui, L., and Glinsky-Olivier, N. (2009). A high-order discontinuous galerkin method for the seismic wave propagation. *EDP Sciences*, ESAIM: Proceedings,27:70–89.

[34] Di Prisco, C., Stupazzini, M., and Zambelli, C. (2007). Nonlinear sem numerical analyses of dry dense sand specimens under rapid and dynamic loading. *International Journal for Numerical and Analytical Methods in Geomechanics*, 31(6):757–788.

[35] Ducellier, A. and Aochi, H. (2012). Interactions between topographic irregularities and seismic ground motion investigated using a hybrid fd-fe method. *Bulletin of Earthquake Engineering*, 10(3):773–792.

[36] Dumbser, M., Käser, M., and Toro, E. F. (2007). An arbitrary high-order discontinuous galerkin method for elastic waves on unstructured meshes-v. local time stepping and p-adaptivity. *Geophysical Journal International*, 171(2):695–717.

[37] Dupros, F., De Martin, F., Foerster, E., Komatitsch, D., and Roman, J. (2010). High-performance finite-element simulations of seismic wave propagation in three-dimensional nonlinear inelastic geological media. *Parallel Computing*, 36(5):308–325.

[38] d'Avila, M. P. S., Semblat, J.-F., and Lenti, L. (2013). Strong ground motion in the 2011 tohoku earthquake: A one-directional three-component modeling. *Bulletin of the Seismological Society of America*, 103(2B):1394–1410.

[39] Electric Power Research Institute, E. (1993). Guidelines for determining design basis ground motions. Technical report, Electric Power Reasearch Institute Technological Report EPRI TR-102293.

[40] Emmerich, H. and Korn, M. (1987). Incorporation of attenuation into time-domain computations of seismic wave fields. *Geophysics*, 52(9):1252–1264.

[41] Etienne, V., Chaljub, E., Virieux, J., and Glinsky, N. (2010). An hp-adaptive discontinuous galerkin finite-element method for 3-d elastic wave modelling. *Geophysical Journal International*, 183(2):941–962.

[42] Faccioli, E., Maggio, F., Paolucci, R., and Quarteroni, A. (1997). 2d and 3d elastic wave propagation by a pseudo-spectral domain decomposition method. *Journal of Seismology*, 1(3):237–251.

[43] Festa, G. and Nielsen, S. (2003). Pml absorbing boundaries. *Bulletin of the Seismological Society of America*, 93(2):891–903.

[44] Festa, G. and Vilotte, J. P. (2005). The newmark scheme as velocity–stress time-staggering: an efficient pml implementation for spectral element simulations of elastodynamics. *Geophysical Journal International*, 161(3):789–812.

[45] Field, E. H., Zeng, Y., Johnson, P. A., and Beresnev, I. A. (1997). Nonlinear sediment response during the 1994 northridge earthquake: Observations and finite source simulations. *Journal of Geophsyical Research*, 103(B11):26869–26883, doi:10.1029/98JB02235.

[46] Fischer, P. F. and Patera, A. T. (1991). Parallel spectral element solution of the stokes problem. *Journal of Computational Physics*, 92(2):380–421.

[47] Fung, Y.-c. (1965). *Foundations of solid mechanics*. Prentice Hall.

[48] Gandomzadeh, A. (2011). *Dynamical soil-structure interactions: Influence of soil behaviour nonlinearities*. PhD thesis, Université Paris-Est.

[49] Gazetas, G., Kallou, P., and Psarropoulos, P. (2002). Topography and soil effects in the ms 5.9 parnitha (athens) earthquake: the case of adames. *Natural Hazards*, 27(1-2):133–169.

[50] Gelagoti, F., Kourkoulis, R., Anastasopoulos, I., Tazoh, T., and Gazetas, G. (2010). Seismic wave propagation in a very soft alluvial valley: sensitivity to ground-motion details and soil nonlinearity, and generation of a parasitic vertical component. *Bulletin of the Seismological Society of America*, 100(6):3035–3054.

[51] Gelis, C., Bonilla, F., Regnier, J., Bertrand, E., , and Duval, A. (2008). On the use of saenger's finite difference stencil to model 2d p-sv nonlinear basin response; application to nice, france. In *In SEISMIC RISK 2008: Earthquake in northwest Europe, Liege, Belgium.*

[52] Gélis, C. and Bonilla, L. F. (2012). 2-dp–sv numerical study of soil–source interaction in a non-linear basin. *Geophysical Journal International*, 191(3):1374–1390.

[53] Gélis, C. and Bonilla, L. F. (2014). Influence of a sedimentary basin infilling description on the 2-dp–sv wave propagation using linear and non-linear constitutive models. *Geophysical Journal International*, 198(3):1684–1700.

[54] Geuzaine, C. and Remacle, J.-F. (2009). Gmsh: A 3-d finite element mesh generator with built-in pre-and post-processing facilities. *International Journal for Numerical Methods in Engineering*, 79(11):1309–1331.

[55] Graves, R. W. (1993). Modeling three-dimensional site response effects in the marina district basin, san francisco, california. *Bulletin of the Seismological Society of America*, 83:1042–1063.

[56] Graves, R. W. (1996). Simulating seismic wave propagation in 3d elastic media using staggered-grid finite differences. *Bulletin of the Seismological Society of America*, 86(4):1091–1106.

[57] Guéguen, P. (2015). Predicting nonlinear site response using spectral acceleration vs pgv/vs30: A case history using the volvi-test site. *Pure and Applied Geophysics*, pages 1–17.

[58] Guidotti, R., Stupazzini, M., Smerzini, C., Paolucci, R., and Ramieri, P. (2011). Numerical study on the role of basin geometry and kinematic seismic source in 3d ground motion simulation of the 22 february 2011 mw 6.2 christchurch earthquake. *Seismological Research Letters*, 82(6):767–782.

[59] Haney, M., Snieder, R., Ampuero, J.-P., and Hofmann, R. (2007). Spectral element modelling of fault-plane reflections arising from fluid pressure distributions. *Geophysical Journal International*, 170(2):933–951.

[60] Hardin, B. O. and Drnevich, V. P. (1972). Shear modulus and damping in soils: measurement and parameter effects. *Journal of Soil Mechanics and Foundations Div*, 98(sm6).

[61] Hartzell, S., Bonilla, L. F., and Williams, R. A. (2004). Prediction of nonlinear soil effects. *Bulletin of the Seismological Society of America*, 94(5):1609–1629.

[62] Hartzell, S., Leeds, A., Frankel, A., Williams, R. A., Odum, J., Stephenson, W., and Silva, W. (2002). Simulation of broadband ground motion including nonlinear soil effects for a magnitude 6.5 earthquake on the seattle fault, seattle, washington. *Bulletin of the Seismological Society of America*, 92(2):831–853.

[63] Hartzell, S., Liu, P., and Mendoza, C. (1996). The 1994 northridge, california, earthquake: Investigation of rupture velocity, risetime, and high-frequency radiation. *Journal of Geophysical Research: Solid Earth*, 101(B9):20091–20108.

[64] Hashash, Y. M. and Park, D. (2001). Non-linear one-dimensional seismic ground motion propagation in the mississippi embayment. *Engineering Geology*, 62(1):185–206.

[65] Hayashi, Y., Tsushima, H., Hirata, K., Kimura, K., and Maeda, K. (2011). Tsunami source area of the 2011 off the pacific coast of tohoku earthquake determined from tsunami arrival times at offshore observation stations. *Earth, planets and space*, 63(7):809–813.

[66] He, C.-H., Wang, J.-T., and Zhang, C.-H. (2016). Nonlinear spectral-element method for 3d seismic-wave propagation. *Bulletin of the Seismological Society of America*.

[67] Holzer, T. L. and Youd, T. L. (2007). Liquefaction, ground oscillation, and soil deformation at the wildlife array, california. *Bulletin of the Seismological Society of America*, 97(3):961–976.

[68] Holzer, T. L., Youd, T. L., and Hanks, T. C. (1989). Dynamics of liquefaction during the 1987 superstition hills, california earthquake. *Science*, 244(4900):56–59.

[69] Iai, S., Matsunaga, Y., and Kameoka, T. (1990a). Parameter identification for a cyclic mobility model. *Report of the Port and harbour Research Institute*, 29(4).

[70] Iai, S., Matsunaga, Y., and Kameoka, T. (1990b). Strain space plasticity model for cyclic mobility. *Report of the port and harbour research institute*, 29:57–83.

[71] Iai, S., Morita, T., Kameoka, T., Matsunaga, Y., and Abiko, K. (1995). Response of a dense sand deposit during 1993 kushiro-oki earthquake. *Soils and Foundations*, 35(1):115–131.

[72] Idriss, I. (2011). Use of vs30 to represent local site condition. In *4th IASPEI/IAEE International Symposium: Effects of Surface Geology on Strong Ground-motion*, volume 30.

[73] Ishibashi, M. P. and Zhang, X. (1993). Unified dynamic shear moduli and damping patios of sand and clay. *Soils and Foundations*, 33(1):182–191.

[74] Ishihara, K. (1985). Stability of natural deposits during earthquakes. *in Proc. of 11th Int. Conf. on Soil Mechanics and Foundation Engineering, Rotterdam, The Netherlands: Balkema*, 1.

[75] Ishihara, K. (1996). *Soil behaviour in earthquake geotechnics*. Clarendon Press; Oxford University Press.

[76] Iwan, W. D. (1967). On a class of models for the yielding behavior of continuous and composite systems. *Journal of Applied Mechanics*, 34(3):612–617.

[77] Jaeger, J. C., Cook, N. G., and Zimmerman, R. (2009). *Fundamentals of rock mechanics*. John Wiley & Sons.

[78] Joyner, W. B. (1975). A method for calculating nonlinear seismic response in two dimensions. *Bulletin of the Seismological Society of America*, 65(5):1337–1357.

[79] Joyner, W. B. and Chen, A. T. (1975). Calculation of nonlinear ground response in earthquakes. *Bulletin of the Seismological Society of America*, 65(5):1315–1336.

[80] Kaklamanos, J., Baise, L. G., Thompson, E. M., and Dorfmann, L. (2015). Comparison of 1d linear, equivalent-linear, and nonlinear site response models at six kik-net validation sites. *Soil Dynamics and Earthquake Engineering*, 69:207–219.

[81] Käser, M. and Dumbser, M. (2006). An arbitrary high-order discontinuous galerkin method for elastic waves on unstructured meshes—i. the two-dimensional isotropic case with external source terms. *Geophysical Journal International*, 166(2):855–877.

[82] Kausel, E. and Assimaki, D. (2002). Seismic simulation of inelastic soils via frequency-dependent moduli and damping. *Journal of Engineering Mechanics*, 128(1):34–47.

[83] Kawase, H. and Aki, K. (1989). A study on the response of a soft basin for incident s, p, and rayleigh waves with special reference to the long duration observed in mexico city. *Bulletin of the Seismological Society of America*, 79(5):1361–1382.

[84] Kazama, M. and Noda, T. (2012). Damage statistics (summary of the 2011 off the pacific coast of tohoku earthquake damage). *Soils and Foundations*, 52(5):780–792.

[85] Kinoshita, S. (1998). Kyoshin net (k-net). *Seismological Research Letters*, 69(4):309–332.

[86] Kokusho, T. (2004). Nonlinear site response and strain-dependent soil properties. *Current science*, 87:1363–1369.

[87] Komatitsch, D., Liu, Q., Tromp, J., Süss, P., Stidham, C., and Shaw, J. H. (2004). Simulations of ground motion in the los angeles basin based upon the spectral-element method. *Bulletin of the Seismological Society of America*, 94(1):187–206.

[88] Komatitsch, D. and Tromp, J. (2003). A perfectly matched layer absorbing boundary condition for the second-order seismic wave equation. *Geophysical Journal International*, 154(1):146–153.

[89] Komatitsch, D. and Vilotte, J. P. (1998a). The spectral element method: An efficient tool to simulate the seismic response of 2d and 3d geological structures. *Bulletin of the seismological society of America*, 88(2):368–392.

[90] Komatitsch, D. and Vilotte, J.-P. (1998b). The spectral element method: An efficient tool to simulate the seismic response of 2d and 3d geological structures. *Bulletin of the seismological society of America*, 88(2):368–392.

[91] Kramer, S. L. (1996). *Geotechnical Earthquake Engineering*. Prentice Hall, Inc., Upper Saddle River, New Jersey.

[92] Kurahashi, S. and Irikura, K. (2011). Source model for generating strong ground motions during the 2011 off the pacific coast of tohoku earthquake. *Earth, planets and space*, 63(7):571–576.

[93] Kwok, A. O., Stewart, J. P., and Hashash, Y. M. (2008). Nonlinear ground-response analysis of turkey flat shallow stiff-soil site to strong ground motion. *Bulletin of the Seismological Society of America*, 98(1):331–343.

[94] Lakes, R. (1999). *Viscoelastic Materials*. Cambridge University Press.

[95] Laurendeau, A., Perrault, M., Mercerat, D., Bonilla, L. F., Courboulex, F., Beauval, C., Barros, J. G., Vasconez, F., Marinière, J., Singaucho, J. C., Ruiz, M., Alvarado, A., and Bertand, E. (2016). Preliminary observations of site effects during the mw 7.8 pedernales (ecuador) earthquake of april 16th 2016. In *5th IASPEI / IAEE International Symposium: Effects of Surface Geology on Seismic Motion August 15-17, 2016, Taipei, Taiwan.*

[96] Lee, M. K. W. and Finn, W. D. L. (1978). *Dynamic effective stress response analysis of soil deposits with energy transmitting boundary including assessment of liquefaction potential*. University of British Columbia, Faculty of Applied Science.

[97] Levander, A. R. (1988). Fourth-order finite-difference p-sv seismograms. *Geophysics*, 53(11):1425–1436.

[98] Liu, P. and Archuleta, R. J. (2006). Efficient modeling of q for 3d numerical simulation of wave propagation. *Bulletin of the Seismological Society of America*, 96(4A):1352–1358.

[99] Lyakhovsky, V., Hamiel, Y., Ampuero, J.-P., and Ben-Zion, Y. (2009). Non-linear damage rheology and wave resonance in rocks. *Geophysical Journal International*, 178(2):910–920.

[100] Lysmer, J. and Drake, L. A. (1972). A finite element method for seismology. *Methods in computational physics*, 11:181–216.

[101] Madariaga, R. (1976). Dynamics of an expanding circular fault. *Bulletin of the Seismological Society of America*, 66(3):639–666.

[102] Madariaga, R., Ampuero, J., and Adda-Bedia, M. (2006). Seismic radiation from simple models of earthquakes. *Earthquakes: Radiated energy and the physics of faulting*, pages 223–236.

[103] Maday, Y. and Patera, A. T. (1989). Spectral element methods for the incompressible navier-stokes equations. In *IN: State-of-the-art surveys on computational mechanics (A90-47176 21-64). New York, American Society of Mechanical Engineers, 1989, p. 71-143. Research supported by DARPA.*, volume 1, pages 71–143.

[104] Marfurt, K. J. and Kurt, J. (1984). Accuracy of finite-difference and finite-element modeling of the scalar and elastic wave equations. *Geophysics*, 49(5):533–549.

[105] Martino, S., Lenti, L., Gélis, C., Giacomi, A. C., Santisi d'Avila, M. P., Bonilla, L. F., Bozzano, F., and Semblat, J. F. (2015). Influence of lateral heterogeneities on strong-motion shear strains: Simulations in the historical center of rome (italy). *Bulletin of the Seismological Society of America*, 105(5):2604–2624.

[106] Masing, G. (1926). Eigenspannungen und verfestigung beim messing (self-stretching and hardening for brass). In *Proceedings of the Second International Congress on Applied Mechanics, Zurich, Switzerland*.

[107] Maufroy, E., Chaljub, E., Hollender, F., Kristek, J., Moczo, P., Klin, P., Priolo, E., Iwaki, A., Iwata, T., Etienne, V., et al. (2015). Earthquake ground motion in the mygdonian basin, greece: the e2vp verification and validation of 3d numerical simulation up to 4 hz. *Bulletin of the Seismological Society of America*.

[108] Meng, L. and Ampuero, J.-P. (2012). Slow rupture and weakly pressure-sensitive strength enables compressional branching: Dynamic rupture simulations of the 2012 off-sumatra earthquake 2. *Geophys. Res. Lett*.

[109] Mercerat, D., Bonilla, F., Martin, F. D., Delavaud, E., Gélis, C., Glinsky, N., Kristek, J., Lenti, L., Moczo, P., Oral, E., Richterova, A., and d'Avila, M. P. S. (2015). Modeling of 1d wave propagation in nonlinear soils using the elasto-plastic iwan model by four numerical schemes. In *Seismological Society of America, 2015 Annual Meeting, Apr 2015, Pasadena, United States*.

[110] Mercerat, E. D., Bonilla, F., Chabot, S., Martin, F. D., Delavaud, E., Gélis, C., Glinsky, N., Kristek, J., Lenti, L., Moczo, P., Oral, E., Richterova, A., and d'Avila, M. P. S. (2016). Modeling of 1d wave propagation in nonlinear soils using the elasto-plastic iwan model by four numerical schemes. In *5th IASPEI / IAEE International Symposium: Effects of Surface Geology on Seismic Motion August 15-17, 2016, Taipei, Taiwan.*

[111] Mercerat, E. D. and Glinsky, N. (2015). A nodal discontinuous galerkin method for non-linear soil dynamics. In *6th International Conference on Earthquake Geotechnical Engineering 1-4 November 2015 Christchurch, New Zealand.*

[112] Mercerat, E. D., Vilotte, J. P., and Sánchez-Sesma, F. J. (2006). Triangular spectral element simulation of two-dimensional elastic wave propagation using unstructured triangular grids. *Geophysical Journal International*, 166(2):679–698.

[113] Meza-Fajardo, K. C. and Papageorgiou, A. S. (2008). A nonconvolutional, split-field, perfectly matched layer for wave propagation in isotropic and anisotropic elastic media: stability analysis. *Bulletin of the Seismological Society of America*, 98(4):1811–1836.

[114] Moczo, P., Bystrický, E., Kristek, J., Carcione, J. M., and Bouchon, M. (2005). Hybrid modeling of p-sv seismic motion at inhomogeneous viscoelastic topographic structures. *Bulletin of the seismological Society of America*, 87(5):1305–1323.

[115] Moczo, P. and Kristek, J. (2005). On the rheological models used for time-domain methods of seismic wave propagation. *Geophysical Research Letters*, 32(1).

[116] Moczo, P., Kristek, J., Vavrycuk, V., Archuleta, R. J., and Halada, L. (2002). 3d heterogeneous staggered-grid finite-difference modeling of seismic motion with volume harmonic and arithmetic averaging of elastic moduli and densities. *Wave motion*, 92(8):3042–3066.

[117] Moczo, P., Labák, P., Kristek, J., and Hron, F. (1996). Amplification and differential motion due to an antiplane 2d resonance in the sediment valleys embedded in a layer over the half-space. *Bulletin of the Seismological Society of America*, 86:1434–1446.

[118] Mroz, Z. (1967). On the description of anisotropic workhardening. *Journal of the Mechanics and Physics of Solids*, 15(3):163–175.

[119] O'Brien, G. S. and Bean, C. J. (2011). An irregular lattice method for elastic wave propagation. *Geophysical Journal International*, 187(3):1699–1707.

[120] Olsen, K. B. and Archuleta, R. (1996a). Three-dimensional simulation of earthquakes on the los angeles fault system. *Bulletin of the Seismological Society of America*, 86:575–596.

[121] Olsen, K. B. and Archuleta, R. J. (1996b). Three-dimensional simulation of earthquakes on the los angeles fault system. *Bulletin of the Seismological Society of America*, 86(3):575–596.

[122] Park, D. and Hashash, Y. M. (2004). Soil damping formulation in nonlinear time domain site response analysis. *Journal of Earthquake Engineering*, 8(2):249–274.

[123] Pavlenko, O. V. and Irikura, K. (2003). Nonlinear behavior of soils revealed from the records of the 2000 tottori, japan, earthquake at stations of the digital strong-motion network kik-net. *Bulletin of the Seismological Society of America*, 96:2131–2145.

[124] Peyrusse, F., Glinsky, N., Gélis, C., and Lanteri, S. (2014). A high-order discontinuous galerkin method for viscoelastic wave propagation. In *Spectral and High Order Methods for Partial Differential Equations-ICOSAHOM 2012*, pages 361–371. Springer.

[125] Pham, V. A. (2013). *Effets de la pression interstitielle sur la reponse sismique des sols : modélisation numérique 1D/ 3 composantes*. PhD thesis, Université Paris-Est.

[126] Prévost, J. H. (1977). Mathematical modelling of monotonic and cyclic undrained clay behaviour. *International Journal for Numerical and Analytical Methods in Geomechanics*, 1(2):195–216.

[127] Priolo, E. and Seriani, G. (1993). Spectral element method with substructuring: an accurate and efficient high-order finite element approach for wave modeling. *Environmental acoustics, scattering and propagation*, 2:509–527.

[128] Pyke, R. M. (2000). Tess: A computer program for nonlinear ground response analyses. *TAGA Engineering Systems and Software, Lafayette, California*.

[129] Régnier, J., Bonilla, L., Bard, P., Bertrand, E., Hollender, F., Kawase, H., Sicillia, D., Marot, M., Assimaki, D., Amorosi, A., Boldini, D., Chiaradonna, A., Martin, F. D., Ebrille, M., Falcone, G., Foerster, E., Foti, S., Gélis, C., Gazetas, G., Gingery, J., Glinsky, N., Harmon, J., Hashash, Y., Iai, S., Jeremic, B., Kramer, S., Kontoe, S., Kristek, J., Lanzo, G., di Lernia, A., Lopez-Caballero, F., Mercerat, E. D., Moczo, P., Montoya-Noguera, S., Musgrove, M., Nieto-Ferro, A., Pagliaroli, A., Pisano, F., Richterova, A., Sajana, S., d'Avila, M. S., Shi, J., Silvestri, F., Tropeano, G., Vernucci, L., Wanabe, K., Chen, L., Ghofrani, A., and McAllister, G. (2016). International benchmark on numerical simulations for 1d, non-linear site response (prenolin): verification phase based on canonical cases. *Bulletin of the Seismological Society of America, under revision*.

[130] Roten, D., Fäh, D., Bonilla, L., Alvarez-Rubio, S., Weber, T., and Laue, J. (2009). Estimation of non-linear site response in a deep alpine valley. *Geophysical Journal International*, 178(3):1597–1613.

[131] Roten, D., Fäh, D., and Bonilla, L. F. (2013). High-frequency ground motion amplification during the 2011 tohoku earthquake explained by soil dilatancy. *Geophysical Journal International*, 193(2):898–904.

[132] Roten, D., Fäh, D., and Bonilla, L. F. (2014). Quantification of cyclic mobility parameters in liquefiable soils from inversion of vertical array records. *Bulletin of the Seismological Society of America*.

[133] Roten, D., Olsen, K., and Pechmann, J. (2012). 3d simulations of m 7 earthquakes on the wasatch fault, utah, part ii: Broadband (0–10 hz) ground motions and nonlinear soil behavior. *Bulletin of the Seismological Society of America*, 102(5):2008–2030.

[134] Roumelioti, Z. and Beresnev, I. A. (2003). Stochastic finite-fault modeling of ground motions from the 1999 chi-chi, taiwan, earthquake: Application to rock and soil sites with implications for nonlinear site response. *Bulletin of the Seismological Society of America*, 93:1691–1702.

[135] Saenger, E. H., Gold, N., and Shapiro, S. A. (2000). Modeling the propagation of elastic waves using a modified finite-difference grid. *Wave motion*, 31(1):77–92.

[136] Sánchez-Sesma, F. J. (1985). Diffraction of elastic sh waves by wedges. *Bulletin of the seismological society of America*, 75(5):1435–1446.

[137] Santisi d'Avila, M. P., Lenti, L., and Semblat, J. F. (2012). Modelling strong seismic ground motion: three-dimensional loading path versus wavefield polarization. *Geophysical Journal International*, 190(3):1607–1624.

[138] Santisi d'Avila, M. P. and Semblat, J. F. (2014). Nonlinear seismic response for the 2011 tohoku earthquake: borehole records versus one-directional three-component propagation models. *Geophysical journal international*, 197(1):566–580.

[139] Schnabel, B., Lysmer, J., and Seed, H. B. (1972). *Shake. A computer Program for Earthquake Response Analysis of Horizontally Layered Sites*. College of Engineering, University of Berkeley, CA. Rep., No. EERC.

[140] Seed, H. B. and Idriss, I. M. (1969). Influence of soil conditions on ground motions during earthquakes. *Journal of the Soil Mechanics and Foundations Division*, 95(1):99–138.

[141] Seed, H. B., Romo, M. P., Sun, A. J., and Lysmer, J. (1998). The mexico earthquake of september 19, 1985 - relationships between soil conditions and earthquake ground motions. *Earthquake spectra*, 4(4):688–729.

[142] Segalman, D. J. and Starr, M. J. (2008). Inversion of masing models via continuous iwan systems. *International Journal of Non-Linear Mechanics*, 43(1):74–80.

[143] Seriani, G. (1998). 3-d large-scale wave propagation modeling by spectral element method on cray t3e multiprocessor. *Computer Methods in Applied Mechanics and Engineering*, 164(1):235–247.

[144] Seriani, G. and Priolo, E. (1991). High-order spectral element method for acoustic wave modeling. In *1991 SEG Annual Meeting*. Society of Exploration Geophysicists.

[145] Singh, S. K., Mena, E., and Castro, R. (1988). Some aspects of source characteristics of the 19 september 1985 michoacan earthquake and ground motion amplification in and near mexico city from strong motion data. *Bulletin of the Seismological Society of America*, 78:451–477.

[146] Smerzini, C., Paolucci, R., and Stupazzini, M. (2011). Comparison of 3d, 2d and 1d numerical approaches to predict long period earthquake ground motion in the gubbio plain, central italy. *Bulletin of Earthquake Engineering*, 9(6):2007–2029.

[147] Smith, S. and Snieder, R. (2010). Seismic modeling and analysis of a prototype heated nuclear waste storage tunnel, yucca mountain, nevada. *Geophysics*, 75(1):T1–T8.

[148] Stacey, R. (1988). Improved transparent boundary formulations for the elastic-wave equation. *Bulletin of the Seismological Society of America*, 78(6):2089–2097.

[149] Stewart, J. P. and Kwok, A. O. L. (2008). Nonlinear seismic ground response analysis: code usage protocols and verification against vertical array data. *Geotechnical Engineering and Soil Dynamics IV, ASCE Geotechnical Special Publication*, (181):1–24.

[150] Stupazzini, M., Paolucci, R., and Igel, H. (2009). Near-fault earthquake ground-motion simulation in the grenoble valley by a high-performance spectral element code. *Bulletin of the Seismological Society of America*, 99(1):286–301.

[151] Stupazzini, M. and Zambelli, C. (2005). Geo-elsevp: a spectral element approach for 2d or 3d dynamic elasto-viscoplastic problems. *Rivista Italiana di Geotecnica*, 39(4):70–82.

[152] Takemiya, H. and Adam, M. (1998). 2d nonlinear seismic ground analysis by fem bem: The case of kobe in the hyogo-ken nanbu earthquake. *Structural Engineering Earthquake Engineering*, 15:19s–28s.

[153] Tokimatsu, K., Tamura, S., Suzuki, H., and Katsumata, K. (2012). Building damage associated with geotechnical problems in the 2011 tohoku pacific earthquake. *Soils and Foundations*, 52(5):956–974.

[154] Towhata, I. and Ishihara, K. (1985). Modelling soil behavior under principal stress axes rotation. In *International conference on numerical methods in geomechanics*, pages 523–530.

[155] Tsuno, S., Chaljub, E., and Bard, P. (2009). Grenoble simulation benchmark: Comparison of results and learnings. In *Third International Symposium on the Effects of Surface Geology on Seismic Motion*, volume 2.

[156] Vincent, J. F. (2012). *Structural biomaterials*. Princeton University Press.

[157] Virieux, J. (1986). P-sv wave propagation in heterogeneous media: velocity-stress finite-difference method. *Geophysics*, 51:889–901.

[158] Vucetic, M. and Dobry, R. (1991). Effect of soil plasticity on cyclic response. *Journal of geotechnical engineering*, 117(1):89–107.

[159] Wang, Z. L., Dafalias, Y. F., and Shen, C. K. (1990). Bounding surface hypoplasticity model for sand. *Journal of engineering mechanics*, 116(5):983–1001.

[160] Yoshida, N. and Iai, S. (1998). Nonlinear site response and its evaluation and prediction. *in Proc. of Second International Symposium on the Effects of Surface Geology on Seismic Motion, K. Irikura, K. Kudo, H. Okada, and T. Sasatani (Editors)*, 1:71–90.

Appendix A

Benchmark of Iwan group (PRENOLIN project)

MODELING OF 1D WAVE PROPAGATION IN NONLINEAR SOILS USING THE ELASTO-PLASTIC IWAN MODEL BY FOUR NUMERICAL SCHEMES

E.D. Mercerat[1], F. Bonilla[2], S. Chabot[1,2], F. De Martin[3], E. Delavaud[4], C. Gelis[4], N. Glinsky[1,2], J. Kristek[5], L. Lenti[2], P. Moczo[5], E. Oral[4], A. Richterova[5] and M.P. Santisi d'Avila[6]

[1]CEREMA DTerMed, Nice, France. [2]IFSTTAR, Paris, France. [3]BRGM (French Geological Survey), Orleans, France. [4]IRSN, Paris, France. [5]Comenius Univ., Bratislava, Slovakia. [6]LJAD, Univ. de Nice, France

Email: diego.mercerat@cerema.fr

The international project PRENOLIN (improvement of PREdiction of soil NOn-LINear effects caused by strong seismic motion) is focused on verification and validation of numerical codes for ground motion simulations including nonlinear soil rheologies. In this particular study, we present different implementations of the elasto-plastic Iwan model (Iwan 1967) into numerical schemes based on the finite-difference, finite-element, spectral-element and discontinuous-Galerkin methods, and the results based on test numerical simulations.

We first studied the amplification of ground motion in a soft layer with nonlinear behavior overlying a half-space with linear behavior. We assumed a vertically incident plane SH wave and several source-time functions (Gabor wavelet and real accelerograms). They differ in amplitude levels and frequency ranges. Special attention was paid to the hysteresis loops and the reversal points in the stress-strain plane, and their effects on the computed seismograms and corresponding transfer functions. In the second step, we calculated and compared synthetic seismograms for a real velocity profile and real nonlinear soil properties. Eventually we compare key aspects of the applied numerical schemes.

Keywords: numerical modeling, seismic motion, site effect, earthquake engineering

INTRODUCTION

In the recent years, advances in computer architectures render large-scale seismic wave propagation simulations feasible in heterogeneous media. Several numerical methods are available and the final choice of the method is clearly problem dependent. On the other side, it is always necessary to assess the advantages and disadvantages of each methodology, in terms of accuracy, robustness and computational performance when dealing with complex wave propagation phenomena. Such types of benchmarking exercises have already been undertaken in computational seismology for elastic and viscoelastic wave propagation (e.g., Chaljub et al. 2010; Moczo et al. 2010; Chaljub et al. 2015; Maufroy et al. 2015). Yet, numerical methods for nonlinear wave propagation have not been compared in a similar way. The Ashigara valley (Japan) and the Turkey Flat (California) experiments (Kwok et al. 2008) made useful efforts. The two efforts were, however, focused on validation (demonstration of the capability of the theoretical model to predict/reproduce observations) rather than verification (demonstration of the consistency of the numerical method with the original mathematical-physical problem). Another recent example is the PRENOLIN benchmark for nonlinear seismic wave propagation (Régnier et al. 2015). The experience from this project led us to investigations presented in this article.

The main objective of the present study is to quantify and to understand differences among numerical codes for modeling 1D nonlinear wave propagation in soils using the classical and widely used rheological model of Iwan (1967). Four different numerical schemes are used: finite-difference (FD), finite-element (FE), spectral-element (SE) and discontinuous Galerkin finite-element (DG). Nonlinear soil behavior is simply characterized by the shear modulus decay curve vs shear strain and modeled by the elasto-plastic Iwan model which can reproduce any type of decay curve (interpolated from laboratory data). As a reference solution, the classical hyperbolic model with extended Masing rules (Masing 1926, Kramer 1996) for the stress-strain hysteresis is chosen. This particular model is implemented by the BRGM (French Geological Survey) team in the open-source code EFISPEC (De Martin 2011; http://efispec.free.fr) based on the spectral-element method.

ELASTO-PLASTIC SOIL MODEL

The elasto-plastic Iwan model (1967) is implemented in four numerical schemes used for seismic wave simulations by different research teams. The model consists of a number of "elements" constituted by an elastic spring and a Coulomb friction element connected in series. Each element remains locked until the stress reaches the yield stress. After the Coulomb friction element yields, the Iwan element begins to contribute to the total strain. Detailed analysis of the series-parallel Iwan model and its application in nonlinear wave propagation can be found in Joyner and Chen (1975). One interesting point is that the model allows following any laboratory curve of shear modulus decay. Given a laboratory curve, the only free parameter is the number of elasto-plastic elements. In this work, we sample an hyperbolic decay curve with 10, 25 and 50 Iwan elements equidistant in log scale (see Figure 1). Note that even if the interpolation points lie exactly on the hyperbolic model curve, the (linear) decay used by the Iwan model in between each pair of points may be quite far from the expected curve.
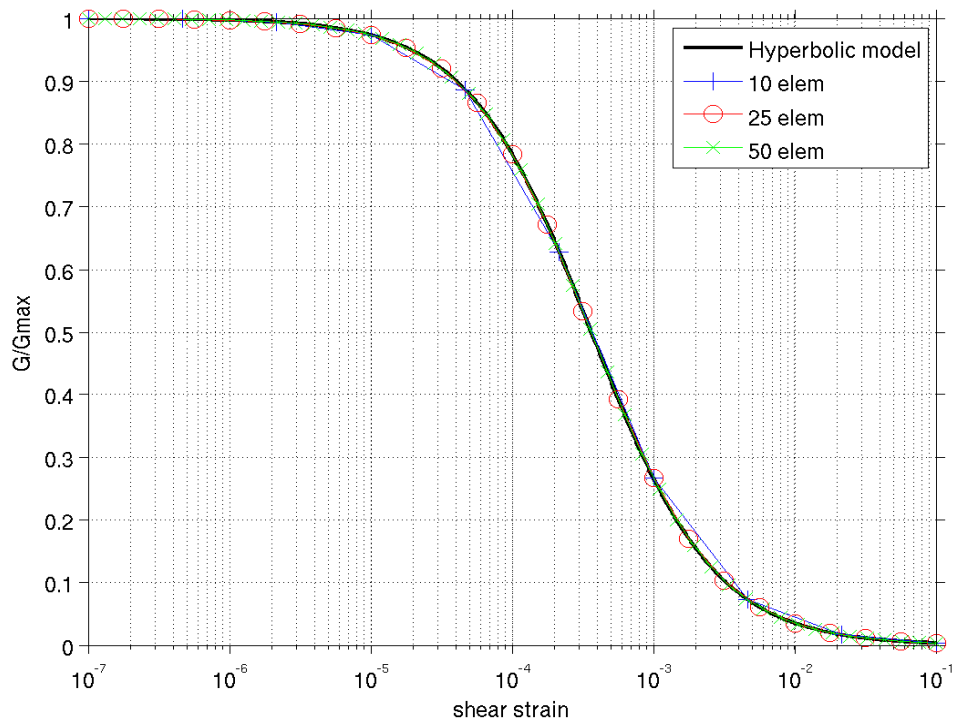
Figure 1: Shear modulus decay curve interpolated by different number of Iwan elements

NUMERICAL SCHEMES

In this paper, we investigate four of the mostly used numerical schemes for seismic wave propagation and earthquake ground motion simulations: finite-difference (FD), finite-element (FE), spectral-element (SE) and discontinuous Galerkin finite-element (DG)). Such wide range of methods allows different spatial and temporal orders of approximation for the continuous elastodynamic problem to be solved. Different strategies for spatio-temporal meshing depending on the desired accuracy and the computational performance can be used. In the first step, we let the different participating teams to choose their order and meshing strategy to be accurate enough for the comparison. In the following step, especially when dealing with 3D wave propagation, these choices can have an impact on the accuracy and performance, and can be further constrained for fair comparison (Chaljub et al, 2015).

In order to perform a comparison of the results obtained by the numerical schemes, we directly compare time histories of stress, strain, velocity and acceleration at different depths of the soil column. In this manner we avoid potential over interpretation when analyzing the results in the frequency domain by smoothing Fourier or response spectra. We assume that a visual comparison of the time histories is sufficient for the intended level of comparison.

The main characteristics of each method are summarized in Table 1. Before we compare results of numerical tests, we will briefly characterize each numerical scheme.

Finite differences (FD)

The FD modeling is based on implementation of the nonlinear stress-strain relation in the 1DFD_DVS code (Moczo et al. 2004). The scheme is based on the displacement-velocity-stress formulation of the equation of motion in 1D. The scheme uses the staggered time-space uniform grid and is 2nd-order

accurate in time and 4th-order accurate in space. The free surface is simulated using the spatially 4th-order adjusted FD scheme for the planar free surface (Kristek et al. 2002). Smooth and discontinuous heterogeneity of the medium is accounted for by effective grid parameters. The effective grid density at a grid position of the particle velocity and displacement is evaluated as an integral arithmetic average of density within a grid cell centered at the grid position of the particle velocity. The effective grid modulus at a grid position of stress is evaluated as an integral harmonic average of modulus within a grid cell centered at the grid position of the stress. Stress is updated from strain at the same grid position at each time level according to Iwan-model stress-strain relation. The size of the spatial grid spacing is determined from a preliminary simulation. This simulation makes it possible to approximate the decrease of speed due to nonlinear behavior.

Continuous finite elements (FE)

Quadratic 1D finite elements with three equidistant nodes are used for spatial discretization. A Newmark algorithm is applied for time discretization with beta=0.3025 and gamma=0.6. This choice allows having an unconditionally stable procedure with numerical damping to reduce high frequency spurious content (Zienkiewicz and Taylor, 1989). Material damping is purely hysteretic. A consistent mass matrix is defined and the dynamic equilibrium equation is directly solved using a small time step (dt=0.0001 sec), consequently at each time step additional iterations are not needed.

Spectral finite elements (SE)

The continuous Galerkin spectral finite elements method (commonly called "spectral elements method") solves the variational formulation of equations of motion. The displacement field and the test vector are expanded in terms of Lagrange polynomials of order n-th (n ranges generally from 4 to 10). The collocation points of the Lagrange polynomials are chosen to be the n+1 Gauss-Lobatto-Legendre (GLL) points (see Canuto et al. 1988, p. 61). The integrals of the variational formulation are computed numerically by a quadrature formulation based on the same GLL points as the one defined for the collocation points. Because of the superimposition of the numerical quadrature points with the collocation points and because of the fundamental property of the Lagrange interpolant, the mass matrix is naturally diagonal (e.g., Zienkiewicz and Taylor, 1989, Ch. 9, pp. 321–322) and, consequently, easily inverted. To take advantage of the diagonal mass matrix, the time-marching is often a fully explicit time scheme (e.g., 2nd order Newmark explicit). The non-linear stress-strain relationship is computed at each GLL points where the stress is computed for a given strain level (itself derived from the displacement computed by the explicit time scheme). For small time steps, no iteration (e.g., Newton-Raphson iteration) to converge to a final displacement is needed.

Discontinous Galerkin finite elements (DG)

The discontinuous Galerkin finite elements are also based on the variational formulation of equations of motion. In this case, a system of two partial differential equations of 1st order in the particle velocity and the shear strain as primal variables are used (Mercerat and Glinsky, 2015). Upwind numerical fluxes are used at each finite element edge. Second-order Lagrange polynomials within each element of the mesh are used to interpolate the strain and velocity fields (nodal approach) and the 4th order Runge-Kutta explicit scheme is used for the time integration (Hesthaven and Warburton, 2008). The Iwan model is explicitly implemented at each interpolation node (belonging to a non-linear finite element of the mesh), that means no iterations are required to obtain a couple stress-velocity compatible with the non-linear system of equations.

Table 1. Main characteristics of the five numerical codes used.

Team	Method	Scheme	Spatial grid	Spatial sampling at minimum λ (G/Gmax = 0.1).	Eq. of motion	Rheology
CUB	FD	Space-Time O(4,2) displ-vel-stress	Uniform Cartesian staggered grid	6 grid points per minimum λ	Strong form	Iwan elastoplastic
BRGM	SE	Lagrange 6th order. GLL integration. 2nd order Newmark explicit	Unstructured grid	7 grid points per minimum λ	Weak form	Hyperbolic model + extended Masing rules
CEREMA	DG	Lagrange interpolation. Upwind fluxes 4th order RK in time	Any FEM grid	5 grid points per minimum λ	Weak form	Iwan elastoplastic
UNICE	FE	Quadratic FE. Gauss integration + Newmark for time integration	3 nodes FE, 3d.o.f per node	10 grid points per minimum λ	Weak form	3D Iwan elastoplastic
IRSN	SE	Lagrange 4th-nth order. GLL integration. 1st order Newmark	Unstructured grid	5 grid points per minimum λ	Weak form	Iwan elastoplastic

NUMERICAL TESTS

As preliminary tests, we verify that the implementations of the elastoplastic Iwan model by different participating teams/codes deliver similar stress-strain curves for the case of simple sinusoidal cyclic loading. After that, each code has been compared in elastic conditions to verify the input motion implementation and the boundary conditions at the bottom of the soil layer. The results (not shown here) are more than satisfactory and all curves match perfectly.

We concentrate then in non-linear 1D wave propagation. In the following three different tests are presented and discussed: a) Gabor input motion - Canonical soil column, b) Real input motion - Canonical soil column; and c) Gabor input motion - Real soil column.

a) Gabor input motion - Canonical soil column

The canonical soil profile considered is borrowed from the PRENOLIN project (P1 profile). It consists of a homogeneous non-linear soil layer of 20 m thickness overlying the bedrock (considered infinitely rigid or elastic). The shear wave velocities (Vs) are 300 m/s and 1000 m/s for the soil and the bedrock, respectively. Thus the resonant frequency of the site is f0 = Vs / 4H = 3.75 Hz.

The numerical grid used for the simulations consists of 20 elements of 1m length. Each team used different spatial interpolations to allow enough sampling of the wavefield even in the case of strong reduction of shear wave velocity (down to G/Gmax=0.1).

The input motion at the bottom of the layer is a Gabor wavelet of fc=3.75 Hz central frequency scaled in amplitude to 1g maximum acceleration. We have investigated lower amplitudes for which the fitting between different codes is similar to the one presented here. The input wavelet and spectrum are shown in Figure 2.

In Figure 3 the output velocity seismograms are shown for every participating team. The output motion for the reference solution is shown (BRGM calculation) and the differences to all the other teams. The results are quite consistent and the maximum relative error is less than 1%. Differences in stress-strain curves are higher, especially for the shear strain calculation as can be seen in Figure 2
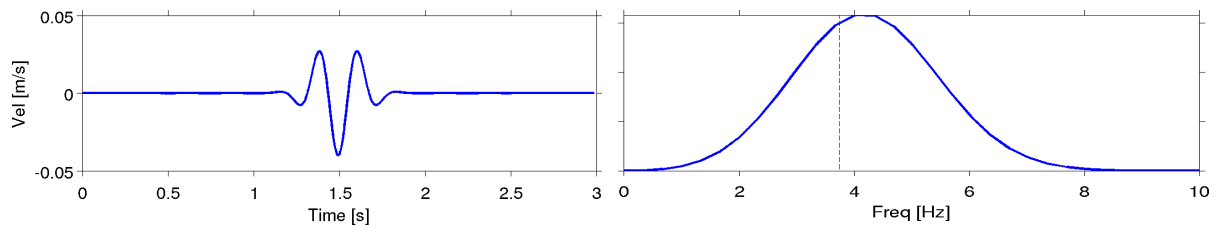

Figure 2: Input Gabor wavelet in time (left) and frequency (right) domains. The resonant frequency of the canonical soil layer is marked with dashed vertical line.
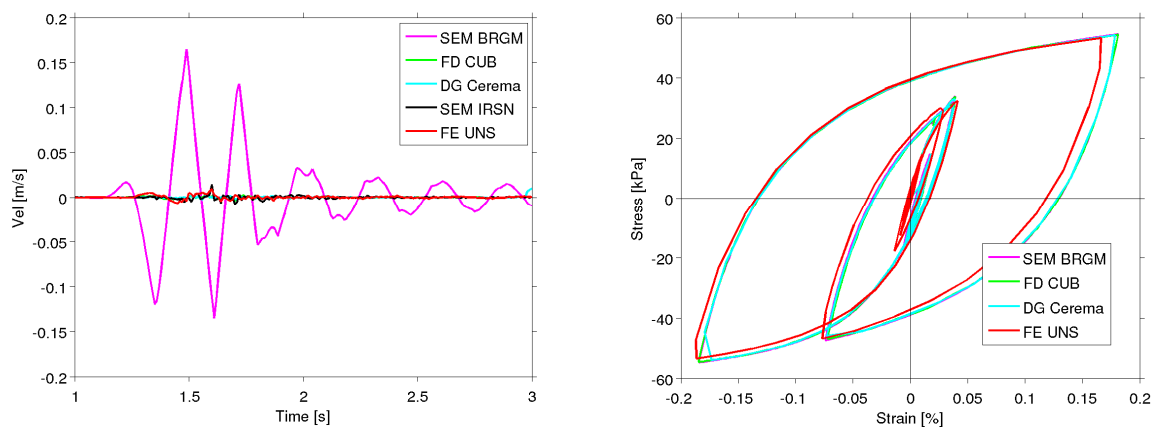

Figure 3: (Left) Velocity seismograms on the top of the soil layer (Z=0 m). The reference solution with hyperbolic non-linear model in pink. Differences to the reference for each team/code in other colors. (Right) Stress-strain curves near the middle of the layer (Z=13 m), Iwan model with 50 elasto-plastic elements at each node.

Further, the influence in the number of elasto-plastic Iwan elements is analyzed. In Figure 4, we can observe the convergence of the solutions (CUB team) to the reference (hyperbolic model) when more than 25 Iwan elements are used at each node. For the moment, we use equidistant interpolation in log-scale of the G/Gmax decay curve. This can be further improved if a non-regular distribution of interpolation points is used.
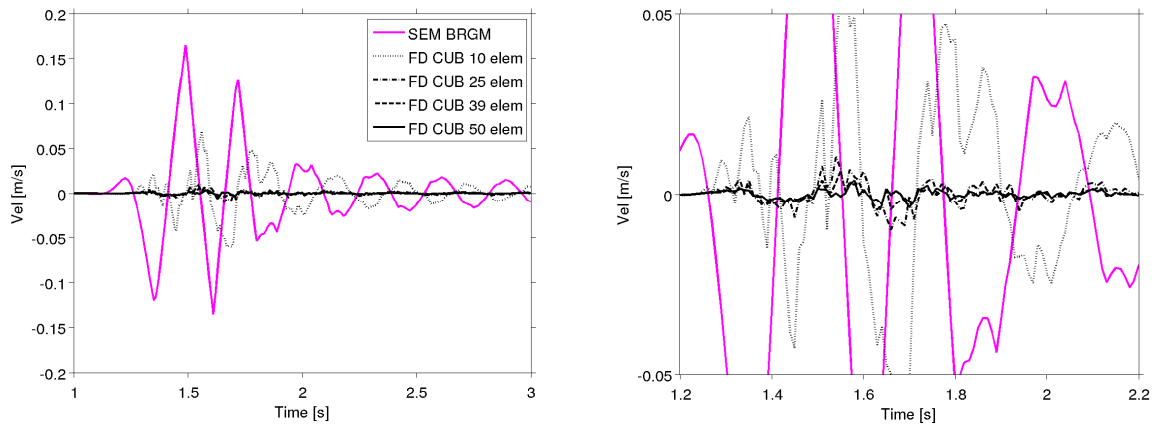
Figure 4: (Left) Velocity seismograms at the top of the soil layer. Reference solution in pink and different solutions for CUB team with different number of Iwan elements per node. (Right) zoom of the previous figure to better appreciate differences between results using increasing number of elements.

b) Real input motions - Canonical soil column

As a second test, we carry out two simulations on the same canonical case as before (P1 profile) using the same discretization and 50 Iwan elements at each node. Two types of input motion are used : one with relatively low frequency content (LF) and another one with higher frequency content (HF). The input motion spectra are shown in Figure 5.
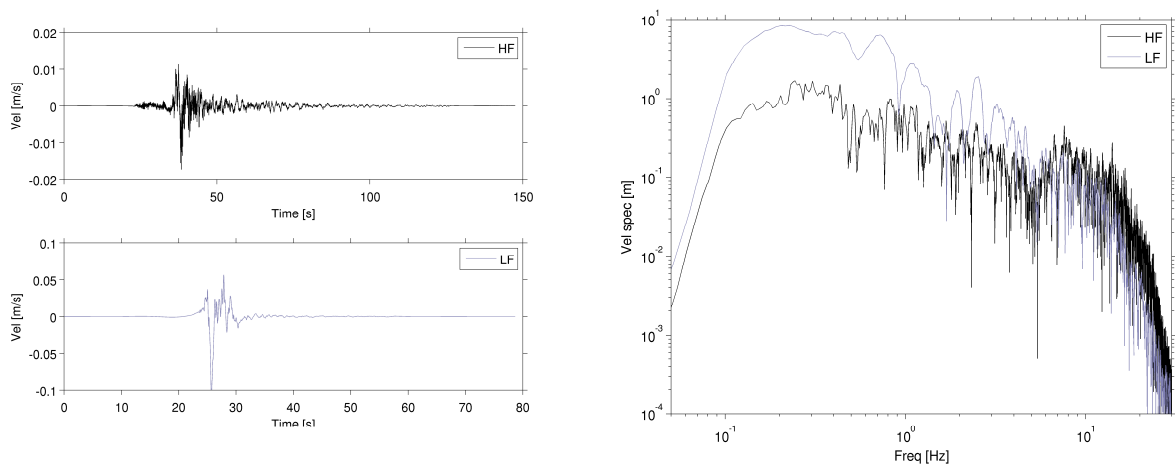

Figure 5: (Left) Velocity input motions at the base of the soil column. (Right) Fourier spectra of the previous traces.
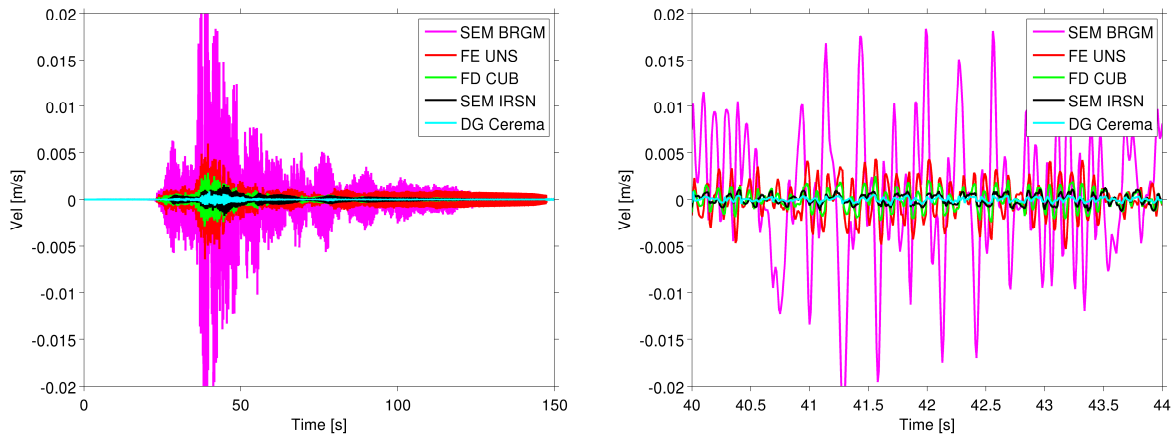
Figure 6: (left) Velocity seismograms at the top of the soil layer for the HF input signal. Reference solution in pink and differences of the other solutions to the reference. (right) Zoom from t=40 s to t=44 s.
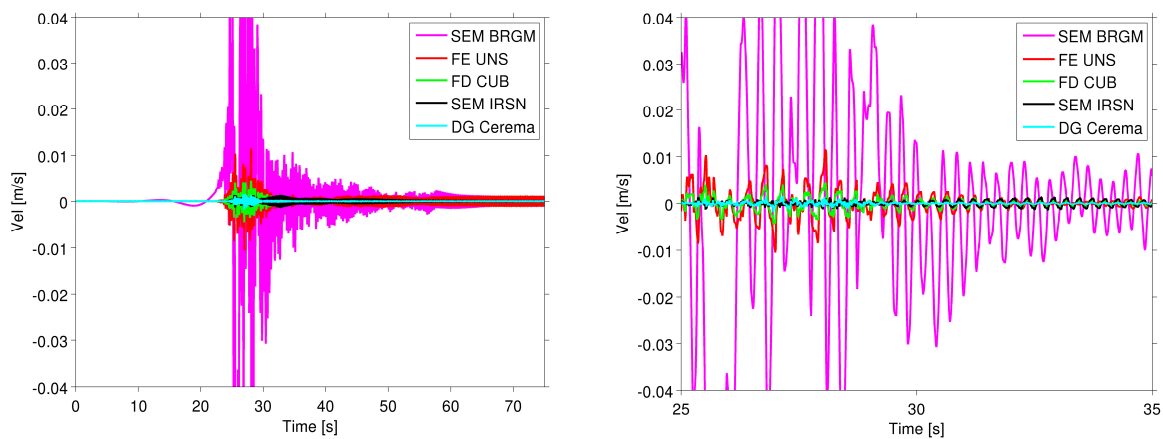

Figure 7: (left) Velocity seismograms at the top of the soil layer for the LF input signal. Reference solution in pink and differences of the other solutions to the reference. (right) Zoom from t=25 s to t=35 s.

In Table 1, the maximum relative differences to the reference solution (taken as the SEM solution for a pure hyperbolic non-linear soil model) are listed for each simulation. Differences between codes are below 10 % and the HF simulations present higher values, surely due to numerical dispersion at higher frequencies.

Table 1. Maximum differences of each team to the reference solution. Relative values to the PGV (peak ground velocity) at Z=0 m.

	FD CUB	SEM IRSN/IFSTTAR	DG CEREMA	FE UNS
HF input motion	0.111	0.066	0.033	0.224
LF input motion	0.041	0.012	0.014	0.102

c) Real soil column (Volvi site)

As a third and final example, the codes are tested in the case of 1D wave propagation in the soil profile near the centre of Volvi basin (northern Greece), a site extensively investigated in several European

projects (EuroSeisTest, EuroSeisRisk, see http://euroseisdb.civil.auth.gr). The distribution of seismic velocities, mass densities and non-linear characteristics of each layer is given in Table 2 (Raptakis et al, 2000). Note that in this case each team/code discretize the soil column independently, and therefore differences are to be expected. Every team accord to use 251 Iwan elements per node in their simulation.

Table 2. Bottom depth and physical parameters of the Volvi soil column (modified from...)

Layer	Depth (m)	Vp(m/s)	Vs(m/s)	ρ(kg/m3)
A	5.5	1500	130	2050
B	17.6	1500	200	2150
C	54.2	1650	300	2075
D	81.2	2050	450	2100
E	131.1	2450	600	2155
F	186.5	2550	700	2200
G	196.4	3500	1250	2500
Rock	206.4	4500	2600	2600
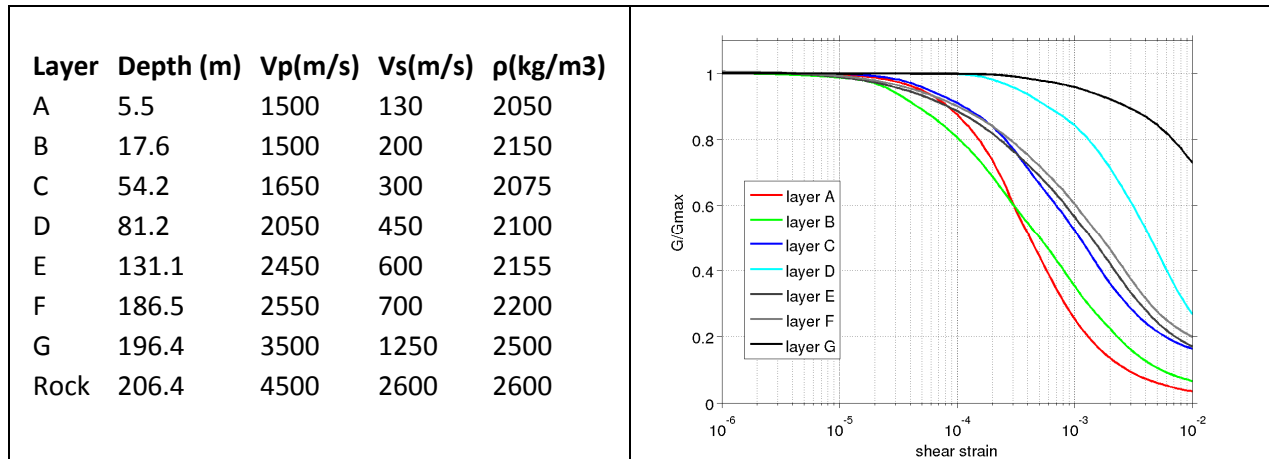
As input motion, a Gabor wavelet is used at the bottom of the soil column. Rigid boundary conditions (imposed input motion) are used at Z=206.4m. The results can be seen in Figure 9 where the velocity seismograms at the top of soil column are compared. Differences are lower than 10% even for this complex soil profile.
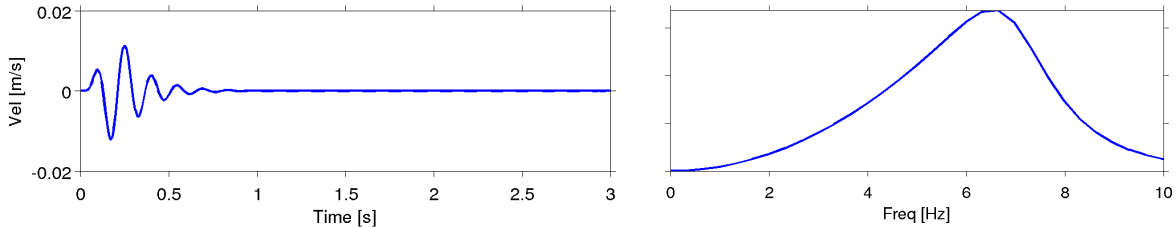

Figure 8: Input motion for the Volvi soil column: (left) velocity time history and (right) Fourier spectrum.
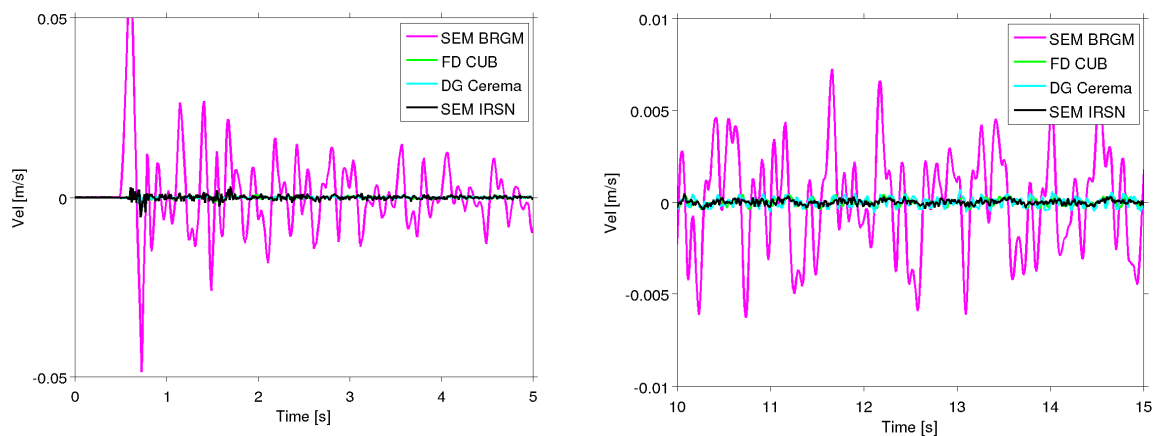

Figure 9: Velocity seismograms at the surface. Volvi soil column: velocity seismogram at Z=0 m of BRGM team in pink and differences to all other teams in other colors (left) between 0 and 5 seconds and (right) between 10 and 15 seconds (different vertical axis).

CONCLUSIONS

We present a detailed comparison of four numerical schemes commonly used in engineering seismology to modeling wave propagation in 1D non-linear media using the Iwan rheological model. Different numerical tests have been carried out in canonical and real soil columns. In a first step we compare the results of different simulations that used the Iwan model against a solution calculated by an analytical expression for the non-linear G/Gmax decay curve. Differences lower than 10% are found between the four different numerical schemes. As a second step, we compare the numerical results of wave propagation in a real soil profile extracted from the Volvi test site, where a non-linear site characterization is also available. In this case the differences remain lower than 10% of the peak ground velocity.

This collaborative work contributes to bring insight in discrepancies commonly encountered in numerical ground motion simulations when different codes are used. As ongoing work, all teams work in the inclusion of the 3D Iwan model for soils. The next step will then concentrate in the comparison of results in the case of coupled seismic wave propagation in 1D soil columns (1D-3C wave propagation) to elucidate if differences will remain the same in 2D/3D non-linear simulations.

REFERENCES

Anderson, J. G. (2004). Quantitative measure of the goodness-of-fit of synthetic seismograms, 13th World Conf. on Earthquake Engineering Conf. Proc., Vancouver, British Columbia, Canada, 1–6 August, Paper Number 243.

Canuto, C., Hussaini, M.Y., Quarteroni, A. & Zang, T.A., (1988). Spectral Methods in Fluid Dynamics, Springer-Verlag, New York.

Chaljub, E., Maufroy, E., Moczo, P., Kristek, J., Hollender, F., Bard, P-Y., Priolo, E., Klin, P., De Martin, F., Zhang, Z., Zhang, W., and Chen, X. (2015). 3D numerical simulations of earthquake ground motion in sedimentary basins: testing accuracy through stringent models. Geophysical Journal International. 201(1), 90-111.

De Martin, F. (2011). Verification of a spectral-element method code for the Southern California Earthquake Center LOH.3 viscoelastic case, Bull. Seismol. Soc. Am. 101, 2855–2865.

Hesthaven J. and Warburton T. (2008) Nodal Discontinuous Galerkin Methods: algorithms, analysis and applications. Springer Verlag.

Kramer, S. (1996) Geotechnical Earthquake Engineering. Prentice-Hall Int.

Kristeková, M., J. Kristek, and P. Moczo (2009). Time-frequency misfit and goodness-of-fit criteria for quantitative comparison of time signals, Geophys. J. Int. 178, 813–825, doi: 10.1111/j.1365-246X.2009.04177.x.

Kristeková, M., J. Kristek, P. Moczo, and S. M. Day (2006). Misfit criteria for quantitative comparison of seismograms, Bull. Seismol. Soc. Am. 96, no. 5, 1836–1850, doi: 10.1785/0120060012.

Raptakis D, F.J. Chavez Garcia, K. Makra, and K. Pitilakis (2000). Site effects at Eurosistest – I Determination of the valley structure and confrontation of observations with 1D analysis, Soil Dynamics and Earthquake Engineering, 19, 1-22.

Zienkiewicz, O. Z., and R. L. Taylor (1989). The Finite Element Method, Fourth Edition, Volume 2: Solid and Fluid Mechanics Dynamics and Non-Linearity, McGraw-Hill, New York.